Lagrangian and vortex-surface fields in turbulence

Thesis by

Yue Yang

In Partial Fulfillment of the Requirements
for the Degree of
Doctor of Philosophy

California Institute of Technology
Pasadena, California

2011
(Defended February 18, 2011)

To my family

Acknowledgments

I wish to acknowledge and thank the many people who have contributed to this thesis.

I am truly grateful to Professor Dale Pullin, my thesis advisor, for his unwavering support and guidance throughout the course of my studies at Caltech. He guided me into an exciting and fascinating research topic that I would not have otherwise thought of. His passion and enthusiasm for research is infectious and will continue to be an enduring inspiration to me. His guidance and encouragement throughout my thesis work made the journey fun and exciting, and enriched my life.

I would like to thank the members of my thesis committee, Professors Anthony Leonard, Yizhao Hou, and Daniel Meiron for their helpful comments, as well as Professor Yao-Tsu Wu for sharing many wonderful experiences on research. My thanks also go to Professor Guo-wei He of the Institute of Mechanics, Chinese Academy of Sciences (CAS), who introduced me to turbulence research when I was a Masters student at CAS, and for his continuous support and encouragement while I studied at Caltech.

My time at Caltech was rich and rewarding. I would like to thank my fellow graduate students at GALCIT and Caltech C, Ivan Bermejo-Moreno, Daniel Chung, Michio Inoue, Andrew Tchieu, and my roommate Ran Duan for their friendships and many research discussions. My special thanks go to Ling Zheng and Yi Liu for their help and support during my first year at Caltech.

Finally, I am forever indebted to my parents and grandparents for their most precious gift to me—love. I can never thank them enough for the love, understanding, patience, and encouragement that they unselfishly gave me when I needed them most.

This research has been supported in part by the National Science Foundation under grants DMS-0714050 and DMS-1016111.

Abstract

In this thesis, we focus on Lagrangian investigations of isotropic turbulence, wall-bounded turbulence and vortex dynamics. In particular, the evolutionary multi-scale geometry of Lagrangian structures is quantified and analyzed. Additionally, we also study the dynamics of vortex-surface fields for some simple viscous flows with both Taylor–Green and Kida–Pelz initial conditions.

First, we study the non-local geometry of finite-sized Lagrangian structures in both stationary, evolving homogenous isotropic turbulence and also with a frozen turbulent velocity field. The multi-scale geometric analysis is applied on the evolution of Lagrangian fields, obtained by a particle-backward-tracking method, to extract Lagrangian structures at different length scales and to characterize their non-local geometry in a space of reduced geometrical parameters. Next, we report a geometric study of both evolving Lagrangian, and also instantaneous Eulerian structures in turbulent channel flow at low and moderate Reynolds numbers. A multi-scale and multi-directional analysis, based on the mirror-extended curvelet transform, is developed to quantify flow structure geometry including the averaged inclination and sweep angles of both classes of turbulent structures at multiple scales ranging from the half-height of the channel to several viscous length scales. Results for turbulent channel flow include the geometry of candidate quasi-streamwise vortices in the near-wall region, the structural evolution of near-wall vortices, and evidence for the existence and geometry of structure packets based on statistical inter-scale correlations.

In order to explore the connection and corresponding representations between Lagrangian kinematics and vortex dynamics, we develop a theoretical formulation and numerical methods for computation of the evolution of a vortex-surface field. Iso-surfaces of the vortex-surface field define vortex surfaces. A systematic methodology is developed for constructing smooth vortex-surface fields for initial Taylor–Green and Kida–Pelz velocity fields by using an optimization approach. Equations describing the evolution of vortex-surface fields are then obtained for both inviscid and viscous incompressible flows. Numerical results on the evolution of vortex-surface fields clarify the continuous vortex dynamics in viscous Taylor–Green and Kida–Pelz flows including the vortex reconnection, rolling-up of vortex tubes, vorticity intensification between anti-parallel vortex tubes, and vortex stretching and twisting. This suggests a possible scenario for explaining the transition from a smooth laminar flow to turbulent flow in terms of topology and geometry of vortex surfaces.

Contents

List of Figures

List of Tables

Chapter 1

Introduction

1.1 Lagrangian studies of turbulence

The Lagrangian method for the study of turbulence, originated by Taylor (1922), is a classical but challenging approach, which involves tracking the trajectories of fluid particles. Recent progress has seen the combination of modern supercomputation and advanced experimental facilities, thus offering real promise for advancing our understanding of Lagrangian turbulence (see Toschi & Bodenschatz, 2009). To date most studies of Lagrangian turbulence have focused on the statistics of single particles (see Yeung, 2002), particle pairs (see Sawford, 2001), and particle triangles or tetrahedrons (e.g., Pumir, Shraiman & Chertkov, 2000). Earlier, Batchelor (1952b) showed that the area of material surface elements increases exponentially as a consequence of conservation of mass of the fluid. The Lagrangian-history, direct interaction approximation developed by Kraichnan (1965) can provide quantitative predictions of single particle or particle-pair statistics in isotropic turbulence. Signature stretching and folding effects on Lagrangian structures in low Reynolds number flows were demonstrated in the chaotic advection theory of Aref (1984). Several stochastic models for local statistical and geometric structure in three-dimensional isotropic turbulence based on the properties of the velocity gradient tensor have been developed to show the material deformation history of fluid elements (e.g., Girimaji & Pope, 1990; Chertkov, Pumir & Shraiman, 1999; Li & Meneveau, 2007). Up to now, however, no general theory for Lagrangian turbulence exists, especially one that clarifies the non-local geometry (in the surface sense) of finite-sized Lagrangian structures or material surfaces in turbulence. Knowledge of Lagrangian structures can also help elucidate various applications in fluid dynamics, for example, scalar mixing (see Warhaft, 2000), premixed combustion (see Pope, 1987), and aquatic animal locomotion (see Peng & Dabiri, 2008).

While recent progress in particle tracking techniques in turbulent experiments have demonstrated a promising capability for investigation of two-particle dispersion and Lagrangian tetrahedrons in three-dimensional turbulence (e.g., Bourgoin et al., 2006; Xu et al., 2008; Salazar & Collins, 2009), in order to follow coherent Lagrangian structures, tens and hundreds of thousands or even millions of particles need to be tracked simultaneously and instantaneously under some specified topological order. This task seems formidable for current experimental facilities. Finally, for numerical simulation, tracking finite-sized Lagrangian structure requires huge computational resources. In evolution, the geometry of Lagrangian structures typically becomes highly convoluted with some portions almost singular and hard to resolve (Pope, Yueng & Girimaji, 1989; Goto & Kida, 2007; Leonard, 2009). Constraints on structure evolution are that the topology should be invariant and the volume conserved. Hence, a stable and topology-preserving method is required to track Lagrangian structures.

1.2 Vortex dynamics in the Lagrangian framework

The Lagrangian formulation provides a revealing theoretical framework for studying kinematics of turbulence and various turbulent transport phenomena. On the other hand, in order to study dynamics of turbulent flows themselves based on the Lagrangian framework, we may need to find a particular scalar field which can be directly mapped to the vorticity field for tracking vortex motions.

Vortex dynamics has become an important paradigm within theoretical fluid mechanics with a substantial impact on many applications in fluid systems (e.g., Saffman, 1992; Majda & Bertozzi, 2001). Helmholtz (1858) obtained a central result in vortex dynamics, namely that vortex lines or surfaces move with fluid in a perfectly inviscid flow. This means that material lines or surfaces that were initially vortex lines or surfaces are vortex lines or surfaces for all time. Presently we define a 'vortex surface' (the term 'vorticity surface' is used instead in some literature)—examples of which are tube-like or sheet-like geometries—as a smooth surface or manifold embedded within a three-dimensional velocity field, which at a time instant t, has the property that the local vorticity vector is tangent at every point on the surface. We further define a 'Lagrangian field', say $\phi(x, y, z, t)$, as a scalar field whose iso-surfaces evolve as Lagrangian material surfaces, and a 'vortex-surface field' (VSF) $\phi_v(x, y, z, t)$ as a smooth scalar field whose iso-surfaces are vortex surfaces, either instantaneously or in evolution. This concept was utilized by Clebsch (1859) in developing a Lagrangian formulation of the Euler equations for incompressible inviscid flow where each vortex line is expressed, at least locally, by the intersection of iso-surfaces of Clebsch potentials. More recently vortex dynamics has been interpreted in terms of the Clebsch potentials (e.g., Lamb, 1932; Truesdell, 1954; Pumir, Shraiman & Siggia, 1992) while the classical Clebsch representation has been extended to build Eulerian–Lagrangian frameworks for Navier–Stokes dynamics (e.g., Constantin, 2001; Ohkitani & Constantin, 2003; Cartes, Bustamante & Brachet, 2007). The global existence of VSFs and smooth Clebsch potentials is, however, less obvious. Although the Helmholtz vorticity theorem has been utilized for more than 150 years, we know of no Lagrangian study of the evolution of complete and globally smooth vortex surfaces in general three-dimensional flows. Challenges exist in both the initial construction and tracking of vortex surfaces or VSFs.

1.3 Evolutionary geometry of Lagrangian structures/vortex surfaces

In the paradigm of the energy cascade, three-dimensional turbulence is often viewed as composed of different scales with energy transferred from large scales to small scales in a self-similar process (e.g., Davidson, 2004). To investigate the temporal evolution of turbulent structures, Lagrangian methods can be useful in clarifying the cascade process. In particular, while for inviscid flow, vortex surfaces are Lagrangian material surfaces, little is understood concerning their evolutionary geometry.

A hierarchy of vortex sizes appears to be involved in this multi-stage process. In recent work, the multi-scale geometrical decomposition of instantaneous passive scalar (Bermejo-Moreno & Pullin, 2008), enstrophy, and dissipation fields (Bermejo-Moreno, Pullin & Horiuti, 2009) showed a geometrical progression from blobs through tubes to sheet-like structures with decreasing physical length scales. Because the Eulerian fields analyzed are obtained at a particular time instant, their geometrical decomposition does not unfold or clarify the geometry of the dynamical eddy evolution or breakdown process itself. This is an important question that is pertinent to cascade ideas put forward by Richardson that have been cast in similarity and statistical form by Kolmogorov and others. Furthermore, the knowledge of geometry of turbulent structures can inform a vorticity-based, small-scale description of turbulence (Lundgren, 1982; Pullin & Saffman, 1993) from which subgrid-scale models suitable for large-eddy simulation (LES) can be constructed (e.g., Misra & Pullin, 1997; Chung & Pullin, 2009). Through the Helmholtz vorticity theorem and the construction of possible VSFs, the evolutionary geometry of vortex surfaces may be relevant to the mechanism of vortex reconnection (Kida & Takaoka, 1994), the scenario of transition from laminar flow to turbulent flow (e.g., Brachet et al., 1983), and the possible finite-time singularity in Euler dynamics (e.g., Kerr, 1993; Hou & Li, 2008).

For wall-bounded turbulence, coherent motions or structures with particular tube-like and hairpin- or Λ-like shapes have been extensively observed and reported from visualizations of laboratory experiments and numerical simulations. Although the mechanisms of turbulent coherent, near-wall structures are still not fully understood, over the past several decades many studies have showed that they are important for drag reduction, turbulent control, and other applications (see Robinson, 1991; Panton, 2001). In addition, the scaling laws and high-order statistics of the mean velocity and velocity fluctuations are influenced by turbulent coherent structures, such as hairpin vortices in the near-wall region (see Adrian, 2007) and large-scale structures in the outer layer (see Hutchins & Marusic, 2007). The quantified, evolutionary geometry of Lagrangian structures may clarify the structural evolution of near-wall vortices, with initially almost spanwise orientation within the buffer region very close to the wall, into possible Λ-like or hairpin vortices at larger wall distance.

1.4 Outline of thesis

In the present work, we begin in § 2 by developing a theoretical formulation describing Lagrangian structures in terms of the Lagrangian field in turbulence. Then, computational methods for tracking the Lagrangian field and a diagnostic tool for analyzing multi-scale geometric features are introduced and applied to homogeneous isotropic turbulence.

For wall-bounded turbulence, in § 3, a systematic framework is introduced to quantify geometries including averaged inclination and sweep angles of flow structures at multiple scales in turbulent channel flows. The multi-scale and multi-directional geometric methodology is applied to investigate the geometry of Lagrangian structures at different length scales in time evolution. For comparison, the geometry of some typical Eulerian structures is also studied.

In § 4, we first develop a systematic methodology for constructing VSFs for both Taylor–Green and Kida–Pelz initial velocity fields and then derive equations describing the evolution of VSFs. This is followed by a study of the local and non-local evolutionary geometry of Lagrangian surfaces, that were initially vortex surfaces, as an approximation to vortex surfaces at later times.

The numerical method for computation of the evolution of the VSF in viscous incompressible flows with simple topology and geometry is developed in § 5. Corresponding numerical results demonstrate continuous vortex dynamics in terms of topology and geometry of vortex surfaces.

Finally, general conclusions are summarized in § 6.

Chapter 2

Lagrangian structures in homogenous isotropic turbulence

2.1 Background and objectives

The main purpose of this chapter is to describe the non-local, multi-scale geometry of Lagrangian structures in the cascade process in turbulence. In Fourier space, the velocity field can be projected onto Fourier basis functions that represent, in some statistical sense, the hierarchy of eddy sizes. Although it is natural to present the energy spectrum in Fourier space, it is often difficult to attribute physical meaning to the amplitudes of the basis-function coefficients in terms, for example of structural elements such as vortical structures with different geometry like tubes and sheets. An attractive physically intuitive idea of energy cascade might be cast in terms of vortex dynamics where vortex stretching is a crucial agent. But the participating eddies may not be the often portrayed cartoon, blob-like structures of different sizes. While sheet and tubes are attractive alternative geometries, there exist few relevant quantitative models with predictive or even postdictive capability. When the Reynolds number is infinite, vortex lines and surfaces can be considered as material lines and surfaces that are progressively stretched by chaotic motion in the inertial range to form highly convoluted shapes. This mechanism can occur at all scales, but the most efficient transfer of energy is perhaps caused by the interaction of vortices with similar sizes. There is, however, no explicit length scale in the vorticity equation in physical space. This suggests that a multi-scale method based on transforms with basis functions that are localized both in Fourier space and physical space is required (e.g., Meneveau, 1991; Farge, 1992). Furthermore, the knowledge of geometry of turbulent structures can inform a vorticity-based, small-scale description of turbulence (Lundgren, 1982; Pullin & Saffman, 1993) from which subgrid-scale models suitable for LES can be constructed (e.g., Misra & Pullin, 1997; Chung & Pullin, 2009).

At the level of diagnostics of large numerical databases obtained from both experiment and direct numerical simulation (DNS), several non-local methodologies have recently been developed for the purpose of identifying structures in turbulence. A scheme for defining 'Lagrangian coherent structures' in three-dimensional flows was constructed by Haller (2001) using direct Lyapunov exponents along fluid trajectories. An extended structural and fractal description of turbulence has been proposed by Moisy & Jiménez (2004) utilizing a box-counting method applied to sets of points of intense vorticity and strain-rate magnitude. Extended dissipation elements were defined by Wang & Peters (2006) as the ensemble of grid cells from which the same pair of extremal points of the scalar field can be reached.

A topic closely related to the Lagrangian description is scalar advection-diffusion at very high Schmidt numbers in turbulence where mixing of passive tracers occurs with an extremely small molecular diffusivity. Recent work has confirmed the existence of intermittently distributed sheet-like structures for scalar gradients (Ruetsch & Maxey, 1992; Brethouwer, Hunt & Nieuwstadt, 2003) or scalar variance dissipation (Schumacher, Sreenivasan & Yeung, 2005). Some iso-contour plots can mimic geometry properties in Lagrangian turbulence but not in a rigorous sense, because there is no smallest scale in Lagrangian scalar dispersion without diffusion and the topology of iso-surfaces of the Lagrangian field must be invariant in evolution.

In this chapter, we address the multi-scale geometric analysis of Lagrangian structures in isotropic turbulence through direct numerical simulations. In § 2.2, a systematic framework is introduced to describe Lagrangian structures by the Lagrangian field in turbulence. In § 2.3, we will describe a backward particle-based method for tracking Lagrangian structures. In § 2.4, based on numerical results and theoretical estimations, we then consider the area growth rate of Lagrangian surfaces and discuss the formation of stretched and rolled-up structures with local flow patterns. § 2.5 describes our application of the multi-scale geometric analysis developed by Bermejo-Moreno & Pullin (2008) to investigate the non-local geometry of Lagrangian structures in time evolution at different length scales. Some conclusions are drawn in § 2.6.

2.2 Description of Lagrangian structures in turbulence

2.2.1 Lagrangian dynamic equations for incompressible flow

Because the Lagrangian description is related directly to motion of individual fluid particles, it can provide a different perspective to the Eulerian description for the study of turbulent transport or the deformation of material surfaces and lines in a turbulent flow (see Monin & Yaglom, 1975). In this section, we will present a brief literature survey on the description of Lagrangian structures in turbulence and establish a formal theoretical framework in this study.

The trajectory of a fluid particle can be calculated by solving the kinematic equation

$$\frac{\partial \boldsymbol{X}}{\partial t} = \boldsymbol{V}, \tag{2.1}$$

where $\boldsymbol{X} = \boldsymbol{X}(\boldsymbol{X}_0, t_0|t)$ is the location at time t of the fluid particle that was located at $\boldsymbol{X}_0$ at the initial time t_0 with $\boldsymbol{X} = (X_1, X_2, X_3)$ and $\boldsymbol{X}_0 = (X_{01}, X_{02}, X_{03})$, and $\boldsymbol{V} = \boldsymbol{V}(\boldsymbol{X}_0, t_0|t)$ is the velocity at time t of the fluid particle with $\boldsymbol{V} = (V_1, V_2, V_3)$. We use an upper case letter to denote a Lagrangian variable and a lower case letter letter for an Eulerian variable. The Lagrangian dynamic equation of incompressible flow is (see Monin & Yaglom, 1975)

$$\begin{aligned}\frac{\partial \boldsymbol{V}}{\partial t} &= \frac{1}{\rho}\left[X_j, X_k, p\right] + \nu\left\{\left[X_2, X_3, \left[X_2, X_3, \frac{\partial X_i}{\partial t}\right]\right]\right.\\ &\left.+\left[X_3, X_1, \left[X_3, X_1, \frac{\partial X_i}{\partial t}\right]\right] + \left[X_1, X_2, \left[X_1, X_2, \frac{\partial X_i}{\partial t}\right]\right]\right\}, \qquad (2.2)\end{aligned}$$

where ρ is the constant fluid density, p is the pressure, ν is the kinematic viscosity, and the abbreviated notation for the Jacobians is

$$[A, B, C] = \frac{\partial(A, B, C)}{\partial(X_{01}, X_{02}, X_{03})}. \qquad (2.3)$$

The numerical solution of either (2.1) and (2.2) or the equations of the equivalent continuum-mechanics formulation (e.g., Marsden & Hughes, 1994) is formidable owing to the cubic and fifth-order nonlinearity for the pressure term and the viscous term, respectively, in the right-hand side of (2.2). Alternatively, the Lagrangian velocity for a fluid particle can be expressed as its local Eulerian velocity

$$\boldsymbol{V}(\boldsymbol{X}_0, t_0|t) = \boldsymbol{u}(\boldsymbol{X}(\boldsymbol{X}_0, t_0|t), t) \qquad (2.4)$$

which can be solved for individual particles using a prior solution of the Navier–Stokes equation in Eulerian coordinates.

2.2.2 Lagrangian infinitesimal line and surface elements

The evolution of Lagrangian infinitesimal line elements $\boldsymbol{l} = \boldsymbol{X}^{(1)} - \boldsymbol{X}^{(2)}$ between a pair of fluid particles and (vector) surface elements $\boldsymbol{A} = \boldsymbol{l}^{(1)} \times \boldsymbol{l}^{(2)}$ in turbulence was first analyzed by Batchelor (1952b). Because the volume of closed Lagrangian surfaces is conserved and any material line is stretched because of the convective nature of turbulence, the surface area $A(t)$ of Lagrangian structures will increase with time in evolution. Batchelor (1952b) proposed the exponential growth of the surface area for infinitesimal material elements

$$A(t) \sim A_0 \exp(\xi t), \qquad (2.5)$$

where ξ is the growth rate and $A_0 \equiv A(t = 0)$, which was then verified numerically by Girimaji & Pope (1990).

By tracking the Cauchy–Green tensor of deformation in isotropic turbulence, Girimaji & Pope

(1990) found that an initially spherical infinitesimal volume of fluid deforms into an ellipsoid with tube-like or sheet-like shapes in a finite time. Similar results were obtained by Pumir et al. (2000) using Lagrangian tetrahedrons. The evolution of infinitesimal elements and the Lagrangian models based on local velocity gradient tensors can provide valuable insight into the geometry of small-scale Lagrangian structures. These approaches cannot however, elucidate the geometry of finite-sized Lagrangian structures that could exhibit multiple scales with differing local geometries in evolution.

2.2.3 Lagrangian field and finite-sized Lagrangian structures

Because two fluid particles, however close initially, tend to separate in turbulent flow (see Sawford, 2001), a finite-sized Lagrangian structure cannot be described by the product of infinitesimal line elements for long times. Its motion can be expressed as that of an ensemble of particles comprising a material surface where each particle is marked by a constant scalar value in evolution in the interval t_0 to t

$$\phi(\boldsymbol{X}(\boldsymbol{X}_0, t_0|t), t) = \phi(\boldsymbol{X}_0, t_0). \tag{2.6}$$

A scalar field can be associated with these particles

$$\phi(\boldsymbol{x}, t) = \int \psi(\boldsymbol{x}, t)\phi(\boldsymbol{X}(\boldsymbol{X}_0, t_0|t), t)\mathrm{d}\boldsymbol{X}, \tag{2.7}$$

by the Lagrangian position function

$$\psi(\boldsymbol{x}, t) \equiv \delta(\boldsymbol{x} - \boldsymbol{X}(\boldsymbol{X}_0, t_0|t)). \tag{2.8}$$

From (2.6) and (2.7), the initial scalar field at $t = t_0$ can be written as

$$\phi(\boldsymbol{x}, t_0) = \int \psi(\boldsymbol{x}, t_0)\phi(\boldsymbol{X}_0, t_0)\mathrm{d}\boldsymbol{X}_0 \tag{2.9}$$

where (see Pope, 2000)

$$\psi(\boldsymbol{x}, t_0) = \delta(\boldsymbol{x} - \boldsymbol{X}_0). \tag{2.10}$$

The Lagrangian position function $\psi(\boldsymbol{x}, t)$ is determined by the particle trajectory $\boldsymbol{X}(\boldsymbol{x}_0, t_0|t)$, solving (2.1) either forward or backward in time. Thus, from (2.7)–(2.10) an instantaneous scalar field can be mapped to the initial scalar field as

$$\phi(\boldsymbol{x}, t) \longleftrightarrow \phi_0 \equiv \phi(\boldsymbol{x}, t_0), \tag{2.11}$$

by an ensemble of marked particles at t_0 and t and their trajectories or Lagrangian characteristics represented by Lagrangian position functions $\psi(\boldsymbol{x}, t)$.

In fact the motion of marked particles can be related to a kind of scalar diffusion (Batchelor, 1952a). Differentiating (2.8) with respect to time yields the equation of motion for ψ

$$\frac{\partial \psi}{\partial t} = -\frac{\partial X_i}{\partial t}\delta_i'(\boldsymbol{x} - \boldsymbol{X}), \tag{2.12}$$

where

$$\delta_1'(\boldsymbol{x} - \boldsymbol{X}) = \delta'(x_1 - X_1)\delta(x_2 - X_2)\delta(x_3 - X_3),$$

with

$$\delta'(x_1 - X_1) = \frac{\partial}{\partial x_1}\delta(x_1 - X_1).$$

Substituting (2.1) and (2.4) into (2.12), we obtain

$$\frac{\mathrm{D}\psi}{\mathrm{D}t} = \frac{\partial \psi}{\partial t} + u_i\frac{\partial \psi}{\partial x_i} = 0. \tag{2.13}$$

Next, integrating (2.13) with an ensemble of marked particles $\phi(\boldsymbol{X}_0, t_0)$ at any initial time t_0 as

$$\int \frac{\mathrm{D}\psi}{\mathrm{D}t}\phi(\boldsymbol{X}_0, t_0)\mathrm{d}\boldsymbol{X}_0 = \frac{\mathrm{D}}{\mathrm{D}t}\int \psi(\boldsymbol{x}, t_0)\phi(\boldsymbol{X}_0, t_0)\mathrm{d}\boldsymbol{X}_0 = 0 \tag{2.14}$$

together with the mapping (2.11) of $\phi(\boldsymbol{x}, t)$ between two time instants shows that the marked particle problem is a special case of the passive scalar dispersion without molecular diffusion

$$\frac{\partial \phi}{\partial t} + \boldsymbol{u}\cdot\nabla\phi = 0. \tag{2.15}$$

In this work, we will use the term ‘Lagrangian field’ to denote the non-diffusive passive scalar $\phi(\boldsymbol{x}, t)$ whose evolution is described by (2.15). The multi-scale geometric analysis of Lagrangian structures will later be obtained from the statistical geometry of iso-surfaces of $\phi(\boldsymbol{x}, t)$ at different scales.

2.2.4 Spectrum of the Lagrangian field

Under the straining motion of a velocity field $\boldsymbol{u}(\boldsymbol{x}, t)$, Lagrangian material surfaces that are iso-surfaces of $\phi(\boldsymbol{x}, t)$ governed by (2.15) are stretched and folded, which will generally amplify the local scalar gradient and thereby cause the characteristic length scale of the scalar field to continually decrease. To investigate this cascade process of the Lagrangian field in a periodic domain we first consider the Fourier expansions

$$\boldsymbol{u}(\boldsymbol{x}, t) = \sum_{\boldsymbol{k}} \hat{\boldsymbol{u}}(\boldsymbol{k}, t)\mathrm{e}^{\mathrm{i}\boldsymbol{k}\cdot\boldsymbol{x}}, \tag{2.16}$$

$$\phi(\boldsymbol{x}, t) = \sum_{\boldsymbol{k}} \hat{\phi}(\boldsymbol{k}, t)\mathrm{e}^{\mathrm{i}\boldsymbol{k}\cdot\boldsymbol{x}}. \tag{2.17}$$

Substituting into (2.15) then gives

$$\frac{\partial}{\partial t}\hat{\phi}(\boldsymbol{k},t) + \mathrm{i}k_m \sum_{\boldsymbol{k}=\boldsymbol{p}+\boldsymbol{q}} \hat{u}_m(\boldsymbol{p},t)\hat{\phi}(\boldsymbol{q},t) = 0, \tag{2.18}$$

which expresses the interaction of wavenumber triads, $\boldsymbol{k}$, $\boldsymbol{p}$, and $\boldsymbol{q}$. The equation of the scalar spectrum density

$$\Phi(\boldsymbol{k},t) = \langle \hat{\phi}(\boldsymbol{k},t)\hat{\phi}(-\boldsymbol{k},t)\rangle \tag{2.19}$$

can then be obtained from (2.18) by multiplying $\hat{\phi}(-\boldsymbol{k},t)$ and averaging

$$\frac{\partial}{\partial t}\Phi(\boldsymbol{k},t) + \mathrm{i}k_m \sum_{\boldsymbol{k}=\boldsymbol{p}+\boldsymbol{q}} \langle \hat{u}_m(\boldsymbol{p},t)\hat{\phi}(\boldsymbol{q},t)\hat{\phi}(-\boldsymbol{k},t)\rangle = 0. \tag{2.20}$$

In general, in high-Reynolds-number turbulence, the Lagrangian scalar cascade transports $\Phi(\boldsymbol{k},t)$ to higher and higher wavenumbers by the nonlinear interaction of wavenumber triads $\boldsymbol{k} = \boldsymbol{p} + \boldsymbol{q}$ without dissipation, which implies that the Lagrangian field with a smooth initial condition may develop exponentially small structures as $t \to \infty$. Furthermore, the Lagrangian field is still able to develop exponentially small-scale structures even in a steady, low-Reynolds-number flow, which is referred as ‘chaotic advection’ (Aref, 1984).

In the sequel, we distinguish between Lagrangian turbulence dynamics and kinematics. The Kolmogorov–Obukhov–Corrsin theory (Monin & Yaglom, 1975) states that, in high-Reynolds-number flow, the cascade process of a passive scalar is controlled by the large eddy turnover time T_e independent of molecular viscosity. This implies that for $t > T_e$, the cascade is dominated by motions with scales smaller than the Kolmogorov length scale, which may be of lesser importance for the Lagrangian dynamics of turbulence. We therefore choose T_e as the largest time in the investigation of the time evolution of Lagrangian structures. Although the analysis above indicates that the characteristic scale of Lagrangian structures decreases as time increases, Fourier-space representation is not well suited to an investigation of the finite geometry of the Lagrangian field and corresponding non-local Lagrangian structures. This issue will be addressed in § 2.4.2 by analysis of the scalar-gradient alignment and in § 2.5 by multi-scale geometric decomposition.

2.3 Simulation overview

2.3.1 Direct numerical simulation

The Navier–Stokes equations for forced homogeneous and isotropic turbulence in a periodic box of side $L = 2\pi$ are written in the general form

$$\left.\begin{aligned} &\frac{\partial \boldsymbol{u}}{\partial t} = \boldsymbol{u} \times \boldsymbol{\omega} - \nabla \left(\frac{p}{\rho} + \frac{1}{2}|\boldsymbol{u}|^2 \right) + \nu \nabla^2 \boldsymbol{u} + \boldsymbol{f}(\boldsymbol{x}, t), \\ &\nabla \cdot \boldsymbol{u} = 0, \end{aligned}\right\} \tag{2.21}$$

where $\boldsymbol{\omega} \equiv \nabla \times \boldsymbol{u}$ is the vorticity. In this study, the flow was driven by a random forcing $\boldsymbol{f}(\boldsymbol{x}, t)$ which is non-zero for the Fourier modes with the wavenumber magnitude less than two.

The DNS of isotropic and homogeneous turbulence was performed using a standard pseudo-spectral method on a 256^3 grid. The flow domain was discretized uniformly into N^3 grid points. Aliasing errors were removed using the two-thirds truncation method. A stationary turbulence was generated by maintaining constant total energy in each of the first two wavenumber shells, with the energy ratio between the two shells consistent with $k^{-5/3}$. The spatial resolution in spectral simulation is evaluated as $k_{max}\eta$, where $\eta \equiv (\nu/\epsilon)^{1/4}$ is the Kolmogorov length scale and the maximum wavenumber k_{max} is about $N/3$. Proper resolution of the Kolmogorov scale requires $k_{max}\eta > 1$. The value of $k_{max}\eta$ was typically larger than 4.3 in our simulation to ensure that we obtained accurate velocity fields for further Lagrangian computations. The Fourier coefficients of the flow velocity were advanced in time using a second-order Adams–Bashforth method. The time step was chosen to ensure that the Courant–Friedrichs–Lewy (CFL) number was less that 0.5 for numerical stability and accuracy.

Table 3.1 lists parameters of the DNS flow fields used in this study, and figure 2.1 plots the resulting energy spectrum. Corresponding Lagrangian statistics for the same box-isotropic turbulent flow at similar Reynolds numbers in DNS and LES are reported in Yang, He & Wang (2008). To demarcate Lagrangian dynamics and Lagrangian kinematics discussed in § 2.2.4, we will investigate the time evolution of Lagrangian structures in two separate cases. The first, referred to as a 'turbulent velocity field', consists of $\boldsymbol{u}(\boldsymbol{x}, t)$ obtained from the previously described DNS in $0 \le t \le T_e$. The second, described as a 'frozen velocity field' consists of an instantaneous field from the DNS $\boldsymbol{u}(\boldsymbol{x}, t = 0)$. The frozen field was the result of running the DNS for $t < 0$ of the order of several T_e. It is therefore an instantaneous snapshot from a fully developed stationary turbulent field but remains frozen in time for the purposes of solving (2.15). The instantaneous energy spectrum of $\boldsymbol{u}(\boldsymbol{x}, t = 0)$ is quantitatively similar to figure 2.1.

Table 2.1: Summary of DNS parameters for isotropic turbulence

Total kinetic energy	$E_{tot} = \langle \sum_{\boldsymbol{k}} \hat{\boldsymbol{u}}\hat{\boldsymbol{u}}^* \rangle/2$	0.915
Mean dissipation rate	$\epsilon = 2\nu\langle \sum_{\boldsymbol{k}} k^2 \hat{\boldsymbol{u}}\hat{\boldsymbol{u}}^* \rangle$	0.141
Root-mean-square velocity fluctuation	$u' = (2E_{tot}/3)^{1/2}$	0.781
Taylor micro length scale	$\lambda_T = (15\nu u'^2/\epsilon)^{1/2}$	0.804
Taylor Reynolds number	$Re_\lambda = u'\lambda_T/\nu$	62
Kolmogorov length scale	$\eta = (\nu^3/\epsilon)^{1/4}$	0.052
Kolmogorov time scale	$\tau_\eta = (\nu/\epsilon)^{1/2}$	0.266
Spatial resolution	$k_{max}\eta$	4.3
Integral length scale	$L_e = \frac{\pi}{2u'^2}\int \mathrm{d}k E(k)/k$	1.76
Eddy turnover time	$T_e = L_e/u'$	2.26

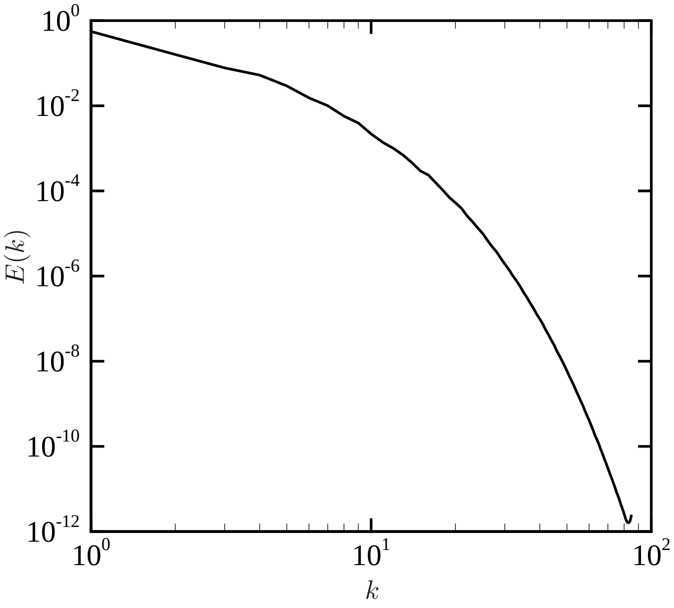

Figure 2.1: Energy spectrum of turbulence

2.3.2 Backward-particle-tracking method

Equation (2.15) is equivalent to the diffusion-less limit of the advection-diffusion equation in Eulerian form. The Eulerian finite-difference method for this pure hyperbolic equation exhibits significant numerical dissipation when the scalar gradient is high (e.g., LeVeque, 1992), which is common in the evolution of Lagrangian fields. To avoid this, we convert the Eulerian equation (2.15) to a set of ordinary differential equations (ODEs) as (2.1) to compute trajectories of fluid particles, which is equivalent to tracing characteristics of (2.15). Another potential problem is that if particles are tracked forward in time from t_0, they will be distributed almost randomly in space at later times, making it hard to reconstruct a continuous scalar field with satisfactory resolution on a Cartesian grid.

Instead, to obtain the Lagrangian field at a particular time t, we applied a backward-particle-tracking method, which is absolutely stable, to deal with the convection term (e.g., Stam, 1999; Nahum & Seifert, 2006). At time t, particles are placed at the grid points of N_p^3, where N_p could be greater than the grid number N of velocity field, i.e., the resolution of the Lagrangian field could be higher than the velocity field. In this study, $N_p = 1024$, which is four times the resolution of the velocity field. Then, particles are released and their trajectories calculated by solving (2.1). A three-dimensional forth-order Lagrangian interpolation scheme is used to calculate fluid velocity at the location of a particle. The trajectory of a particle is then obtained by the explicit second-order Adams–Bashforth scheme. The time increment is selected to capture the finest resolved scales in the velocity field. All the accuracy of numerical schemes and parameters in this study for particle tracking satisfies the criteria proposed by Yeung & Pope (1988) so that the computation of particle trajectories or Lagrangian characteristics are sufficiently accurate.

It is noted that the Eulerian velocity field here is reversed in time. In the simulation, we save the Eulerian velocity fields from DNS on disk at every time step and subsequently perform backward tracking from the particular time t to the initial time t_0 with the reversed Eulerian velocity fields saved previously. After the backward tracking, we can obtain initial locations of particles $\boldsymbol{X}_0$, which is equivalent to obtaining the Lagrangian position function $\psi(\boldsymbol{x}, t)$ for each particle located at the grid at t. From a given initial condition consisting of a smooth Lagrangian field $\phi(\boldsymbol{x}, t_0)$, we can obtain the Lagrangian field at time t on the Cartesian grid by (2.6) and (2.7), or the simple mapping (2.11) with Lagrangian coordinates and position functions.

In implementation, we store the position $\boldsymbol{X}_0$ at $t = 0$ and $\boldsymbol{X}(\boldsymbol{X}_0, t_0|t)$ at a given time for each particle with the same index as binary files after the backward tracking, which is equivalent to saving the information of $\psi(\boldsymbol{x}, t)$ of all the particles. Then we can apply arbitrarily many different initial conditions to obtain corresponding Lagrangian fields at the particular t from the same particle position files $\boldsymbol{X}_0$ and $\boldsymbol{X}(\boldsymbol{X}_0, t_0|t)$ in a single run. The tradeoff is that independent simulations are required for each time t at which $\phi(\boldsymbol{x}, t)$ is sought. Because $\phi(\boldsymbol{x}, t)$ is obtained via the direct mapping (2.11) from the initial field, the probability density function (PDF) of $\phi(\boldsymbol{x}, t)$ is invariant with time and the scalar fluctuation variance

$$\mathrm{Var}(\phi) \equiv \langle (\phi(\boldsymbol{x}, t) - \langle \phi(\boldsymbol{x}, t) \rangle)^2 \rangle$$

is also invariant with time. Hence, in principle there is no numerical dissipation in the computation of the Lagrangian field by the backward-particle-tracking method.

As $t \to \infty$, the Lagrangian field with a smooth initial condition may become discontinuous or else develop exponentially small structures. If the backward particle integration from t to t_0 was exact for each particle, then the solution values on the N_p^3 grid would correspond to

$$\phi(i\Delta x, j\Delta y, k\Delta z, t) = \int_0^L \int_0^L \int_0^L \phi(x,y,z,t)\delta(x-i\Delta x)\delta(y-j\Delta y)\delta(z-k\Delta z)\mathrm{d}x\mathrm{d}y\mathrm{d}z$$
$$i=1,\cdots,N_p, \quad j=1,\cdots,N_p, \quad k=1,\cdots,N_p \tag{2.22}$$

where $\phi(x,y,z,t)$ on the right-hand side is the exact continuous solution. Thus our calculation of ϕ at time t on the discrete field would be exact but interpolated values may have $O(1)$ errors for sufficiently large t. In practice, we find that the largest time for which we can obtain accurate, smooth, and well-resolved Lagrangian fields simulated at the present resolution 1024^3 is the large-eddy turnover time T_e defined in table 3.1.

To illustrate the Lagrangian field at longer times using higher resolution with the backward-particle-tracking method, we place particles at one cross-section (or any desired sub domain) of the entire three-dimensional field prior to tracking. We can then obtain the Lagrangian field in a plane-cut. Figure 2.2(a) shows the Lagrangian field on a plane cut $0 \leq x \leq 2\pi$, $0 \leq y \leq 2\pi$, $z=\pi$ with a 4096^2 grid at $t=2.5T_e$ from a smooth initial condition $\phi_0=\cos x$ at $t=t_0=0$ driven by a turbulent velocity field. The scalar field has become extremely convoluted with signature stretched and spiral structures. The effects of resolution for a detail of the scalar field, in the sense of (2.22), are shown in figures 2.2(b)–(d). This demonstrates the effectiveness of the backward-particle-tracking method in capturing the finest scale features with increasing particle numbers for large t. The scalar field with the same initial condition and the same time lapse in the frozen velocity field is shown in figure 2.3. This shows substantially less detailed structure than for the turbulent flow. Because straining and vortex motions in the frozen field are fixed, the stretched and spiral structures are concentrated only in a small number of local regions.

2.3.3 Three initial conditions of the Lagrangian field

In this study, we investigated the evolution of Lagrangian fields with three different initial conditions $\phi_0^{(i)}$ in the same domain of the velocity field. The iso-surfaces of these initial fields are closed surfaces. These are as follows:

i. $\phi_0^{(1)} = g(x_0)g(y_0)g(z_0)$ where the Gaussian function

$$g(x) = \exp(-0.5(x-\pi)^2).$$

The iso-surfaces of $\phi_0^{(1)}$ are concentric spheres/blob-like surfaces.

(a) Plane-cut of the full three-dimensional scalar field with resolution 4096^2, $0 \leq x \leq 2\pi$ and $0 \leq y \leq 2\pi$.

(b) 1024^2 (c) 2048^2 (d) 4096^2

Figure 2.2: The x–y plane-cut at $z = \pi$ from the three-dimensional Lagrangian field at $t = 2.5T_e$ with the initial condition $\phi_0 = \cos x$ in the forced stationary homogeneous and isotropic turbulence, and zoomed parts of plane-cuts at a small region $2.5 \leq x \leq 2.9$ and $3.6 \leq y \leq 4$ with increasing resolutions

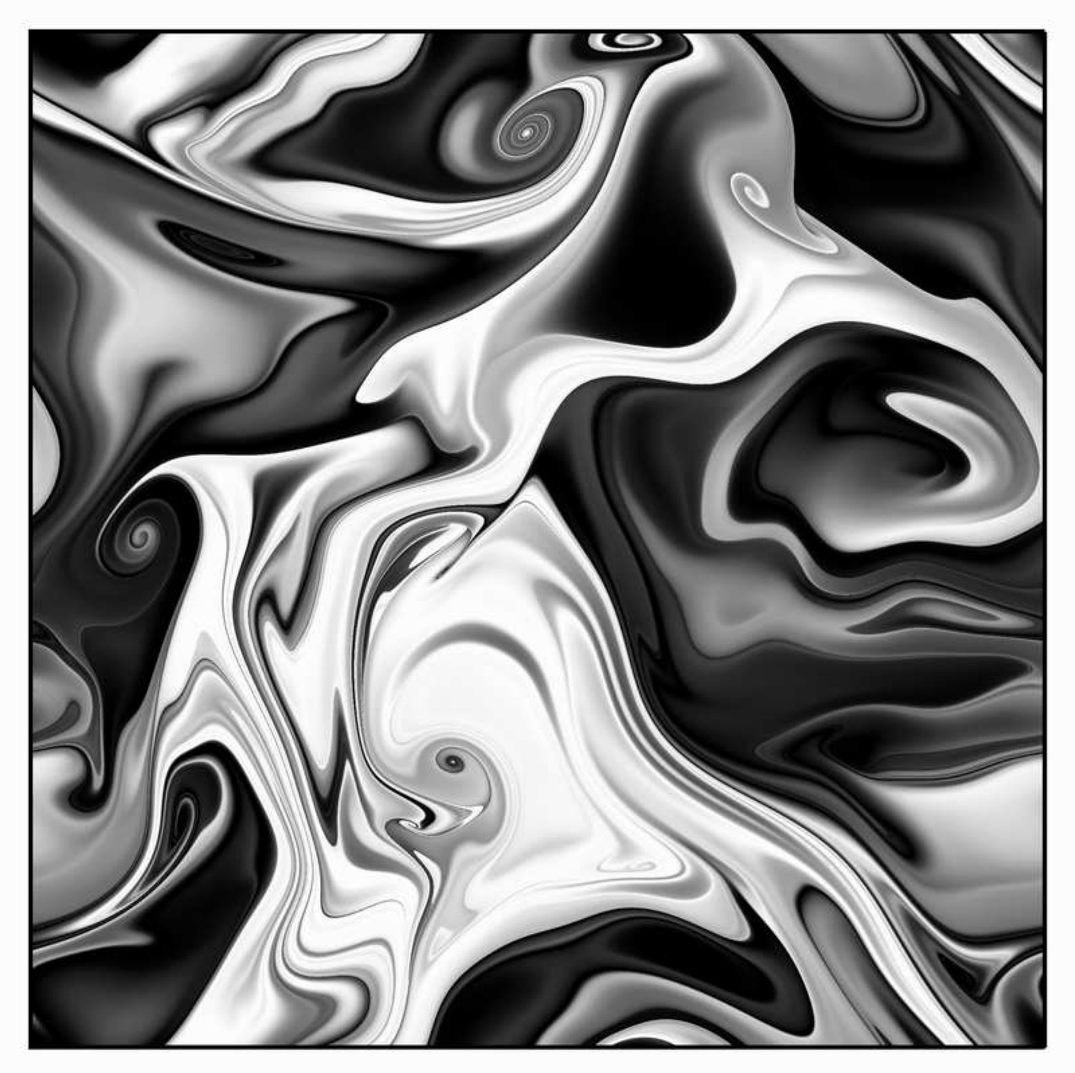

Figure 2.3: The x–y plane-cut at $z = \pi$ from the three-dimensional Lagrangian field at $t = 2.5T_e$ with the initial condition $\phi_0 = \cos x$ and resolution 4096^2 in the frozen turbulent field

ii. $\phi_0^{(2)} = g(x_0)g(y_0)F_0$ where the filter function $F_0 = f(x_0)f(y_0)f(z_0)$ with

$$f(x) = \exp\left(-6\left(\frac{x-\pi}{\pi}\right)^6\right),$$

which corresponds to iso-surfaces that are coaxial and tube-like in the z-direction. The filter function F_0 used here makes the corners of iso-surfaces curved for improved identification (Bermejo-Moreno & Pullin, 2008).

iii. $\phi_0^{(3)} = g(x_0)F_0$, which corresponds to mostly parallel planes along the x-axis.

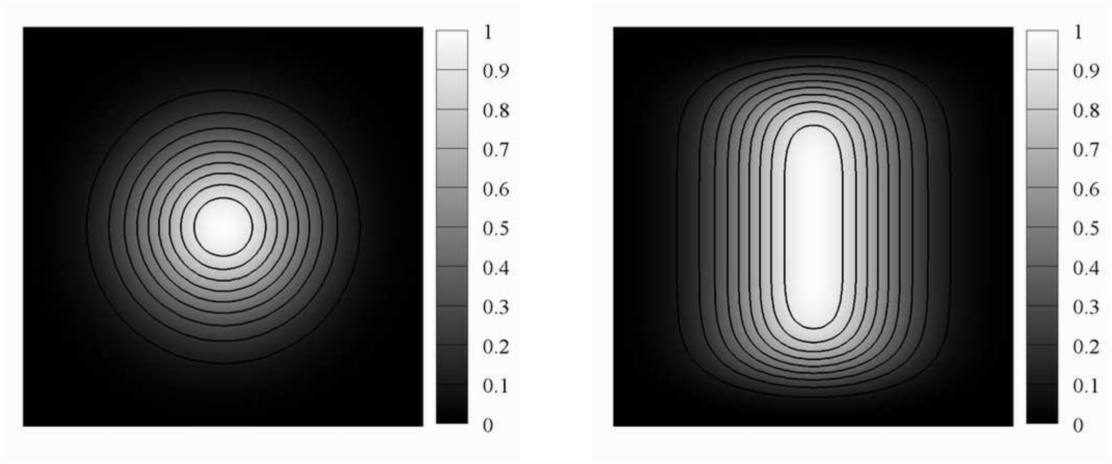

(a) $g(x_0)g(y_0)$

(b) $g(x_0)f(y_0)$

Figure 2.4: Typical plane-cuts with iso-contour lines of three initial Lagrangian fields

Two typical plane-cuts of these three initial fields are shown in figure 2.4. The characteristic length scale of the initial fields is comparable with the integral length scale L_e in turbulence. It is noted that topological properties of Lagrangian structures are invariant in time. For example, if an iso-surface is topological sphere (i.e., simply connected) at $t = 0$, then it remains so for all finite t.

2.4 Evolution of Lagrangian fields

2.4.1 Growth rate of the surface area of Lagrangian structures

The particle simulations for the Lagrangian fields were done with 1024^3 and correspond to an evolution time from initial conditions $\phi_0^{(i)}, i = 1, 2, 3$, from $t = 0$ to $t = T_e$. At times $t = \alpha T_e$, where $\alpha = \{1/16, 1/8, 1/4, 1/2, 3/4, 1\}$, Lagrangian fields $\phi(\boldsymbol{x}, \alpha T_e)$ were obtained with three different initial conditions. For example, the evolution of the Lagrangian structure with the blob-like initial condition $\phi_0^{(1)}$ corresponding to the iso-surface $\phi = 0.3$ in turbulence is shown in figure 2.5. From a simple sphere, after a finite time, the iso-surface is distorted to a highly convoluted shape with small-scale rolled-up structures. The spreading or widening of the spectrum of $\phi(t)$ in figure 2.6 shows a cascade process from large scales to small scales for the $\phi(t)$ field in stationary isotropic turbulence and the frozen turbulent field. The difference between spectra from two cases is very small at the early time, but then becomes noticeable with increasing time. The Lagrangian scalar cascade in turbulence is faster than that in the frozen field by dynamic convection motions. At a longer time, the difference in spectra should be more apparent as implied in figure 2.2 and figure 2.3.

The exponential growth of the surface area $A(t)$ of Lagrangian structures, initially proposed by Batchelor (1952b) for infinitesimal material elements, was also verified numerically by Goto & Kida (2007) using finite-sized material surfaces. To validate this in the present study, typical Lagrangian

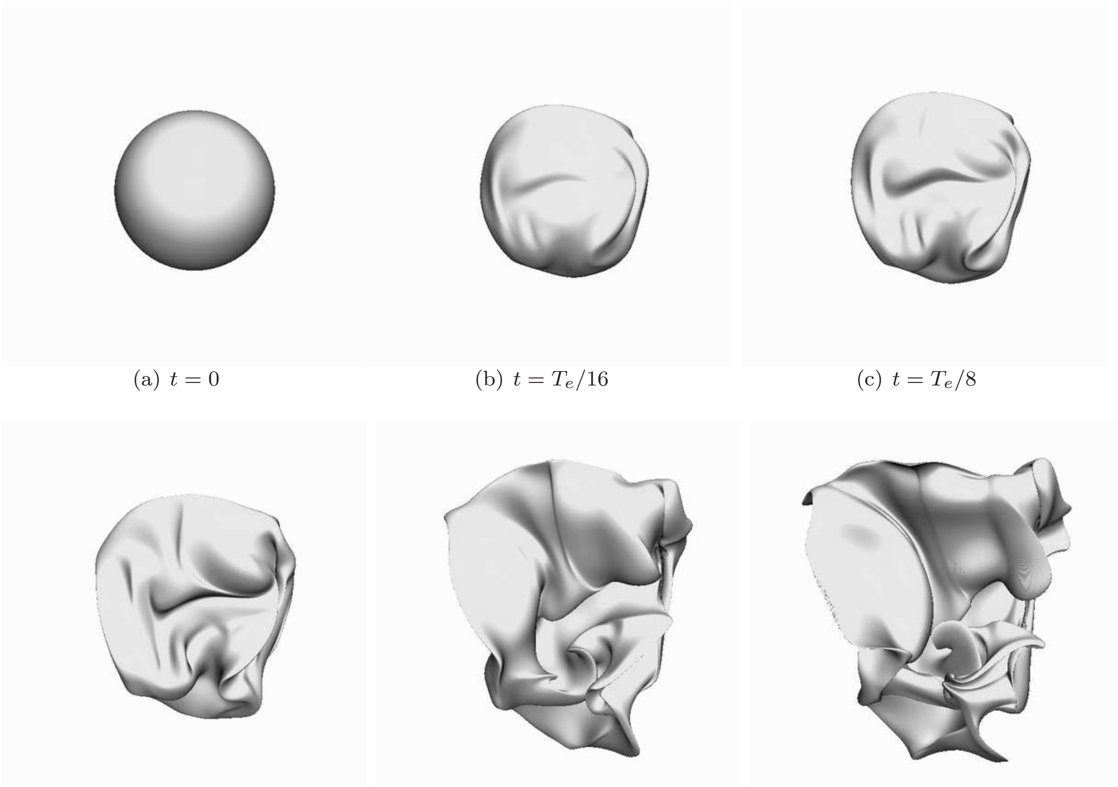

(a) $t = 0$ (b) $t = T_e/16$ (c) $t = T_e/8$

(d) $t = T_e/4$ (e) $t = T_e/2$ (f) $t = 3T_e/4$

Figure 2.5: Iso-surfaces ($\phi = 0.3$) of three-dimensional Lagrangian fields with the blob-like initial $\phi_0^{(1)}$ at different times

structures were selected as iso-surfaces at iso-contour levels $\phi = \{0.1, 0.2, ..., 0.9\}$. Each iso-surface is discretized on a triangular mesh, and the total area is the sum of areas of all the individual triangles. The area growth rate

$$\xi(t) = \frac{1}{t} \log\left(\frac{A(t)}{A_0}\right) \tag{2.23}$$

is computed by (2.5) and then the average growth rate $\langle \xi(t) \rangle$ at a particular time was presently obtained by taking an average over iso-surfaces of ϕ at nine contour levels. As shown in figure 2.7, following a rapid, monotonic growth in 2–3 Kolmogorov times, the average stretching rate approaches a statistical stationary state around $\xi = (0.33 \pm 0.4)\tau_\eta^{-1}$ in turbulence. This observation is consistent with that of Goto & Kida (2007).

2.4.2 Alignment of the Lagrangian scalar gradient in turbulent and frozen flows

The evolutionary geometry of Lagrangian structures may be related to the turbulent velocity field or vorticity field by preferred alignments of the scalar gradient with the background vector

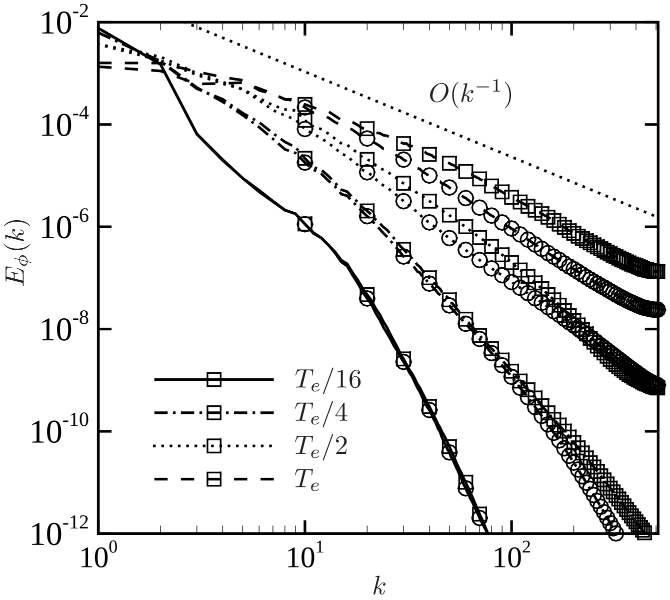

Figure 2.6: Spectra of Lagrangian fields with the blob-like initial $\phi_0^{(1)}$ at different times in stationary isotropic turbulence (□) and the frozen turbulent field (○)

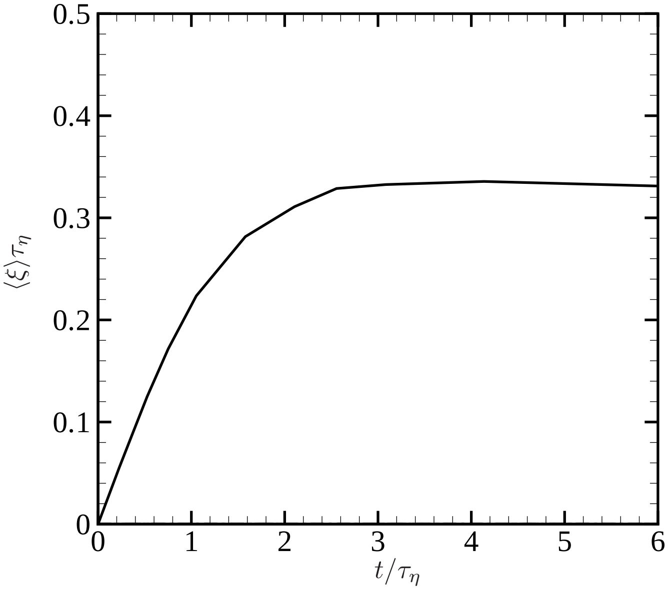

Figure 2.7: Temporal evolution of the average stretching rate $\langle\xi\rangle$ rescaled by the reciprocal of the Kolmogorov time scale τ_η of Lagrangian structures that are obtained from iso-surfaces of $\phi = \{0.1, 0.2, ..., 0.9\}$ with $\phi_0^{(1)}$ in stationary isotropic turbulence

fields. Batchelor (1952b) predicted that the vorticity $\boldsymbol{\omega}$ and the Lagrangian scalar gradient $\nabla\phi$ tend to become perpendicular. To investigate the time evolution of this alignment, we define the cosine of the angle between these vectors as

$$\lambda_\omega = \frac{\boldsymbol{\omega}\cdot\nabla\phi}{|\boldsymbol{\omega}||\nabla\phi|}. \tag{2.24}$$

Similarly, the cosine of the angle between $\boldsymbol{u}$ and $\nabla\phi$ can be defined as

$$\lambda_u = \frac{\boldsymbol{u}\cdot\nabla\phi}{|\boldsymbol{u}||\nabla\phi|}. \tag{2.25}$$

Figure 2.8 shows the temporal evolution of PDFs of $|\lambda_\omega|$ and $|\lambda_u|$ for both the turbulent (upper row) and the frozen (lower row) velocity fields. The PDFs of $|\lambda_\omega|$ in isotropic turbulence in figure 2.8(a) indicates evolution from an almost uniform distribution in the initial condition at $t = 0$ towards a strong peak at $\pi/2$. We also find that $\nabla\phi$ tends to become normal to the local velocity as illustrated in figure 2.8(b) showing the PDFs of $|\lambda_u|$. The time evolution of PDFs of $|\lambda_\omega|$ and $|\lambda_u|$ in the frozen turbulent field is shown in figures 2.8(c, d). A comparison of figure 2.8(a) with figure 2.8(b) shows that Lagrangian surfaces in stationary turbulence tend to align with vortex lines rather than streamlines at $t = T_e$. In contrast, as shown in figures 2.8(c, d), Lagrangian surfaces advected by the frozen velocity field over long times appear to preferentially align with streamlines rather than vortex lines.

2.4.3 Transport equations for alignment angles

These observations on alignment angles can be understood by analysis of the transport equations for $|\lambda_\omega|$ and $|\lambda_u|$. We assume $\langle\boldsymbol{u}\rangle = 0$. From (2.15), we can obtain the vector identity for $\nabla\phi$, $\boldsymbol{u}$, and a vector $\boldsymbol{v}$

$$\frac{\mathrm{D}}{\mathrm{D}t}(\boldsymbol{v}\cdot\nabla\phi) = \left(\frac{\partial\boldsymbol{v}}{\partial t} + \boldsymbol{u}\cdot\nabla\boldsymbol{v} - \boldsymbol{v}\cdot\nabla\boldsymbol{u}\right)\cdot\nabla\phi, \tag{2.26}$$

and then transport equations for $\boldsymbol{\omega}\cdot\nabla\phi$ and $\boldsymbol{u}\cdot\nabla\phi$

$$\frac{\mathrm{D}}{\mathrm{D}t}(\boldsymbol{\omega}\cdot\nabla\phi) = \left(\frac{\partial\boldsymbol{\omega}}{\partial t} + \nabla\times(\boldsymbol{\omega}\times\boldsymbol{u})\right)\cdot\nabla\phi, \tag{2.27}$$

$$\frac{\mathrm{D}}{\mathrm{D}t}(\boldsymbol{u}\cdot\nabla\phi) = \left(\frac{\partial\boldsymbol{u}}{\partial t}\right)\cdot\nabla\phi. \tag{2.28}$$

Introducing the unit vector $\boldsymbol{n}_\phi = \nabla\phi/|\nabla\phi|$, we can obtain the transport equation for $|\nabla\phi|$ from (2.15)

$$\frac{\mathrm{D}|\nabla\phi|}{\mathrm{D}t} = -(\boldsymbol{n}_\phi\cdot\boldsymbol{S}\cdot\boldsymbol{n}_\phi)|\nabla\phi|, \tag{2.29}$$

where $\boldsymbol{S} = \frac{1}{2}(\partial u_i/\partial x_j + \partial u_j/\partial x_i)$ is the rate-of-strain tensor. In an unsteady flow, from (2.27),

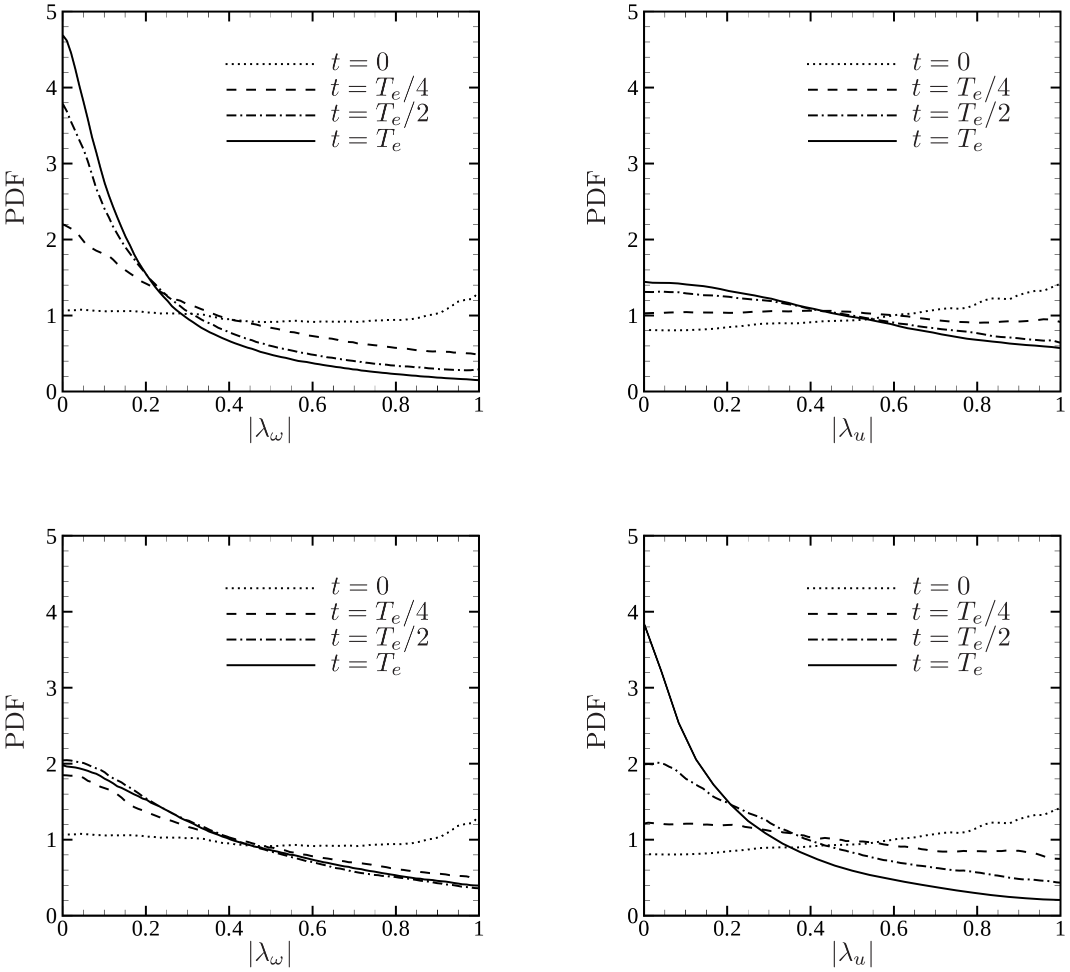

Figure 2.8: Temporal evolution of PDFs of $|\lambda_\omega|$ and $|\lambda_u|$ obtained from the Lagrangian field with $\phi_0^{(1)}$ in stationary isotropic turbulence (upper row) and the frozen turbulent field (lower row), where λ_ω is the cosine of the angle between $\boldsymbol{\omega}$ and $\nabla\phi$, and λ_u is the cosine of the angle between $\boldsymbol{u}$ and $\nabla\phi$

(2.28), and the vorticity equation in a viscous flow

$$\frac{\mathrm{D}\boldsymbol{\omega}}{\mathrm{D}t} = \boldsymbol{\omega} \cdot \nabla \boldsymbol{u} + \nu \nabla^2 \boldsymbol{\omega}, \tag{2.30}$$

we can derive equations for λ_ω and λ_u

$$\frac{\mathrm{D}\lambda_\omega}{\mathrm{D}t} = \left(\boldsymbol{n}_\phi \cdot \boldsymbol{S} \cdot \boldsymbol{n}_\phi - \frac{1}{|\boldsymbol{\omega}|} \frac{\mathrm{D}|\boldsymbol{\omega}|}{\mathrm{D}t} \right) \lambda_\omega + \frac{\nu}{|\boldsymbol{\omega}|} \nabla^2 \boldsymbol{\omega} \cdot \boldsymbol{n}_\phi, \tag{2.31}$$

$$\frac{\mathrm{D}\lambda_u}{\mathrm{D}t} = \left(\boldsymbol{n}_\phi \cdot \boldsymbol{S} \cdot \boldsymbol{n}_\phi - \frac{1}{|\boldsymbol{u}|} \frac{\mathrm{D}|\boldsymbol{u}|}{\mathrm{D}t} \right) \lambda_u + \frac{1}{|\boldsymbol{u}|} \left(\frac{\partial \boldsymbol{u}}{\partial t} \right) \cdot \boldsymbol{n}_\phi. \tag{2.32}$$

In the frozen velocity field, $\partial \boldsymbol{u}/\partial t = 0$, and then

$$\frac{\mathrm{D}}{\mathrm{D}t}(\boldsymbol{\omega} \cdot \nabla\phi) = (\nabla \times (\boldsymbol{\omega} \times \boldsymbol{u})) \cdot \nabla\phi, \tag{2.33}$$

$$\frac{\mathrm{D}}{\mathrm{D}t}(\boldsymbol{u} \cdot \nabla\phi) = 0, \tag{2.34}$$

so the equations for λ_ω and λ_u become

$$\frac{\mathrm{D}\lambda_\omega}{\mathrm{D}t} = \left(\boldsymbol{n}_\phi \cdot \boldsymbol{S} \cdot \boldsymbol{n}_\phi - \frac{1}{|\boldsymbol{\omega}|}\boldsymbol{u} \cdot \nabla|\boldsymbol{\omega}|\right)\lambda_\omega + \frac{1}{|\boldsymbol{\omega}|}(\nabla \times (\boldsymbol{\omega} \times \boldsymbol{u})) \cdot \boldsymbol{n}_\phi, \tag{2.35}$$

$$\frac{\mathrm{D}\lambda_u}{\mathrm{D}t} = (\boldsymbol{n}_\phi \cdot \boldsymbol{S} \cdot \boldsymbol{n}_\phi - \boldsymbol{n}_u \cdot \nabla|\boldsymbol{u}|)\lambda_u, \tag{2.36}$$

where $\boldsymbol{n}_u = \boldsymbol{u}/|\boldsymbol{u}|$.

On a fluid particle, the solution of (2.29) is given by

$$|\nabla\phi(t)| = |\nabla\phi(t_0)| \exp\left(-\int_{t_0}^{t} \boldsymbol{n}_\phi \cdot \boldsymbol{S} \cdot \boldsymbol{n}_\phi \, \mathrm{d}t'\right). \tag{2.37}$$

For both the turbulent and the frozen velocity fields we may write for the scalar gradient

$$\langle|\nabla\phi(t)|\rangle = \left(2\int_0^\infty k^2 E_\phi(k,t)\mathrm{d}k\right)^{1/2}. \tag{2.38}$$

A consequence of the widening scalar spectrum $E_\phi(k,t)$ discussed in § 2.2.4 and (2.38), where the integral is weighted by k^2, is the progressive amplification of $\langle|\nabla\phi(t)|\rangle$. This implies that in (2.37), statistically

$$\langle \boldsymbol{n}_\phi \cdot \boldsymbol{S} \cdot \boldsymbol{n}_\phi \rangle < 0. \tag{2.39}$$

Let the principal strain rates for $\boldsymbol{S}$ be Γ_α, Γ_β, Γ_γ, with corresponding unit vectors along the principal axes of strain $\boldsymbol{e}_\alpha$, $\boldsymbol{e}_\beta$, $\boldsymbol{e}_\gamma$. In incompressible flow, $\Gamma_\alpha + \Gamma_\beta + \Gamma_\gamma = 0$ and we specify the order $\Gamma_\alpha \geq \Gamma_\beta \geq \Gamma_\gamma$. Ashurst et al. (1987) showed that statistically $\Gamma_\alpha > \Gamma_\beta > 0$ and $\Gamma_\gamma < 0$ in isotropic turbulence. In addition, the alignment vector $\lambda_i = \boldsymbol{n}_\phi \cdot \boldsymbol{e}_i$ is defined as the cosine of the angle between $\boldsymbol{n}_\phi$ and $\boldsymbol{e}_i$. Because the passive scalar gradient tends to align with the most compressive strain direction in turbulent flow (e.g., Ashurst et al., 1987; Ruetsch & Maxey, 1992; Brethouwer et al., 2003) and referring to (2.39), we hypothesize that in turbulent flow or the frozen turbulent flow,

$$\langle \boldsymbol{n}_\phi \cdot \boldsymbol{S} \cdot \boldsymbol{n}_\phi \rangle = \langle \Gamma_\alpha \lambda_\alpha^2 \rangle + \langle \Gamma_\beta \lambda_\beta^2 \rangle + \langle \Gamma_\gamma \lambda_\gamma^2 \rangle \sim O(\Gamma_\gamma) < 0. \tag{2.40}$$

The magnitude of the term $\langle \boldsymbol{n}_u \cdot \nabla|\boldsymbol{u}| \rangle$ in (2.36) can be reasonably assumed small in comparison with that of $\langle \boldsymbol{n}_\phi \cdot \boldsymbol{S} \cdot \boldsymbol{n}_\phi \rangle$, because there is no preferred alignment between $\boldsymbol{n}_u$ and $\nabla|\boldsymbol{u}|$. Thus, from (2.36) and (2.40), in general the volume-averaged $|\lambda_u|$ can be expected to decrease exponentially with time in the frozen turbulent field as

$$\langle|\lambda_u|\rangle \sim \langle|\lambda_{u0}|\rangle \exp(\Gamma t), \tag{2.41}$$

with $\Gamma < 0$ and $\lambda_{u0} \equiv \lambda_u(t=0)$. In other words, the Lagrangian field in the frozen velocity field is attracted to a stream-surface field whose iso-surfaces are stream surfaces comprised of steady stream lines.

On the other hand, $\mathrm{D}\langle|\boldsymbol{\omega}|\rangle/\mathrm{D}t \approx 0$ for stationary turbulence, which implies that (2.31) could be simplified as

$$\frac{\mathrm{D}\lambda_\omega}{\mathrm{D}t} \approx (\boldsymbol{n}_\phi \cdot \boldsymbol{S} \cdot \boldsymbol{n}_\phi)\lambda_\omega + \nu O(R_\omega), \tag{2.42}$$

where ν is small in high Reynolds number turbulent flow and $R_\omega = |\nabla^2 \boldsymbol{\omega}|/|\boldsymbol{\omega}|$. By (2.42) the approximation for the volume-averaged $|\lambda_\omega|$ in turbulent flow could be

$$\langle|\lambda_\omega|\rangle \sim \langle|\lambda_{\omega 0}|\rangle \exp(\Gamma t) + \nu \frac{O(R_\omega)}{\Gamma}(1 - \exp(\Gamma t)), \tag{2.43}$$

with $\Gamma < 0$ and $\lambda_{\omega 0} \equiv \lambda_\omega(t=0)$. The exponential decay in (2.43) appears to be similar as that in (2.41) for small time t, which is then attenuated for larger t owing to the cumulative effect of the small, inhomogeneous viscous term. Hence the analysis suggests that the Lagrangian field in stationary turbulence may tend initially to be attracted towards a vortex-surface field whose iso-surfaces are vortex surfaces comprised of vortex lines, but that perfect, long-time alignment is inhibited owing to small but persistent viscous effects.

Furthermore, the last inhomogeneous terms in both (2.32) and (2.35) could be nontrivial. Hence, the evolution of $\langle|\lambda_u|\rangle$ in turbulence may perhaps be described qualitatively by the model

$$\langle|\lambda_u|\rangle \sim \langle|\lambda_{u0}|\rangle \exp(\Gamma t) + \langle f_u(\lambda_u)\rangle, \tag{2.44}$$

with a similar model for the evolution of $\langle|\lambda_\omega|\rangle$ in the frozen field

$$\langle|\lambda_\omega|\rangle \sim \langle|\lambda_{\omega 0}|\rangle \exp(\Gamma t) + \langle f_\omega(\lambda_\omega)\rangle. \tag{2.45}$$

Here, the functions $\langle f_u(\lambda_u)\rangle$ and $\langle f_\omega(\lambda_\omega)\rangle$ are not expected to be as small as the last term in (2.43) due to the additional nontrivial inhomogeneous terms in the governing equations of λ_ω and λ_u. This suggests that the Lagrangian field appears to show only a weak tendency to be attracted to the stream-surface field in turbulence and to the vortex-surface field in the frozen field for long times.

The temporal evolution of the normalized volume-averaged statistics,

$$\widetilde{\lambda}_\omega \equiv \langle|\lambda_\omega|\rangle/\langle|\lambda_{\omega 0}|\rangle \qquad \text{and} \qquad \widetilde{\lambda}_u \equiv \langle|\lambda_u|\rangle/\langle|\lambda_{u0}|\rangle$$

is plotted in figure 2.9. As shown in (2.41), the evolution of $\widetilde{\lambda}_u$ in the frozen field shows strong exponential decay from $t = 0$ to $t = T_e$, which implies that Lagrangian structures are progressively attracted to frozen stream surfaces. The evolution of $\widetilde{\lambda}_\omega$ in isotropic turbulence shows even faster exponential decay from $t = 0$ to $t = T_e/2$ than that of $\widetilde{\lambda}_u$ in the frozen field, but then as estimated in (2.43), the viscous effect tends to slow down the decay corresponding to the tendency that Lagrangian structures become attracted to vortex surfaces in turbulence. Furthermore, the evolution of $\widetilde{\lambda}_u$ in isotropic turbulence and $\widetilde{\lambda}_\omega$ in the frozen field rapidly approaches a statistical stationary state as shown in the approximations (2.44) and (2.45), which implies relatively weak alignments in both cases. These evolutions of alignments and corresponding tendencies of attractions of stream surfaces or vortex surfaces at early and late stages are summarized in table 2.2. Here, we remark that the numerical results for the alignment issue are based on the initial condition $\phi^{(1)}$ with the large initial length scale L_e. The corresponding results with initial conditions $\phi^{(2)}$ and $\phi^{(3)}$ show quantitatively similar behaviors.

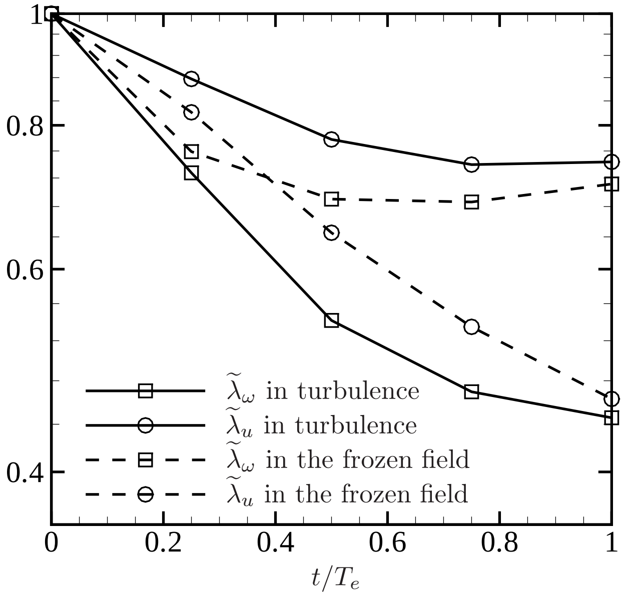

Figure 2.9: The log–linear plot of the temporal evolution of $\widetilde{\lambda}_\omega$ and $\widetilde{\lambda}_u$ in stationary isotropic turbulence and the frozen turbulent field

2.4.4 Formation of spiral and stretched Lagrangian structures

An interesting observation from figure 2.5 is the rolled-up or spiral structures at later stages of the Lagrangian evolution. This phenomenon was discussed by Ruetsch & Maxey (1992) as multiply layered sheets or spiral structures of strong passive scalar gradient when $Sc \gg 1$. Previous studies

Table 2.2: Summary of the evolution of alignments for the Lagrangian field

Cases	Approximation	Attractor	Tendency (early → late)
$\widetilde{\lambda}_\omega$ in stationary isotropic turbulence	(2.43)	Vortex surface	Strong → weak
$\widetilde{\lambda}_u$ in stationary isotropic turbulence	(2.44)	Stream surface	Medium → weak
$\widetilde{\lambda}_\omega$ in the frozen turbulent field	(2.45)	Vortex surface	Medium → weak
$\widetilde{\lambda}_u$ in the frozen turbulent field	(2.41)	Stream surface	Strong → strong

(e.g., Ruetsch & Maxey, 1992; Brethouwer et al., 2003) observed that vortex tubes are surrounded by scalar gradient sheets over a wide range of Prandtl or Schimdt numbers. It is notable that rolled-up structures, perhaps generated by vortex tubes, have themselves been observed mainly in scalar simulations at high Schmidt numbers. These highly convoluted Lagrangian structures were denoted as 'folding effects' by Goto & Kida (2007), who argued that the folding is produced by coherent counter-rotating eddy pairs. Presently, we hypothesize that the formation of spiral structures of ϕ in eddies corresponding to rolled-up shapes of Lagrangian structures can be also explained as the alignment discussed in §§ 2.4.2 and 2.4.3 between the gradient of ϕ and other vectors obtained from the local velocity field.

A simple kinematic model can be constructed: consider a two-dimensional exact solution of the scalar dispersion (e.g., Rhines & Young, 1983). The governing equations for scalar $\phi(r,\theta,t)$, vorticity $\omega(r,\theta,t)$, and stream function $\psi(r,\theta,t)$ in two-dimensional polar coordinates are

$$\frac{\partial \phi}{\partial t} + \frac{1}{r}\left(\frac{\partial \psi}{\partial \theta}\frac{\partial \phi}{\partial r} - \frac{\partial \phi}{\partial \theta}\frac{\partial \psi}{\partial r}\right) = 0, \tag{2.46}$$

$$\frac{\partial \omega}{\partial t} + \frac{1}{r}\left(\frac{\partial \psi}{\partial \theta}\frac{\partial \omega}{\partial r} - \frac{\partial \omega}{\partial \theta}\frac{\partial \psi}{\partial r}\right) = 0, \tag{2.47}$$

$$\omega = \left(\frac{1}{r}\frac{\partial}{\partial r} r \frac{\partial}{\partial r} + \frac{1}{r^2}\frac{\partial^2}{\partial \theta^2}\right)\psi. \tag{2.48}$$

For illustrative purposes we consider initial conditions corresponding to a linear scalar gradient embedded within an axisymmetric vortex

$$\phi(r,\theta,0) = r\sin\theta, \qquad \omega(r,\theta,0) = \frac{1}{r}\frac{d}{dr}r^2\Omega, \qquad \Omega = e^{-r^2}, \tag{2.49}$$

but emphasize that the following scenario is more general. The vortex remains steady while ϕ evolves as

$$\phi(r,\theta,t) = r\sin(\theta - \Omega t). \tag{2.50}$$

The evolution of (2.50) is plotted in figure 2.10, where it is seen that the linear scalar gradient

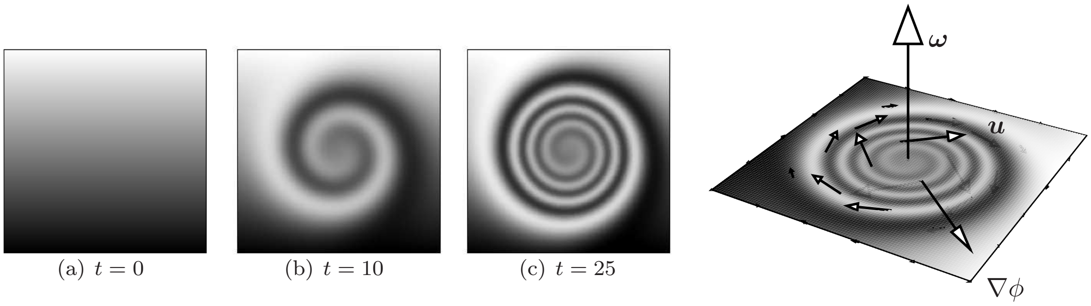

(a) $t = 0$ (b) $t = 10$ (c) $t = 25$

Figure 2.10: Evolution of spiral structures for the two-dimensional solution (2.50). The illustration of orthogonality between $\boldsymbol{u}$ and $\nabla\phi$ is shown in the rightmost subfigure

is wound into tight spirals by convective action of the vortex. It is straightforward to obtain λ_u as

$$\lambda_u = -\frac{\cos(\theta - \Omega t)}{\sqrt{\cos^2(\theta - \Omega t) + (\sin(\theta - \Omega t) + 2\Omega r^2 t \cos(\theta - \Omega t))^2}}. \tag{2.51}$$

At $t = 0$, $|\lambda_u| = |\cos\theta|$ where the probability of θ is uniformly distributed in $0 \le \theta < 2\pi$, so the PDF of $x = |\lambda_u|$ in the entire two-dimensional plane is a monotonic increasing function $(2/\pi)(1 - x^2)^{-1/2}$ with $0 \le x < 1$. As $t \to \infty$, from (2.51), $|\lambda_u| \to 0$ everywhere, so the PDF of $|\lambda_u|$ is asymptotic to a delta function $\delta(x - \epsilon)$, $\epsilon \to 0$. The evolution of the PDF of $|\lambda_u|$ in this two-dimensional case is qualitatively consistent with that shown in figures 2.8(b) and 2.8(d). Since Lagrangian structures are topologically invariant, then starting from any ϕ_0 except $\boldsymbol{u} \cdot \nabla\phi_0 = 0$, this model supports the hypothesis that the spiral is the most probable structure within eddies. In figure 2.11, we can visually observe spatial coincidences between spiral Lagrangian structures represented by iso-contour lines of $\phi(t = T_e)$ and vortical structures represented by regions of high enstrophy $(\omega_i\omega_i)^{1/2}$ in isotropic turbulence. Additionally, elongated Lagrangian structures induced by strong stretching motions are observed to wrap vortex tubes.

2.4.5 Lagrangian R–Q analysis

The local topology of flow field can be classified by the invariants Q and R of the velocity gradient tensor $A_{ij} = \partial u_i/\partial x_j$ (Chong, Perry & Cantwell, 1990), where

$$Q = -\frac{1}{2}A_{ij}A_{ij}, \qquad R = -\frac{1}{3}A_{ij}A_{jk}A_{ki}. \tag{2.52}$$

One way to quantify the relation between Lagrangian structures and local flow patterns in turbulence is to use the mean value of the norm of the scalar gradient $|\nabla\phi|$ conditioned on Q and R at $t = T_e$. We denote this by $\langle|\nabla\phi|\,|\,Q, R\rangle$. As shown in figure 2.12, the curve $(27/4)R^2 + Q^3 = 0$ divides the R–Q plane into four regions, each with different local flow structure. Details of the local flow pattern

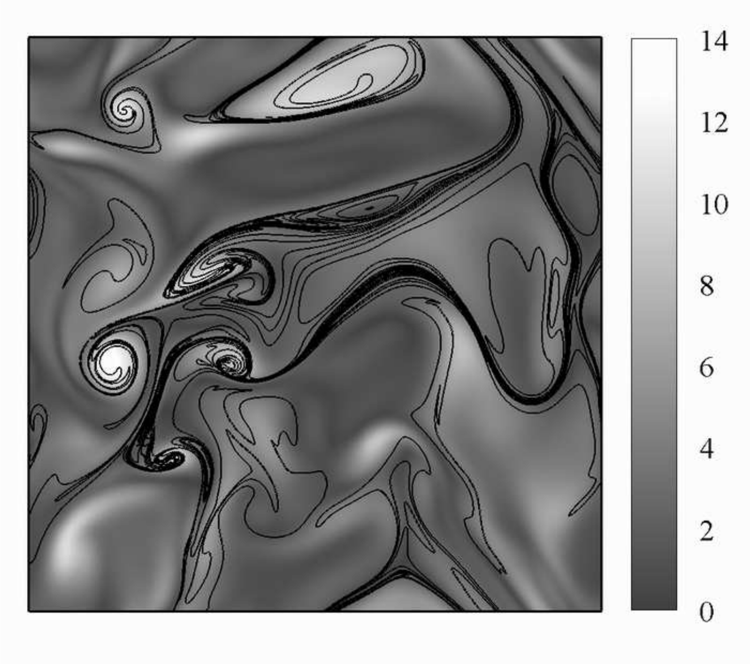

Figure 2.11: Iso-contour lines of $\phi(t = T_e)$ and contours of the enstrophy at $t = T_e$ on the x–y plane-cut at $z = \pi$ with the blob-like initial $\phi_0^{(1)}$ in stationary isotropic turbulence

for each region are described by Brethouwer et al. (2003) and references therein. Because the number of samples is too small outside the pear-shaped contour to determine an accurate $\langle |\nabla\phi| \,|\, Q, R\rangle$, the values in the white regions are ignored. We observe steep scalar gradients in regions dominated by bi-axial strains, which is consistent with the result obtained by scalar simulation with $Sc = 0.7$ from Brethouwer et al. (2003). This result corresponds to the scenario of stretched Lagrangian structures in straining regions. In particular, we also observe strong scalar gradients in regions inside stretched vortex tubes, which could correspond to the scenario of spiral Lagrangian structures in eddies as shown in figures 2.2 and 2.11.

2.5 Multi-scale geometric analysis of Lagrangian structures

2.5.1 Description of the methodology

In this section, we apply the multi-scale geometric methodology of Bermejo-Moreno & Pullin (2008) to explore the non-local geometry of Lagrangian structures at different length scales. Starting from a given periodic three-dimensional field, this methodology has three main steps: extraction, characterization, and classification. The extraction of structures is itself done in two main stages. In the first stage, the curvelet transform (see Candès et al., 2006) applied to the full three-dimensional Lagrangian field at an instant in time provides a multi-scale decomposition into a finite set of

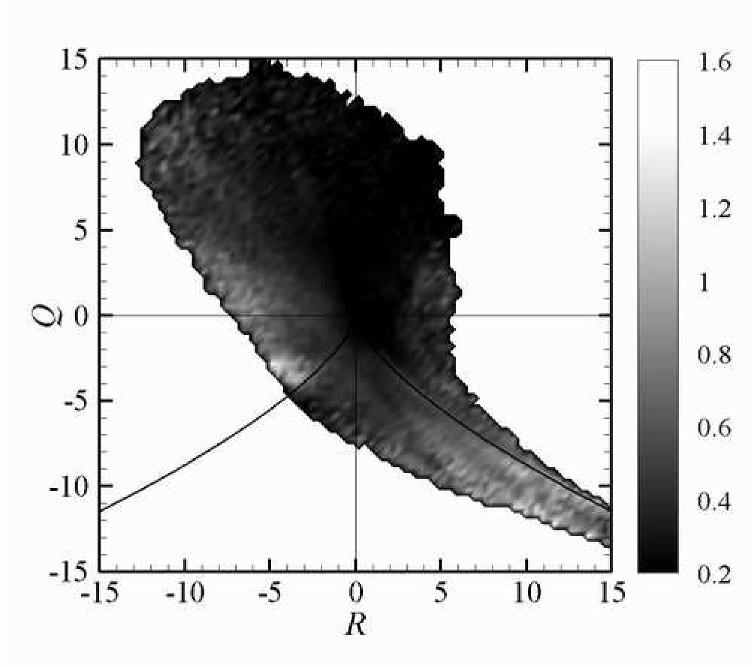

Figure 2.12: The mean value of the gradient $|\nabla\phi|$ of the Lagrangian field conditioned on Q and R at $t = T_e$ in stationary isotropic turbulence. The whole plane is divided into four regions by the curve $(27/4)R^2 + Q^3 = 0$. The local flow patterns for each region are: upper left: stretched vortex; upper right: compressed vortex; lower left: axial strain; lower right: bi-axial strain

component three-dimensional fields, one per scale. Second, by iso-contouring each component field at one or more iso-contour levels, a set of closed iso-surfaces is obtained that represent the structures at that scale.

The basis functions of the curvelet transform, curvelets, are oriented needle-shaped elements in space and a wedge in frequency, and they are localized in scale (Fourier space), position (physical space), and orientation. The projection of the scalar field onto the curvelet basis produces a set of decomposed fields, each characterized by a radial (in Fourier space) index j. Let the number of grid points in each spatial direction be 2^n. Then for each scale $j = j_0, \ldots, j_e$, with $j_0 = 2$, $j_e = \log_2(n/2)$, the associated curvelet radial basis function has support near the dyadic corona $[2^{j-1}, 2^{j+1}]$ in Fourier space. This gives a multi-scale decomposition of the original scalar field into a total of $j_e - j_0 + 1$ scale-dependent fields. For convenience we will subsequently label scale-dependent fields by the index $i = j - 2$, $i = 0, \ldots, j_e - 2$, with $i = 0$ corresponding to the largest-scale field and $i = j_e - 2$ the smallest resolved-scale field. Curvelets are naturally suited for detecting, organizing, or providing a compact representation of multi-dimensional structures. The latest studies on applications of curvelets to turbulence were reported by Bermejo-Moreno et al. (2009) and Ma et al. (2009).

The characterization stage begins with the joint PDF, in terms of area coverage on each individual surface, of two differential-geometry properties, the absolute value of the shape index S and the dimensionless curvedness C,

$$S \equiv \left| -\frac{2}{\pi} \arctan\left(\frac{\kappa_1 + \kappa_2}{\kappa_1 - \kappa_2} \right) \right|, \quad C \equiv 3\frac{V}{A}\sqrt{\frac{\kappa_1^2 + \kappa_2^2}{2}}, \tag{2.53}$$

where κ_1 and κ_2 are principal curvatures, A is the surface area, and V is the volume contained within the three-dimensional surface. Characterization is based on the construction of a finite set of parameters defined by algebraic functions of dimensionless forms of first and second moments of the joint PDF of S and C for each individual surface. An additional parameter,

$$\lambda \equiv \sqrt[3]{36\pi}\frac{V^{2/3}}{A}, \tag{2.54}$$

measures the geometrical global stretching of the individual surface. Taken together, this parameter set defines the geometrical signature of the iso-surface by specifying its location as a point in a multidimensional 'feature-space'.

A subset of the feature space is the so-called 'visualization space'. This comprises a subspace of three parameters $(\hat{S}, \hat{C}, \lambda)$ where feature centers $\hat{S}$ and $\hat{C}$ are respectively dimensionless forms of weighted first-order moments of the joint PDF of S and C. Each closed iso-surface is then represented by a single point in the visualization space $(\hat{S}, \hat{C}, \lambda)$. At each scale, the cloud of points in visualization space represents all structures at that scale, for a specified iso-contour value. We remark that, for the full field, iso-surfaces of ϕ are topologically invariant in time. This is not the case for the multi-scale component fields after curvelet decomposition, where, in general, many individual disconnected iso-surfaces are generated. Nonetheless, the set of iso-surfaces at each scale can be interpreted as containing information on the statistical geometry of structures at that scale.

Finally, the geometry of a structure is classified by its location $(\hat{S}, \hat{C}, \lambda)$ in the visualization space. An analysis of a generic surface shows that different regions in the visualization space can be viewed as representing different geometry shapes. Blob-like structures occupy the region near the point $(1, 1, 1)$ that corresponds to spheres. Tube-like structures are localized near the $(1/2, 1, \lambda)$ axis where λ is an indication of how stretched the tube is, and the transition to sheet-like structures occurs as $\hat{C}$ and λ decrease. An illustration for three typical geometry shapes in the present study and corresponding feature centers on the $\hat{S}$–$\hat{C}$ plane with the predominantly blob-, tube-, and sheet-like regions sketched are shown in figure 2.13. More details on the classification and the visualization space $(\hat{S}, \hat{C}, \lambda)$ are shown in figures 6 and 7 of Bermejo-Moreno & Pullin (2008). The clustering algorithm in the original methodology was not applied in this study.

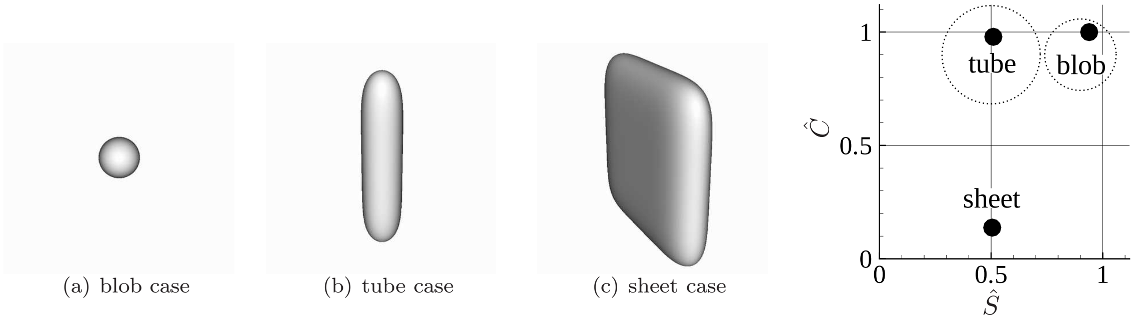

(a) blob case (b) tube case (c) sheet case

Figure 2.13: Iso-surfaces of three initial fields for the contour level $\phi_0^c = 0.95$ and corresponding feature centers on the $\hat{S}$–$\hat{C}$ plane with the predominantly blob-, tube- and sheet-like regions sketched

2.5.2 Multi-scale diagnostics

Next, we analyze the non-local geometry in the evolution of $\phi_0^{(1)}$ of § 2.3.3 corresponding to Lagrangian blobs. Figures 2.14 and 2.15 show x–y plane-cuts at $z = \pi$ of the full Lagrangian fields with color intensity proportional to ϕ, $0 < \phi \leq 1$ for sphere/blob-like initial $\phi_0^{(1)}$ at different times αT_e in stationary isotropic turbulence and the frozen turbulent field, respectively. The evolution of ϕ in the two cases is similar in the early stages at $t = T_e/16$ and $t = T_e/8$. Then the Lagrangian structures in turbulence are stretched or wound by dynamic turbulent motions, producing alignment between Lagrangian surfaces and vortex lines as discussed in §§ 2.4.2 and 2.4.4. In contrast, in the frozen turbulent field, Lagrangian structures are attracted onto a frozen stream surface and are therefore strained only in fixed regions to form more nearly-singular local structures, as shown in (2.41).

The multi-scale methodology described in § 2.5.1 was applied to the three-dimensional Lagrangian fields at each instantaneous time. For the given resolution of 1024^3 grid points, we will analyze the first six scales provided by the curvelet transform. They will be denoted by a scale number, from 0 to 5. Increasing values of the scale number correspond to smaller scales. For example, the plane-cuts of ϕ at $t = T_e$ in turbulence for each one of the filtered scales resulting from the multi-scale analysis are shown in figure 2.16, which corresponds to the original field shown in figure 2.14 (f).

Volume-data PDFs obtained for the Lagrangian field for each one of the filtered scales are shown in figure 2.17. The widening of the PDFs at small scales indicates that there is an increasing population of small-scale structures appearing in the Lagrangian field with increasing time: this corresponds to the cascade process in Fourier space as illustrated in figure 2.6. In figure 2.18, exponential tails in normalized PDFs at intermediate and small scales are observed. This shows the strong intermittency in the Lagrangian field at $t = T_e$, which corresponds to the sheet-like small-scale structures as shown in figures 2.14(f) and 2.16(d–f). The spectra of ϕ at $t = T_e$ associated with the original scalar field for each one of the filtered scales are shown in figure 2.19. Combined with figure 2.16, we observe

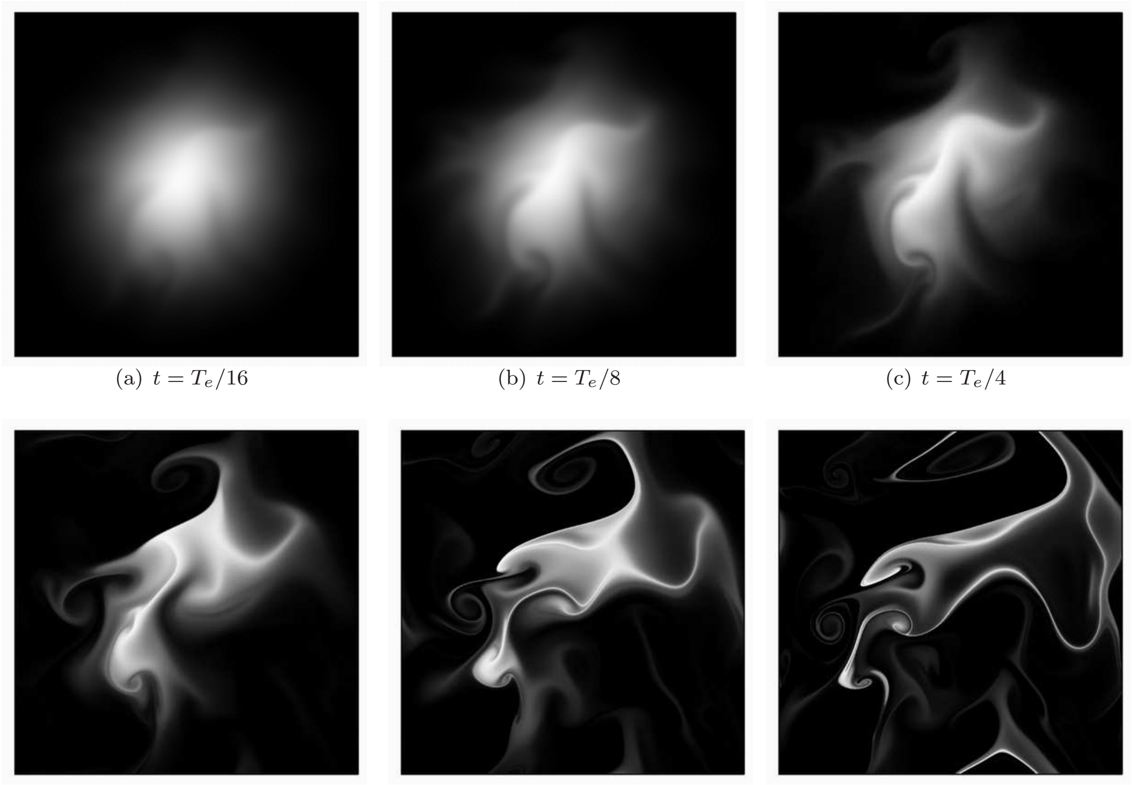
(a) $t = T_e/16$ (b) $t = T_e/8$ (c) $t = T_e/4$

(d) $t = T_e/2$ (e) $t = 3T_e/4$ (f) $t = T_e$

Figure 2.14: Plane-cuts normal to the z-axis at its midpoint of the original three-dimensional Lagrangian fields with the blob-like initial $\phi_0^{(1)}$ in stationary isotropic turbulence at different times

localization in both Fourier and physical domains through the curvelet filtering.

2.5.3 Geometry of Lagrangian structures

Iso-surfaces of $\phi(\boldsymbol{x}, \alpha T_e)$ with three different initial conditions of § 2.3.3 were obtained for each of the filtered scales after the multi-scale decomposition. The contour values ϕ_i^c at scale i are computed from the volume PDFs as

$$\phi_i^c = \langle \phi_i \rangle + 2\sqrt{\mathrm{Var}(\phi_i)} + \Delta, \qquad i = 1 \sim 5, \tag{2.55}$$

with $\Delta = |\phi_{max} - \phi_{min}| \times 5\%$. This choice eliminates artificial, tiny high-frequency oscillations induced by the curvelet transform near the boundary of computational domain. We argue that the sample of iso-surfaces corresponding to the same relative contour value represents the typical statistical geometric properties at each scale. An additional step in the extraction is applied to periodically reconnect those structures which penetrate the box boundaries, to properly account for their geometry.

The largest scale $i = 0$ strongly depends on the initial conditions. This is of less relevance in this

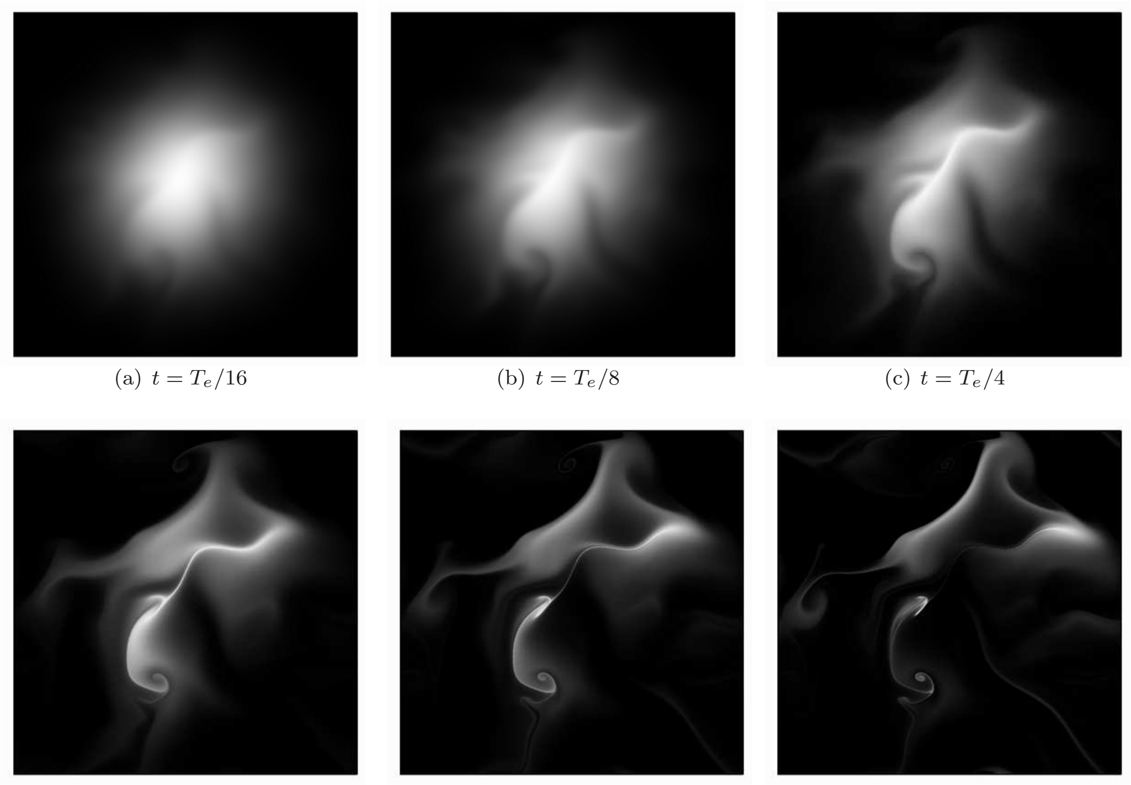

(a) $t = T_e/16$ (b) $t = T_e/8$ (c) $t = T_e/4$

(d) $t = T_e/2$ (e) $t = 3T_e/4$ (f) $t = T_e$

Figure 2.15: Plane-cuts normal to the z-axis at its midpoint of the original three-dimensional Lagrangian fields with the blob-like initial $\phi_0^{(1)}$ in the frozen turbulent field at different times

analysis and the contouring for scale 0 was only applied for the iso-contour level $\phi_0^c = 0.95$ at $t = 0$ and $t = T_e/16$ to show the difference among three initial conditions. Corresponding iso-surfaces of three initial fields and feature centers on the $\hat{S}$–$\hat{C}$ plane are shown in figure 2.13. A minimum number of points, $N_{min} = 1500$, is considered a threshold for a structure to be analyzed, so that it is sufficiently smooth for a reliable calculation of its differential-geometry properties. We remark that this number is higher than $N_{min} = 300$ used in Bermejo-Moreno & Pullin (2008) and Bermejo-Moreno et al. (2009), because near-singular structures tend to be more relevant in Lagrangian fields than in Eulerian scalar or enstrophy fields with a finite viscosity. This threshold avoids spurious features from fragmentation while retaining most sample structures in the characterization step for this case.

The structures at each scale in turbulence are now characterized and represented in the visualization space $(\hat{S}, \hat{C}, \lambda)$ as described in § 2.5.1. Figures 2.20 and 2.21 show the depiction of the multi-scale iso-surfaces in visualization space and the $\hat{S}$–$\hat{C}$ plane, a corresponding subspace, with increasing t. Each component graph shows all iso-surfaces across all scales color coded for scale as indicated in the captions. Sizes of symbols in these figures are scaled by the logarithm of the surface

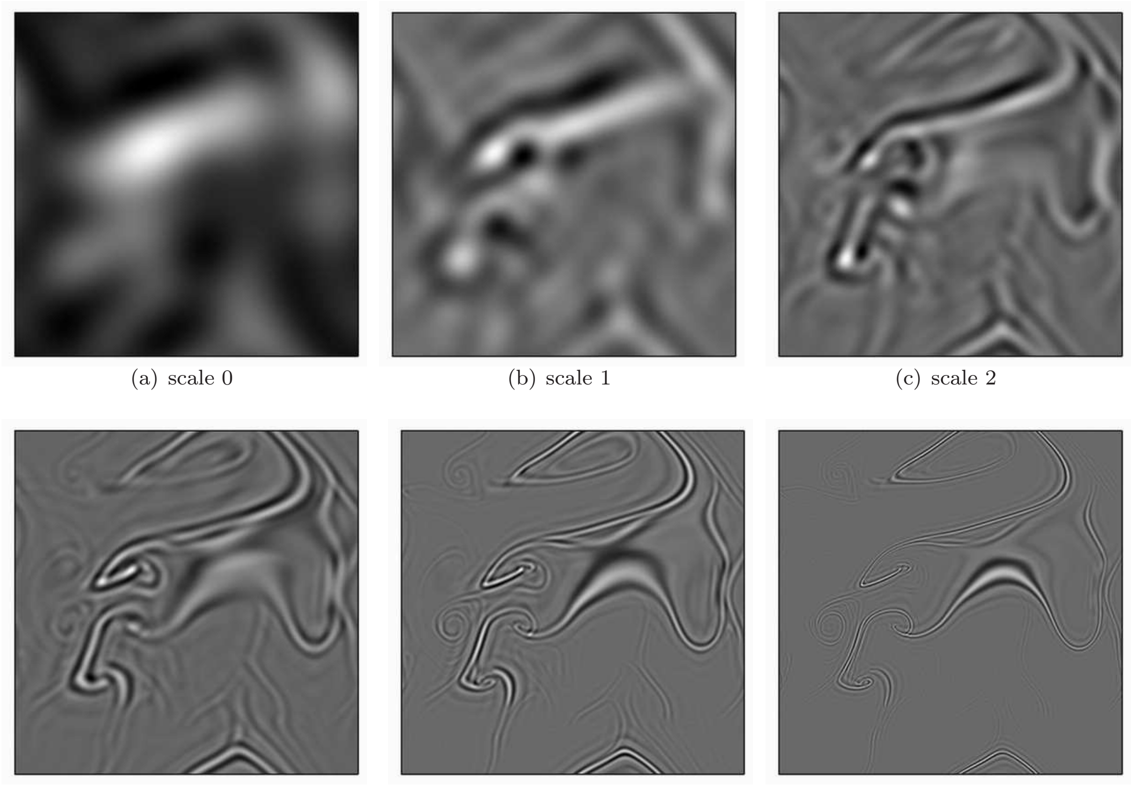
(a) scale 0 (b) scale 1 (c) scale 2

(d) scale 3 (e) scale 4 (f) scale 5

Figure 2.16: Plane-cuts normal to the z-axis at its midpoint of the Lagrangian field at $t = T_e$ for the blob-like initial $\phi_0^{(1)}$ in stationary isotropic turbulence for each one of the filtered scales resulting from the multi-scale analysis

area of the structures. At $t = T_e/16$, there are only a few iso-surfaces that are clustered in the upper-right of the visualization space in the view shown. This corresponds to blob-like structures. As t increases, progressively, most structures are stretched towards the sheet-like region with low $\hat{C}$ and λ, while we find only a few structures that appear to migrate first through the tube-like region near the axis $\{\hat{S} = 1/2, \hat{C} = 1, \lambda\}$. For example, at $t = T_e/2$, structures with low values of $\hat{C}$ are dominant, and a few get close to the tube-like region in figure 2.21(d). This could be interpreted as the evolutionary breakdown of Lagrangian blobs that first distort, while a few portions might be rolled up into tube-like structures, and then are either broken down or stretched laterally into sheets, or else are perhaps part of vortices whose velocity fields strain small-scale structures into sheet-like form.

Furthermore, it seems the appearance of tube-like structures occurs later in that time evolution. In figures 2.21(e) and (f), between $t = 3T_e/4$ and $t = T_e$, more structures appear in the vicinity of the tube-like region. Details of the multi-scale decomposition within the visualization space of the component fields at $t = T_e$ with the blob-like initial condition $\phi_0^{(1)}$ are shown in figure 2.22. This depicts clouds of points, corresponding to each of scales 1 through 5 in the $\hat{S}$–$\hat{C}$ plane. We observe

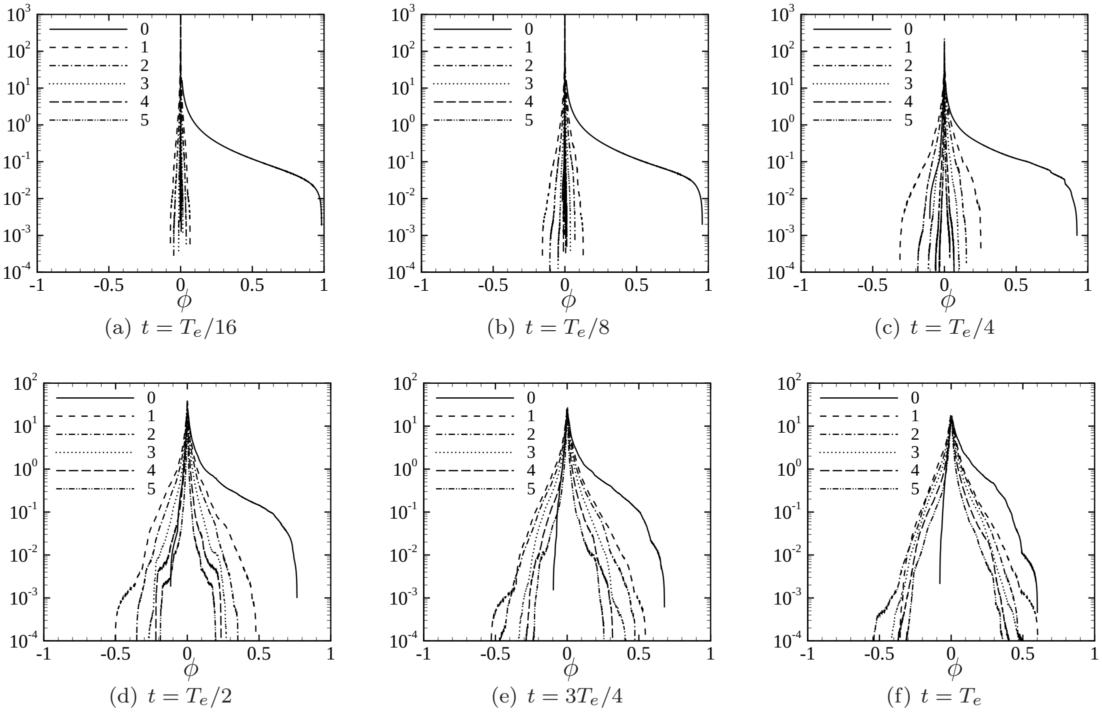

(a) $t = T_e/16$ (b) $t = T_e/8$ (c) $t = T_e/4$

(d) $t = T_e/2$ (e) $t = 3T_e/4$ (f) $t = T_e$

Figure 2.17: Volume-data PDFs of Lagrangian component scalar fields of different scales with $\phi_0^{(1)}$ at different times in stationary isotropic turbulence

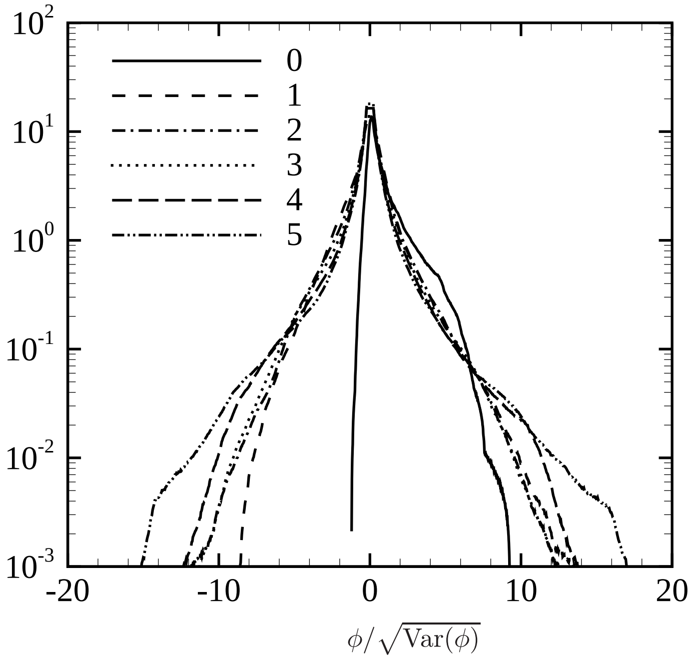

Figure 2.18: Normalized volume-data PDFs of Lagrangian component scalar fields of different scales with $\phi_0^{(1)}$ at $t = T_e$ in stationary isotropic turbulence

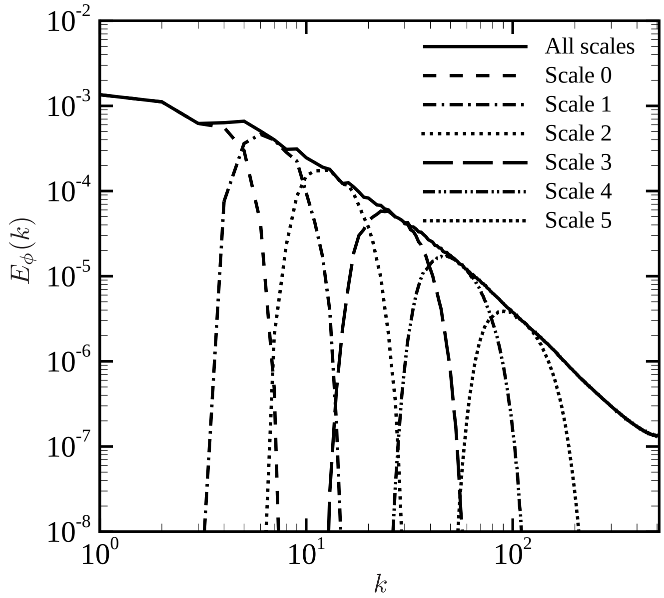

Figure 2.19: Spectra of the full Lagrangian field and component fields with $\phi_0^{(1)}$ at $t = T_e$

a geometrical progression from blobs through tubes to sheet-like structures with decreasing length scale. Here, we note that a spiral-like sheet of small thickness could fill a substantial volume with the space in between its turns deformed into a tube-like geometry as the sheet rolls up. After filtering, this composite structure would appear as a virtual tube with a larger cross-sectional scale, in terms of averaged radius, than the thickness of the sheet itself.

It is notable that the region of visualization space occupied by the cloud of all Lagrangian scale-structures at $t = T_e$ is similar in shape to the region of visualization space occupied by the Eulerian enstrophy and dissipation across all scales in figures 12 and 13 of Bermejo-Moreno et al. (2009). The former is a consequence of Lagrangian evolution whilst the latter are instantaneous Eulerian fields. There are differences, however, in which Lagrangian structures tend to show more sheet-like geometry at intermediate and small scales. The cloud of Lagrangian structures at scale 1 in the visualization space occupies a similar region of the visualization space to that of the Eulerian enstrophy at scale 3 (Bermejo-Moreno et al., 2009), and a passive scalar with $Sc = 0.7$ at scale 4 (Bermejo-Moreno & Pullin, 2008). The corresponding wavenumber range of scale 1 is approximately between 3 and 20. This implies that the geometry transition of Lagrangian structures from blob-like shape to sheet-like shape begins earlier in scale space than for Eulerian fields. This is possibly due to the lack of viscous dissipation for Lagrangian evolution. As described in § 2.4.4, Lagrangian structures are exposed by persistent straining motions and wound by vortices, but are not subject to smoothing by a dissipation mechanism. The dominant sheet-like structures with strong scalar gradients have an

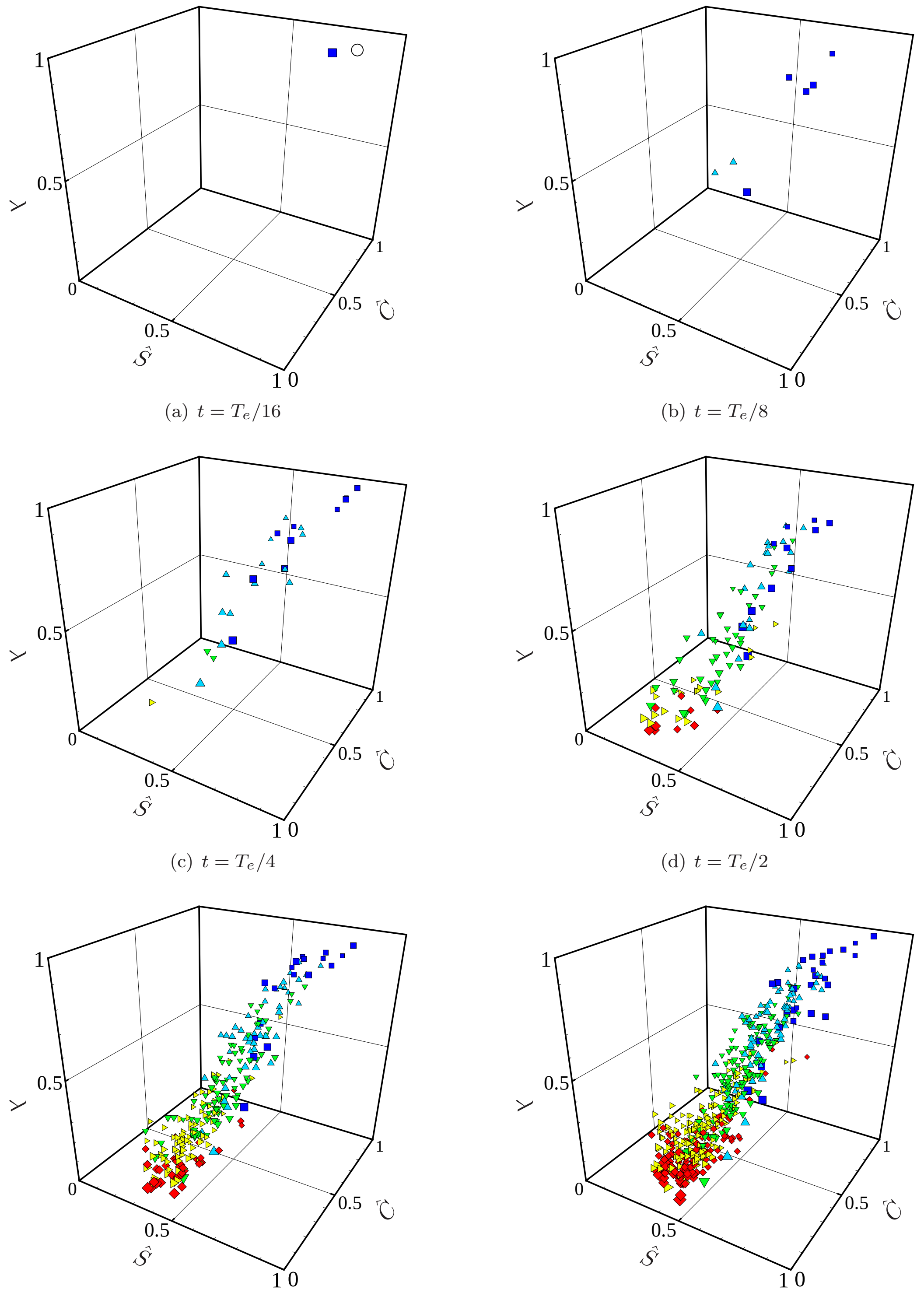

(a) $t = T_e/16$

(b) $t = T_e/8$

(c) $t = T_e/4$

(d) $t = T_e/2$

(e) $t = 3T_e/4$

(f) $t = T_e$

Figure 2.20: Visualization space for Lagrangian structures with the blob-like initial $\phi_0^{(1)}$ at different scales in stationary isotropic turbulence (○ scale 0; □ scale 1; △ scale 2; ▽ scale 3; ▷ scale 4; ◇ scale 5). The sizes of symbols are scaled by the log of surface area

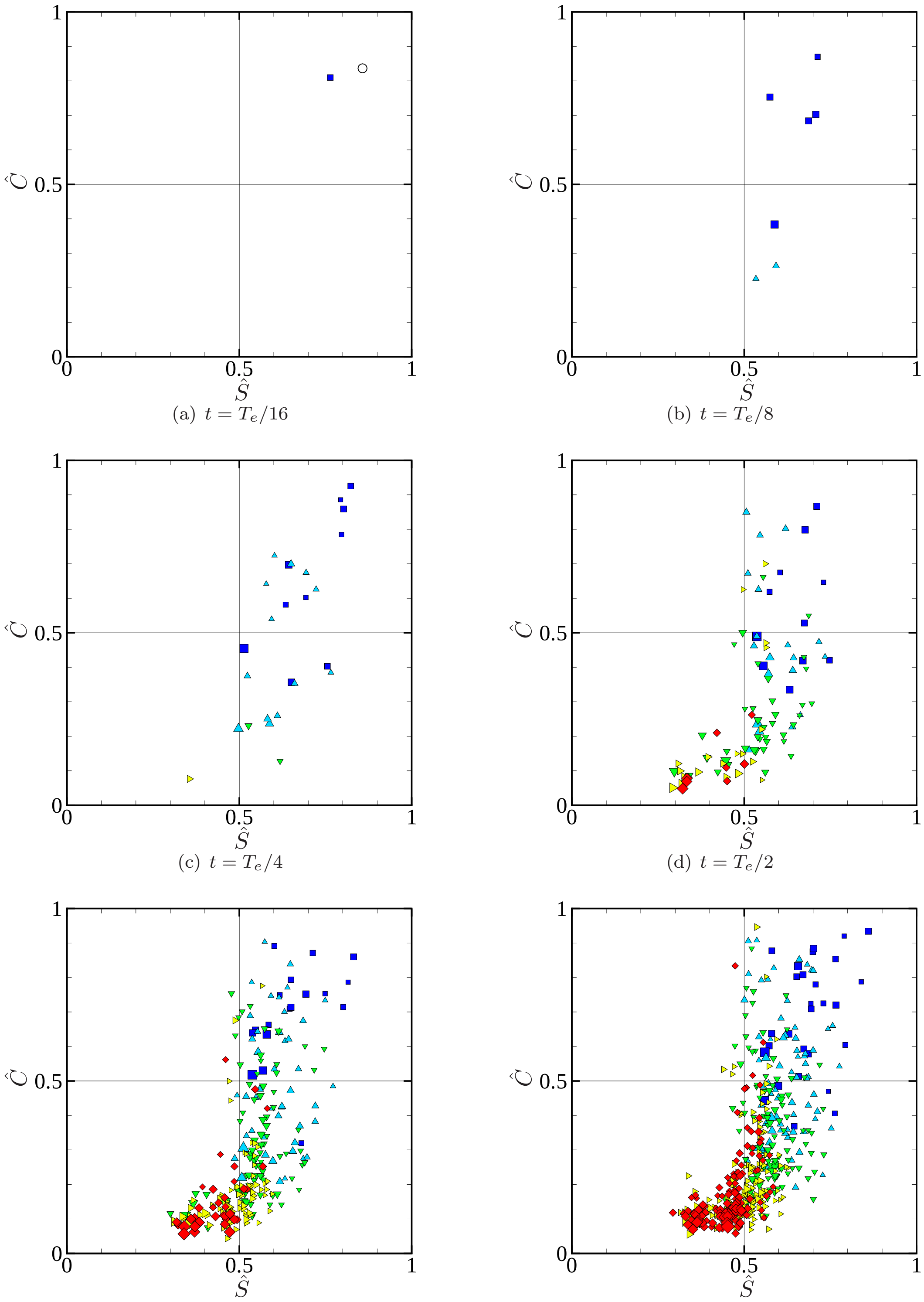

(a) $t = T_e/16$

(b) $t = T_e/8$

(c) $t = T_e/4$

(d) $t = T_e/2$

(e) $t = 3T_e/4$

(f) $t = T_e$

Figure 2.21: $\hat{S}$–$\hat{C}$ plane of the visualization space for Lagrangian structures with the blob-like initial $\phi_0^{(1)}$ at different scales in stationary isotropic turbulence ($\bigcirc$ scale 0; $\square$ scale 1; $\triangle$ scale 2; $\triangledown$ scale 3; $\triangleright$ scale 4; $\diamond$ scale 5). The sizes of symbols in this figure are scaled by the log of surface area

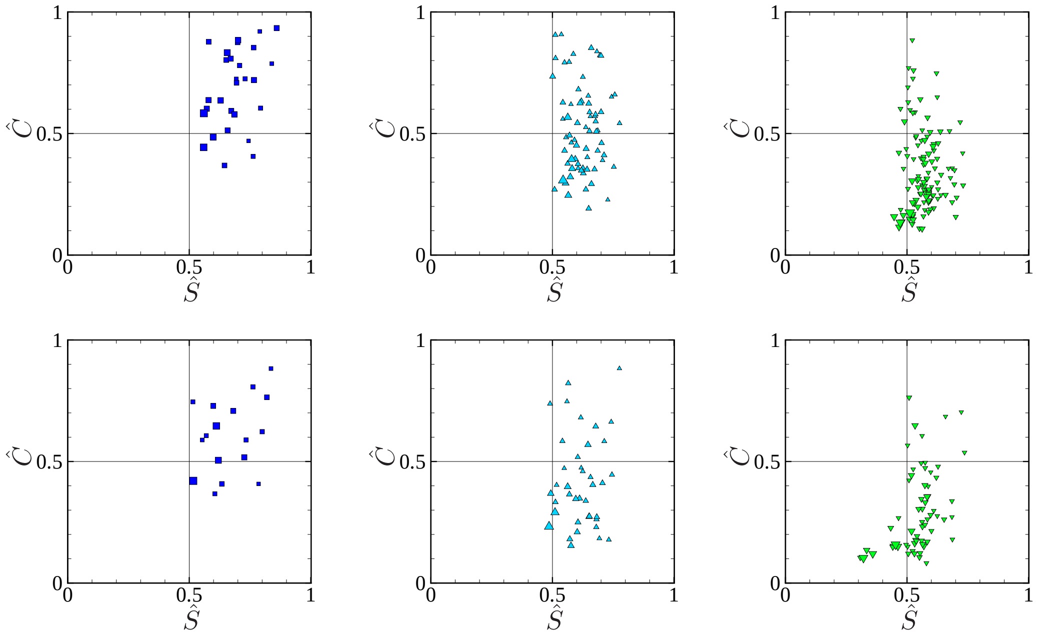

(a) scale 1 (b) scale 2 (c) scale 3

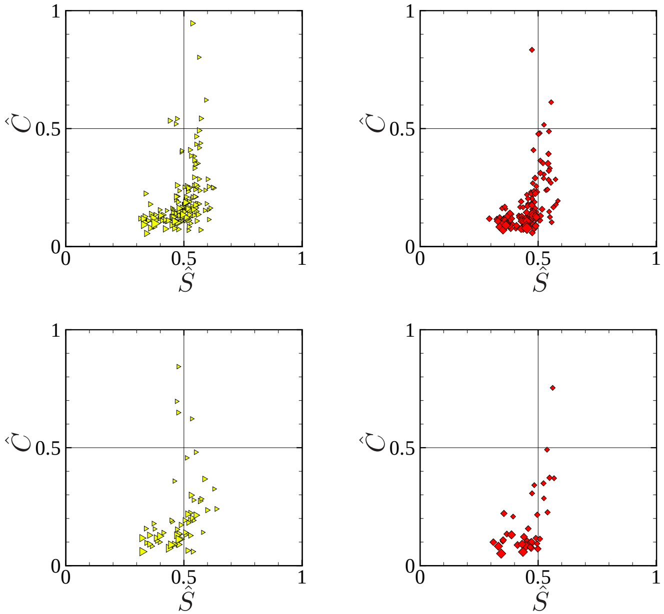

(d) scale 4 (e) scale 5

Figure 2.22: $\hat{S}$–$\hat{C}$ plane of the visualization space for each one of the filtered scales with the blob-like initial field $\phi_0^{(1)}$ at $t = T_e$ in stationary isotropic turbulence (upper row in each sub-figure) and the frozen turbulent field (lower row in each sub-figure). The sizes of symbols in this figure are scaled by the log of surface area

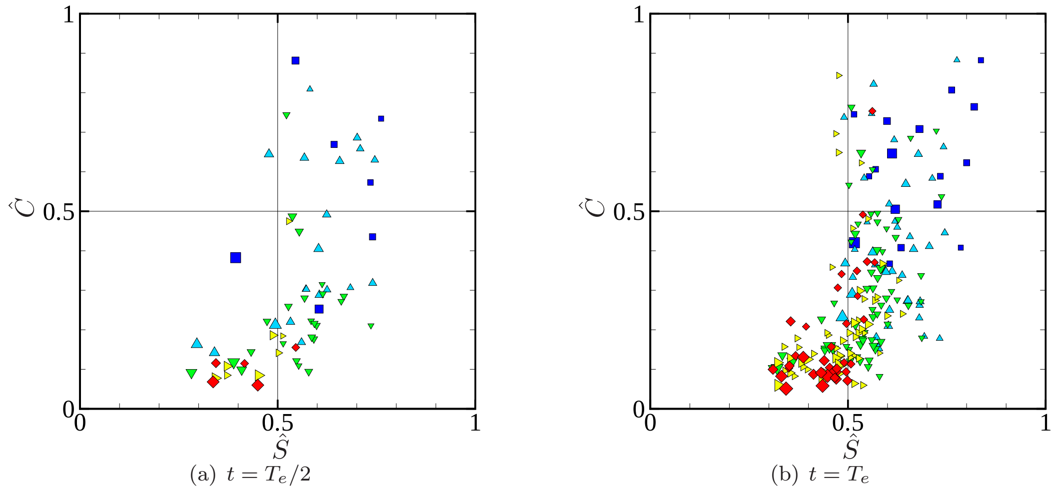

(a) $t = T_e/2$

(b) $t = T_e$

Figure 2.23: $\hat{S}$–$\hat{C}$ plane of the visualization space for Lagrangian structures with the blob-like initial $\phi_0^{(1)}$ at different scales in the frozen turbulent field (□ scale 1; △ scale 2; ▽ scale 3; ▷ scale 4; ◇ scale 5). The sizes of symbols are scaled by the log of surface area

impact on accelerating passive scalar variance dissipation with a finite diffusivity and cause strong intermittency in passive scalar statistics (see Warhaft, 2000). Furthermore, the similar-shaped clouds at scales 4 and 5 in figure 2.22 might imply the self-similar geometry of Lagrangian structures at small scales, which could provide some support for structure-based subgrid scale modeling. To better investigate this possible self-similar geometry feature, simulations of ϕ in higher Reynolds number turbulence with a larger inertial range could be helpful. This requires, however, much higher resolution for both the turbulent field and the Lagrangian field than is employed presently.

Results from the multi-scale geometric analysis applied to Lagrangian structures in the frozen turbulent field are shown in figures 2.22 and 2.23. We find a similar geometry transition as that in turbulence but with less small-scale structures at the later stages, which is consistent with the comparison of spectra shown in figure 2.6. Moreover, in general smaller $\hat{S}$ and $\hat{C}$ at intermediate and small scales indicate that Lagrangian structures in the frozen velocity field exhibit more sheet-like shapes. These observations can be better understood by considering average feature centers over all the structures obtained from the extraction step in the multi-scale decomposition for each scale. The three average geometric feature centers in visualization space are plotted in figure 2.24. The differences of $\langle\hat{C}\rangle_i$, $\langle\hat{S}\rangle_i$, and $\langle\lambda\rangle_i$ in the two flow cases show that near-singular structures tend to be formed more easily in the frozen turbulent field, because strong straining regions are always located at the same spatial regions as clearly indicated in figures 2.3 and 2.15.

The evolution of Lagrangian structures with the tube-like and sheet-like initial Lagrangian fields corresponding to $\phi_0^{(2)}$ and $\phi_0^{(3)}$ of § 2.3.3 in turbulence is shown in figures 2.25 and 2.26, respectively. At early times, the geometries of large-scale structures represented by the feature centers at scale 0 at $t = T_e/16$ are different in all three cases. But we observe that all fields evolve so as to produce similar-

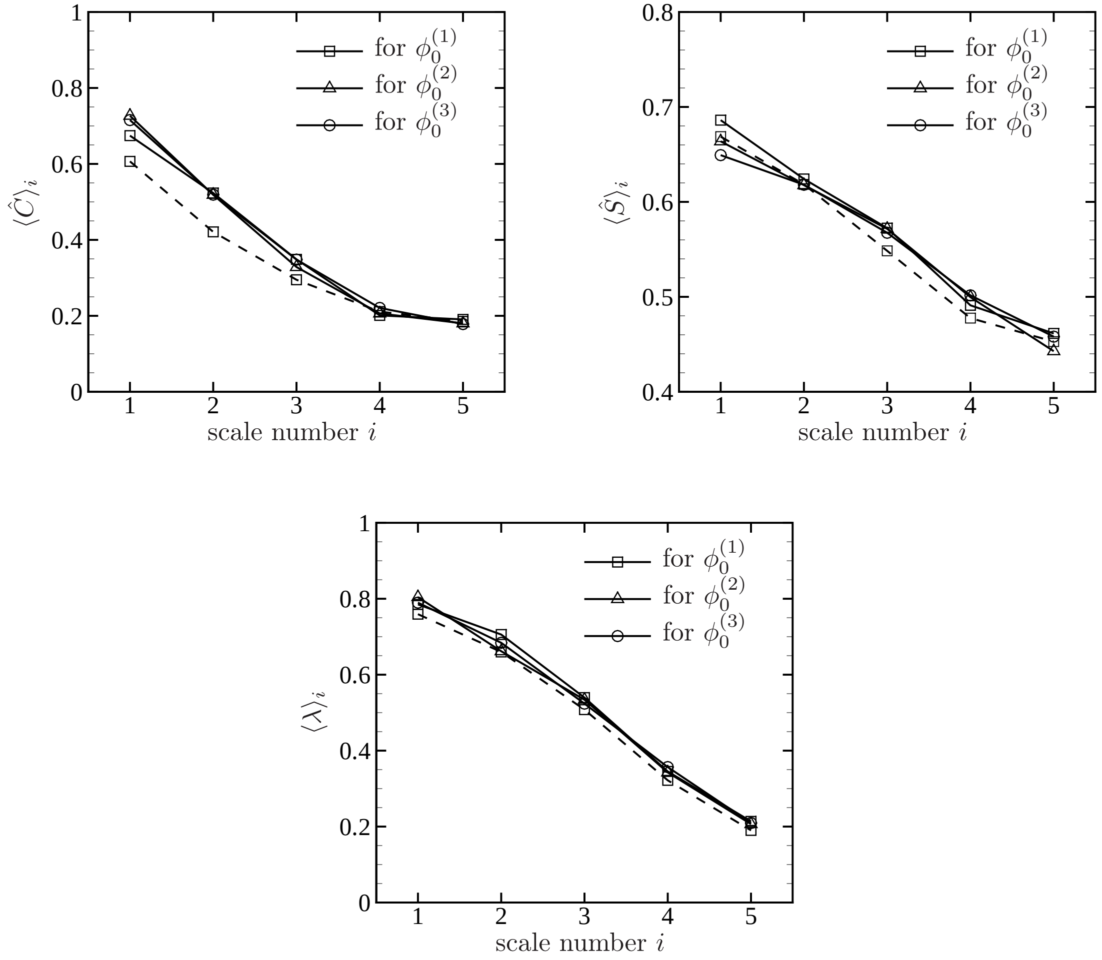

Figure 2.24: Average feature centers at different scales for the Lagrangian field with different initial conditions at $t = T_e$ in stationary isotropic turbulence (solid lines) and the frozen turbulent field (dashed lines)

shaped clouds of structures at $t = T_e$, which is verified by similar average feature centers at each scale shown in figure 2.24. This suggests that the cloud shape shown in figure 2.21 (f) is a Lagrangian attractor that is sensibly independent of the details of initial ϕ. In this interpretation, the memory of the initial geometric property of the Lagrangian fades after the Lagrangian integral time $T_L \approx 3T_e/4$ in chaotic motion, where T_L is obtained from the Lagrangian velocity autocorrelation (Yang et al., 2008). An alternative, but perhaps related, explanation is that the similarity in visualization space at late times of all three present evolved Lagrangian fields and instantaneous Eulerian fields could be a consequence of the statistically steady character of the underlying forced box turbulence DNS, i.e., Lagrangian structures tend to follow and to be attracted to vortex surfaces in high-Reynolds-number turbulence.

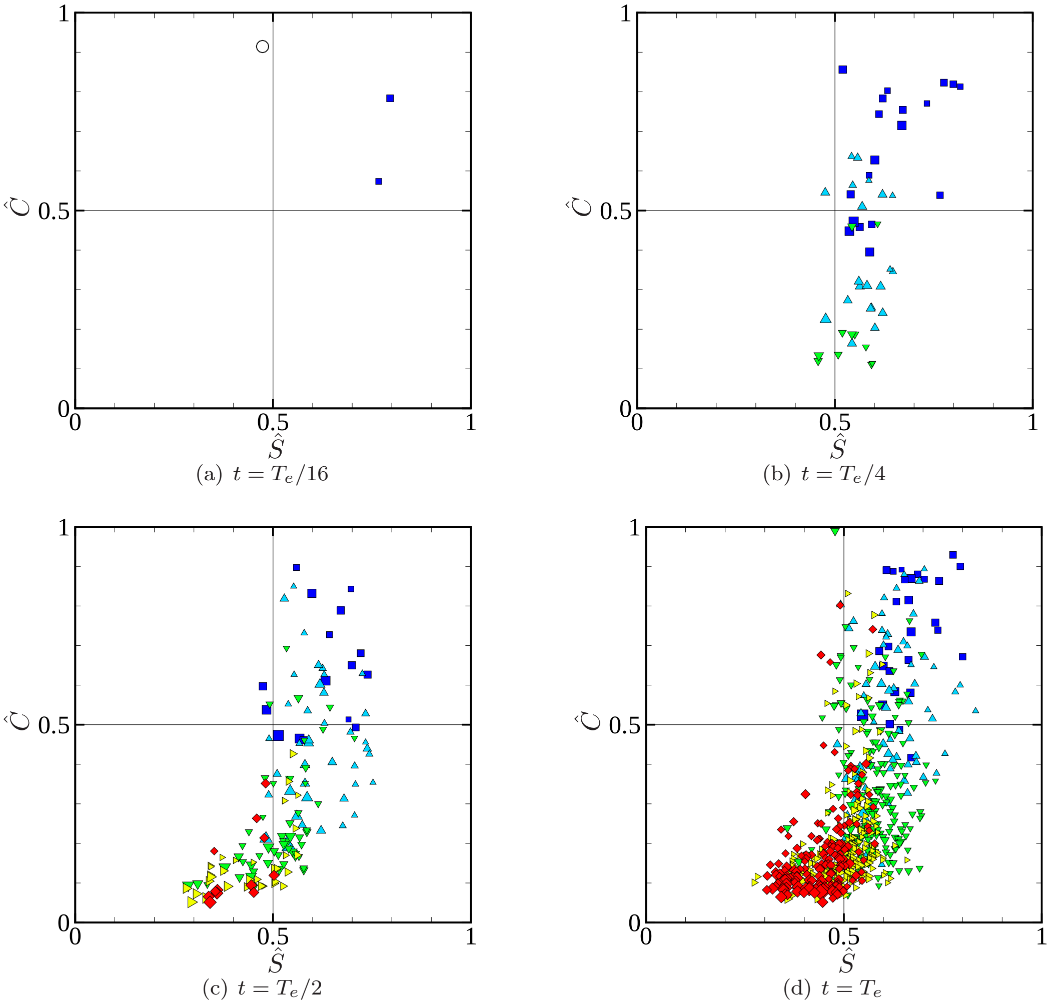

(a) $t = T_e/16$

(b) $t = T_e/4$

(c) $t = T_e/2$

(d) $t = T_e$

Figure 2.25: $\hat{S}$–$\hat{C}$ plane of the visualization space for Lagrangian structures with the tube-like initial $\phi_0^{(2)}$ at different scales in stationary isotropic turbulence (○ scale 0; □ scale 1; △ scale 2; ▽ scale 3; ▷ scale 4; ◇ scale 5). The sizes of symbols are scaled by the log of surface area

2.6 Results and discussion

In this study, the backward-particle-tracking method was applied to the computation of the temporal evolution of high-resolution Lagrangian fields $\phi(\boldsymbol{x}, t)$ in velocity fields from unsteady, forced, stationary isotropic turbulence and also from a velocity field obtained from a turbulence simulation but frozen in time. Lagrangian structures were extracted as iso-surfaces of the Lagrangian field $\phi(\boldsymbol{x}, t)$. From the evolution of finite-sized Lagrangian structures in turbulence, exponential surface area growth is verified, and the growth rate normalized by the reciprocal of the Kolmogorov time scale is approximately 0.33 ± 0.4. Stretched structures are observed in highly straining flow regions and rolled-up structures are found in stretched vortex tubes. The formation of rolled-up or spiral structures in the Lagrangian field is consistent with observed alignment between the scalar gradient

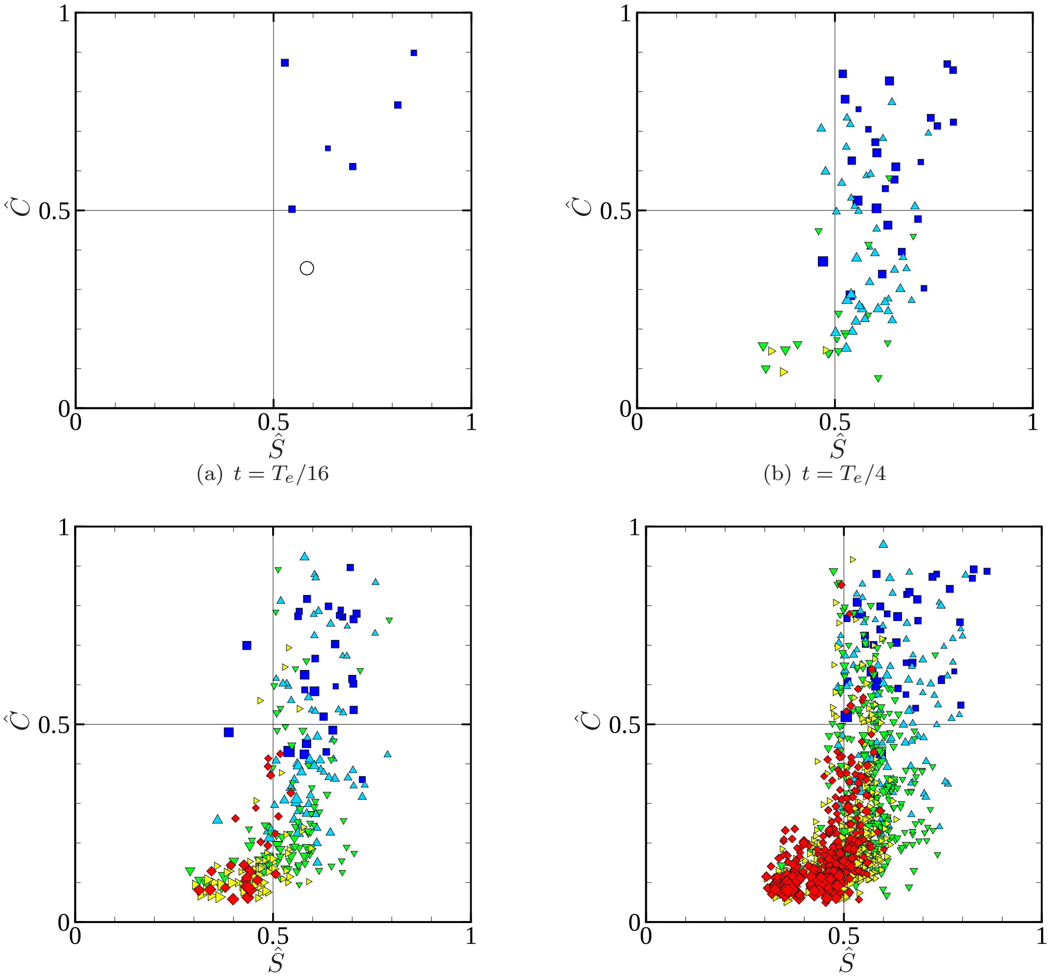

(a) $t = T_e/16$ (b) $t = T_e/4$

(c) $t = T_e/2$ (d) $t = T_e$

Figure 2.26: $\hat{S}$–$\hat{C}$ plane of the visualization space for Lagrangian structures with the sheet-like initial $\phi_0^{(3)}$ at different scales in stationary isotropic turbulence (○ scale 0; □ scale 1; △ scale 2; ▽ scale 3; ▷ scale 4; ◇ scale 5). The sizes of symbols are scaled by the log of surface area

and vorticity, and the moderate normal alignment scalar gradient and the local velocity. A simple two-dimensional model of a scalar field wound by an axisymmetric vortex reproduces these features.

We find that iso-surfaces of the Lagrangian field are attracted to steady stream surfaces in the frozen velocity field. In contrast, these tend to follow and almost attach to vortex surfaces for the turbulent velocity field, but ultimate, long-time alignment is repressed by the cumulative action of viscous effects. Furthermore, the tendency for the formation of near-singular, sheet-like Lagrangian structures is more apparent in the frozen versus the turbulent velocity field owing to the presence of time-invariant straining regions in the former. It is expected that these two differing alignment scenarios would lead to quite different long-time behaviors and that this constitutes a principal distinction separating the kinematics from the turbulent dynamics of Lagrangian structures. Moreover we suggest that this could lend support to hypotheses both concerning geometric similarities between Lagrangian fields and corresponding vorticity fields, and also the independence of geometric signatures of Lagrangian structures on initial conditions of the Lagrangian field.

A multi-scale geometric analysis (Bermejo-Moreno & Pullin, 2008) was used to study the statistical, evolutionary geometry of the Lagrangian field for both the turbulent and the frozen velocity fields. The evolutionary breakdown of Lagrangian blobs, from $t = 0$ to $t = T_e$, was represented in a space of reduced geometrical parameters representative of the shape of individual structures. As time increases, we observed that, for the turbulent velocity field, multi-scale structures appear to migrate from the blob-like region to the sheet-like region of that space. A few large-scale, tube-like structures appear at later times because of the roll-up phenomenon. Somewhat similar behavior was qualitatively observed for the frozen field but the population of small-scale structures at $t = T_e$ was found to be much diminished in comparison with the turbulent velocity field. In comparison with instantaneous passive scalar and enstrophy fields in turbulence studied by Bermejo-Moreno & Pullin (2008) and Bermejo-Moreno et al. (2009), Lagrangian structures show predominantly more sheet-like geometry in intermediate and small scales, perhaps owing to the lack of viscous dissipation. Moreover, the geometry of Lagrangian structure from blob-like, tube-like, and sheet-like initial Lagrangian fields is very similar at $t = T_e$. This could imply that the geometry of Lagrangian structures at the later stage does not depend on initial configurations.

A natural line of extension of the work presented in this chapter is to the study on the geometry of Lagrangian structures in a turbulent wall-bounded flow, which will be addressed in § 3. Furthermore, the methodology for the geometric analysis is applicable to experimental data sets. The multi-scale decomposition in the extraction step is based on the curvelet transform and is currently implemented to treat domain boundaries by periodization. The characterization and classification of educed structures (Bermejo-Moreno & Pullin, 2008) can then be immediately applied. Another direction is the investigation of the evolution of vortex surfaces. We will discuss this issue in §§ 4 and 5.

Chapter 3

Lagrangian and Eulerian structures in turbulent channel flow

3.1 Background and objectives

Coherent motions or structures with identifiable tube-like shapes that appear to contain concentrated vorticity have been extensively observed and reported for wall-bounded turbulent flows. Although the role played by turbulent coherent structures is still not fully understood, many studies have provided evidence supporting the hypothesis that these structures constitute, in some statistical sense, basic elemental vortices that participate in the dynamics of near-wall turbulence, and are important for drag reduction, turbulent control, and other applications (see Robinson, 1991; Panton, 2001). In what follows, we will generally use the term ‘quasi-streamwise vortices’, which has been hypothesized in the cited references, to denote individual inclined structures or objects that exist in near-wall turbulence. In the present work, we describe geometry-based metrics that further support the existence of these structures.

Both Lagrangian- and Eulerian-based approaches have been used to study wall turbulence. Lagrangian methods typically track trajectories of fluid particles, often using visualization techniques. Particle tracers such as hydrogen bubbles (e.g., Kline et al., 1967) or passive scalars such as smoke or dye (e.g., Head & Bandyopadhyay, 1981) show evolving flow structures. These visual studies revealed rich geometries in turbulent structures but remain mainly qualitative (Robinson, 1991). Eulerian methodologies benefited from the development of DNS (e.g., Kim, Moin & Moser, 1987) and experimental particle-image velocimetry (PIV) (e.g., Liu et al., 1991) that provide full, two- or three-dimensional instantaneous velocity fields. The Eulerian structures are usually extracted using either iso-surfaces of vorticity magnitude or popular vortex identification criteria (e.g., Hunt, Wray & Moin, 1988; Chong, Perry & Cantwell, 1990; Jeong & Hussain, 1995).

Major observations on coherent structures in wall turbulence include that the streamwise velocity field close to the wall is organized into alternating narrow streaks of high- and low-speed velocity

(Kline et al., 1967) and that candidate hairpin- or Λ-like vortices may exist in the logarithmic region, while the turbulent motion appears to be less active in the outer layer. The conceptual model of the hairpin vortex was developed by Theodorsen (1952) and supported by experiment (Head & Bandyopadhyay, 1981) and computation visualizations (Moin & Kim, 1982). The modern model of the hairpin vortex is usually described as a combination eddy composed of a hairpin body and two relatively short counter-rotating quasi-streamwise vortices that create low-speed streaks in the buffer layer (Adrian, 2007). Furthermore, recent DNS and PIV studies provide evidence that hairpin-like structures can autogenerate to form packets that occupy a significant volume fraction of the boundary layer (e.g., Zhou et al., 1999).

Although observation of Eulerian structures can perhaps elucidate turbulence flow physics at a time instant, the Lagrangian approach seems better suited for investigation of the temporal evolution of turbulent coherent structures and their dynamical role in turbulent transition and mixing. This issue was discussed by Green, Rowley & Haller (2007) who showed the evolution of single vortex-like structures into a packet of similar structures in turbulent channel flow by identifying 'Lagrangian coherent structures' (Haller, 2001). In § 2, we illustrated and quantified the evolutionary geometry in the breakdown of initially large-scale Lagrangian structures in isotropic turbulence using a multi-scale geometric analysis.

Consensus on the accepted geometry of vortical structures in wall-bounded turbulence remains elusive. From flow visualization studies of the turbulent boundary layer, Falco (1977) showed that large-scale structures of the smoke concentration field, with typical length scales from δ to 3δ, inclined to the wall at a characteristic angle 20°–25°, while Head & Bandyopadhyay (1981) measured an inclination angle 40°–50° for candidate hairpins. Using LES and correlation studies, Moin & Kim (1985) obtained a most probable inclination angle of local vorticity vector as 45°, while Honkan & Andreopoulos (1997) found that the vorticity is inclined at 35° from multi-probe, hot wire measurements. Using PIV experiments and statistical tools, Ganapathisubramani et al. (2006) identified individual vortex cores most frequently inclined at 45°. The model developed by Bandyopadhyay (1980) gives that the inclination angle of candidate hairpin packets is 18°. Christensen & Adrian (2001) found an inclination angle of 12°–13° for the envelope of a series of swirling motions. In contrast, contour-dynamics simulation (Pullin, 1981) of a two-dimensional uniform vorticity layer adjacent to a wall showed inclined structures that resemble flow features observed in the smoke visualization (Falco, 1977) of the interface between turbulent and non-turbulent fluid in the outer part of a turbulent boundary layer. This suggests that at least these outer features may not be generated entirely by three-dimensional effects. Open questions remain whose resolution may depend on the scale of structures, Reynolds numbers and the usage of Lagrangian or Eulerian methods in investigations.

The geometry of eddies is also of interest for structure-based models of near-wall turbulence.

Predictive models have been developed, based on the attached eddy hypothesis (Townsend, 1976), that utilize random superpositions of hierarchies of either hairpins (Perry & Chong, 1982; Perry, Henbest & Chong, 1986; Perry & Marusic, 1995) or hairpin packets (Marusic, 2001). A particular geometry or shape of hairpin or Λ-like vortices is assumed. Additionally, geometrical issues may inform near-wall, subgrid-scale modeling for LES based on small-scale vortical structures (Chung & Pullin, 2009). The existence of coherent structures with characteristic geometric features may suggest a possible sparse representation for reconstructing a whole channel flow with a greatly reduced number of optimal basis functions utilizing either a wavelet- or curvelet-based extraction method (e.g., Okamoto et al., 2007; Ma et al., 2009).

In this chapter, the multi-scale geometric analysis of both Lagrangian and Eulerian structures in isotropic turbulence (see § 2) is extended to turbulent channel flow by introducing the multi-directional decomposition and mirror-extended data. The extended geometric analysis, which is based on the mirror-extended curvelet transform (see Candès et al., 2006; Demanet & Ying, 2007), will include both multi-scale and multi-directional decompositions of a specific scalar field with non-periodic boundary conditions in wall turbulence. This provides quantitative statistics on the orientation of turbulent structures at different locations, scales, and Reynolds numbers. Phenomena in wall turbulence to be investigated include the follwing: first, the detailed geometry of quasi-streamwise vortices and other structures in the near-wall region (about $5\delta_\nu$ to 0.3δ); second, the structural evolution of near-wall vortices, with initially almost spanwise orientation within the buffer region very close to the wall, into possible Λ-like or hairpin vortices at a larger wall distance; third, the existence and geometry of packets, based on statistical evidence obtained from the multi-scale analysis.

We begin in § 3.2 by giving a simulation overview for the DNS, using a spectral method, and the computation of Lagrangian fields with the backward-particle-tracking method. In § 3.3, a systematic framework is introduced to quantify geometries including averaged inclination and sweep angles of flow structures at multiple scales. § 3.4 shows the application of the multi-scale and multi-directional geometric analysis to investigate the geometry of Lagrangian structures at different length scales in time evolution. In § 3.5 we investigate the geometry of multi-scale, Eulerian structures and provide statistical evidence supporting the formation of structure packets. Finally, some conclusions are drawn in § 3.6.

3.2 Simulation overview

3.2.1 Direct numerical simulation

For turbulent channel flow in a domain with sides $L_x \times L_y \times L_z$ and grids $N_x \times N_y \times N_z$, the incompressible Navier–Stokes equations are non-dimensionalized by the channel half-height δ and the friction velocity u_τ as

$$\left.\begin{aligned}&\frac{\partial \boldsymbol{u}}{\partial t}+\boldsymbol{u}\cdot\nabla\boldsymbol{u}=-\nabla p+\boldsymbol{P}_0+\frac{1}{Re_\tau}\nabla^2\boldsymbol{u},\\&\nabla\cdot\boldsymbol{u}=0.\end{aligned}\right\}\tag{3.1}$$

Here, the friction Reynolds number is defined as $Re_\tau = u_\tau\delta/\nu$, where the friction velocity is $u_\tau = \sqrt{\tau_w/\rho}$. The viscous, near-wall length scale is $\delta_\nu = \nu/u_\tau$, with wall shear stress τ_w. In the present simulations, we set $\delta = 1$ and $u_\tau \approx 1$. A constant pressure gradient $\boldsymbol{P}_0$ in (3.1) is used to drive the flow. A diagram of the computational domain is shown in figure 3.1, where U is the mean velocity in the streamwise direction.

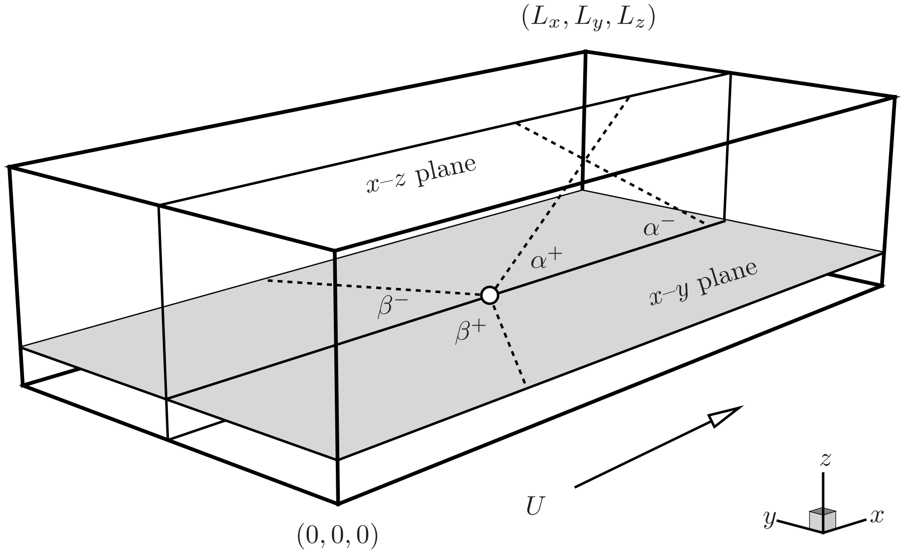

Figure 3.1: Diagram of the computational domain and definition of characteristic angles of structures. Possible structures are sketched by dashed lines

The DNS is performed using a spectral method (see Kim, Moin & Moser, 1987): Fourier series in the streamwise x- and spanwise y-directions, and the Chebyshev polynomial expansion in the wall-normal z-direction. Aliasing errors are removed using the two-thirds truncation method. The low-storage third-order semi-implicit Runge–Kutta method (Spalart, Moser & Rogers, 1991) is applied for the temporal discretization and the CFL number

$$\Delta t \max\left(\frac{|u_x|}{\Delta x}, \frac{|u_y|}{\Delta y}, \frac{|u_z|}{\Delta z}\right)$$

was set to unity, where Δt is the time step size and Δx, Δy, and Δz are the mesh sizes in three directions. A summary of DNS parameters is listed in table 3.1, where U_c is the mean centerline velocity at $z = \delta$ and the superscript '+' denotes a non-dimensional quantity scaled by δ_ν. It is noted that the runs with $L_x = 2\pi\delta$ were mainly used to investigate the geometric statistics of structures at intermediate and small scales in the present study. On the other hand, large L_x in runs L1 and L2 were chosen for the investigation of hypothesized long structures that may extend over 10δ in the streamwise direction (e.g., Kim & Adrian, 1999; Jiménez et al., 2004; Guala et al., 2006). Statistical steady state, mean velocity profiles for $Re_\tau = 180, 395, 590, 950$ are shown in figure 3.2, which agree with the results in Moser, Kim & Mansour (1999) and del Álamo et al. (2004).

Table 3.1: Summary of DNS parameters for turbulent channel flows

Run	Re_τ	L_x/δ	L_y/δ	L_z/δ	N_x	N_y	N_z	δ_ν	U_c/u_τ	Δx^+	Δy^+
S1	180	4π	2π	2	192	192	193	0.00556	18.28	11.77	5.89
S2	395	2π	π	2	384	192	193	0.00253	20.02	6.47	6.47
S3	590	2π	π	2	384	384	385	0.00165	21.27	9.92	4.96
S4	950	2π	π	2	768	576	385	0.00105	22.68	7.77	5.18
L1	180	16π	2π	2	768	192	97	0.00556	18.15	11.77	5.89
L2	395	16π	2π	2	1536	384	193	0.00253	19.93	12.93	6.47
L3	590	8π	π	2	1152	384	385	0.00165	21.16	12.87	4.96

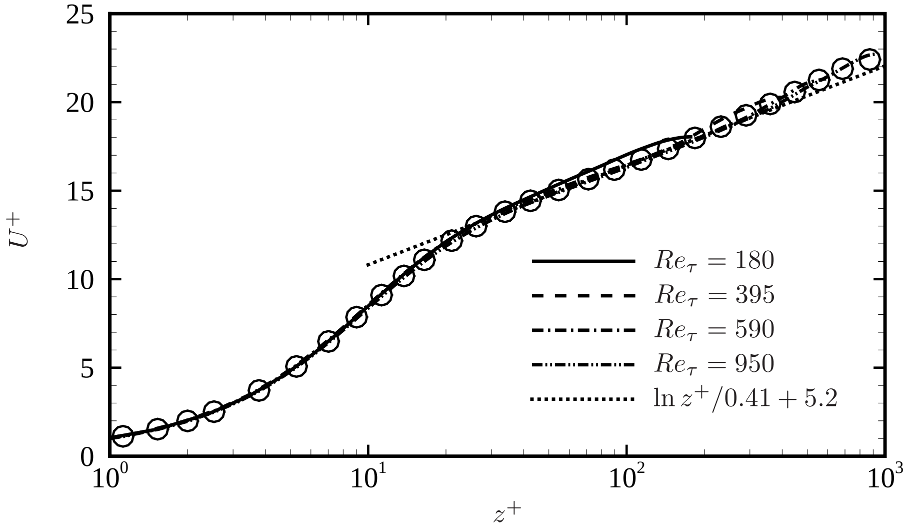

Figure 3.2: Mean velocity profiles from the DNS. Symbols denote the results at $Re_\tau = 950$ in del Álamo et al. (2004)

3.2.2 Backward-particle-tracking method

The three-dimensional Lagrangian field $\phi(\boldsymbol{x}, t)$ is computed from the scalar convection equation (2.15) by the backward-particle-tracking method described in § 2.3.2. First, the Navier–Stokes equations (3.1) are solved numerically on the $N_x \times N_y \times N_z$ grid in some time interval from t_0 to $t > t_0$ and the full Eulerian velocity field is saved on disk in this simulation period. The time increment is selected to capture the finest resolved scales in the velocity field. At time t at the end of the solution period, particles are placed at the uniform grid points of $N_x^L \times N_y^L \times N_z^L$. Presently, the resolution of the Lagrangian field is two times that of the velocity field in order to capture fine-scale Lagrangian structures in the evolution. Then, particles are released and their trajectories calculated by solving (2.1) backwards in time. A three-dimensional, fourth-order Lagrangian interpolation scheme was used to calculate fluid velocity at the particle location. The trajectory of each particle was then obtained using an explicit, second-order Adams–Bashforth scheme. For each particle the backward tracking is performed from t to the initial time t_0 with the reversed Eulerian velocity fields saved previously. After the backward tracking, initial locations of particles $\boldsymbol{x}_0$ can be obtained. From a given initial condition consisting of a smooth Lagrangian field $\phi(\boldsymbol{x}_0, t_0)$ we can then obtain $\phi(\boldsymbol{x}, t)$ on the Cartesian grid by a simple mapping (2.11) with Lagrangian coordinates.

3.3 Multi-scale and multi-directional methodology

3.3.1 Multi-scale and multi-directional filter based on curvelet transform

When a scalar field has preferential orientations, e.g., streaks in an image, the Fourier transform of the scalar field should have high intensities at some particular localized regions in Fourier space. Thus, the directional decomposition of the scalar field can be obtained by spectral directional/fan filters, which have been used in computer vision, seismology, and image compression (e.g., Bamberger & Smith, 1992). Presently, to obtain statistical, geometric information on preferential orientations in a three-dimensional field at different scales, we apply a multi-scale directional filter based on the curvelet transform (see Candès et al., 2006, and references therein) to a sequence of two-dimensional plane-cuts and then compute the angular spectrum and corresponding averaged angles.

An arbitrary two-dimensional scalar field $\varphi(\boldsymbol{x})$ can be represented by the Fourier expansion

$$\varphi(\boldsymbol{x}) = \sum_{\boldsymbol{k}} \hat{\varphi}(\boldsymbol{k})\, \mathrm{e}^{\mathrm{i}\boldsymbol{k}\cdot\boldsymbol{x}}, \tag{3.2}$$

where $\boldsymbol{x} = (x_1, x_2)$, $\boldsymbol{k} = (k_1, k_2)$, and the Fourier coefficient

$$\hat{\varphi}(\boldsymbol{k}) = \frac{1}{2\pi} \int \varphi(\boldsymbol{x})\, \mathrm{e}^{-\mathrm{i}\boldsymbol{k}\cdot\boldsymbol{x}}\, \mathrm{d}\boldsymbol{x}. \tag{3.3}$$

In the numerical implementation, $\varphi(x_1, x_2)$ is discretized on a rectangular domain of side $L_1 \times L_2$ using an $N_1 \times N_2$ grid with indices (n_1, n_2) in physical space. The corresponding Fourier space can be discretized on the grid $N_1 \times N_2$ with indices (m_1, m_2). The discrete Fourier transform (DFT) and inverse DFT of $\varphi(\boldsymbol{x})$ are

$$\hat{\varphi}(k_{1,m_1}, k_{2,m_2}) = \frac{1}{N_1}\frac{1}{N_2}\sum_{n_1=0}^{N_1-1}\sum_{n_2=0}^{N_2-1}\varphi(x_{1,n_1}, x_{2,n_2})\,\mathrm{e}^{-\mathrm{i}(k_{1,m_1}x_{1,n_1}+k_{2,m_2}x_{2,n_2})}, \tag{3.4}$$

$$\varphi(x_{1,n_1}, x_{2,n_2}) = \sum_{m_1=0}^{N_1-1}\sum_{m_2=0}^{N_2-1}\hat{\varphi}(k_{1,m_1}, k_{2,m_2})\,\mathrm{e}^{\mathrm{i}(k_{1,m_1}x_{1,n_1}+k_{2,m_2}x_{2,n_2})}, \tag{3.5}$$

respectively, with

$$k_{i,m_i} = m_i\Delta k_i, \quad x_{i,n_i} = n_i\Delta x_i, \quad \Delta x_i = L_i/N_i, \quad \Delta k_i = 2\pi/L_i. \tag{3.6}$$

A filtered $\varphi(\boldsymbol{x})$ at scale j and along the direction l can then be extracted from $\hat{\varphi}(\boldsymbol{k})$ in Fourier space by the frequency window function

$$U_j(r,\theta) = 2^{-3j/4}W(2^{-j}r)V(t_l(\theta)), \tag{3.7}$$

in polar coordinates (r,θ) with $r = \sqrt{k_1^2+k_2^2}$ and $\theta = \arctan(k_2/k_1)$. The frequency window function $U_j(r,\theta)$ is based on the curvelet transform (Candès et al., 2006), which is a combination of the radial window function (e.g., Ma et al., 2009)

$$W(r) = \begin{cases} \cos(\pi\mu(5-6r)/2), & 2/3 \le r \le 5/6, \\ 1, & 5/6 \le r \le 4/3, \\ \cos(\pi\mu(3r-4)/2), & 4/3 \le r \le 5/3, \\ 0, & \text{else}, \end{cases} \tag{3.8}$$

and the angular window function

$$V(t_l) = \begin{cases} 1, & |t_l| \le 1/3, \\ \cos(\pi\mu(3|t_l|-4)/2), & 4/3 \le t_l \le 5/3, \\ 0, & \text{else}, \end{cases} \tag{3.9}$$

with the smoothing function $\mu(x) = 3x^2 - 2x^3$ satisfying

$$\mu(x) = \begin{cases} 1, & x \le 0, \\ 0, & x \ge 1, \end{cases} \qquad \mu(x) + \mu(1-x) = 1. \tag{3.10}$$

Both radial and angular window functions satisfy the admissibility conditions:

$$\sum_{r=-\infty}^{\infty} W^2(2^j r) = 1, \qquad r > 0, \tag{3.11}$$

$$\sum_{t_l=-\infty}^{\infty} V^2(t_l) = 1. \qquad t_l \in \mathbb{R}. \tag{3.12}$$

The frequency window functions in Fourier space are plotted in figure 3.3. Each is supported on a region bounded by two neighboring circular wedges in the range of wavenumbers $2^{j-1} \leq r \leq 2^{j+1}$. The localization of $U_j(r, \theta)$ in Fourier space implies that the corresponding spatial structure in physical space is a needle-shaped element ('curvelet'), whose envelope has the geometric scaling relation (Candès et al., 2006)

$$\text{length} \approx 2^{-j/2}, \qquad \text{width} \approx 2^{-j}. \tag{3.13}$$

From (3.13), the characteristic length scale is $\mathcal{L}_j \approx 2^{-j}$ at scale j, which is the characteristic width of the 'curvelet' at scale j in physical space. The breakdown of the normalized characteristic length scales of structures after the multi-scale decomposition is given in table 3.2.

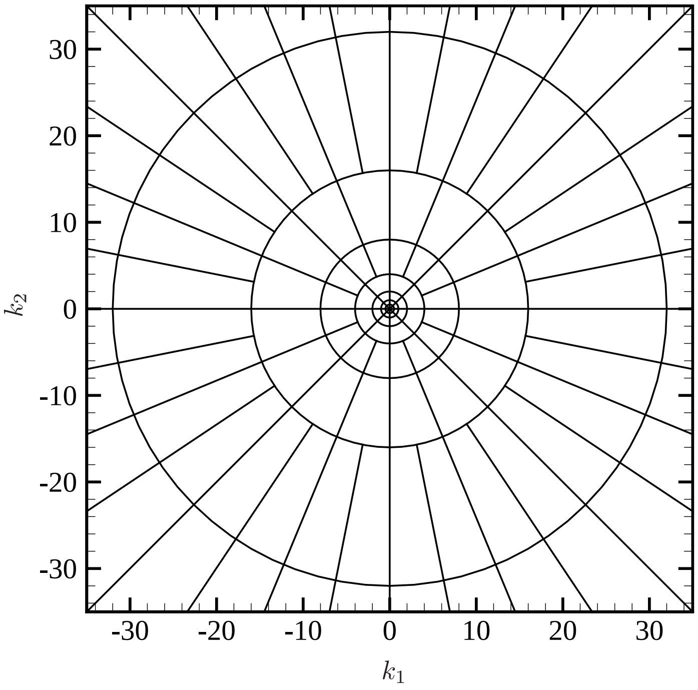

Figure 3.3: Frequency window functions $U_j(r, \theta)$ supported on circular wedges in Fourier space

The frequency windows cover the whole Fourier domain at characteristic length scales

$$2^{-j}, \qquad j = -1, 0, 1, 2, 3, \ldots \tag{3.14}$$

Table 3.2: Breakdown of characteristic length scales for the filtered scales j in terms of the half-height δ and viscous length scale δ_ν in turbulent channel flow.

Re_τ	Length	1	2	3	4	5	6	7	8
	$\mathcal{L}_j/\delta$	0.5	0.25	0.125	0.0625	0.0313	0.0156	0.0078	0.0039
180	$\mathcal{L}_j/\delta_\nu$	90.0	45.0	22.50	11.25	5.625	2.813	1.406	0.703
395	$\mathcal{L}_j/\delta_\nu$	197.5	98.75	49.38	24.69	12.34	6.172	3.086	1.543
590	$\mathcal{L}_j/\delta_\nu$	295.0	147.5	73.75	36.88	18.44	9.219	4.609	2.305
950	$\mathcal{L}_j/\delta_\nu$	475.0	237.5	118.8	59.38	29.69	14.84	7.422	3.711

and the equidistant sequence of rotation angles

$$\theta_{j,l} \equiv \pi l 2^{-\lceil j/2 \rceil}/2, \qquad l = 0, 1, \ldots, 4 \cdot 2^{\lceil j/2 \rceil} - 1, \tag{3.15}$$

where $\lceil x \rceil$ gives the smallest integer greater than or equal to x.

3.3.2 Multi-scale and multi-directional decomposition

By applying the radial window function $W(r)$ on the Fourier coefficients $\hat{\varphi}(\boldsymbol{k})$ and then using the inverse Fourier transform as

$$\varphi_j(\boldsymbol{x}) = \int \hat{\varphi}(\boldsymbol{k})\, W(2^{-j} r)\, \mathrm{e}^{\mathrm{i}\boldsymbol{k}\cdot\boldsymbol{x}}\, \mathrm{d}\boldsymbol{x}, \tag{3.16}$$

for each scale $j = j_0, \ldots, j_e$, with $j_0 = 0$ and $j_e = \log_2(\min(N_1 \Delta k_1, N_2 \Delta k_2)/2)$, we can obtain a multi-scale decomposition of the original scalar field $\varphi(\boldsymbol{x})$ into a total of $j_e - j_0 + 1$ scale-dependent fields. For convenience we will subsequently label scale-dependent fields by the index $j = 0, \ldots, j_e$, with $j = 0$ corresponding to the largest-scale field and $j = j_e$ the smallest resolved-scale field. Subsequently, and according to table 3.2, $\mathcal{L}_j > 0.2\delta$ will be referred to as 'large scale', $\mathcal{L}_j < 10\delta_\nu$ as 'small scale', and in between as 'intermediate scale'. The filter for the largest scale is defined as

$$|W_0(r)|^2 = 1 - \sum_{j \geq 1} |W(2^{-j} r)|^2. \tag{3.17}$$

The characteristic direction l' of $\varphi(\boldsymbol{x})$ in physical space is orthogonal to that in Fourier space. The discrete deviation angle away from the horizontal axis in physical space

$$\Delta\theta = 2^{-\lceil j/2 \rceil} \frac{\pi l'}{2}, \qquad l' = -2^{\lceil j/2 \rceil}, \ldots, -1, 0, 1, \ldots, 2^{\lceil j/2 \rceil}, \tag{3.18}$$

is sketched in figure 3.4(a) for scale j. The multi-scale orientation information of $\varphi(\boldsymbol{x})$ can be defined as the normalized angular spectrum

$$\Phi_j(\Delta\theta) \equiv \frac{\int \hat{\varphi}(\boldsymbol{k}) U_j(r,\theta)\,\mathrm{d}\boldsymbol{k}}{\int U_j(r,\theta)\,\mathrm{d}\boldsymbol{k}}, \qquad -\frac{\pi}{2} \le \Delta\theta \le \frac{\pi}{2} \tag{3.19}$$

at scale j and direction l, where $t_l = (\frac{\pi}{2} - \theta + \theta_{j,l'})/\theta_{j,1}$ for the angular window function $V(t_l)$ in $U_j(r,\theta)$.

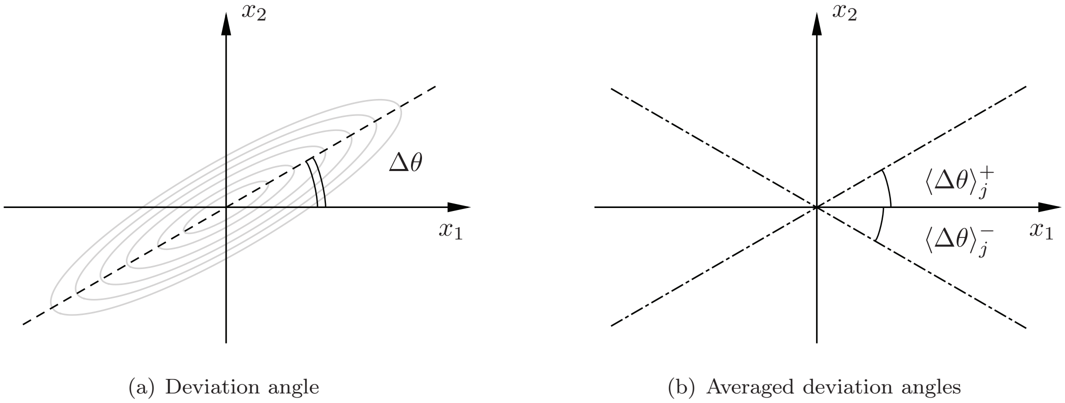

(a) Deviation angle

(b) Averaged deviation angles

Figure 3.4: Diagram of the deviation angles away from the horizontal axis in physical space

The averaged deviation angles away from the horizontal direction are sketched in figure 3.4(b). They can be obtained as

$$\langle\Delta\theta\rangle_j^+ \equiv \frac{\sum_{l'=0}^{l'_{max}} \Phi_j(\Delta\theta)\,\Delta\theta}{\sum_{l'=0}^{l'_{max}} \Phi_j(\Delta\theta)} \quad \text{and} \quad \langle\Delta\theta\rangle_j^- \equiv \frac{\sum_{l'=l'_{min}}^{0} \Phi_j(\Delta\theta)\,\Delta\theta}{\sum_{l'=l'_{min}}^{0} \Phi_j(\Delta\theta)} \tag{3.20}$$

where $l'_{max} = 2^{\lceil j/2 \rceil}$ and $l'_{min} = -2^{\lceil j/2 \rceil}$, which we take to define characteristic angles of a two-dimensional scalar field in the statistical sense. As an example, the scale decomposition of an image of a cross

$$\varphi(x',y') = \exp(-100x'^2) + \exp(-100y'^2) - \exp(-100(x'^2 + y'^2)) \tag{3.21}$$

with

$$x' = x\cos 45^\circ - y\sin 45^\circ \quad \text{and} \quad y' = x\sin 45^\circ + y\cos 45^\circ$$

is shown in figure 3.5. The angular spectrum from the directional decomposition and averaged deviation angles defined in (3.20) are shown in figure 3.6, which show characteristic angles ±45° of the image.

We remark that the multi-scale and multi-directional decomposition in the present study is based on the continuous curvelet transform rather than the fast discrete curvelet transform (see Candès et al., 2006). This is because we find that using the frequency window functions in the continuous curvelet transform, e.g., (3.8) and (3.9) supported on the circular wedges as shown in figure 3.3, gives

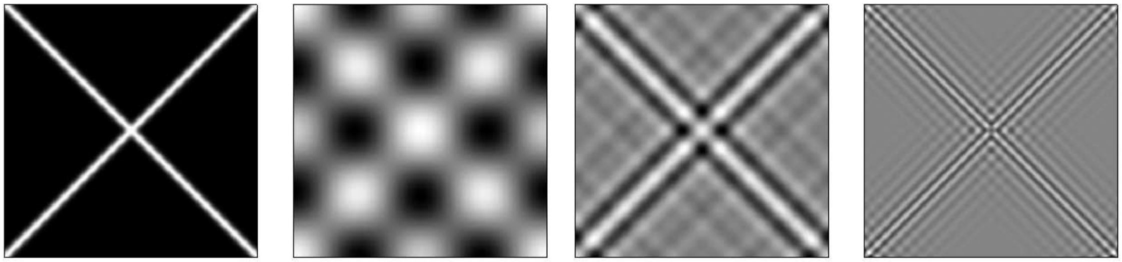

(a) Original (b) Scale 1 (c) Scale 3 (d) Scale 5

Figure 3.5: Scale decomposition of an image of the cross

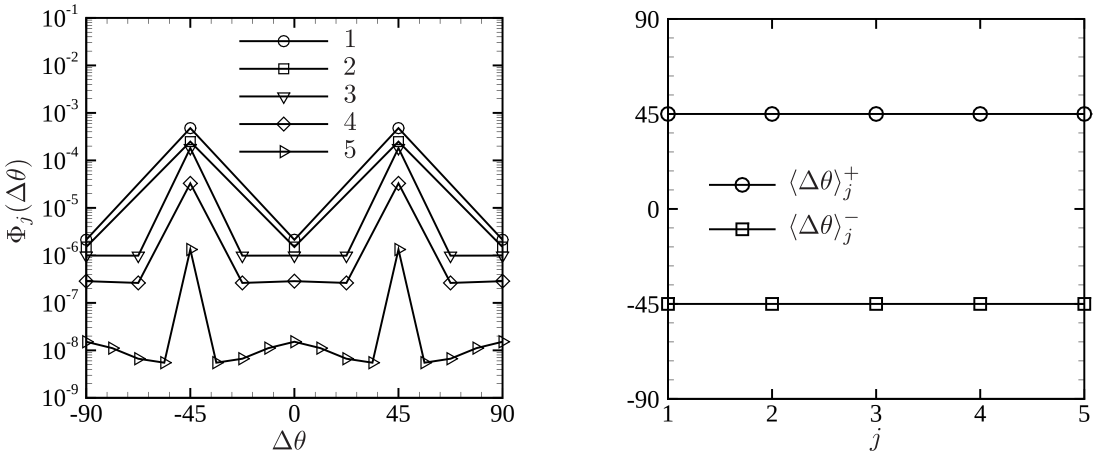

(a) Angular spectrum (b) Average deviation angles (degrees)

Figure 3.6: Directional decomposition of an image of the cross at different scales

more accurate multi-scale angular spectra (3.19) than those from the window functions supported on the sheared trapezoid wedges in the fast discrete curvelet transform algorithm.

When a scalar field has nonperiodic boundaries, e.g., φ on the x–z plane in channel flows, the DFT in (3.4) may result in numerical-oscillatory artifacts near boundaries. This can be resolved by using the discrete cosine transform instead of the DFT in the direction with nonperiodic boundaries. This is equivalent to applying the DFT or the fast Fourier transform (FFT) to the mirror-extended scalar field and corresponds to the mirror-extended curvelet transform (Demanet & Ying, 2007). Presently, before the FFT, we copy and flip the two-dimensional scalar field by the one-dimensional mirror extension in the wall-normal direction with non-periodic boundary conditions as

$$\{\varphi_1, \varphi_2, ..., \varphi_{N-1}, \varphi_N\} \to \{\varphi_1, \varphi_2, ..., \varphi_{N-1}, \varphi_N, \varphi_{N-1}, ..., \varphi_2\}. \tag{3.22}$$

3.4 Lagrangian structures in turbulent channel flow

3.4.1 Geometry of Lagrangian structures on the x–z (streamwise and wall-normal) plane

By tracking the three-dimensional Lagrangian field $\phi(\boldsymbol{x}, t)$ in turbulent channel flow, Lagrangian structures are extracted as iso-contours of ϕ at different times. In this section, we will use a time series of Eulerian velocity fields from runs S1 and S2 (see table 3.1) for two Reynolds numbers to solve the ϕ-equation (2.15). It is noted that the investigation of Lagrangian structures is computationally intensive, requiring storage of sequences of time-resolved Eulerian velocity fields for the backward-particle-tracking method.

Previous studies showed that the important geometric feature of leaning or slanting vortex structures is that they tend to incline at an angle to the streamwise direction in the logarithmic law region (see Adrian, 2007). For studying Lagrangian structures on the x–z plane, we utilize an initial Lagrangian field $\phi_0 \equiv \phi(\boldsymbol{x}, t = 0) = \sin 3x \sin \pi z$, with length scale equal to the half-height $\delta = 1$. To distinguish turbulent dynamics and kinematics, we choose the largest time $t_c = 4$ for tracking the Lagrangian field ϕ according to the typical period of the 'cyclic' process of the evolving near-wall turbulent structures (see Hinze, 1975), where the large-scale, non-dimensional time is $t_c = t\, U_c/\delta$. Since a large-scale Lagrangian structure is imposed by the initial condition, next we investigate only structures with scales $j \geq 3$.

The temporal evolution of the Lagrangian field with color intensity proportional to $\phi \in [-1, 1]$ on the x–z plane in turbulent channel flow at $Re_\tau = 395$ is shown in figure 3.7. We can see that the initial regular, periodical blob-like objects are stretched into ramp-shaped structures by the mean shear and small-scale turbulent motions. Unlike the scalar properties for previous smoke visualization in turbulent boundary layer experiments (e.g., Head & Bandyopadhyay, 1981), the Lagrangian scalar field is non-diffusive, so we can visualize and analyze fine structures with a high resolution grid for ϕ. In figure 3.7, the vivid contrast evident between smooth and chaotic regions illustrates the strong intermittency present in the Lagrangian field for the present turbulent channel flow.

As shown in figure 3.1, we define the inclination angle α between an inclined structure projected on the x–z plane and the x-direction. In terms of the variables in the multi-scale and multi-directional method as shown in figure 3.4, we have $\phi(x, y = y_p, z) \leftrightarrow \varphi$, $x \leftrightarrow x_1$, $z \leftrightarrow x_2$, $\alpha^+ \leftrightarrow \langle\Delta\theta\rangle^+$ and $\alpha^- \leftrightarrow \langle\Delta\theta\rangle^-$. Evolution of individual components of the Lagrangian field can be obtained following the scale decomposition of ϕ on the x–z plane by (3.16). These are shown, at $Re_\tau = 395$, for the intermediate scale $j = 4$ and small scale $j = 6$ in figures 3.8 and 3.9, respectively. The characteristic length scale for each scale index j is quantified in table 3.2. Then, the orientation information of $\phi(\boldsymbol{x}, t)$ on the x–z plane at different scales can be obtained by the normalized angular spectra $\Phi_j(\Delta\theta)$

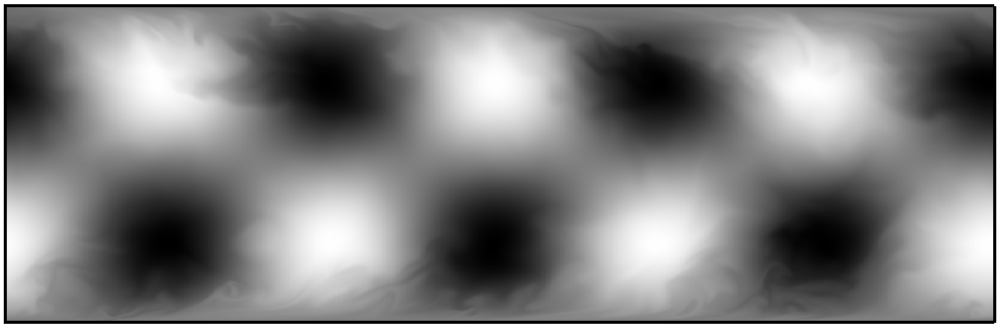

(a) $t_c = 0.5$

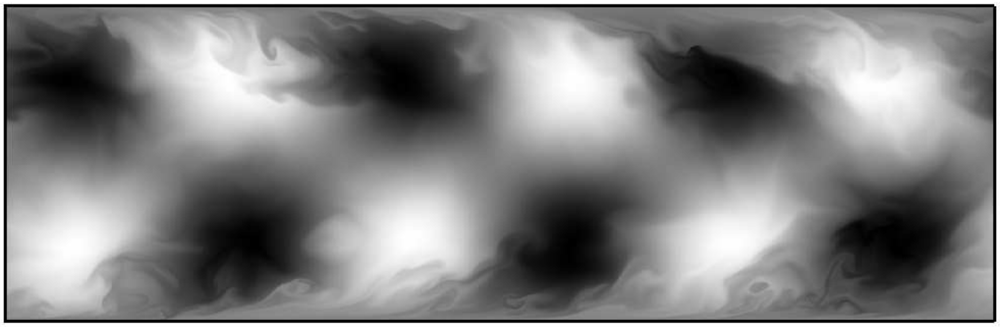

(b) $t_c = 1$

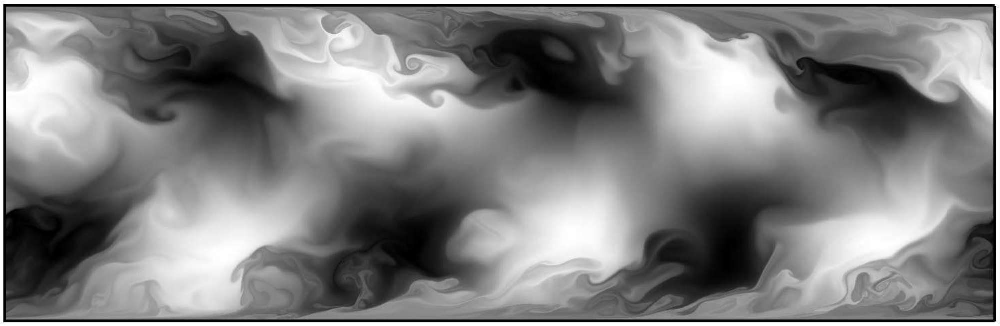

(c) $t_c = 2$

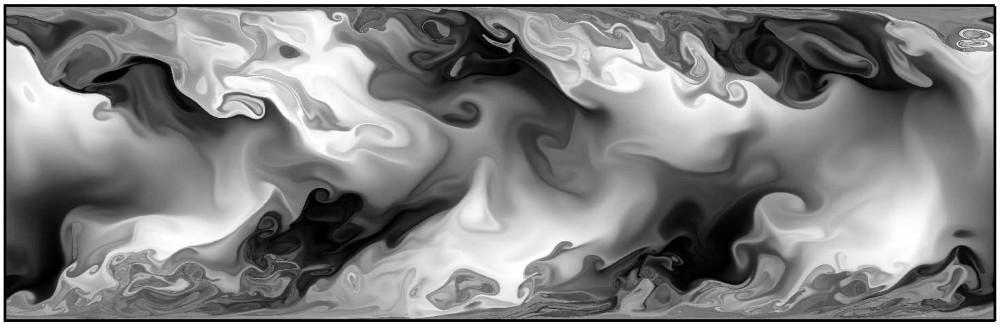

(d) $t_c = 4$

Figure 3.7: Evolution of Lagrangian structures on the x–z plane ($0 \leq x \leq 2\pi$, $0 \leq z \leq 2$) in turbulent channel flow for $Re_\tau = 395$ (run S2)

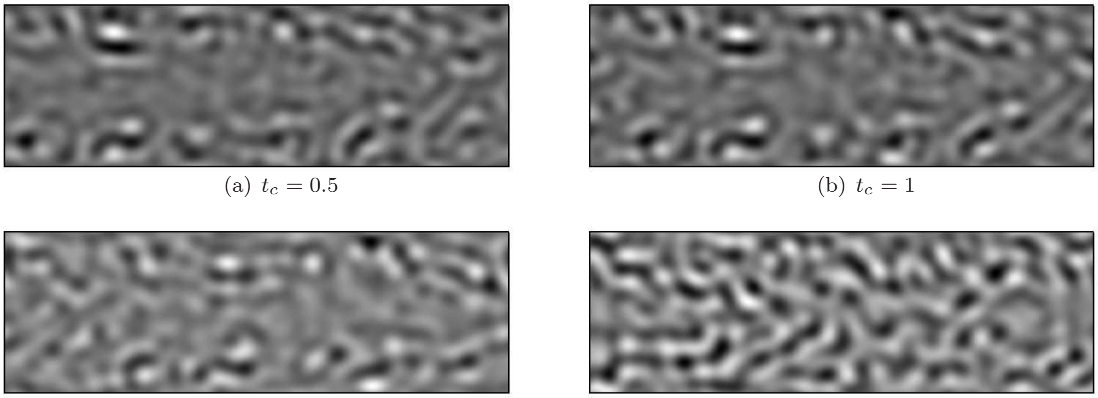

(a) $t_c = 0.5$

(b) $t_c = 1$

(c) $t_c = 2$

(d) $t_c = 4$

Figure 3.8: Evolution of Lagrangian structures at scale 4 on the x–z plane ($0 \leq x \leq 2\pi$, $0 \leq z \leq 2$) in turbulent channel flow for $Re_\tau = 395$ (run S2)

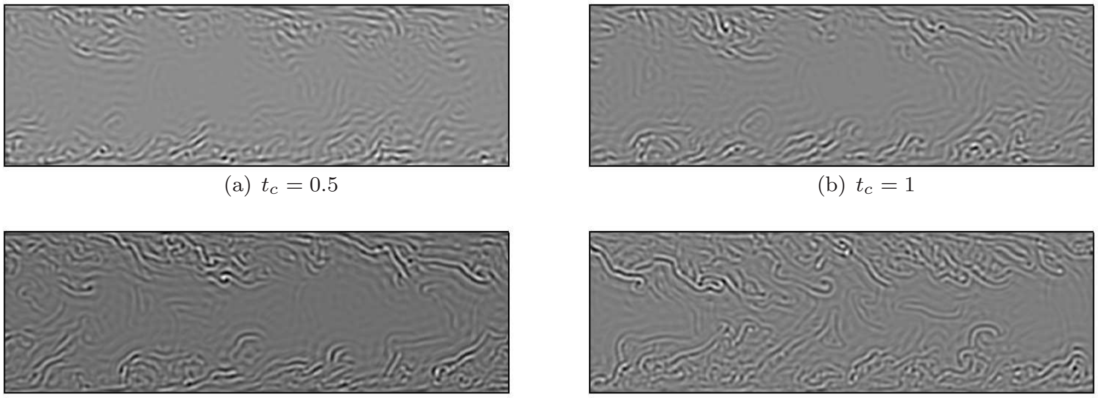

(a) $t_c = 0.5$

(b) $t_c = 1$

(c) $t_c = 2$

(d) $t_c = 4$

Figure 3.9: Evolution of Lagrangian structures at scale 6 on the x–z plane ($0 \leq x \leq 2\pi$, $0 \leq z \leq 2$) in turbulent channel flow for $Re_\tau = 395$ (run S2)

defined in (3.19), which are shown in figure 3.10 at $t_c = 1$ and $t_c = 4$. The increasing $\Phi_j(\Delta\theta)$ at scales $j \geq 3$ shows a cascade process from large scales to small scales for ϕ in the temporal evolution. At each time, smaller-scale structures appear to show a greater tendency to 'attach' to the wall than larger structures in the sense of the predominance of small deviation angles in $\Phi(\Delta\theta)$ for large j.

As shown in figure 3.10, the angular spectra are almost symmetric for all scales. Therefore, assuming the symmetry of inclined structures with the centerline on the x–z plane in the statistical sense, we define the averaged inclination angle $\langle\alpha\rangle = (\langle\alpha^+\rangle + \langle\alpha^-\rangle)/2$. Figure 3.11(a) shows the temporal evolution of $\langle\alpha\rangle$ for Lagrangian structures at intermediate and small scales (also refer to figures 3.8 and 3.9). Here, the additional averaging on $\langle\alpha\rangle$ was taken over 50 x–z planes at $y = y_p$ uniformly distributed between $y = 0$ and $y = L_y$. As shown in figure 3.9(a), the small-scale structures with small $\langle\alpha\rangle$ appear at early times, around $t_c = 0.5$, produced by intense near-wall shear motions. Then, the small-scale structures are up-lifted as shown in figures 3.9(b) and 3.9(c), which

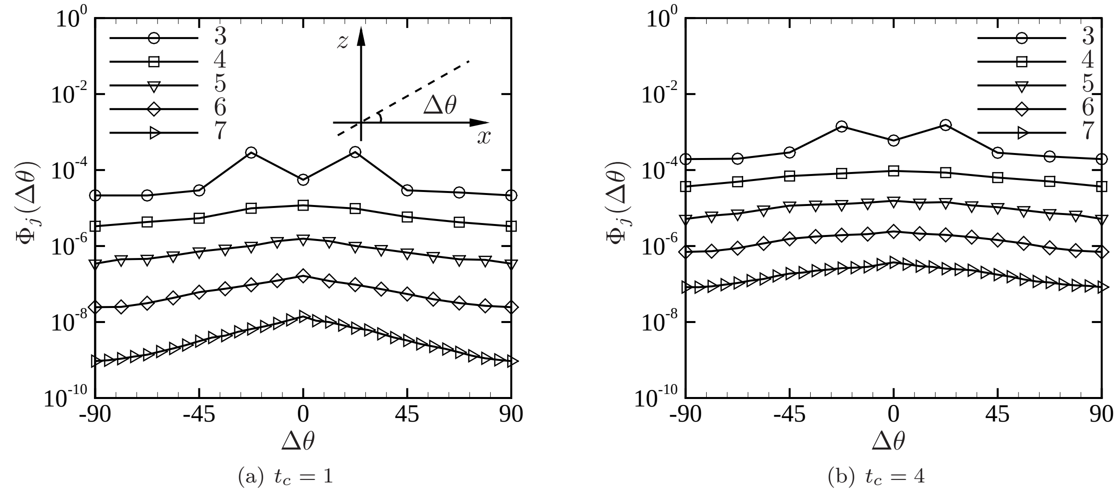

(a) $t_c = 1$ (b) $t_c = 4$

Figure 3.10: Angular spectra of Lagrangian fields at different scales on the x–z plane in turbulent channel flow for $Re_\tau = 395$ (run S2). The deviation angle $\Delta\theta$ is illustrated in the upper-right of figure 3.10(a)

may signal ejections of low-speed fluid outward from the wall. Finally, some small-scale structures are bent downwards to the wall, which may be imprints of the sweeps of high-speed fluid towards the wall. In figure 3.11(a), $\langle\alpha\rangle$ grows with increasing time; the trend is slightly slower for $t_c > 3$. These observations are consistent with the conceptual ejection-sweep-burst-inrush process (Hinze, 1975). At $t_c = 1$ and $t_c = 4$, $\langle\alpha\rangle$ at different scales is shown in figure 3.11(b). We find that $\langle\alpha\rangle$ of Lagrangian structures at scales smaller than $20\delta_\nu$ are higher for $Re_\tau = 395$ than for $Re_\tau = 180$, which may imply stronger turbulent transport in higher-Reynolds-number flows by coherent motions that eject more fluid from the viscous sublayer to the logarithmic region.

In addition, from simulations using different initial fields, e.g., $\phi_0 = \sin 3x$ and $\phi_0 = \pi z$ (not shown), we find that the resulting Lagrangian structures produce quantitatively similar averaged inclination angles at intermediate scales and small scales for long times to those described above. This suggests that an attractor for geometries of Lagrangian structures, discussed in §§ 2.4 and 2.5 for forced isotropic turbulence, may also exist in a turbulent channel flow.

3.4.2 Geometry of Lagrangian structures on the x–y (streamwise and spanwise) plane

Quasi-streamwise vortices within candidate hairpin- or Λ-vortices show, in addition to the wall inclination, another geometric feature that can be characterized by the sweep angle β between the elongated structure and the x-direction on the x–y plane at $z = z_p$ (see figure 3.1). In terms of the variables in the multi-scale and multi-directional method as shown in figure 3.4, we have $\phi(x, y, z = z_p) \leftrightarrow \varphi$, $x \leftrightarrow x_1$, $y \leftrightarrow x_2$, $\beta^+ \leftrightarrow \langle\Delta\theta\rangle^+$ and $\beta^- \leftrightarrow \langle\Delta\theta\rangle^-$. Although an individual structure may

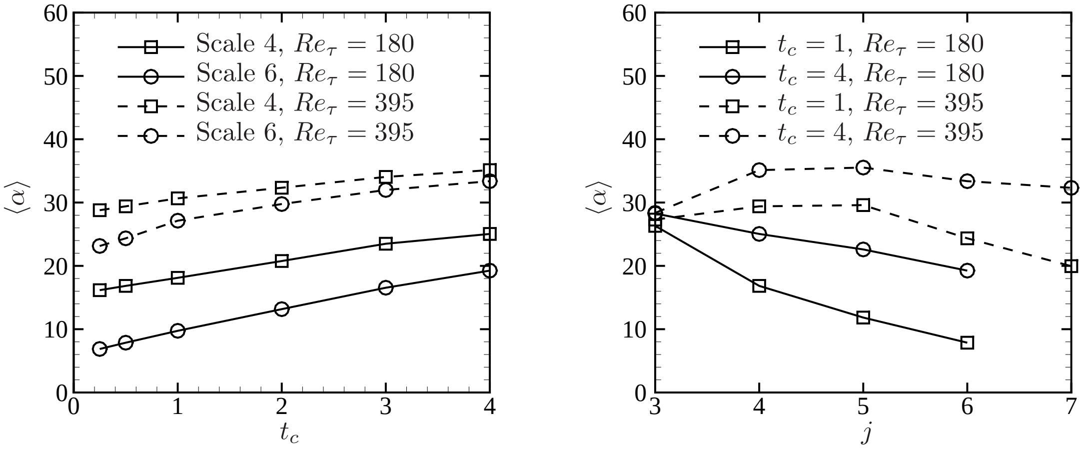

(a) Different times

(b) Different scales

Figure 3.11: Evolution of the averaged inclination angle (degrees) of Lagrangian structures on the x–z plane in turbulent channel flow for $Re_\tau = 180$ (run S1) and $Re_\tau = 395$ (run S2)

have asymmetrical legs in low-Reynolds-number flows (Robinson, 1991), we find that the difference of $\langle\beta^+\rangle$ and $\langle\beta^-\rangle$ is typically less than 10% for each plane. Hence, we assume statistically symmetry over structures in the channel and define the averaged sweep angle $\langle\beta\rangle = (\langle\beta^+\rangle + \langle\beta^-\rangle)/2$.

For investigating the evolutionary geometry of Lagrangian structures on the x–y plane, the initial Lagrangian field is chosen as $\phi_0 = \sin 3x$. Starting from streaks with characteristic scale δ normal to the streamwise direction, at a typical time $t_c = 2$, figure 3.12 shows different geometries of Lagrangian structures on the x–y plane in different regions as characterized by Pope (2000). In the viscous sublayer, spiky-like, long narrow streaks in the x-direction are observed, which may be generated by the shear motion from high- and low-speed alternating streamwise velocity streaks very close to the wall. We can see that the structures are still relatively smooth, which shows that turbulent fluctuations are relatively small in the viscous sublayer (Kline et al., 1967). In the buffer layer and the logarithmic region, we find obvious predominant Λ-like structures, while structures in the buffer layer with active turbulent energy production that exhibit the 'bursting process' (Kline et al., 1967) appear to be more chaotic than those in the logarithmic region. In comparison, structures in the outer layer are much smoother and less perturbed than those in the inner layer.

The averaged sweep angle $\langle\beta\rangle$ for two Reynolds numbers is plotted in figure 3.13. We find that, in general, $\langle\beta\rangle$ at all scales increases with wall distance z^+ as revealed in figure 3.12. Using hot-wire measurements, Ong & Wallace (1998) found that the sweep angle of vorticity vectors increased with distance from the wall, which is consistent with our results for Lagrangian structures. The averaged sweep angle $\langle\beta\rangle$ of structures at several scales increases rapidly with increasing z^+ in the buffer layer with $5 \leq y^+ \leq 30$, and in the logarithmic law region with $y^+ \geq 30$ and $y/\delta \leq 0.3$, and grows slower in the outer layer with $y^+ > 50$. This might be related to active turbulent production occurring

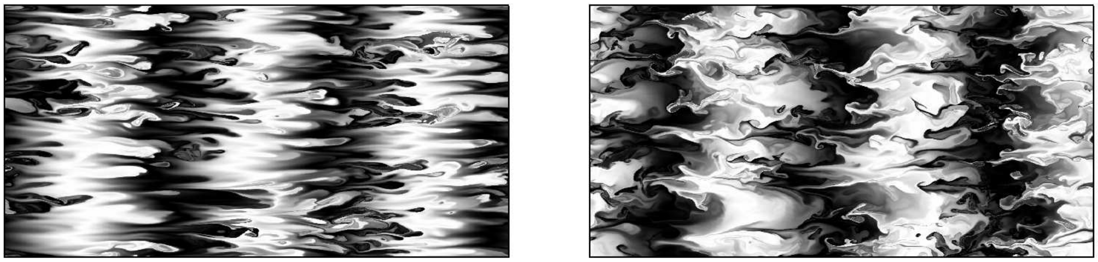

(a) $z^+ = 5$, viscous sublayer

(b) $z^+ = 30$, buffer layer

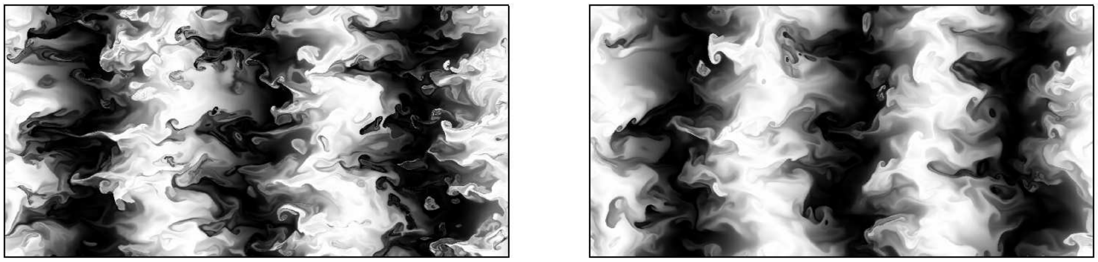

(c) $z^+ = 60$, logarithm law region

(d) $z^+ = 120$, outer layer

Figure 3.12: Lagrangian structures on the x–y plane ($0 \leq x \leq 2\pi$, $0 \leq y \leq \pi$) at $t_c = 2$ in turbulent channel flow for $Re_\tau = 395$ (run S2)

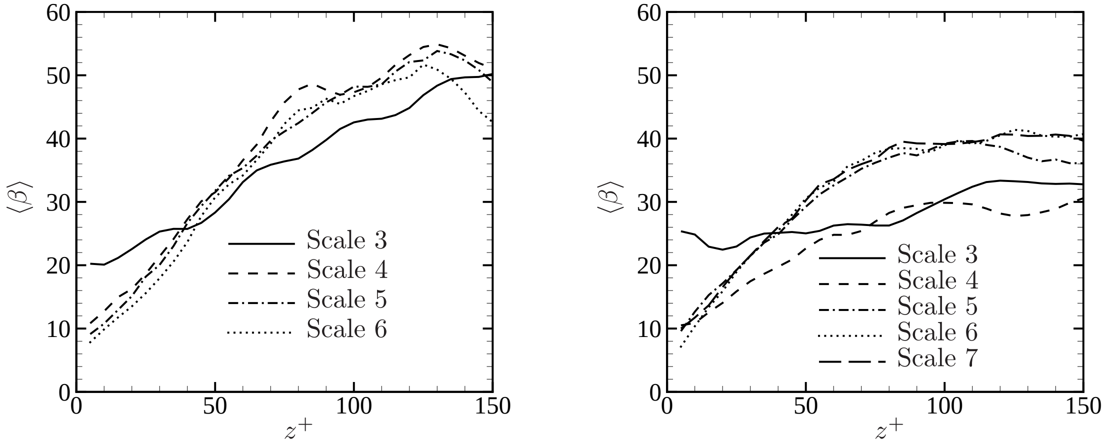

(a) $Re_\tau = 180$

(b) $Re_\tau = 395$

Figure 3.13: Averaged sweep angle (degrees) of Lagrangian structures on the x–y plane at $t_c = 2$ in turbulent channel flow for $Re_\tau = 180$ (run S1) and $Re_\tau = 395$ (run S2)

in this region, with less activity in the outer layer (e.g., Adrian, 2007). On the other hand, the growth of $\langle\beta\rangle$ at the intermediate scale around $50\delta_\nu$ is slower than those at smaller scales. The corresponding visual inspection is also shown in figure 3.14.

The temporal evolution of Lagrangian structures on the x–y plane in the buffer layer of turbulent channel flow at $Re_\tau = 395$ and at different times is shown in figure 3.15. Starting with smooth tube-like shapes, we can see the Λ-shape structures induced by the near-wall, low-speed streaks at

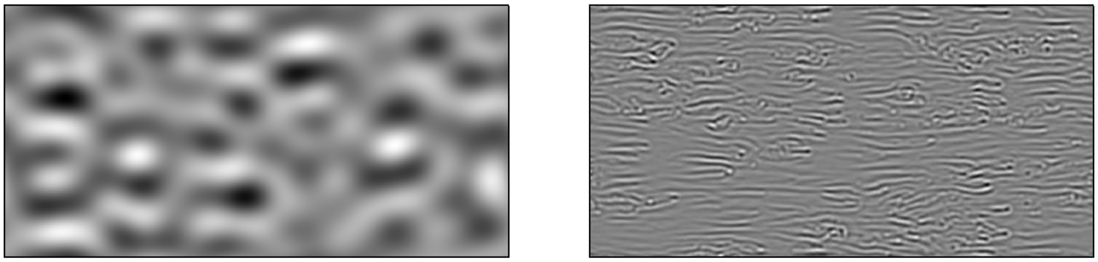

(a) Scale 3, $z^+ = 5$, viscous sublayer
(b) Scale 6, $z^+ = 5$, viscous sublayer

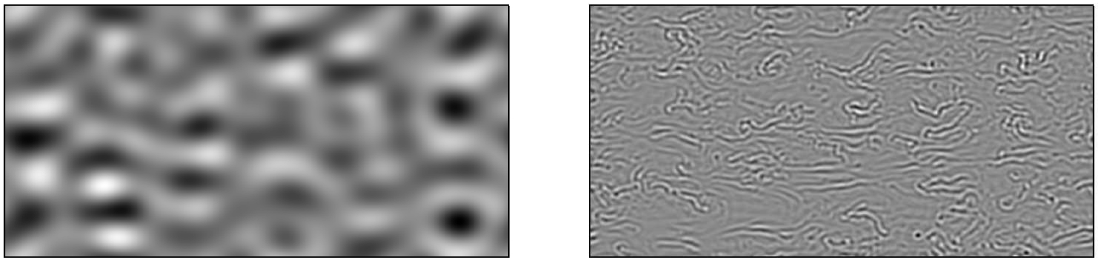

(c) Scale 3, $z^+ = 30$, buffer layer
(d) Scale 6, $z^+ = 30$, buffer layer

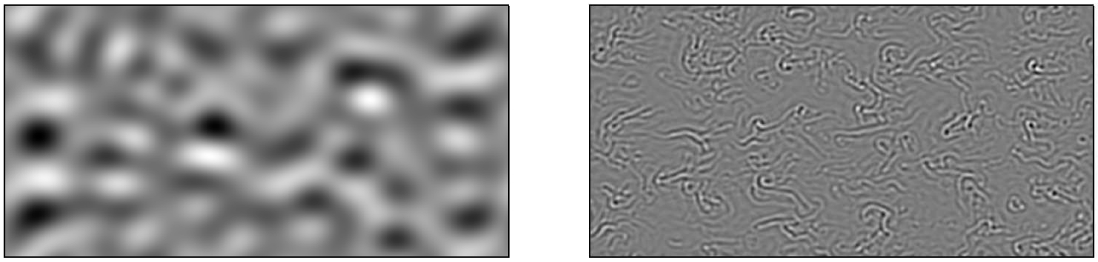

(e) Scale 3, $z^+ = 60$, logarithm law region
(f) Scale 6, $z^+ = 60$, logarithm law region

Figure 3.14: Lagrangian structures on the x–y plane ($0 \leq x \leq 2\pi$, $0 \leq y \leq \pi$) at $t_c = 2$ and different scales in turbulent channel flow for $Re_\tau = 395$ (run S2)

early time followed by intense fluctuations at later time, which shows active energy production and transfer in the buffer layer. In figure 3.16, the corresponding temporal evolution of $\langle\beta\rangle$ in the channel flow at $Re_\tau = 395$ shows that the averaged sweep angle of Lagrangian structures grows with time. Combined with the results shown in § 3.4.1, we show that, starting from initial smooth large-scale blob- or tube-like shapes, Lagrangian structures may break down and evolve into possible hairpin- or Λ-like shapes at intermediate and small scales.

3.5 Eulerian structures in turbulent channel flow

3.5.1 Geometry of Eulerian structures on the x–z plane or x–y plane

We extract Eulerian structures as iso-contours of the instantaneous swirling strength field λ_{ci} in turbulent channel flow. Here, λ_{ci} is the imaginary part of the complex eigenvalue of the velocity

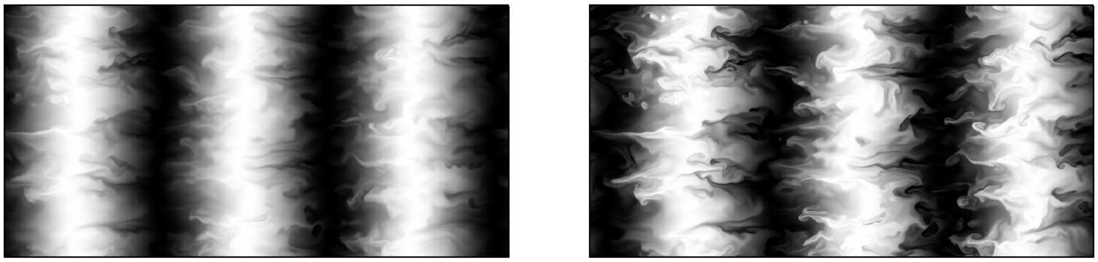

(a) $t_c = 0.5$ (b) $t_c = 1$

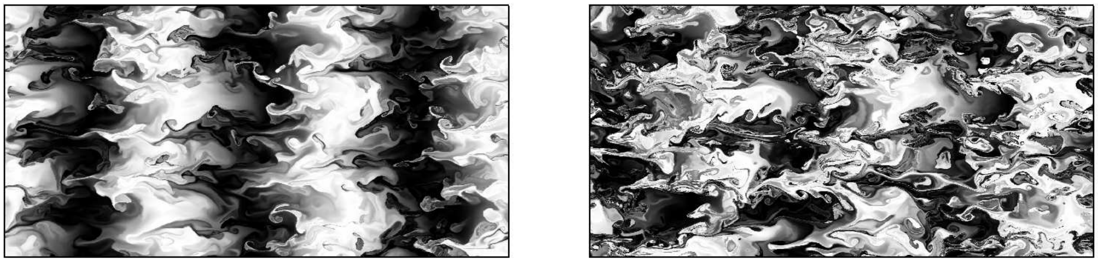

(c) $t_c = 2$ (d) $t_c = 4$

Figure 3.15: Evolution of Lagrangian structures at $z^+ = 45$ on the x–y plane ($0 \le x \le 2\pi$, $0 \le y \le \pi$) in turbulent channel flow for $Re_\tau = 395$ (run S2)

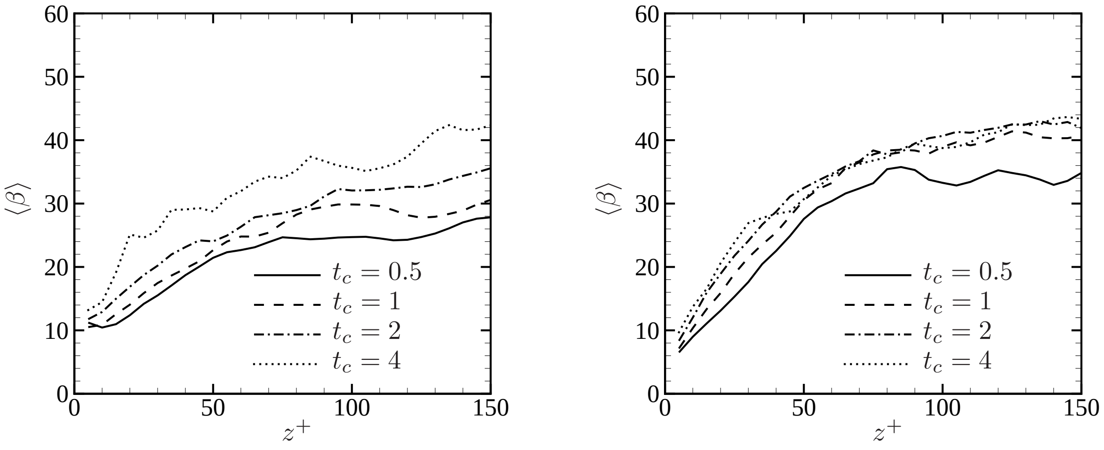

(a) Scale 4 (b) Scale 6

Figure 3.16: Evolution of the averaged sweep angle (degrees) of Lagrangian structures on the x–y plane in the turbulent channel flow for $Re_\tau = 395$ (run S2)

gradient tensor $\nabla \boldsymbol{u}$ (see Zhou et al., 1999), which is often used to identify vortical structures in wall turbulence. Similarities and differences between the swirling strength and other vortex identification criteria were discussed in Chakraborty, Balachandar & Adrian (2005). Remarkably similar looking vortical structures, obtained using their criteria with the given proposed usage of threshold, were observed in a canonical turbulent flow example. The visualization of iso-surfaces at $\lambda_{ci}/\lambda_{ci,max} = 0.1$ in turbulent channel flows is shown in figure 3.17. Numerous tube-like structures extended in the streamwise direction and inclined to the wall, can be seen. Some appear to form complete or incomplete hairpin- or Λ-like structures. Similar observations were also made by Adrian & Liu (2002) and Ganapathisubramani et al. (2006).

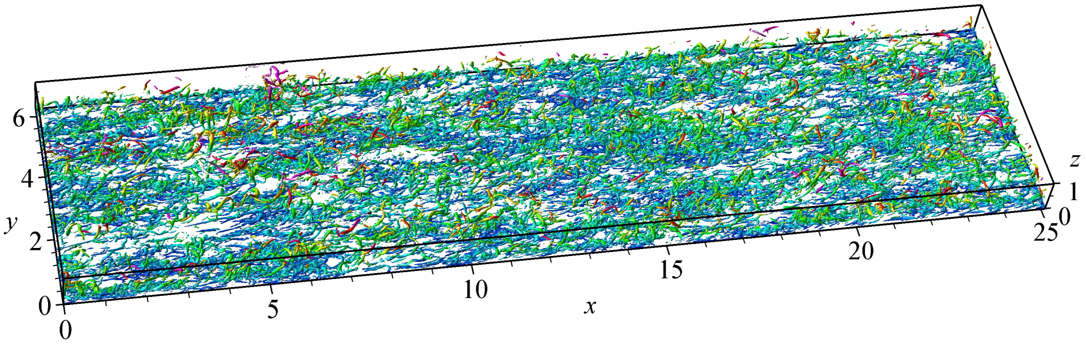

(a) $Re_\tau = 395$ (run L2)

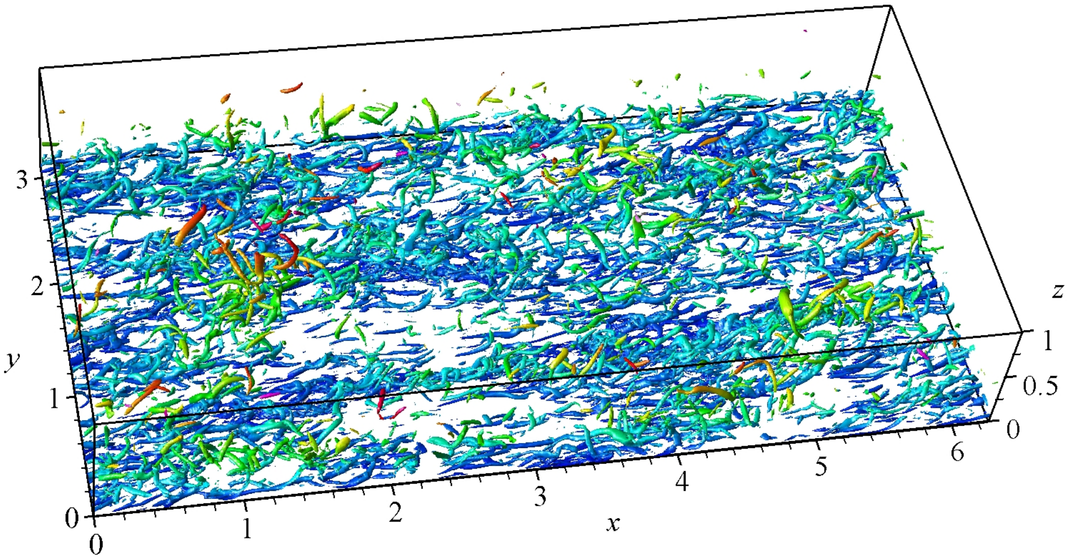

(b) $Re_\tau = 590$ (run S3)

Figure 3.17: Snapshots of Eulerian structures (iso-surfaces at $\lambda_{ci}/\lambda_{ci,max} = 0.1$) in turbulent channel flows. The color on the surfaces is coded by z

After interpolating λ_{ci} on a uniform grid with resolution $2N_x \times N_y \times N_z$, the multi-scale and multi-directional methodology described in § 3.3 is applied on a sequence of λ_{ci}-fields on the x–y or x–z planes. In this subsection, we will use Eulerian velocity fields from runs L1, L2, S3, and S4 (see table 3.1) for four Reynolds numbers. The scale decomposition of Eulerian structures on each plane is obtained by (3.16), where the scalar field $\varphi = \lambda_{ci}(x, y = y_p, z)$. For example, the scale decomposition of the λ_{ci}-field on the x–z plane for $Re_\tau = 590$ is shown in figure 3.18. Clearly evident are decreasing characteristic length scales with increasing scale indices, as quantified in table 3.2.

The λ_{ci}-field on the x–z plane with non-periodic boundaries is mirror-extended as (3.22) for the purpose of further analysis. The averaged inclination angle $\langle\alpha\rangle$ of Eulerian structures on the x–z plane at different scales and Reynolds numbers is shown in figure 3.19(a). Additional averaging on $\langle\alpha\rangle$ was taken over 50 x–z planes at $y = y_p$ uniformly distributed between $y = 0$ and $y = L_y$ from five independent realizations of the DNS. We can see that the averaged inclination angles, $\langle\alpha\rangle$, of large-scale Eulerian structures are small, while structures at intermediate scales have maxima $\langle\alpha\rangle$ in the range 40°–45°, while small-scale structures have moderate $\langle\alpha\rangle$ around 30°. In figure 3.19(b), the $\langle\alpha\rangle$ profiles, in terms of the viscous scale δ_ν, appear to collapse for all four Reynolds numbers, in a way similar to inner-scaling for turbulent velocity or vorticity profiles (e.g., Moser et al., 1999). The maximum $\langle\alpha\rangle$ corresponds to the scale around $20\delta_\nu$. Combined with the visualizations in figure 3.18, we conclude that the quasi-streamwise vortices represented by iso-surfaces of λ_{ci} exhibit an inclined geometry with intermediate scale $20\delta_\nu$, $\langle\alpha\rangle \approx 45^\circ$ and with 'curved legs' leading to scale $5\delta_\nu$ and $\langle\alpha\rangle \approx 30^\circ$ near the wall.

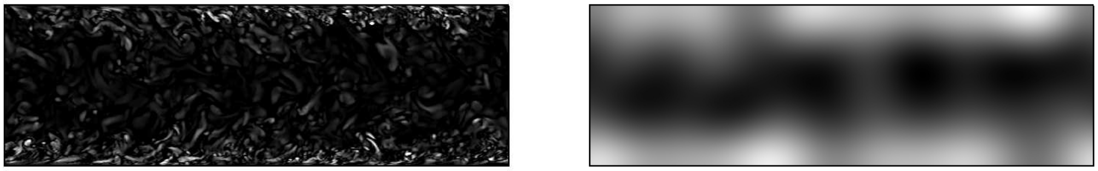
(a) Original
(b) Scale 2

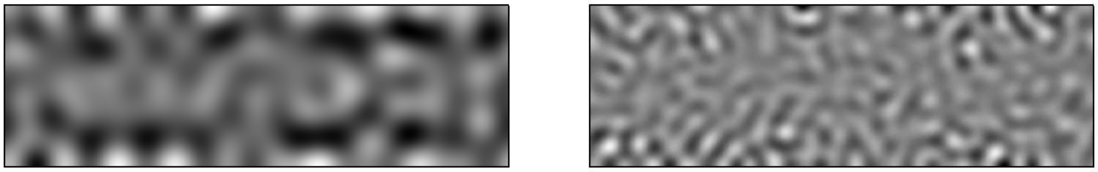
(c) Scale 3
(d) Scale 4

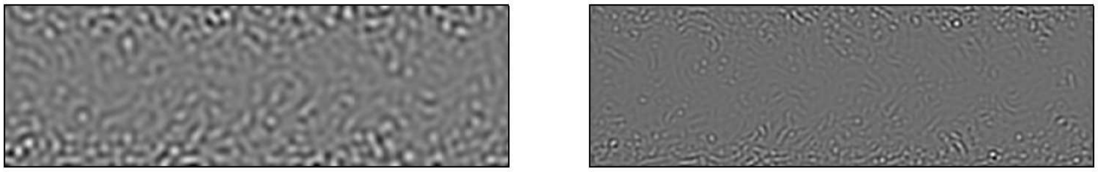
(e) Scale 5
(f) Scale 6

Figure 3.18: Scale decomposition of Eulerian structures on the x–z plane ($0 \leq x \leq 2\pi$, $0 \leq z \leq 2$) in turbulent channel flow for $Re_\tau = 590$ (run S3)

After averaging over results from five realizations of the DNS, the averaged sweep angle $\langle\beta\rangle$ of Eulerian structures on the x–z plane as a function of the wall distance z^+ for four Reynolds numbers is also shown in figure 3.20. This resembles the equivalent results for Lagrangian structures shown in § 3.4. The rapid change of the sweep angle in the near-wall region implies high curvature of three-dimensional small-scale Eulerian structures (e.g., Adrian, 2007).

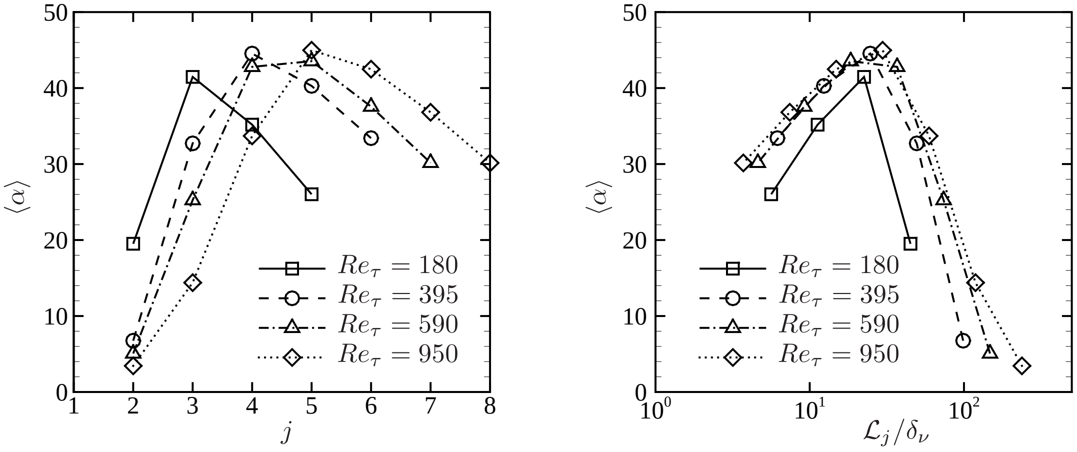

(a) Scaled by scale indices

(b) Scaled by viscous length scales

Figure 3.19: Averaged inclination angle (degrees) of Eulerian structures on the x–z plane

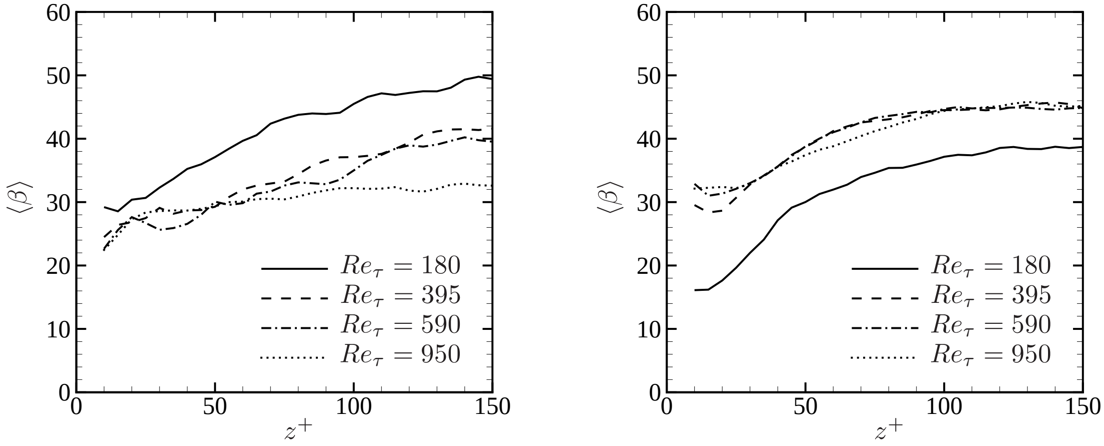

(a) Scale 3

(b) Scale 5

Figure 3.20: Averaged sweep angle (degrees) of Eulerian structures on the x–y plane at different z^+

3.5.2 Statistical evidence of structure packets

Recent DNS and PIV studies have provided evidence that near-wall vortices may group together to form large-scale packets (Zhou et al., 1999; Christensen & Adrian, 2001; Adrian & Liu, 2002). We observed that similar long and narrow structures appear to be organized by a number of individual small-scale structures in figure 3.17. To investigate this issue by quantified statistics, we use the cross-correlation coefficients between the λ_{ci} fields on the x–z plane at scale i and scale j:

$$\gamma_{ij} = \frac{\langle(|\lambda_{ci}^{(i)}(\boldsymbol{x})| - \langle|\lambda_{ci}^{(i)}(\boldsymbol{x})|\rangle)(|\lambda_{ci}^{(j)}(\boldsymbol{x})| - \langle|\lambda_{ci}^{(j)}(\boldsymbol{x})|\rangle)\rangle}{\sigma^{(i)}\sigma^{(j)}}, \tag{3.23}$$

where $i < j$ and the standard deviation of each scalar field is

$$\sigma^{(j)} = \sqrt{\langle (|\lambda_{ci}^{(j)}(\boldsymbol{x})| - \langle |\lambda_{ci}^{(j)}(\boldsymbol{x})| \rangle)^2 \rangle}. \tag{3.24}$$

In the multi-scale geometric methodology, the structures are represented by fluctuations of $\lambda_{ci}^{(j)}$. Thus, high γ_{ij} means possible coincidence of structures at scales i and j appearing within the same region. In figure 3.21, γ_{ij} is computed by (3.23) on the x–z plane in channel flows for four Reynolds numbers. We can see noticeable cross-correlations between large-scale structures with the characteristic height 0.25δ and small-scale structures with the length around $5\delta_\nu$ in both long channel (runs L1, L2, and L3) and short channel (runs S2, S3, and S4), which implies that candidate structure packets may exist in the near-wall region of channel flows at a range of Reynolds numbers. This feature can be observed from visualizations of the x–z plane-cuts in figure 3.22. The small-scale structures presented by the fluctuations of the background shading of $\lambda_{ci}^{(5)}$ for $Re_\tau = 180$ or $\lambda_{ci}^{(6)}$ for $Re_\tau = 395$ are grouped in large-scale packets presented by dashed contour lines of $\lambda_{ci}^{(2)}$.

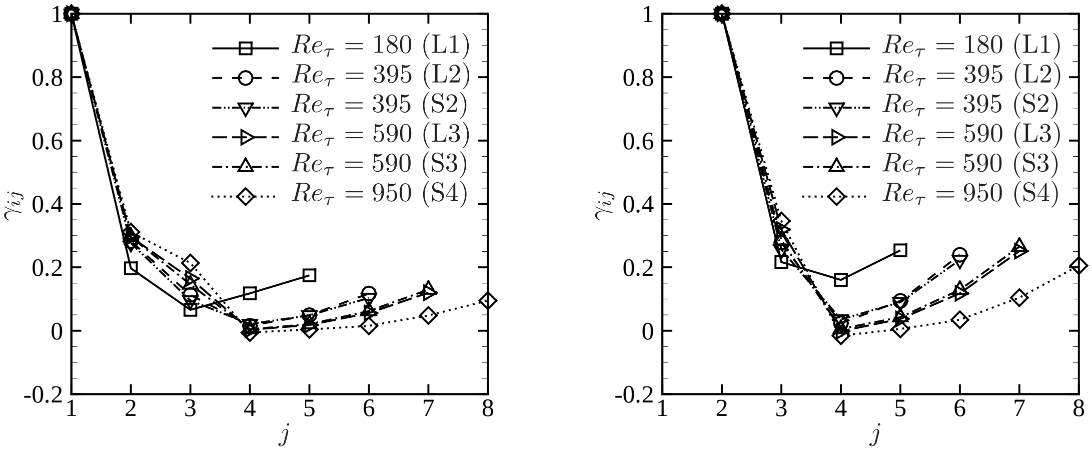

(a) $i = 1$ (b) $i = 2$

Figure 3.21: Cross-correlation coefficients between Eulerian structures at scale i and scale j from different runs

Additionally, in long channel flows with $L_x \approx 50\delta$ at $Re_\tau = 180$ and $Re_\tau = 395$ (runs L1 and L2), as shown in figure 3.23, large-scale structures in the higher-Reynolds-number flow are much longer in the streamwise direction than those in the lower-Reynolds-number flow. A characteristic length of structures at scale j in the x-direction can be defined as the integral length scale

$$L_x^{(j)} = \int_0^{L_x/2} R_x^{(j)}(r_x) \mathrm{d}r_x, \tag{3.25}$$

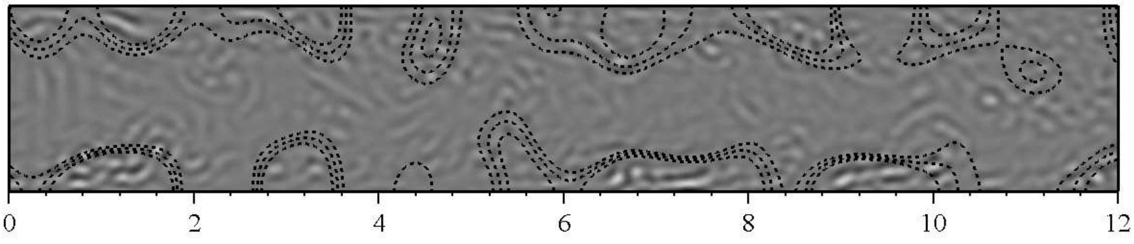

(a) $Re_\tau = 180$ (run L1), $i = 2$, $j = 5$

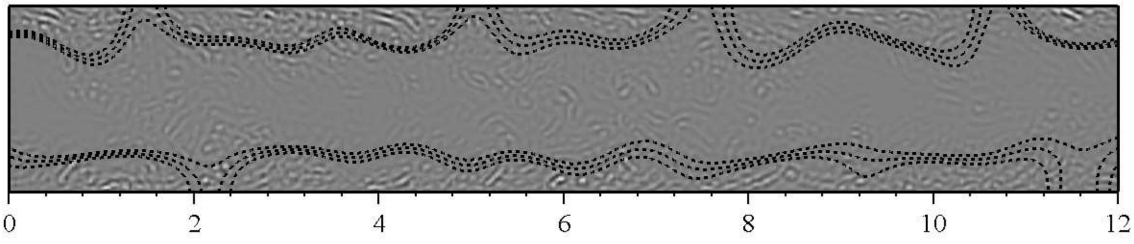

(b) $Re_\tau = 395$ (run L2), $i = 2$, $j = 6$

Figure 3.22: Interactions between Eulerian large-scale structures at scale i (contour lines: $\lambda_{ci}^{(i)}/\lambda_{ci,\max}^{(i)} = 0.15, 0.2, 0.25$) and small-scale structures at scale j (background shading) on the x–y plane in a long channel

where the correlation in the streamwise direction is

$$R_x^{(j)}(r_x) = \frac{\langle(\lambda_{ci}^{(j)}(\boldsymbol{x}) - \langle\lambda_{ci}^{(j)}(\boldsymbol{x})\rangle)(\lambda_{ci}^{(j)}(x + r_x, y = y_p, z) - \langle\lambda_{ci}^{(j)}(\boldsymbol{x})\rangle)\rangle}{\langle(\lambda_{ci}^{(j)}(\boldsymbol{x}) - \langle\lambda_{ci}^{(j)}(\boldsymbol{x})\rangle)^2\rangle}. \tag{3.26}$$

We find that the maximum $L_x^{(j)}$ are obtained when $j = 2$ in both Reynolds-number flows, while $L_x^{(2)} \approx 4\delta$ in the flow at $Re_\tau = 180$ and $L_x^{(2)} \approx 14\delta$ in the flow at $Re_\tau = 395$, which might imply that it is easier to form very long structure packets in higher-Reynolds-number flows than in low-Reynolds-number flows. The latter result is reminiscent of that obtained from the streamwise spectra in the experiments of turbulent pipe flow over a range of Reynolds numbers (e.g., Kim & Adrian, 1999; Guala, Hommema & Adrian, 2006).

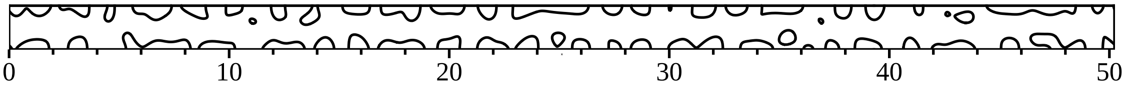

(a) $Re_\tau = 180$ (run L1)

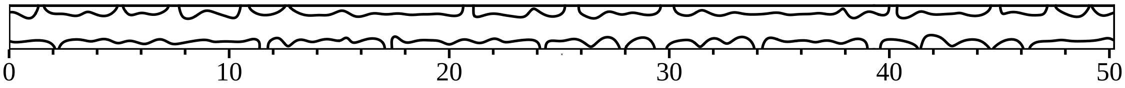

(b) $Re_\tau = 395$ (run L2)

Figure 3.23: Eulerian structures (contour lines: $\lambda_{ci}^{(j)}/\lambda_{ci,\max}^{(j)} = 0.2$) at scale 2 on the x–z plane ($0 \le x \le 16\pi$, $0 \le z \le 2$) in long channel flows

3.5.3 Comparisons of Lagrangian and Eulerian structures

Eulerian structures show many geometric features that are qualitatively similar to those of Lagrangian structures. This similarity also supports the existence of quasi-streamwise vortices in turbulent channel flow. There are nonetheless notable differences in our analysis of these two classes of fields. Some of these, for example the averaged inclination and sweep angles of structures, may result from the Lagrangian/Eulerian identification methods themselves, while other may have a more physical basis. Lagrangian structures tend to be stretched by the persistent shear motions, thereby generating elongated, curved structures partially attached to the wall as illustrated in figure 3.8. In Eulerian fields, the swirling-strength field appears to identify vortex cores in the logarithmic region with relatively short geometry as shown in figure 3.18. This can be expected to produce smaller averaged inclination angles for Lagrangian objects than those seen for Eulerian structures at intermediate scales.

Another notable difference is that, in contrast to the observation of structure packets in terms of correlations for Eulerian structures (figure 3.21), we do not presently find substantial cross correlations between large- and small-scale components of Lagrangian objects. This could be a consequence of the limited time over which we are able to track the latter, which may not be sufficiently long for inter-scale Lagrangian correlations to develop. An alternative is that the Eulerian correlations are in fact a consequence of the collective vortex dynamics of near-wall flows. Presently we do not have a suitable method available for the long-time tracking of a Lagrangian field that is unambiguously related to identifiable vortex structures; see further discussion below.

One clear distinction between Lagrangian and Eulerian fields is that the former are the result of evolution from essentially arbitrary initial conditions, while the latter follow from iso-surfaces of scalar quantities chosen at least in part based on vorticity physics. In § 2.5, we found Lagrangian structures in isotropic turbulence that were broadly independent of initial fields with blob-like, tube-like or sheet-like iso-surfaces. Presently we find a similar trend for a turbulent channel flow.

A connection between Lagrangian and Eulerian field geometries could perhaps be educed by choice of initial conditions for the Lagrangian simulation that correspond to a physically interesting Eulerian field. In order to investigate Lagrangian mechanisms and vortex dynamics, we will introduce the vortex-surface field $\phi = \phi_v$ in § 4 satisfying $\lambda_\omega = 0$, where λ_ω the cosine of the angle between $\boldsymbol{\omega}$ and $\nabla\phi$ is defined in (2.24). In a strictly inviscid flow, the Helmholtz vorticity theorem shows that $\phi(\boldsymbol{x}, t = 0)$ satisfying $\lambda_\omega = 0$ at $t = 0$ will do so for $t > 0$. This fails for a viscous flow. Furthermore, for a given vorticity field, there are open existence and uniqueness questions concerning the determination of ϕ satisfying $\lambda_\omega = 0$. A surrogate field may nevertheless be useful. For the present turbulent channel flows, we find that the choice $\phi = \lambda_{ci}$ or $\phi = |\boldsymbol{\omega}|$ obtained from the instantaneous Eulerian velocity field gives $\langle|\lambda_\omega|\rangle \approx 0.5$. While neither of these is then close to a vortex-surface field, they may nevertheless provide interesting initial Lagrangian fields. Hence, in addition to the initial Lagrangian fields described in §§ 3.4.1 and 3.4.2 we also performed simulations of Lagrangian structures evolving from initial conditions defined by the three-dimensional, filtered λ_{ci}-field at scale 2. This produced Lagrangian fields at a later time similar to those presented in §§ 3.4.1 and 3.4.2.

3.6 Results and discussion

We have developed a general multi-scale, multi-directional methodology based on the mirror-extended curvelet transform to investigate the geometry of Lagrangian and Eulerian structures, extracted respectively from a time sequence of the Lagrangian fields and from the instantaneous swirling-strength field in turbulent channel flow, for low and moderate Reynolds numbers. This is used to quantify the statistical geometry, including the averaged inclination and sweep angles, of both classes of structures over a range of scales varying from the half-height of the channel to several viscous length scales. Quasi-streamwise Lagrangian and Eulerian vortical structures were detected in the near-wall region and their geometries quantified. These comprise inclined objects, the averaged inclination angle of which is $35°$–$45°$ principally within the logarithmic region. The averaged sweep angle is $30°$–$40°$ and the characteristic scale is $20\delta_\nu$. 'Curved legs' are found in the viscous sublayer and buffer layer, for which the averaged inclination angle is $20°$–$30°$, the averaged sweep angle is $15°$–$30°$ and the scale is $5\delta_\nu$–$10\delta_\nu$. The sweep angle of both structures increases rapidly in the buffer and logarithmic regions and grows mildly in the outer layer. The temporal evolution of Lagrangian structures shows increasing inclination and sweep angles with time. The increasing magnitude in terms of both angles varies from $10°$ to $20°$ within the typical 'cyclic' period from $t_c = 0.5$ to $t_c = 4$. This may quantify the lifting process of quasi-streamwise vortices and the conceptional ejection-sweep-burst-inrush scenario. Both structures have slightly different geometries in flows for different Reynolds numbers. Although the averaged geometrical features of these objects are consistent with the expected signatures of conceptual structures previously characterized as hairpin or Λ-vortices, we remark that the current methodology cannot distinguish between hairpin-like structures composed of two connected tubes and inclined tube-like structures that are not connected to each other via vortex lines.

The evidence for the existence of large-scale, Eulerian structure packets, comprising collections of individual small-scale geometrical objects, was obtained by finite cross-correlations between large- and small-scale Eulerian structures. The large-scale packets are located within the near-wall region with the typical height 0.25δ and may extend over 10δ in the streamwise direction in moderate-Reynolds-number, long channel flows.

The current methodology is based on a sequence of plane-cuts normal or parallel to the streamwise direction in channel flows, and so may also be suitable and convenient for analyzing experimental PIV data. The extension to fully three-dimensional data could be achieved using the three-dimensional curvelet transform (Ying et al., 2005). The fast discrete curvelet transform algorithm with circular frequency window functions may be required for this. In addition, combined with the mirror-extension, the multi-scale geometric analysis (Bermejo-Moreno & Pullin, 2008) using the fast three-dimensional curvelet transform can, in principle, be applied to detect coherent structures in wall turbulence in order to study alternative non-local geometry signatures based on principal curvatures. This could provide a means of testing an assumed structure in simplified models for wall turbulence (e.g., Perry & Chong, 1982; Perry et al., 1986), structure-based subgrid models for the LES of near-wall channel (Chung & Pullin, 2009) or boundary layer flows, and the possible sparse representation of wall turbulence with the curvelet-based extraction method.

While the data analyzed in this study are from low to moderate Reynolds-number channel flows, the present multi-scale and multi-directional methodology can easily be applied to high-Reynolds-number data (e.g., Marusic et al., 2010) for turbulent channel, or boundary layer flows to explore more geometric features such as the superstructures in the outer layer (e.g., Hutchins & Marusic, 2007) and the structural evolution in the turbulent transition (e.g., Wu & Moin, 2009). Moreover, since high-Reynolds-number wall turbulence exhibits scale separation, it would be interesting to investigate various inter-scale interactions such as the large-scale modulation of small-scale motions and Reynolds stresses using the curvelet multi-scale decomposition with quadrant analysis (e.g., Wallace, Brodkey & Eckelman, 1972).

Chapter 4

Lagrangian and vortex-surface fields in Taylor–Green and Kida–Pelz flows

4.1 Background and objectives

In order to explore basic Lagrangian mechanisms of turbulence and vortex dynamics, an interesting choice of the initial Lagrangian field is to choose its iso-surfaces to be vortex surfaces in some particular initial flow fields. Here, the vortex surface is a smooth surface or manifold embedded within a three-dimensional velocity field, which has the property that the local vorticity vector is tangent at every point on the surface. In this chapter, we will develop a theoretical formulation on the construction and evolution of such a three-dimensional smooth scalar field called vortex-surface field (VSF). Iso-surfaces of the VSF define vortex surfaces.

In dynamical system theory, the construction of vortex surfaces from a given velocity field is related to finding two-dimensional invariant manifolds of a three-dimensional vector field. Although, in general, global manifolds cannot be found analytically, there are several numerical methods under development for computing a manifold of a vector field (see Krauskopf et al., 2005). In the present study, we find that flows that begin from Taylor–Green (TG) and Kida–Pelz (KP) initial conditions are good candidates for the study of vortex surfaces, because their initial topology is relatively simple and both of these periodic flows have many symmetries to facilitate construction of initial vortex surfaces. In particular, we will develop a high-accuracy method for finding space-filling, VSFs for these two defined velocity fields. At the same time, the recent development of tracking methodologies for the Lagrangian field (see § 2.3.2) and finite-sized Lagrangian structures (e.g., Lindsay & Krasny, 2001; Goto & Kida, 2007) offer effective approaches to numerically simulate the evolution of vortex surfaces in a high-Reynolds-number flow or even an inviscid flow with the aid of substantial computational resources.

In general, a vortex surface will be persistently stretched in inviscid and perhaps high-Reynolds-number flows, which causes the growth of vorticity. This mechanism is crucial for the cascade process and dissipation distribution in turbulence. To express them in mathematical form, Taylor & Green (1937) proposed a divergence-free velocity field with Fourier basis functions, as the initial condition of the Navier–Stokes equations to show that, when the Reynolds number is high, the mean-squared vorticity increased at the early stage and reached a maximum after a finite time. Subsequently this so-called TG flow was investigated by Brachet et al. (1983) using numerical simulations. From this simple sinusoidal vector field with certain reflectional and rotational symmetries, Brachet et al. (1983) found that a TG flow can develop characteristics of Kolmogorov statistics of turbulence at a later stage in a high-Reynolds-number flow. Another typical flow with simple initial conditions, the KP flow, was introduced by Kida (1985), who showed that it contains more symmetries than the TG flow. Flows with KP initial conditions have been studied in both viscous and inviscid cases (e.g., Boratav & Pelz, 1994; Pelz, 2001).

The topology and geometry in evolution of VSFs and vortex surfaces are important for many aspects in theoretical fluid mechanics. From the Helmholtz vorticity theorem, for a strictly inviscid flow, a vortex surface is a Lagrangian structure (material surface), which is topologically invariant in time provided that the velocity field remains smooth. The nature of solutions of the three-dimensional Euler equations remains a challenging open problem (e.g., Majda & Bertozzi, 2001; Kerr, 1993). Some studies showed that nearly singular, sheet-like vortex structure may deplete the growth of nonlinearity so as to prevent finite-time singularity formation in Euler flows (e.g., Hou & Li, 2008). Constantin, Majda & Tabak (1994) introduced a two-dimensional analogy using a scalar gradient as the analog of vorticity and level sets of the scalar field as the analog of vortex lines. Their analysis showed that flow in the vicinity of hyperbolic saddles is highly nonlinear and potentially singular. Describing the evolution of vortex surfaces in general three-dimensional flow, however, appears to pose difficulties. It is expected that the topology of vortex surfaces will change when the Reynolds number is finite owing to vortex reconnection, for example in the collapse of two vortex tubes under excessive straining (see Kida & Takaoka, 1994). Subsequent roll-up of vortex sheets induced by Kelvin–Helmholtz instability may provide an agent of transition from laminar flow to turbulent flow. In these scenarios, knowledge of the geometry of vortex surfaces may help us to construct vortex models of the inertial-range and fine-scale range of high-Reynolds-number turbulence (Pullin & Saffman, 1998).

Unlike the velocity, which can be rapidly redistributed over all space by the pressure field, an initially localized distribution of vorticity tends to remain localized, which implies that the vorticity field may contain persistent structures. An agreed-upon definition for vortical structures, however, remains elusive. Iso-surfaces of vorticity magnitude provides one method for visualizing instantaneous vortical structures, but this may be inadequate, in particular, for detecting coherent structures in wall-bounded and homogeneous shear flows (Jeong & Hussain, 1995). Hence several popular criteria to identify vortical structures are presently available, most based on invariants or eigenvalues of the local velocity gradient tensor, for example the Q-criterion (Hunt, Wray & Moin, 1988), the Δ-criterion (Chong, Perry & Cantwell, 1990) and the λ_2-criterion (Jeong & Hussain, 1995). Similarities and differences between these criteria were discussed in Chakraborty, Balachandar & Adrian (2005). An alternative to these Eulerian measures is provided by the frame-independent criterion (Haller, 2005), which, in a Lagrangian sense, appears to be capable of exposing detailed vortical structures. According to the Helmholtz theorem, a primitive approach based on the identification of vortex surfaces has a clear physical meaning and unique topological and geometrical interpretation. It will, however, be seen that for a given vorticity field, the set of vortex surfaces is not unique. Nonetheless, observation of the evolution of three-dimensional vortex surfaces might be helpful in clarifying some aspects of vortex identification.

In this chapter, we begin in § 4.2 by introducing a systematic methodology for constructing VSFs for both TG and KP initial velocity fields. Equations describing the evolution of VSFs are then obtained in § 4.3 and their existence and uniqueness properties are discussed for both inviscid and viscous incompressible flows. In § 4.4, we review the numerical methods used presently for tracking Lagrangian structures, including the pseudo-spectral method for the Eulerian velocity field and the backward-particle-tracking method for the Lagrangian field. The growth of the divergence of evolving Lagrangian fields away from their VSF initial conditions in a high-Reynolds-number viscous flow is studied and quantified in § 4.5. Finally, we investigate the non-local and local geometries of approximate vortex surfaces in time evolution. Some conclusions are drawn in § 4.6.

4.2 Construction of vortex-surface fields

4.2.1 Partial-differential-equation formulation

We develop a methodology for construction of VSFs for some simple given velocity fields. A discussion of their evolution in time and their relation to Lagrangian fields is postponed until § 4.3. A vortex line is defined by

$$\frac{\mathrm{d}\boldsymbol{X}}{\mathrm{d}s} = \frac{\boldsymbol{\omega}}{|\boldsymbol{\omega}|}, \tag{4.1}$$

where s is arclength along the vortex line. For the given vorticity field we now assume the existence of a smooth, space-filling scalar function $\phi(\boldsymbol{x})$ that has the property that the vorticity vector is tangent to iso-surfaces of $\phi(\boldsymbol{x})$ everywhere except perhaps at a finite number of critical points. It follows that

$$\frac{\mathrm{d}\phi}{\mathrm{d}s} = \frac{\mathrm{d}\phi}{\mathrm{d}\boldsymbol{X}}\frac{\mathrm{d}\boldsymbol{X}}{\mathrm{d}s} = 0. \tag{4.2}$$

Substituting (4.1) into (4.2) yields the constraint for ϕ

$$\boldsymbol{\omega} \cdot \nabla \phi = \omega_x(x,y,z)\frac{\partial \phi}{\partial x} + \omega_y(x,y,z)\frac{\partial \phi}{\partial y} + \omega_z(x,y,z)\frac{\partial \phi}{\partial z} = 0. \tag{4.3}$$

We will take (4.3) as our fundamental definition of a VSF. For given $\boldsymbol{\omega}$ we can view this as a homogeneous first-order partial differential equation (PDE) for ϕ. We will see that (4.3) does not admit unique solutions, but it may admit useful solutions. Equation (4.3) is similar to the PDE formulation proposed by Dieci et al. (1991) for computing numerical approximations to invariant tori corresponding to ODEs like (4.1). An alternative form of this PDE formulation is to find a two-dimensional invariant manifold in a three-dimensional real space with a local parametrization $(x, y, g(x, y))$. Then the graph of $g(x, y)$ should be tangential to a given vector field $f(x, y, g(x, y))$ as

$$\left(\frac{\partial}{\partial x} g(x,y), \frac{\partial}{\partial y} g(x,y), -1\right) \cdot f(x,y,g(x,y)) = 0. \tag{4.4}$$

The major difference between our proposed relation (4.3) and (4.4) is that, from (4.3), we seek a set of invariant manifolds as space-filling iso-surfaces of ϕ within the whole domain of some particular vector field, while only an individual invariant manifold can be found from (4.4).

Equation (4.4) was solved by finite difference methods and Newton's iteration in Dieci et al. (1991), while Mingyu et al. (1997) showed that a Fourier method is more accurate for computing invariant tori of a vector field with periodic boundary conditions. To find a ϕ satisfying (4.3) in the present study, at an initial time for a class of simple vorticity fields with periodic boundary conditions, we expand $\boldsymbol{\omega}$ and ϕ as Fourier series

$$\omega_\alpha = \sum_{k_1,k_2,k_3} \Omega^{\alpha}_{k_1,k_2,k_3} \mathrm{e}^{\mathrm{i} k_\beta x_\beta}, \quad \alpha = 1,2,3, \quad \beta = 1,2,3, \tag{4.5}$$

$$\phi = \sum_{k_1,k_2,k_3} \Phi_{k_1,k_2,k_3} \mathrm{e}^{\mathrm{i} k_\beta x_\beta}, \quad \beta = 1,2,3, \tag{4.6}$$

where $\Omega^{\alpha}_{k_1,k_2,k_3}$ are given by the vorticity, Φ_{k_1,k_2,k_3} are to be determined, and $k_\beta x_\beta$ denotes the summation convention over β. Substituting both Fourier expansions into (4.3) and then collecting coefficients of each Fourier mode by symbolic manipulation yields

$$\sum_{k_1,k_2,k_3} \Pi_{k_1,k_2,k_3} \mathrm{e}^{\mathrm{i} k_\beta x_\beta} = 0, \tag{4.7}$$

where Π_{k_1,k_2,k_3} is a linear polynomial in terms of unknown Φ_{k_1,k_2,k_3}. Substituting all $\Pi_{k_1,k_2,k_3} = 0$ into (4.7), we obtain a system of homogenous linear equations

$$\boldsymbol{C}\boldsymbol{\Phi} = 0, \tag{4.8}$$

where $\boldsymbol{C}$ is the $m_c \times n_c$ coefficient matrix for Φ_{k_1,k_2,k_3} with rank r_c, and $\boldsymbol{\Phi}$ is a suitably constructed Fourier coefficient vector in (4.6). If there exists a VSF $\phi(\boldsymbol{x})$ exactly satisfying the relation (4.3), the corresponding homogeneous system (4.8) with $r_c < n_c$ must have $n_c - r_c$ nontrivial solutions. Otherwise, if $r_c = n_c$ we have to seek an approximate solution of (4.8). We now show how to construct such initial VSFs for three typical simple flows using this methodology.

4.2.2 Taylor–Green flow

The generalized initial condition $\boldsymbol{u}(x, y, z, t = 0)$ of the TG flow is given by, up to an arbitrary real multiplicative constant of θ (see Brachet et al., 1983)

$$\begin{aligned}
u_x &= \frac{2}{\sqrt{3}} \sin\left(\theta + \frac{2\pi}{3}\right) \sin x \cos y \cos z, \\
u_y &= \frac{2}{\sqrt{3}} \sin\left(\theta - \frac{2\pi}{3}\right) \cos x \sin y \cos z, \\
u_z &= \frac{2}{\sqrt{3}} \sin\theta \cos x \cos y \sin z.
\end{aligned} \tag{4.9}$$

The corresponding vorticity is

$$\begin{aligned}
\omega_x &= -(\sqrt{3}\sin\theta + \cos\theta) \cos x \sin y \sin z, \\
\omega_y &= (\sqrt{3}\sin\theta - \cos\theta) \sin x \cos y \sin z, \\
\omega_z &= 2\cos\theta \sin x \sin y \cos z.
\end{aligned} \tag{4.10}$$

Based on the mirror and rotational symmetries in the TG flow, the region $0 \leq x, y, z \leq 2\pi$ is conventionally termed the 'periodicity box'; the region $0 \leq x, y, z \leq \pi$ is termed the 'impermeable box'; the region $0 \leq x, y, z \leq \pi/2$ is termed the 'fundamental box' (see Brachet et al., 1983).

From (4.10), the wavenumbers for the Fourier expansion of ω_α are ± 1 in the TG flow at $t = 0$. Assume that the corresponding ϕ has the same Fourier modes, namely

$$\phi = \sum_{k_1,k_2,k_3=\pm 1} \Phi_{k_1,k_2,k_3} \mathrm{e}^{\mathrm{i} k_\beta x_\beta}. \tag{4.11}$$

The expansion (4.5) for the vorticity is obtained from (4.10) by symbolic manipulation. Substituting (4.5) and (4.11) into (4.3) and then setting all the Fourier coefficients in (4.7) equal to zero leads to an 18×8 coefficient matrix $\boldsymbol{C}$ with $r_c = 7$ in (4.8). Thus, we can obtain a nontrivial fundamental solution $(1, 1, 1, 1, 1, 1, 1, 1)^T$. If we let $\Phi_{1,1,1} = 1/8$ in (4.11), then we have the solution

$$\phi_{TG} = \cos x \cos y \cos z, \tag{4.12}$$

and every iso-surface of ϕ_{TG} is a vortex surface for the TG flow with an arbitrary θ at the initial time. An example of a vortex surface as an iso-surface of (4.12) is shown in figure 4.1(a). All the vortex lines computed by (4.1) and (4.10) with $\theta = 0$ lie on the surface. The special case with $\theta = 0$ in (4.9) was discussed at length in Brachet et al. (1983), and this will be used for all computations in this paper.

We note that (4.12) is not unique. Since ϕ_{TG} satisfies (4.3) then, by the chain rule, so does any function $Q(\phi_{TG})$. If $\phi_{TG} \to Q$ is $1-1$ this is just a relabeling so that iso-surfaces $\phi_{TG}(x, y, z) = C$ and $Q(x, y, z) = Q(C)$ are identical geometrically. But for a given vorticity field it appears that vortex lines can be bundled or arranged on smooth surfaces in infinitely many different ways. Hence we cannot rule out solutions to (4.3) that are continuous scalar fields not equivalent to either a relabeling of ϕ_{TG} or to a mapping under the symmetries of the TG flow, and whose iso-surfaces could therefore have a different topology or geometry. The existence of additional classes of VSFs that are not connected by relabeling mappings may enable the construction of nontrivial Clebsch potentials (e.g., Lamb, 1932). This issue is revisited in § 4.2.5.

In some special cases such as $\theta = \pm\pi/6, \pm\pi/2, \pm 5\pi/6$ in (4.9), one vorticity component in (4.10) is zero. For example, as $\theta = \pm\pi/2$, $\omega_z = 0$, the constraint (4.3) is reduced to

$$\omega_x(x, y, z)\frac{\partial \phi}{\partial x} + \omega_y(x, y, z)\frac{\partial \phi}{\partial y} = 0. \tag{4.13}$$

Therefore, as long as $\phi(x, y)$ satisfies (4.13), $\phi(x, y)f(z)$ can be the initial VSF satisfying (4.3). Here, $f(z)$ is an arbitrary function, which implies iso-surfaces of this VSF have a nonunique topology. From our methodology, two fundamental solutions, $\cos x \cos y \exp(\pm \mathrm{i} z)$, can be obtained from (4.8) for this case. The real part of this solution is equivalent to (4.12). Thus, presently we will take (4.12) as our basic VSF solution of (4.3) for the TG initial vorticity field with $\theta = 0$. The issue of nonuniqueness for both the definition of ϕ and its evolution will be revisited subsequently.

In addition, it is obvious that for a given three-dimensional vorticity field with only one nontrivial component, the VSF must exist and its topology is nonunique. For example, in cylindrical coordinates (r, θ, z), consider the initial vorticity field of a vortex ring centered at $(0, 0, 0)$ with radius R and vorticity $\boldsymbol{\omega}_{VR} = (0, \mathrm{e}^{-((r-R)^2+z^2)}, 0)$. Any regular scalar field $\phi(r, z)$ can satisfy $\boldsymbol{\omega}_{VR} \cdot \nabla\phi = 0$, such as $\phi = \mathrm{e}^{-((r-R)^2+z^2)}$ with the topology of the torus in figure 4.1(b) or $\phi = \mathrm{e}^{-(r^2+z^2)}$ with the topology of the sphere.

4.2.3 Kida–Pelz flow

The TG flow is a special case for which we can find a simple scalar field (4.12) satisfying the constraint (4.3). For other vorticity fields with more Fourier modes, for example, the KP flow, we are unable to find a simple exact solution, because it appears that $r_c = n_c$ in (4.8) with a finite set

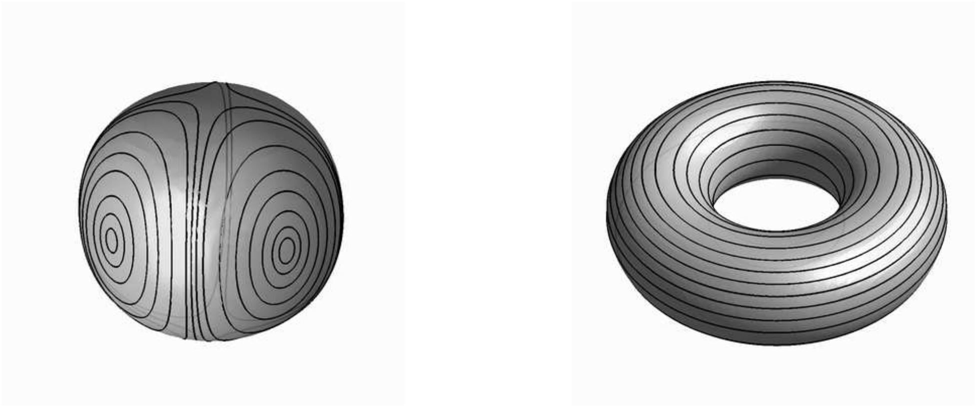

(a) TG flow (b) vortex ring

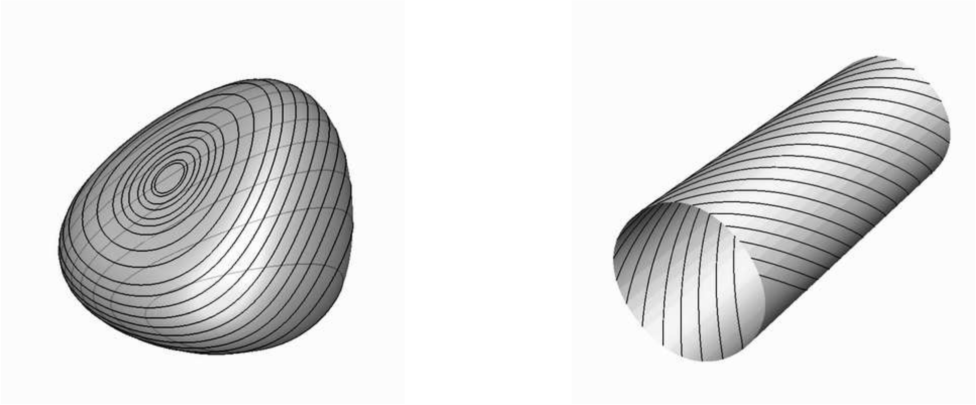

(c) KP flow (d) ABC flow (integrable)

Figure 4.1: Typical vortex surfaces and vortex lines in simple flows at the initial time

of Fourier modes. The initial condition of the KP flow is defined as

$$\begin{aligned} u_x &= \sin x(\cos 3y \cos z - \cos y \cos 3z), \\ u_y &= \sin y(\cos 3z \cos x - \cos z \cos 3x), \\ u_z &= \sin z(\cos 3x \cos y - \cos x \cos 3y), \end{aligned} \tag{4.14}$$

and the corresponding vorticity is

$$\begin{aligned} \omega_x &= -2\cos 3x \sin y \sin z + 3\cos x(\sin 3y \sin z + \sin y \sin 3z), \\ \omega_y &= -2\cos 3y \sin z \sin x + 3\cos y(\sin 3z \sin x + \sin z \sin 3x), \\ \omega_z &= -2\cos 3z \sin x \sin y + 3\cos z(\sin 3x \sin y + \sin x \sin 3y). \end{aligned} \tag{4.15}$$

We now develop an optimization methodology for obtaining ϕ_{KP} that approximately satisfies (4.3) for the KP flow at the initial time. We note that the scale of this problem mainly depends on the number of unknown coefficients in (4.8)

$$n_c = N_F = (2K_F + 1)^3, \tag{4.16}$$

where K_F is the maximum wavenumber in (4.6). The cubic growth of N_F with increasing K_F in the Fourier expansion generally makes the convergence rate very slow. The scale of this problem solved by a direct method used for the TG initial condition is thus unaffordable for the KP case.

Equation (4.15) implies that vortex lines in the KP flow have reflectional and octahedral symmetries (see Kida, 1985; Pelz, 2001). In particular, as shown in figure 4.2, we find a family of closed and unknotted vortex lines that is confined within a fundamental tetrahedron with vertices at, e.g., $(0, 0, 0)$, $(-\pi/2, \pi/2, -\pi/2)$, $(-\pi/2, -\pi/2, -\pi/2)$, and $(0, 0, -\pi/2)$. Four fundamental tetrahedrons with rotational symmetries can constitute a pyramid drawn in solid thick lines in figure 4.2. The box drawn in dotted lines lies in $-\pi/2 \le x, y, z \le \pi/2$. It comprises six pyramids with rotational and reflectional symmetries. Finally, the box with periodic boundary conditions lies in $-\pi/2 \le x, y, z \le 3\pi/2$ consisting of eight such boxes in dotted lines with additional rotational and reflectional symmetries. This box with side 2π thus has 192 fundamental tetrahedrons. These symmetries suggest the construction of new orthogonal basis functions $\widetilde{\psi}_i$ to obtain faster convergence. Presently, the development of $\widetilde{\psi}_i$ utilizes a tailored numerical scheme, described in detail in appendix A. A sparse representation, ϕ_{KP} can then be expanded in these basis functions as

$$\phi_{KP} = \sum_{i=1}^{N_\psi} \Psi_i \widetilde{\psi}_i. \tag{4.17}$$

The expansion (4.17) can be converted to Fourier space by symbolic manipulations

$$\phi_{KP} = \sum_{k_1,k_2,k_3}^{K_F} \Phi^{KP}_{k_1,k_2,k_3} \mathrm{e}^{\mathrm{i}k_\beta x_\beta}, \quad \beta = 1, 2, 3, \tag{4.18}$$

where $\Phi^{KP}_{k_1,k_2,k_3}$ is a linear polynomial in terms of the unknown coefficient Ψ_i in (4.17) and K_F is the maximum wavenumber.

Substituting (4.17) and (4.5) with the vorticity (4.15) into (4.3), we can obtain an expansion as in (4.7). Note that Π_{k_1,k_2,k_3} is a linear polynomial in terms of the coefficient Ψ_i of the basis function $\widetilde{\psi}_i$ rather than $\Phi^{KP}_{k_1,k_2,k_3}$ in the Fourier expansion (4.18). This leads to a significantly faster convergence rate for obtaining an accurate approximate solution. From appendix A, the number of coefficients for $\widetilde{\psi}_i$ with the same K_F in (4.18) is

$$N_\psi = (K_F^4 + 24K_F^2 - 112)/2048. \tag{4.19}$$

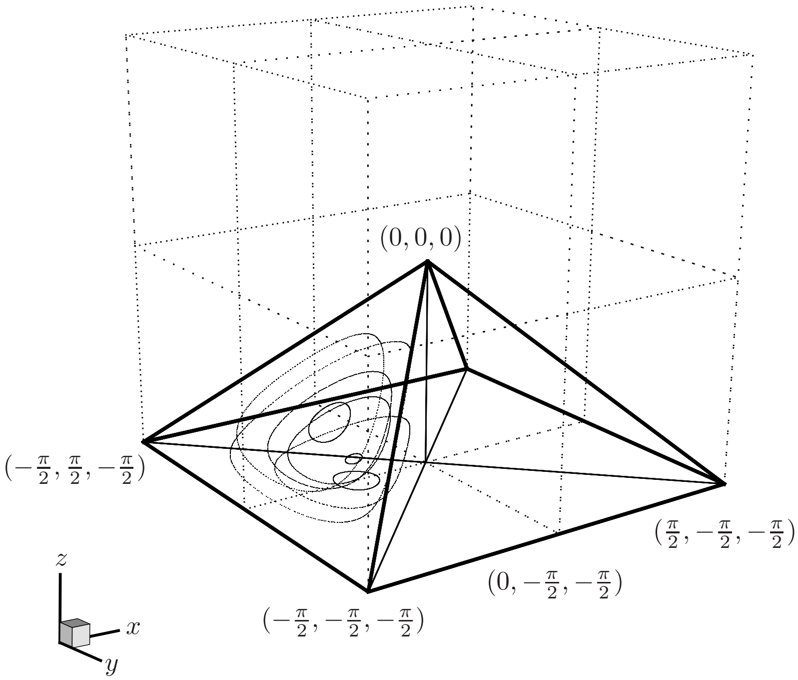

Figure 4.2: Symmetries of vortex lines in the KP flow. Some vortex lines are integrated from random points in a fundamental tetrahedron. The dotted box lies in $-\pi/2 \le x, y, z \le \pi/2$

Compared with the equivalent Fourier coefficient number (4.16), we can find that when K_F is not too large, $N_\psi \ll N_F$ for the same resolution expressed by K_F.

Setting $\Pi_{k_1,k_2,k_3} = 0$ in (4.7) with Ψ_i, we have a homogenous linear system

$$\boldsymbol{C}\boldsymbol{\Psi} = 0, \tag{4.20}$$

where $\boldsymbol{\Psi}$ is the corresponding coefficient vector in (4.17). The overdetermined system (4.20) with a finite number of coefficients appears to have only a trivial solution. To obtain a nontrivial coefficient vector $\boldsymbol{\Psi}$, we let $\Psi_1 = 1$ in (4.17), which is equivalent to assuming the full octahedral symmetry on large-scale structures in the approximate solution, noting that $\widetilde{\psi}_1$ (see appendix A) is proportional to

$$(\cos 3x \cos y - \cos x \cos 3y)(\cos 3y \cos z - \cos y \cos 3z)(\cos 3z \cos x - \cos z \cos 3x).$$

Let $\boldsymbol{C} = (-\boldsymbol{b}\ \boldsymbol{A})$ and $\boldsymbol{\Psi} = (\Psi_1\ \boldsymbol{\Psi'})^T$. Then we can obtain a nonhomogeneous overdetermined system

$$\boldsymbol{A}\boldsymbol{\Psi'} = \boldsymbol{b}. \tag{4.21}$$

This system may have a least-squares solution by

$$\min_{\boldsymbol{\Psi}'} \|\boldsymbol{A\Psi'} - \boldsymbol{b}\|_2^2, \tag{4.22}$$

where $\|\cdot\|_2$ denotes the L^2 norm. As shown in figure 4.3, the residual $\|\boldsymbol{A\Psi'} - \boldsymbol{b}\|_2$ decreases exponentially with increasing N_ψ, which shows a strong convergence rate. Satisfactory accuracy could be obtained with $N_\psi = 666$ with the corresponding $K_F = 34$, while in the full Fourier expansion (4.6), the equivalent unknown coefficient number $N_F = 328,509$. This shows a significant scale reduction in this optimization problem using the proposed basis function $\widetilde{\psi}_i$.

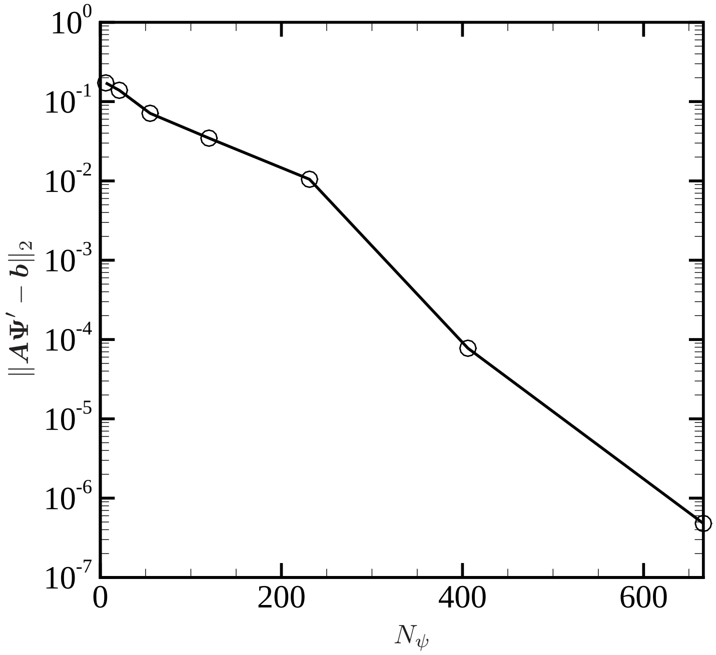

Figure 4.3: Convergence rate with N_ψ for the approximate solution of the initial scalar field in the KP flow ϕ_{KP}, where N_ψ is computed from $K_\psi = 3, 5, \cdots, 17$ by (A.2) and (A.6)

In implementation of the optimization method, we found that the iso-surface of ϕ_{KP} from (4.22) at very small contour levels may exhibit non-smoothness. This could be a numerical consequence of non-uniqueness of solutions to (4.3) or perhaps to instability in solving the large-scale linear system as N_ψ is large. For $N_\psi = 666$, the matrix $\boldsymbol{A}$ with size 53,536 by 665 is sparse. Hence, an additional constraint on $\|\boldsymbol{\Psi}'\|_2$ was applied in this least-squares problem which will both improve the smoothness of the approximate solution at very small contour levels and at the same time provide uniqueness at the numerical level. This results in a quadratic optimization problem

$$\min_{\boldsymbol{\Psi}'} \|\boldsymbol{A}\boldsymbol{\Psi}' - \boldsymbol{b}\|_2^2 + \lambda\|\boldsymbol{\Psi}'\|_2^2, \tag{4.23}$$

where the ridge parameter $\lambda = 3.75 \times 10^{-8}$ is introduced to obtain the local minimum value of $|\nabla\phi_{KP}|_{max}$. This ridge regression problem has an analytical solution (see Golub & Van Loan, 1996)

$$\boldsymbol{\Psi}' = (\boldsymbol{A}^T\boldsymbol{A} + \lambda\boldsymbol{I})^{-1}\boldsymbol{A}^T\boldsymbol{b}. \tag{4.24}$$

To solve this quadratic optimization problem numerically by the highly efficient driver routine with the QR method in LAPACK (Anderson et al., 1999), (4.23) is converted to a linear least-squares problem

$$\min_{\boldsymbol{\Psi}'} \left\| \begin{pmatrix} \boldsymbol{A} \\ \sqrt{\lambda}\boldsymbol{I} \end{pmatrix} \boldsymbol{\Psi}' - \begin{pmatrix} \boldsymbol{b} \\ 0 \end{pmatrix} \right\|_2^2 .$$

Finally, ϕ_{KP} was obtained from (4.18) by the inverse FFT. The volume-averaged $|\nabla\phi_{KP} \cdot \boldsymbol{\omega}|$ is very small as $O(10^{-7})$ and $|\phi_{KP}|_{max} \approx 0.648$, which shows that ϕ_{KP} obtained by the optimization methodology is an accurate nontrivial solution for (4.3). The spectrum of ϕ_{KP} in figure 4.4 also illustrates the good spectral convergence of this solution. An iso-surface of ϕ_{KP} in a fundamental tetrahedron with vortex lines on it is shown in figure 4.1(c), which can represent a vortex surface in the KP flow at the initial time. The code for the methodology in §§ 4.2.2 and 4.2.3 was written in Mathematica (Wolfram Research, 2008) for symbolic manipulations and Fortran 90 for matrix computations. Furthermore, the optimization methodology in this section can also be utilized for the TG initial condition to uniquely determine the VSF (4.12).

4.2.4 Arnold–Beltrami–Childress flow

Another well-known simple flow is the Arnold–Beltrami–Childress (ABC) flow. The velocity field is

$$\begin{aligned} u_x &= A\sin z + C\cos y, \\ u_y &= B\sin x + A\cos z, \\ u_z &= C\sin y + B\cos x. \end{aligned} \tag{4.25}$$

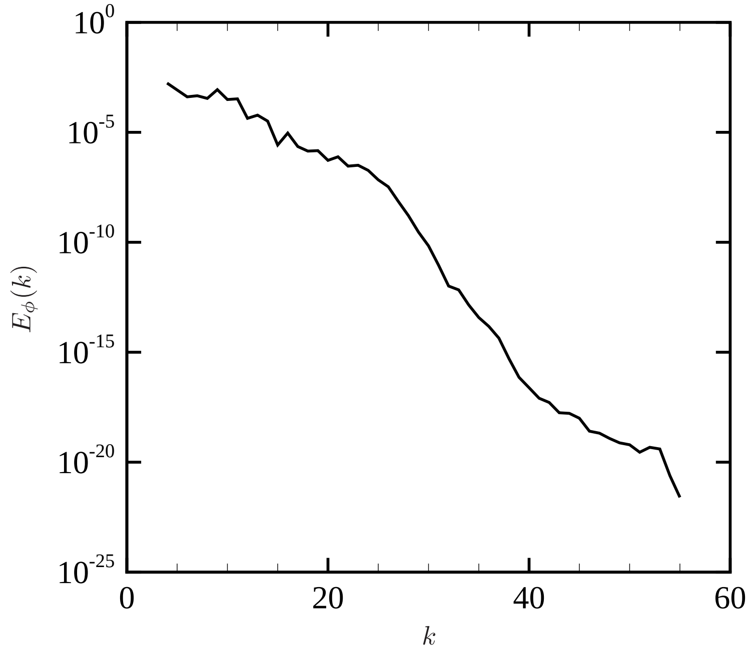

Figure 4.4: The spectrum of ϕ_{KP}

The streamlines, which are equivalent to vortex lines, in the ABC flow are chaotic for most values of the parameters A, B, and C (Dombre et al., 1986). For the integrable case, where

$$\boldsymbol{u} = (A\sin z, B\sin x + A\cos z, B\cos x),$$

we can find a scalar field $\phi_{ABC} = B\sin x + A\cos z$ to satisfy the constraint (4.3). The iso-surface of ϕ_{ABC} corresponds to a simple vortex tube as shown in figure 4.1(d). However, even for nearly integrable cases, the vortex lines become chaotic so that it appears to be difficult to find such a scalar field exactly satisfying (4.3), and in fact no such ϕ may exist. Moreover, we note that the ABC flow is stationary, so we cannot study the dynamics of vortex surfaces in this flow. The general problem of the existence of some nontrivial ϕ satisfying (4.3) for an arbitrary, spatially periodic vorticity field of the type encountered at a time instant in either forced or decaying homogeneous (box) turbulence, remains, to the best of our knowledge, an open problem.

4.2.5 Vortex-surface fields and Clebsch potentials

VSFs are also helpful in representing the full Eulerian velocity field in terms of Lagrangian variables. Clebsch (1859) established an appealing Hamiltonian formulation as a compromise between Eulerian and Lagrangian descriptions of fluid dynamics (see also Lamb, 1932; Truesdell, 1954;

Salmon, 1988). In the Clebsch representation, the incompressible fluid velocity at any time instant can be expressed locally in terms of three scalar fields as

$$\boldsymbol{u}(\boldsymbol{x}) = \varphi_1 \nabla \varphi_2 - \nabla \varphi_3 \tag{4.26}$$

where $\varphi_1(\boldsymbol{x})$ and $\varphi_2(\boldsymbol{x})$, which can evolve as Lagrangian fields, are often called Clebsch potentials, and φ_3 is used for the solenoidal projection. Sometimes $\varphi_1 \nabla \varphi_2$ is referred to as the 'impulse' variable (e.g., Russo & Smereka, 1999). It follows that the vorticity can be expressed by

$$\boldsymbol{\omega}(\boldsymbol{x}) = \nabla \varphi_1 \times \nabla \varphi_2, \tag{4.27}$$

with the interesting geometric interpretation that vortex lines are the intersection of iso-surfaces of φ_1 and φ_2.

The global existence of the Clebsch potentials is, however, restricted to inviscid flows with vanishing helicity $H \equiv \int \boldsymbol{u} \cdot \boldsymbol{\omega} \, \mathrm{d}\boldsymbol{x}$ (see Salmon, 1988). When $H = 0$, e.g., in inviscid TG and KP flows, it is easy to verify from (4.27) that nontrivial φ_1, φ_2, and φ_3 satisfy the constraint for the VSF (4.3). This suggests that we can construct explicit Clebsch potentials from multiple independent VSFs, if the latter exist, for a given velocity field. We note that, when $H \neq 0$, it is still possible to find VSFs in some particular flows, such as the integrable ABC flow.

For the TG initial velocity field we seek $n > 1$ independent VSFs of the form

$$\phi^{(i)} = A_i \cos^{a_i} x \cos^{b_i} y \cos^{c_i} z, \qquad i = 1, 2, \ldots, n, \tag{4.28}$$

where a_i, b_i, and c_i should be integers larger than or equal to zero for smooth and real VSFs and satisfy, using (4.3) and (4.10),

$$(a_i + b_i - 2c_i) \cos\theta + \sqrt{3}(a_i - b_i) \sin\theta = 0. \tag{4.29}$$

Hence, the geometry of vortex lines in figure 4.1(a) can be expressed by the intersections of iso-surfaces of two independent VSFs as shown in figure 4.5.

Any three VSFs cannot be guaranteed to satisfy the Clebsch representation (4.26). We therefore take $\varphi_1 = \phi^{(1)}$ and $\varphi_2 = \phi^{(2)}$. Then, from (4.26), (4.27), and (4.29), we can find families of independent solutions for the Clebsch representation of the general TG initial field (4.9) of the form

$$\varphi_1 = A_1 \cos^{a_1} x \cos^{b_1} y \cos^{c_1} z, \ \varphi_2 = A_2 \cos^{a_2} x \cos^{b_2} y \cos^{c_2} z, \ \varphi_3 = A_3 \cos x \cos y \cos z, \tag{4.30}$$

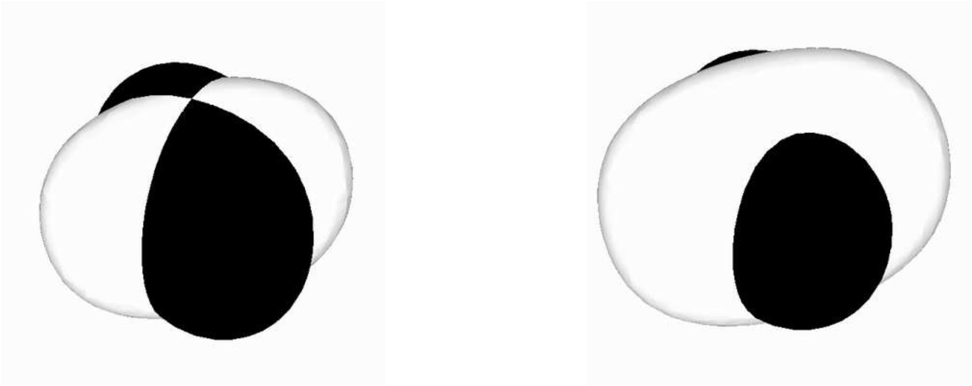

(a) $\phi^{(1)} = 0.5$ and $\phi^{(2)} = 0.5$ (b) $\phi^{(1)} = 0.5$ and $\phi^{(2)} = 0.4$

Figure 4.5: Examples of the vortex lines in figure 4.1(a) expressed by intersections of iso-surfaces of two independent VSFs $\phi^{(1)} = \cos x \cos^3 y \cos^2 z$ (dark surface) and $\phi^{(2)} = \cos^3 x \cos y \cos^2 z$ (light surface) for the TG initial field (4.9) with $\theta = 0$

where

$$a_1 = d_0, \quad a_2 = 1 - d_0, \quad b_1 = d_0 - \frac{2\cos\theta}{A_1 A_2}, \quad b_2 = 1 - d_0 + \frac{2\cos\theta}{A_1 A_2},$$
$$c_1 = d_0 + \frac{\sqrt{3}\sin\theta - \cos\theta}{A_1 A_2}, \quad c_2 = 1 - d_0 - \frac{\sqrt{3}\sin\theta - \cos\theta}{A_1 A_2},$$
$$A_3 = A_1 A_2 (1 - d_0) - \frac{\sqrt{3}}{3}\sin\theta + \cos\theta,$$

with arbitrary constants d_0, A_1, and A_2. We can verify that (4.30) must have singularities or imaginary values in some spatial domains. Taking $\theta = 0$, $d_0 = 1$, and $A_1 = A_2 = \sqrt{2}$, for example, (4.30) becomes $\varphi_1 = \sqrt{2}\cos x \sqrt{\cos z}$ and $\varphi_2 = \sqrt{2}\cos y \sqrt{\cos z}$. This particular solution was given in Nore, Abid & Brachet (1997), and the sign function was then introduced to remove imaginary values to obtain TG Clebsch potentials with weak singularities.

It is difficult to determine Clebsch potentials from approximate numerical solutions for VSFs such as those obtained presently for the KP flow in § 4.2.3. Explicit KP Clebsch potentials with singularities or imaginary values are known (Ohkitani, 2008) but are generally not useful for the construction of smooth VSFs for investigating the evolutionary geometry of the vorticity in physical space.

Finally, a comparison of some properties of VSFs and Clebsch potentials is given in table 4.1. Both VSFs and Clebsch potentials exist perhaps only in some subsets of general flows, in particular, flows with the simple topology and geometry.

Table 4.1: Comparisons between VSFs and classical Clebsch potentials

	VSFs	Clebsch potentials
Global existence when $H = 0$	Possible	Possible
Global existence when $H \neq 0$	Possible	No
Satisfying $\boldsymbol{\omega} \cdot \nabla\phi = 0$ when $H = 0$	Yes	Yes
Requirement on the global smoothness	Yes	No

4.3 Evolution of Lagrangian and vortex-surface fields

4.3.1 Evolution equations

As described in § 2.2.3, we define a Lagrangian field $\phi(\boldsymbol{x}, t)$ satisfying (2.15) as one for which iso-surfaces $\phi = C$, for each constant C, $\phi_{min} \leq C \leq \phi_{max}$, are always composed of the same particles. Iso-surfaces of ϕ are then referred to as material or Lagrangian surfaces. In this section, for a given velocity/vorticity field, we use $\phi_v(\boldsymbol{x}, t)$ to denote a VSF, which we distinguish from the Lagrangian field $\phi(\boldsymbol{x}, t)$. In the sequel these two fields will generally be taken to be identical at an initial time $t = 0$.

Now, in an incompressible flow, consider $\boldsymbol{\omega}(\boldsymbol{x}, t)$ and $\phi_v(\boldsymbol{x}, t)$ that, respectively, satisfy (2.30) and

$$\frac{\mathrm{D}\phi_v}{\mathrm{D}t} = L_1 + \nu\mathcal{L}. \tag{4.31}$$

In order to define an evolution of a VSF, we seek $\phi_v(\boldsymbol{x}, t)$ with L_1 and $\mathcal{L}$ such that

$$\frac{\mathrm{D}}{\mathrm{D}t}\left(\boldsymbol{\omega} \cdot \nabla\phi_v\right) = 0, \tag{4.32}$$

with an initial condition that satisfies

$$\boldsymbol{\omega} \cdot \nabla\phi_v(\boldsymbol{x}, t = 0) \equiv 0 \tag{4.33}$$

for all $\boldsymbol{x}$. It follows that if (4.33) is satisfied at $t = 0$, then it is preserved for $t > 0$. Hence, $\phi_v(\boldsymbol{x}, t)$ evolves as a VSF. It is noted that (4.32) is equivalent to Ertel's theorem (Ertel, 1942), when $\phi_v = \phi$, and it also satisfies (2.15).

From (2.30) it can be shown that

$$\frac{\mathrm{D}}{\mathrm{D}t}\left(\boldsymbol{\omega} \cdot \nabla\phi_v\right) = \nu\nabla\phi_v \cdot \nabla^2\boldsymbol{\omega} + \boldsymbol{\omega} \cdot \nabla\left(\frac{\mathrm{D}\phi_v}{\mathrm{D}t}\right), \tag{4.34}$$

and using (4.31)

$$\frac{\mathrm{D}}{\mathrm{D}t}\left(\boldsymbol{\omega} \cdot \nabla\phi_v\right) = \nu\nabla\phi_v \cdot \nabla^2\boldsymbol{\omega} + \boldsymbol{\omega} \cdot \nabla\left(L_1 + \nu\mathcal{L}\right). \tag{4.35}$$

Comparing (4.35) with (4.32) it follows that for $\phi_v(\boldsymbol{x},t)$ to describe the evolution of a VSF, we require that

$$\nu\left(\nabla\phi_v\cdot\nabla^2\boldsymbol{\omega}+\boldsymbol{\omega}\cdot\nabla\mathcal{L}\right)+\boldsymbol{\omega}\cdot\nabla L_1=0. \tag{4.36}$$

4.3.2 Inviscid incompressible flow

First, consider the inviscid case $\nu=0$. Equation (4.36) becomes

$$\boldsymbol{\omega}\cdot\nabla L_1=0, \tag{4.37}$$

with solution $L_1(\boldsymbol{x})=F(\phi_v(\boldsymbol{x},t))$ where F is any smooth function. Hence $\phi_v(\boldsymbol{x},t)$ must evolve as

$$\frac{\mathrm{D}\phi_v}{\mathrm{D}t}=F(\phi_v(\boldsymbol{x},t)). \tag{4.38}$$

Comparison of (4.38) with (2.15) shows that the choice $F=0$ makes ϕ_v a Lagrangian field for $t>0$. This is the Helmholtz vorticity theorem. In our terminology, this states that a Lagrangian surface (Lagrangian field) that is a vortex surface (VSF) at some initial time remains so for all time. Hence to track the evolution of a VSF in an inviscid flow it is sufficient to determine $\phi_v(\boldsymbol{x},t=0)$ that satisfies (4.33), choose $\phi(\boldsymbol{x},t=0)=\phi_v(\boldsymbol{x},t=0)$, and solve (2.15) for $t>0$ along with the velocity/vorticity dynamics.

Any non-zero $F(\phi_v)$, however, also provides an evolution for a VSF with the initial condition $\phi_v(\boldsymbol{x},t=0)$ that satisfies (4.33). Iso-surfaces of $\phi_v(\boldsymbol{x},t)$ then remain vortex surfaces for $t>0$, but $\phi_v=C$ for some C is then not a Lagrangian surface, and so ϕ_v is not a Lagrangian field. This demonstrates nonuniqueness of the evolution of a VSF from an initial condition that satisfies (4.33). Thus, an initial VSF does not have a unique evolution for $t>0$ but there exists a unique evolution for which ϕ_v is also a Lagrangian field namely $F=0$. In other words, in inviscid incompressible flow, a Lagrangian field that was initially a VSF remains so for all time. But one can define the evolution of VSFs that are not Lagrangian fields. We remark that this nonuniqueness appears to be distinct from that associated with the definition of ϕ_v at $t=0$. The latter is a relabeling

We can, however, show that solutions to (4.38) for a reasonable but arbitrary choice of F are equivalent to a relabeling of the Lagrangian field from the same initial condition. First, consider $\phi(\boldsymbol{x},t)$ satisfying (2.15) with $\phi(\boldsymbol{x},t=0)=\phi_0(\boldsymbol{x})$, given ϕ_0, and second, $\phi_v(\boldsymbol{x},t)$ satisfying (4.38), given $F(\phi_v)$. Choose $\phi_v(\boldsymbol{x},t=0)=\phi_0$. Next consider the change of variables $\phi_v\leftrightarrow\phi$ given by

$$G(\phi_v)=t+G(\phi),\qquad G(\eta)\equiv\int\frac{\mathrm{d}\eta}{F(\eta)}, \tag{4.39}$$

where $F(\phi)$ satisfies the (strong) condition that (4.39) is regular and 1–1 for all t. Then it is straightforward to show that under (4.39), (4.38) is mapped to (2.15). Further, from (4.39) at $t=0$,

$\phi_v(\boldsymbol{x}, t = 0) = \phi(\boldsymbol{x}, t = 0) = \phi_0(\boldsymbol{x})$. It follows that, given a solution at time t of (2.15) with $\phi(\boldsymbol{x}, t = 0) = \phi_0(\boldsymbol{x})$, the solution of (4.38) at time t with the same initial condition is

$$\phi_v(\boldsymbol{x}, t) = G^{-1}\left(t + G(\phi(\boldsymbol{x}, t)\right), \tag{4.40}$$

where G^{-1} denotes the inverse function. In particular iso-surfaces of ϕ_v and ϕ are mapped into each other by (4.40). Nonuniqueness then exists only up to a relabeling: at $t > 0$ the fields ϕ_v and ϕ are geometrically isomorphic in that the geometry of iso-surfaces for respective constants satisfying (4.39) are identical. In this sense, F has been scaled out of the evolution. As an example, the choice $F = \phi_v$ gives $\phi_v(\boldsymbol{x}, t) = \exp(t)\phi(\boldsymbol{x}, t)$ and is regular for all t. We remark that choices of F for which (4.39) is singular for some $t > 0$ implies that the evolution of ϕ_v can develop a singularity in a finite time. An example is $F = \phi_v^2$. This has no physical significance.

4.3.3 Viscous incompressible flow

In the viscous case, $\nu > 0$, we can, without loss of generality, either put $L_1 \equiv 0$ or absorb L_1 into $\mathcal{L}$ in (4.36) so that, for $\phi_v(\boldsymbol{x}, t)$ to be a VSF for $t > 0$ we must solve

$$\frac{\mathrm{D}\phi_v}{\mathrm{D}t} = \nu\mathcal{L}, \tag{4.41}$$

along with the velocity–vorticity equations, where $\mathcal{L}(\phi_v, \boldsymbol{\omega})$ is determined by

$$\nabla\phi_v \cdot \nabla^2\boldsymbol{\omega} + \boldsymbol{\omega} \cdot \nabla\mathcal{L} = 0. \tag{4.42}$$

While there is clearly no solution for ϕ_v which is a Lagrangian field, given $\boldsymbol{\omega}$ and ϕ_v satisfying (4.33) at some t, say $t = 0$, it is of interest to enquire if there exist solutions to (4.42) that define the evolution of $\phi_v(\boldsymbol{x}, t)$ as a VSF for $t > 0$. In particular can a unique solution be defined that is in some sense the continuation in $\nu > 0$ of the inviscid case? Equation (4.42) is an inhomogeneous, non-constant coefficient equation for $\mathcal{L}$. If solutions exist, it is easy to show that they are not unique: for if $\mathcal{L}_p$ is a particular solution, then since by (4.33) the homogeneous form of (4.42) is satisfied by an arbitrary function $H(\phi_v)$, $\mathcal{L}_p + H(\phi_v)$ is also a solution. Unlike the inviscid case it appears that this cannot be reduced to a geometrical isomorphism.

Furthermore, from (2.30), (4.41), and (4.42), we can obtain transport equations for $|\boldsymbol{\omega}|$ and $|\nabla\phi_v|$

$$\frac{\mathrm{D}|\boldsymbol{\omega}|}{\mathrm{D}t} = (\boldsymbol{n}_\omega \cdot \boldsymbol{S} \cdot \boldsymbol{n}_\omega + \nu R_\omega \boldsymbol{n}_\omega \cdot \boldsymbol{n}_{\Delta\omega})\,|\boldsymbol{\omega}|, \tag{4.43}$$

$$\frac{\mathrm{D}|\nabla\phi_v|}{\mathrm{D}t} = (-\boldsymbol{n}_v \cdot \boldsymbol{S} \cdot \boldsymbol{n}_v - \nu R_\omega \boldsymbol{n}_\omega \cdot \boldsymbol{n}_{\Delta\omega})|\nabla\phi_v|, \tag{4.44}$$

where the rate-of-strain tensor $\boldsymbol{S}$ has entries $S_{ij} = \frac{1}{2}(\partial u_i/\partial x_j + \partial u_j/\partial x_i)$, and unit vectors and a dimensionless ratio, respectively, are

$$\boldsymbol{n}_\omega = \frac{\boldsymbol{\omega}}{|\boldsymbol{\omega}|}, \quad \boldsymbol{n}_{\Delta\omega} = \frac{\nabla^2\boldsymbol{\omega}}{|\nabla^2\boldsymbol{\omega}|}, \quad \boldsymbol{n}_v = \frac{\nabla\phi_v}{|\nabla\phi_v|}, \quad R_\omega = \frac{|\nabla^2\boldsymbol{\omega}|}{|\boldsymbol{\omega}|}. \tag{4.45}$$

The evolution of the spatial averaged $|\boldsymbol{\omega}|$ and $|\nabla\phi_v|$ can then be expressed as

$$\langle|\boldsymbol{\omega}(t)|\rangle = \langle|\boldsymbol{\omega}_0|\rangle \exp\left(\int_{t0}^{t} \langle \boldsymbol{n}_\omega \cdot \boldsymbol{S} \cdot \boldsymbol{n}_\omega\rangle + \langle \nu R_\omega \boldsymbol{n}_\omega \cdot \boldsymbol{n}_{\Delta\omega}\rangle \,\mathrm{d}t'\right), \tag{4.46}$$

$$\langle|\nabla\phi_v(t)|\rangle = \langle|\nabla\phi_{v0}|\rangle \exp\left(\int_{t0}^{t} -\langle \boldsymbol{n}_v \cdot \boldsymbol{S} \cdot \boldsymbol{n}_v\rangle - \langle \nu R_\omega \boldsymbol{n}_\omega \cdot \boldsymbol{n}_{\Delta\omega}\rangle \,\mathrm{d}t'\right). \tag{4.47}$$

Here, in general a viscous flow, statistically the enstrophy production rate $\langle \boldsymbol{n}_\omega \cdot \boldsymbol{S} \cdot \boldsymbol{n}_\omega\rangle$ in (4.46) is positive owing to predominant vortex stretching. It follows that the viscous term $\langle \nu R_\omega \boldsymbol{n}_\omega \cdot \boldsymbol{n}_{\Delta\omega}\rangle$ should be negative to keep $\langle|\boldsymbol{\omega}|\rangle$ finite. But this implies that the same viscous term would increase $\langle|\nabla\phi_v|\rangle$ in (4.47). Without the viscous mechanism, it appears to be difficult to give an estimation on the upper bound of $\langle|\nabla\phi_v|\rangle$, which may cause numerical issues in the computation of evolving VSFs in a viscous flow.

Thus, for viscous flow with TG and KP initial conditions, we will presently follow Lagrangian fields ϕ whose evolution is defined by (2.15) and which are VSFs at $t = 0$ as determined in § 4.2. We will show that, for small viscosity or large Reynolds number, such a Lagrangian field can remain a good approximation to a VSF before significant topological changes, for example vortex reconnection. The problem of the evolution of VSFs in a viscous flow at low and intermediate Reynolds numbers is discussed further in § 5 and appendix B.

4.4 Simulation overview

4.4.1 Eulerian velocity field in Taylor–Green and Kida–Pelz flows

A VSF as defined presently can be considered as a Lagrangian field only in an inviscid flow. However, considering the requirement of huge computational resources and open issues concerning unresolved computations in the simulation of the Euler equation (see Hou & Li, 2008), in § 4.5, we will investigate the approximation of vortex surfaces in a slightly viscous flow. The corresponding Navier–Stokes equations for incompressible TG and KP flows in a periodic box of side $L = 2\pi$ are written in the general form

$$\left.\begin{aligned} &\frac{\partial \boldsymbol{u}}{\partial t} = \boldsymbol{u} \times \boldsymbol{\omega} - \nabla\left(\frac{p}{\rho} + \frac{1}{2}|\boldsymbol{u}|^2\right) + \nu\nabla^2\boldsymbol{u}, \\ &\nabla \cdot \boldsymbol{u} = 0. \end{aligned}\right\} \tag{4.48}$$

The numerical simulations were performed using a standard pseudo-spectral method (see § 2.3.1).

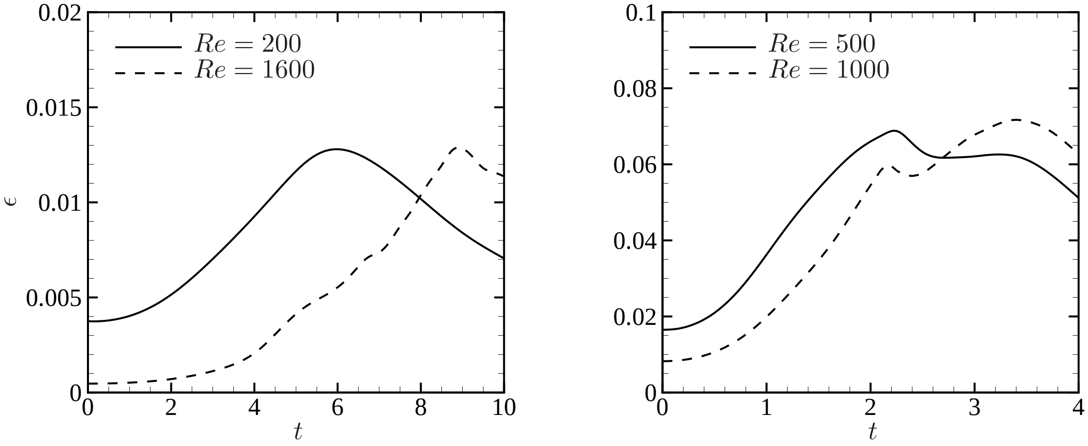

(a) TG flow (b) KP flow

Figure 4.6: Dissipation rate

Table 4.2: Parameters of the study for TG and KP flows

Run	TG1	TG2	KP1	KP2
Re	200	1600	500	1000
N^3	256^3	512^3	512^3	512^3

The flow domain was discretized uniformly into N^3 grid points. Aliasing errors were removed using the two-thirds truncation method. The Fourier coefficients of the flow velocity were advanced in time using a second-order Adams–Bashforth method for the nonlinear term and an exact integration for the linear viscous term. The time step was chosen to ensure that the CFL number was 0.25 or less for numerical stability and accuracy. An important feature of both flows is that the dissipation rate $\varepsilon = \nu \langle \nabla \boldsymbol{u} : \nabla \boldsymbol{u} \rangle$ is increased at early time and approaches a peak after a finite time as shown in figure 5.1. This reproduced the results in Brachet et al. (1983) and Boratav & Pelz (1994). More details about the computation of TG and KP flows can be found in these two references. Parameters of runs carried out in this study are listed in table 5.1, where $Re = 1/\nu$, considering that the length and velocity scales in (4.9) and (4.14) are $O(1)$.

4.4.2 Lagrangian field

To solve the governing equation (2.15) of the Lagrangian field, the backward-particle-tracking method, which is stable, topology preserving and without numerical dissipation, was used. Details of this method are demonstrated in § 2.3.2.

First, the Navier–Stokes equations (4.48) are solved numerically on the N^3 grid in some time interval $t_0, t > t_0$ and the full Eulerian velocity field in the impermeable box is saved on disk at every time step over this simulation period. The time increment is selected to capture the finest resolved scales in the velocity field. At time t at the end of the solution period, particles are placed at the grid points of N_p^3 in the periodicity box. As discussed in § 2.3.2, here N_p is greater than the grid number N of velocity field to capture some nearly singular Lagrangian structures in the evolution. Then, particles are released and their trajectories calculated by solving (2.1) backwards in time. When particles run out of the impermeable box, the reflectional symmetries in $\boldsymbol{u}(\boldsymbol{x}, t)$ need to be considered (see Brachet et al., 1983). After the backward tracking, we can then obtain the Lagrangian field at time t on the Cartesian grid from a given initial smooth Lagrangian field $\phi(\boldsymbol{x}_0, t_0)$ by a simple mapping (2.11) with Lagrangian coordinates.

Next, initial conditions ϕ_{TG} and ϕ_{KP} developed in §§ 4.2.2 and 4.2.3 are, respectively, applied to obtain the corresponding Lagrangian field in TG and KP flows at the particular time by (2.11). Additional interpolations from ϕ_{KP} are required in the computation of (2.11) for the KP flow. Taking an advantage of symmetries in both flows, we can simulate ϕ only in the fundamental box with resolution $(N_p/4+1)^3$, where $N_p = 4096$ in the present study. Then, ϕ in the impermeable box can be reconstructed by following steps with rotational symmetries

$$\begin{aligned}
\phi(x,y,z) &= -\phi(y,\pi-x,z), \quad \pi/2 \le x \le \pi, \quad 0 \le y \le \pi/2, \quad 0 \le z \le \pi/2, \\
\phi(x,y,z) &= -\phi(\pi-y,x,z), \quad 0 \le x \le \pi/2, \quad \pi/2 \le y \le \pi, \quad 0 \le z \le \pi/2, \\
\phi(x,y,z) &= \phi(\pi-x,\pi-y,z), \quad \pi/2 \le x \le \pi, \quad \pi/2 \le y \le \pi, \quad 0 \le z \le \pi/2, \\
\phi(x,y,z) &= \phi(x,\pi-y,\pi-z), \quad 0 \le x \le \pi, \quad 0 \le y \le \pi, \quad \pi/2 \le z \le \pi.
\end{aligned}$$

Finally ϕ in the periodicity box can be obtained from ϕ in the impermeable box by reflectional symmetries with the planes $x, y, z = \pi$. In addition, ϕ can be simulated only in the fundamental tetrahedron for the KP flow to make a further reduction on the computation size.

4.5 Numerical simulation and results

4.5.1 Error estimation in the evolution of the vortex-surface field

If the flow is inviscid, an iso-surface of the Lagrangian field $\phi(\boldsymbol{x}, t)$ is a vortex surface. When the viscosity is nonzero, even very small, a Lagrangian surface that was a vortex surface at the initial time, will, in general no longer remain a vortex surface. Iso-surfaces of ϕ, however, which started as vortex surfaces could still be a good approximation to a vortex surface within a finite time for a high-*Re* flow. We presently investigate this approximation.

A measure of the deviation of a Lagrangian surface $\phi =$ constant from a vortex surface $\phi_v =$ constant is the cosine of the angle χ between $\boldsymbol{\omega}$ and $\nabla\phi$, i.e., $\lambda_\omega \equiv \cos\chi$ where λ_ω is defined in (2.24). Using (2.15) and (2.30) and replacing ϕ_v by ϕ in (4.34) provide a corresponding transport equation for λ_ω

$$\frac{\mathrm{D}\lambda_\omega}{\mathrm{D}t} = \mathcal{A}\lambda_\omega + \mathcal{B}, \tag{4.49}$$

where

$$\mathcal{A}(\boldsymbol{x}, t) = \boldsymbol{n}_\phi \cdot \boldsymbol{S} \cdot \boldsymbol{n}_\phi - \boldsymbol{n}_\omega \cdot \boldsymbol{S} \cdot \boldsymbol{n}_\omega - \nu R_\omega \boldsymbol{n}_\omega \cdot \boldsymbol{n}_{\Delta\omega}, \tag{4.50}$$

$$\mathcal{B}(\boldsymbol{x}, t) = \nu R_\omega \boldsymbol{n}_\phi \cdot \boldsymbol{n}_{\Delta\omega}, \tag{4.51}$$

with notations in (4.45) and $\boldsymbol{n}_\phi = \nabla\phi/|\nabla\phi|$. On a fluid particle, the solution of (4.49) has the form of

$$\lambda_\omega(t) = \lambda_{\omega 0} \exp\left(\int \mathcal{A}(t)\mathrm{d}t\right) + \exp\left(\int \mathcal{A}(t)\mathrm{d}t\right) \int \exp\left(-\int \mathcal{A}(t)\mathrm{d}t\right) \mathcal{B}(t)\mathrm{d}t, \tag{4.52}$$

with $\lambda_{\omega 0} \equiv \lambda_\omega(t = 0)$.

For the initial VSF, $\boldsymbol{\omega}$ is normal to $\nabla\phi$ and $\lambda_{\omega 0} = 0$ everywhere, and (4.52) becomes

$$\lambda_\omega(t) = \exp\left(\int \mathcal{A}(t)\mathrm{d}t\right) \int \exp\left(-\int \mathcal{A}(t)\mathrm{d}t\right) \mathcal{B}(t)\mathrm{d}t. \tag{4.53}$$

Therefore, λ_ω is always zero in an inviscid flow with $\mathcal{B} = 0$. In viscous TG and KP flows, although $\mathcal{B}(t = 0) = 0$ for both TG and KP initial conditions, the transport equation for $\nabla\phi \cdot \nabla^2\boldsymbol{\omega}$,

$$\frac{\mathrm{D}}{\mathrm{D}t}(\nabla\phi \cdot \nabla^2\boldsymbol{\omega}) = \left(\frac{\partial}{\partial t}\nabla^2\boldsymbol{\omega} + \nabla \times (\nabla^2\boldsymbol{\omega} \times \boldsymbol{u})\right) \cdot \nabla\phi \tag{4.54}$$

implies that $|\mathcal{B}(t)| > 0$ and then $|\lambda_\omega(t)|$ should increase with time after $t = 0$. The relative error can be defined by the normalized deviation angle between the tangent plane and the vorticity at each of its points on the iso-surface of ϕ

$$\Delta\chi = (1 - 2|\chi|/\pi) \times 100\%, \quad |\chi| \le \pi/2. \tag{4.55}$$

The time evolution of the volume-averaged quantity $\langle|\lambda_\omega|\rangle$ in TG and KP flows is plotted in figure 4.7. Here, $\langle|\lambda_\omega|\rangle$ for the KP flow is computed only in the region with $\hat{\phi} \ge 10^{-3}$ to avoid the effect of errors in the approximate solution ϕ_{KP} at small contour levels on the evolution of $|\lambda_\omega|$. Here, the normalized iso-contour level is defined by

$$\hat{\phi} = \phi/|\phi|_{max}. \tag{4.56}$$

Exponential increase of $\langle|\lambda_\omega|\rangle$ is observed in both flows at different Reynolds numbers, and $\langle|\lambda_\omega|\rangle$ in a low-Re flow grows faster than in a high-Re flow due to the effect of viscosity. However, the errors before $t = 4$ in the TG flow at $Re = 1600$, and $t = 2$ in the KP flow at $Re = 1000$ are relatively small ($\Delta\chi < 5\%$). Therefore, we may reasonably assume that vortex surfaces are still well approximated by Lagrangian surfaces at the early stages of both high-*Re* flows because the vortex dynamics in high-*Re* flows are essentially inviscid (Brachet et al., 1983).

All vortex surfaces at the initial time are simply connected closed surfaces in TG and KP flows. In viscous flows, this topology will be maintained until vortex reconnection. The issue of formation of a finite-time singularity for an inviscid Euler flow remains an important open question (see Majda & Bertozzi, 2001). Without assuming singularity formation for an inviscid flow, we will nonetheless subsequently use the symbol t^* to refer to estimates of possible singularity formation time for both TG and KP initial conditions. According to Brachet et al. (1992) and Boratav & Pelz (1994), $t^* \approx 4$ and $t^* \approx 2$ for inviscid TG and KP flows, respectively. As pointed out in Kida & Takaoka (1994), vortex reconnection in the inviscid limit requires the occurrence of a finite-time singularity, which suggests that violent topological changes may occur at about t^* in a viscous flow. The topology, however, is invariant for Lagrangian structures. This contradiction appears to lead to noticeable errors ($\Delta\chi$ is around or larger than 5%) near or after t^* in figure 4.7.

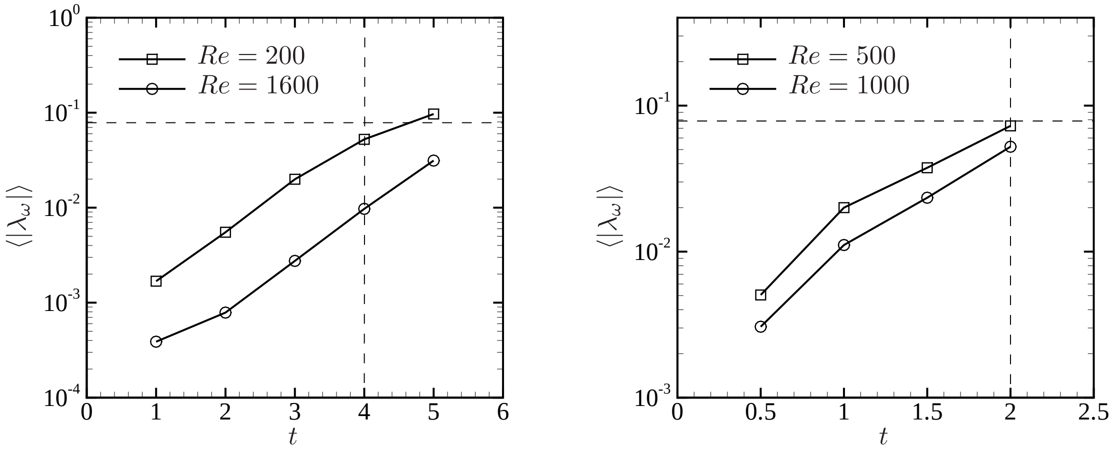

(a) TG flow

(b) KP flow

Figure 4.7: Temporal evolution of the volume-averaged $|\lambda_\omega|$. The horizontal dashed line denotes the relative error $\Delta\chi = 5\%$ and the vertical dashed line denotes the approximate potential singularity time t^*

The PDF of $|\lambda_\omega|$ in a TG flow at $Re = 1600$ (figure 4.8(a)) shows that the distribution of the deviation $|\lambda_\omega|$ at later times, $t = 4$ and $t = 5$, is intermittent. To investigate the source of the error, $|\lambda_\omega|$ conditioned on the scalar gradient $|\nabla\phi|$ is plotted in figure 4.8(b). When the scalar gradient is high, the deviation is also large accordingly. This observation emphasizes the distinction between Lagrangian surfaces and vortex surfaces when they are in close vicinity within a viscous flow. The topologically invariant Lagrangian surfaces cannot reconnect whereas vortex surfaces can change topology during a reconnection event. The latter then leads to increases in $|\lambda_\omega|$, corresponding to tilting of the vorticity vector off the Lagrangian surface, which are correlated with the corresponding increases of $|\nabla\phi|$ within the Lagrangian field.

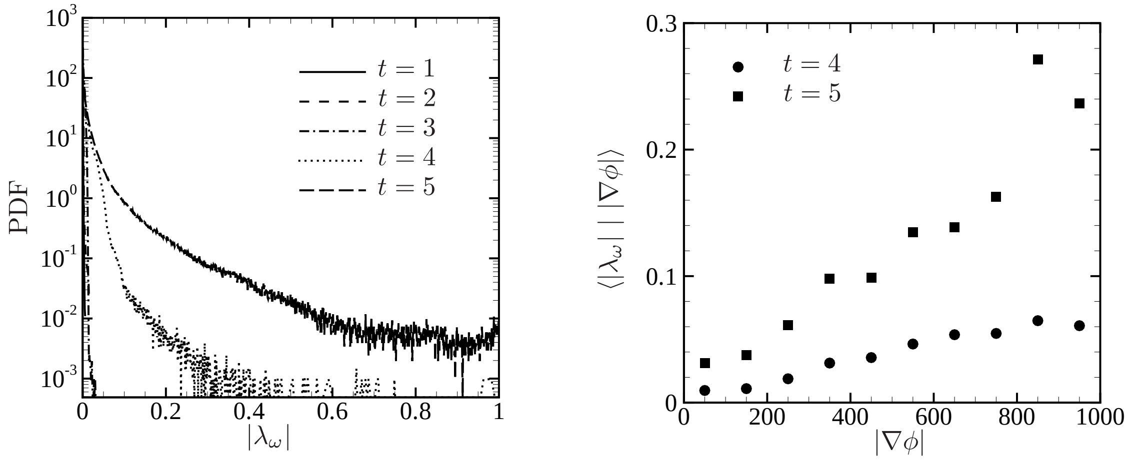

Figure 4.8: PDFs of $|\lambda_\omega|$ at different times (left) and the conditional mean of $|\lambda_\omega|$ on $|\nabla\phi|$ (right) in the TG flow at $Re = 1600$

On the basis of our error estimation, we will next assume that Lagrangian structures that were initially vortex surfaces in high-Re flows, e.g., the TG flow at $Re = 1600$ and the KP flow at $Re = 1000$ can, before t^*, be approximated as vortex surfaces with relative error $\Delta\chi < 5\%$. The temporal evolution of cross-sections of a set of vortex surfaces from two views in the TG flow at $Re = 1600$ represented by contour lines of $\phi(\boldsymbol{x}, t)$ are shown in figures 4.9 and 4.10. The initially blob-like vortex surfaces are progressively distorted into sheet-like surfaces and neighboring vortex surfaces approach each other. We observe that the thickness of vortex surfaces and the minimum distance between neighboring ones decay from $t = 0$ to $t = 4$. The latter produces high gradients of ϕ near $t = t^*$ and suggests the onset of vortex reconnection in the viscous flow.

After $t = t^*$, in figure 4.11 we plot two y–z plane-cuts at $x = \pi/16$ in the fundamental box with resolution 8192^2 for the periodicity box. These show more complicated multi-layered spiral Lagrangian surfaces in the TG flow at the later stages of the numerical simulation. The extremely large $|\nabla\phi|$ generated within these spiral layers is an example of the exponentially small structures produced within the evolving Lagrangian field. The Lagrangian surfaces can then no longer be considered as a good approximation to vortex surfaces.

For long times, both TG and KP flows become decaying turbulence after transitions (Brachet et al., 1983; Boratav & Pelz, 1994). The preferred alignment between the passive scalar gradient and the most compressive strain direction of $\boldsymbol{S}$ in turbulence implies that $\langle \boldsymbol{n}_\phi \cdot \boldsymbol{S} \cdot \boldsymbol{n}_\phi \rangle < 0$, and the preferred alignment between the vorticity and the intermediate stretching strain direction of $\boldsymbol{S}$ implies that $\langle \boldsymbol{n}_\omega \cdot \boldsymbol{S} \cdot \boldsymbol{n}_\omega \rangle > 0$ (e.g., Ashurst et al., 1987; Ruetsch & Maxey, 1992). Thus, in (4.52) and (4.53), statistically $\mathcal{A}(t) < 0$ and $\mathcal{B}(t) \sim O(\nu R_\omega)$ for a long time. Using dimensional analysis,

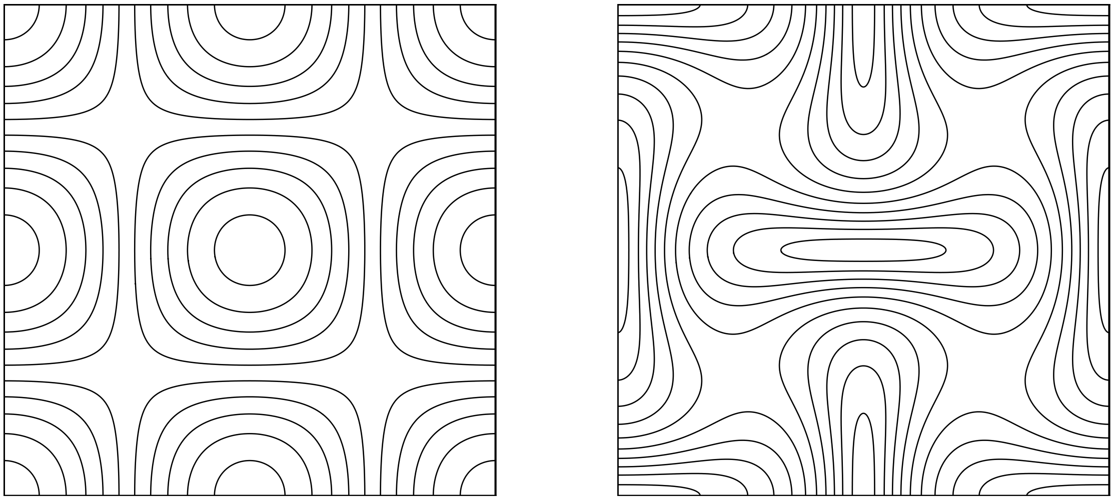

(a) $t = 0$ (b) $t = 1$

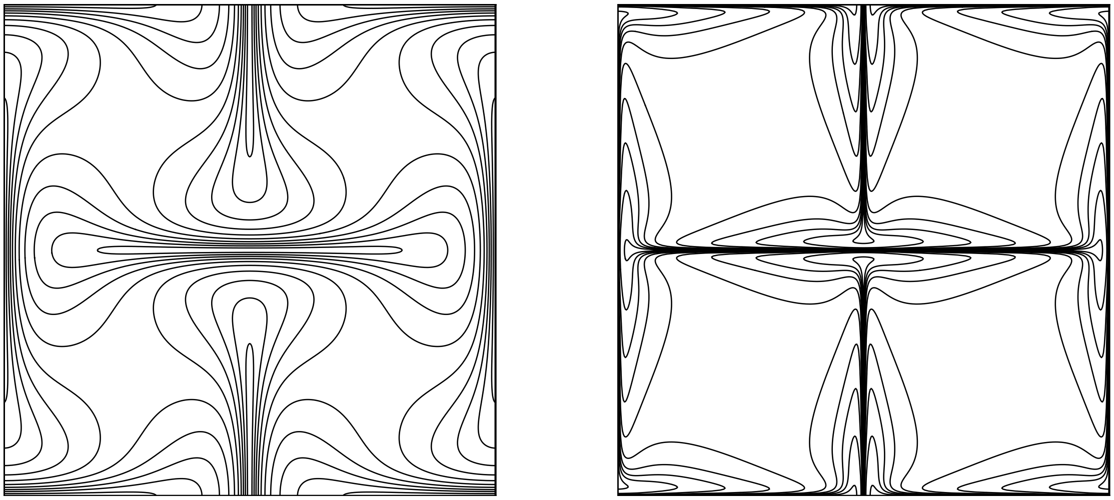

(c) $t = 2$ (d) $t = 4$

Figure 4.9: Iso-contour lines of $\hat{\phi} = \{\pm 0.1, \pm 0.3, \pm 0.5, \pm 0.7, \pm 0.9\}$ on the x–y plane-cut at $z = 0$ in the periodicity box for the TG flow at $Re = 1600$

at a moderate Reynolds number, we can obtain an estimate for the inhomogeneous term as

$$\mathcal{B}(t) \sim \epsilon / E, \tag{4.57}$$

where the total energy of flow $E = |\boldsymbol{u}|^2/2$. This implies that, as shown in figure 4.7(a) and figure 4.12, the evolution of $|\lambda_\omega|$ with the initial VSF $|\lambda_{\omega 0}| = 0$ increases exponentially in the early stage of evolution owing to violation of the Helmholtz theorem in a viscous flow, whereafter the increasing trend is mitigated at later times. Finally, this appears to move towards a stationary stage, which might be controlled by $O(\mathcal{B}(t))$, as shown in figure 4.12 and implied in (4.53). In contrast, § 2.4

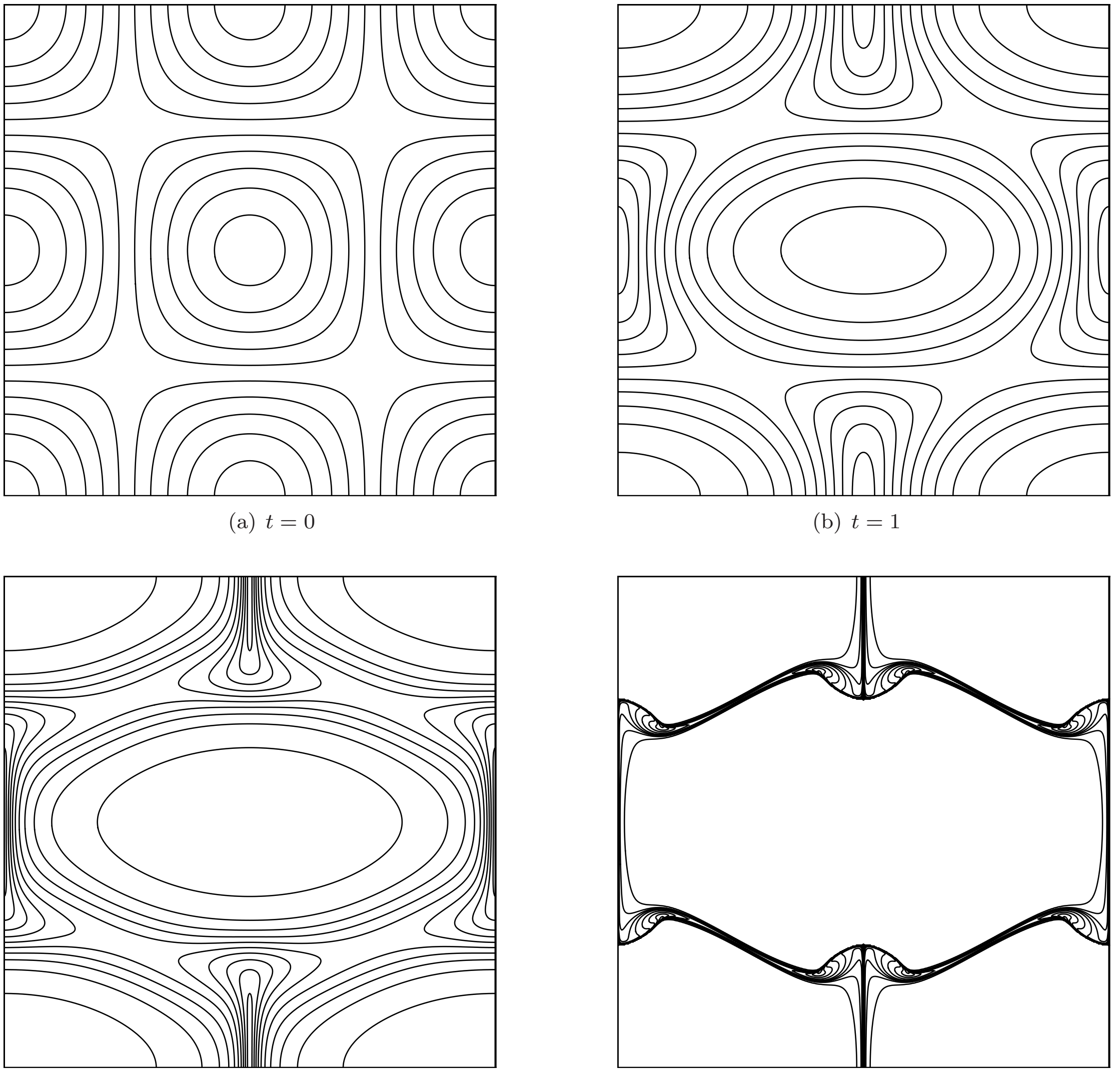

(a) $t = 0$

(b) $t = 1$

(c) $t = 2$

(d) $t = 4$

Figure 4.10: Iso-contour lines of $\hat{\phi} = \{\pm 0.1, \pm 0.3, \pm 0.5, \pm 0.7, \pm 0.9\}$ on the x–z plane-cut at $y = 0$ in the periodicity box for the TG flow at $Re = 1600$

showed that a Lagrangian field, starting from an arbitrary initial condition with a moderate $|\lambda_{\omega 0}|$ in stationary isotropic turbulence, appeared to exhibit a tendency to move towards a VSF of the evolving flow, but this is mitigated by cumulative viscous effects. In the TG flow, from an arbitrary initial Lagrangian field $\phi_0 = \sin x \sin y \sin z$, we also observed a similar decreasing trend for $|\lambda_\omega|$ in figure 4.12. Together, these results suggest that there may exist an intermediate state or 'attractor' for the long-time behavior of the alignment angle between $\boldsymbol{\omega}$ and $\nabla\phi$ with different initial scalar fields.

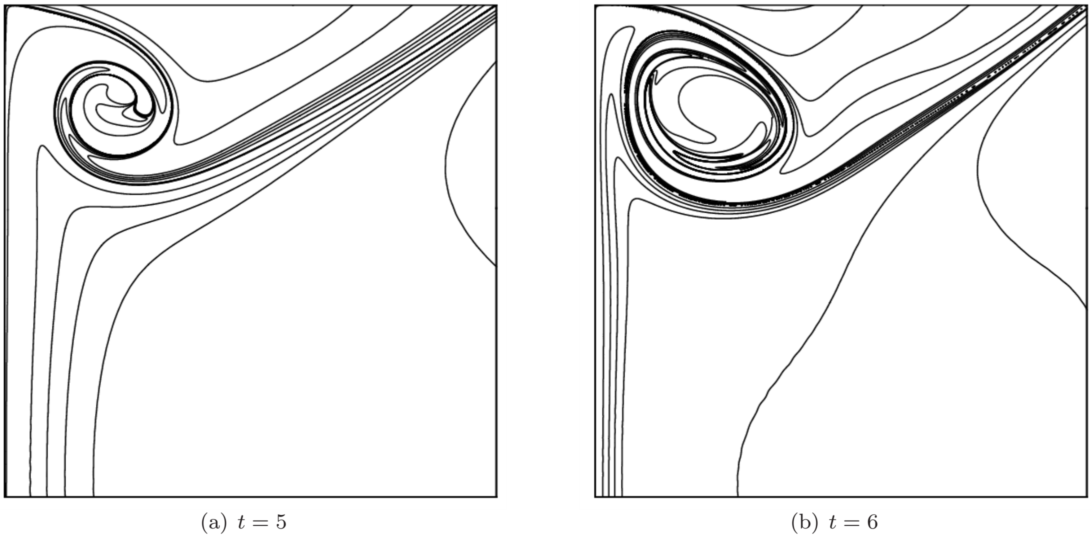
(a) $t = 5$ (b) $t = 6$

Figure 4.11: Iso-contour lines of ϕ on the y–z plane-cut at $x = \pi/16$ in the fundamental box for the TG flow at $Re = 1600$

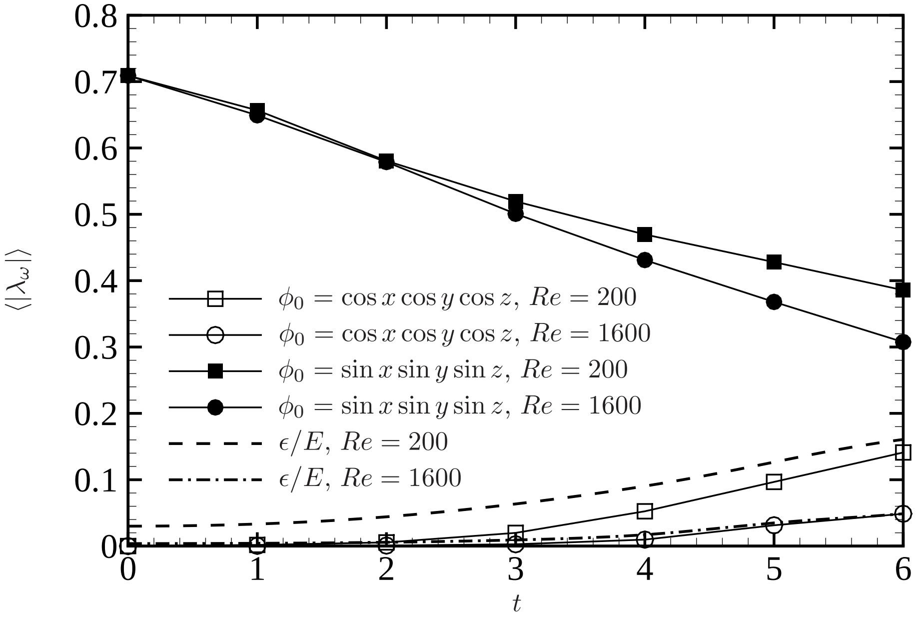

Figure 4.12: Temporal evolution of the volume-averaged $|\lambda_\omega|$ in the TG flow with the initial VSF $\phi_0 = \cos x \cos y \cos z$ and an arbitrary initial condition $\phi_0 = \sin x \sin y \sin z$

4.5.2 Geometry of vortex surfaces in evolution

The geometry in evolution of vortex lines and surfaces is important for quantifying local vorticity growth and subsequent instability phenomenon and transition in flows with smooth initial conditions.

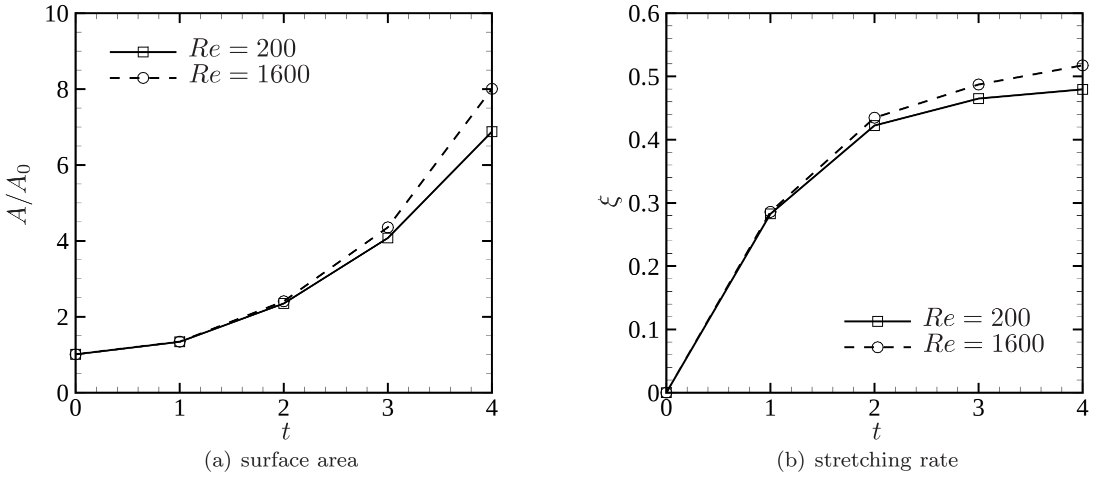

(a) surface area (b) stretching rate

Figure 4.13: Exponential growth of the surface area of vortex surfaces in the TG flow

The collective geometry properties of vortex surfaces at a particular time were presently obtained by taking an average over iso-surfaces of ϕ at contour levels $\hat{\phi} = 0.1, 0.2, ..., 0.9$. Since the volume of vortex surfaces is conserved, the surface area $A(t)$ will increase with time in evolution by stretching. The exponential growth of the normalized surface area A by the initial area A_0, averaged as described above, is shown in figure 4.13(a) and the corresponding stretching rate ξ defined in (2.23) is shown in figure 4.13(b). It is apparent that in the high-Re flow, the stretching rate is higher than the low-Re flow after $t \approx 2$, indicating that the flattening process of vortex surfaces is faster in the higher Re flow.

In addition to the surface area growth, measures of curvature on the Lagrangian surface can characterize the local topology. To quantify the non-local geometry (in the surface sense), we utilize two differential geometry properties, the absolute value of the shape index S and dimensionless curvedness C defined in (2.53). The local topology can be represented by S where $0 \leq S \leq 1$. An umbrella-like shape, e.g., the spherical cap or dome, is represented by high S; a parabolic shape, e.g., a ridge, is represented by medium S; and a hyperbolic shape, e.g., a symmetrical saddle or a saddle ridge, is represented by low S (Koenderink & Van Doorn, 1992). The evolution of three-dimensional vortex surfaces is visualized in figure 4.14. The corresponding area-based joint PDFs of S and C, with color intensity to express the joint PDF from low to high, are shown below the corresponding visualization of vortex surfaces. The non-local geometry of the surface can be represented by the feature centers ($\hat{S}$, $\hat{C}$) marked by ⊞ in figure 4.14, which are respectively dimensionless forms of the weighted first-order moments of the joint PDF of S and C. For details, a number of representative shapes and the corresponding S–C joint PDFs are shown in figure 13 in Bermejo-Moreno & Pullin (2008). The S–C joint PDF at $t = 4$ in figure 4.14 shows that the distribution of C is intermittent. Most surface elements are very flat with low curvatures except for a small number of elements with very high curvatures. From figure 4.14(d), we can see very thin and flat large-scale structures in the middle surrounded by thin edges with very sharp corners. There is a preponderance of surface elements on the vortex surface with hyperbolic or parabolic shapes near t^*, while most shapes of elements at the early stage are umbrella-like or parabolic. This observation is also visualized as the appearance of rolled-up structures at the edge of the vortex surface in figure 4.14(d).

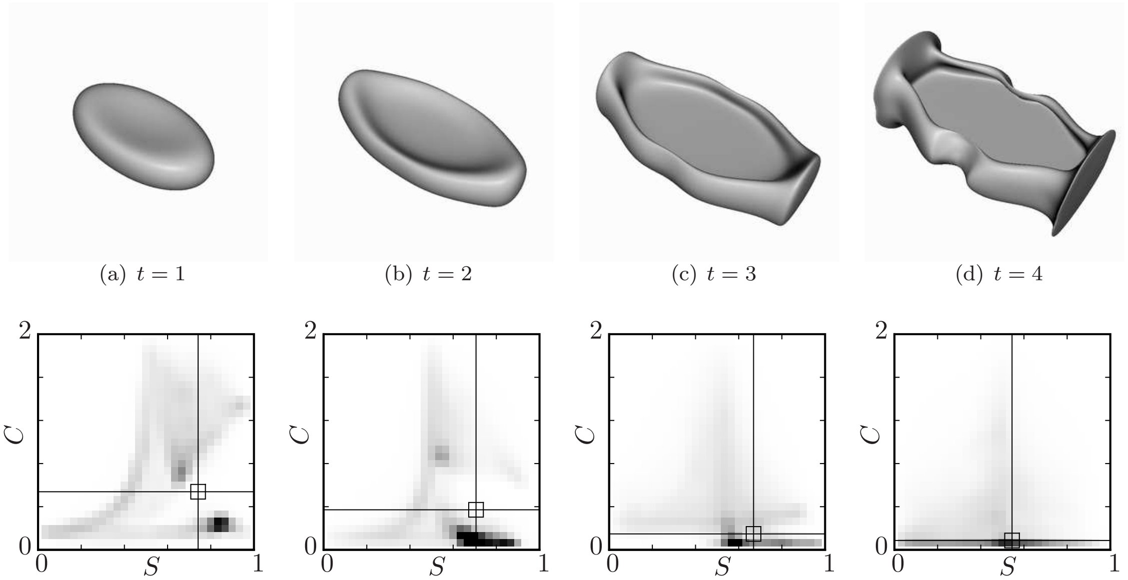

(a) $t = 1$ (b) $t = 2$ (c) $t = 3$ (d) $t = 4$

Figure 4.14: Vortex surfaces (iso-surfaces of $\hat{\phi} = 0.4$) in the TG flow at $Re = 1600$ and corresponding feature centers $(\hat{S}, \hat{C})$ are marked by ⊞ in S–C joint PDFs at the bottom

To quantify these observations in the evolution, $\langle \hat{C} \rangle$ and $\langle \hat{S} \rangle$ are averaged over vortex surfaces at nine contour levels from 0.1 to 0.9 in the TG flow at $Re = 1600$. As shown in figure 4.15(a), we can see that the averaged curvedness $\langle \hat{C} \rangle$ of vortex surfaces decreases exponentially with increasing time, which shows the strong flattening process of vortex surfaces corresponding to the growth of surface area, but in the sense of curvatures of surfaces. From figure 4.15(b), we find the averaged absolute value of the shape index $\langle \hat{S} \rangle$ appears to decrease with time and the value approaches to 0.5 at $t = 4$. Furthermore, lower $\langle \hat{C} \rangle$ and $\langle \hat{S} \rangle$ are obtained in the high-Re flow. This indicates that the vortex surfaces in the high-Re flow tend to be more nearly singular than those in the low-Re flow, which may imply extreme, near-singular structures in the inviscid flow when $t \to t^*$.

4.5.3 Relations between vortex-surface fields and vorticity fields

As shown in figure 4.16, the geometry of vortex surfaces differs from that of the iso-surfaces of vorticity magnitude in the TG flow. In particular, in figure 4.16(b), the 'vorticity pancakes' represented by the high vorticity regions as shown in Brachet et al. (1992) appear to be generated between neighboring vortex surfaces when they approach each other. The sheet-like structure of

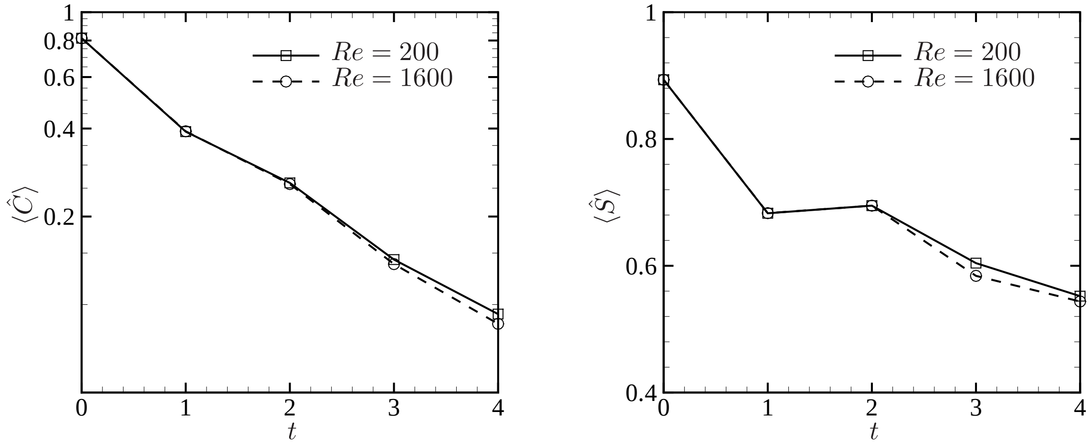

Figure 4.15: Averaged feature centers $\langle\hat{C}\rangle$ and $\langle\hat{S}\rangle$ at different times in the TG flow

the high vorticity region in simulations with other initial conditions (e.g., Pumir & Siggia, 1990; Kerr, 1993) could be induced by the similar approaching process of paired vortices. Referring to figure 4.10, vortex surfaces appear to reveal strong dynamics in the evolution of vortical structures, including stretching and subsequent roll-up. Since, for inviscid flow, a vortex surface is topologically invariant, tracking the Lagrangian structure unfolds a continuous dynamic process. In contrast, the vorticity-magnitude iso-surface obeys no continuous dynamical form. Its instantaneous geometry thus results in many segmented structures with less implications for dynamics.

Compared with the TG flow, the vortex surface in the KP flow shows more interesting vortex dynamics in producing predominant large-scale spiral signatures. The evolution of eight vortex surfaces which lie in the x–y plane with $-\pi/2 \le x, y \le \pi/2$ at $z = 0$ is shown in figure 4.17 and the corresponding cross-sections of vortex surfaces are shown in figure 4.18. At the initial time, eight head-to-tail connected (without contact) vortex surfaces form a ring. The neighboring vortex surfaces are not shown for clarity. We remark that, at a particular iso-contour level, there are 192 vortex surfaces with certain symmetries in the box with $-\pi/2 \le x, y, z \le 3\pi/2$. We can find two evolutionary geometries of vortex surfaces in the KP flow, which are, respectively, represented by white and black in figure 4.17. The blob-like vortex surfaces are progressively distorted into two types of shell-like shapes. As shown in figure 4.17(d), each white vortex surface is wrapped by a black one and connected with another black one. The rolled-up structure will appear at the edge of vortex surfaces as indicated in figure 4.18(d). From the iso-contour lines in figure 4.18, we can see that the geometry of vortex surfaces is more regular than the vorticity contour lines shown in Boratav & Pelz (1994) and better exemplify the vortex dynamics. All the vortex surfaces are wound in the clockwise direction on the x–y plane-cut at $z = 0$. In figure 4.18(d), multi-layered structures are generated at the joint of vortex surfaces at the later stages of our simulation.

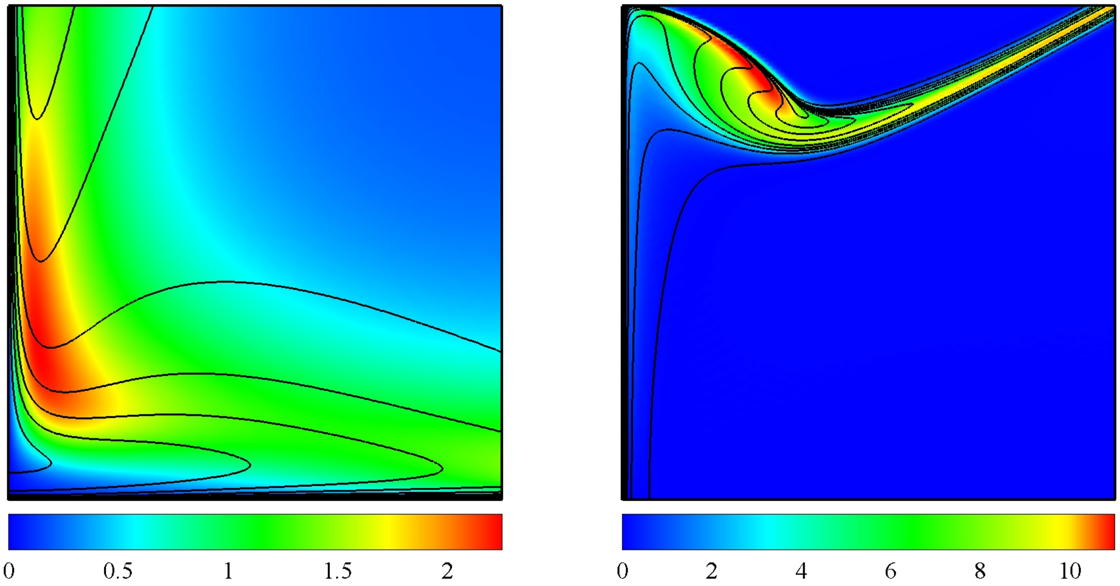

(a) x–y plane-cut at $z = 0$ (b) y–z plane-cut at $x = 0$

Figure 4.16: Relations between vortex surfaces and vorticity fields at $t = 4$ in the TG flow at $Re = 1600$. Vortex surface cross-sections are expressed by contour lines of ϕ and the magnitude of $|\boldsymbol{\omega}|$ in shadings on the plane-cuts in the fundamental box

The accumulation of vorticity may be related to the local geometry of vortex surfaces. Using a two-dimensional analogy, Constantin et al. (1994) found that rapid growth of vorticity appears to be induced at hyperbolic saddles of vortex lines. By solving the Euler–Lagrange equations for the associated variational problem, Lu & Doering (2008) observed that vorticity is concentrated at the same place where vortex stretching occurs in a three-dimensional flow with the estimation of the maximum enstrophy growth rate. From figure 4.16(b) and figure 4.19, local hyperbolic or stretched shapes are also observed in the vicinity of high vorticity regions in the present three-dimensional flows. This suggests that highly localized vorticity intensification may be produced by the roll-up of vortex surfaces induced by non-parallel stretched vortex lines that comprise them. Thus, in terms of vortex-surface evolution, transition from the smooth initial flow condition to a flow state with almost-singular structures, or even subsequent turbulent flow, can perhaps be understood in the following scenario: initially, blob-like vortices are stretched and they approach each other. The edges of stretched vortex surfaces are then gradually rolled up. Very high vorticity appears within the rolled-up structures at their edges and at the interface between neighboring vortex surfaces. The hyperbolic structures near the high vorticity regions might then become more unstable by viscosity-induced instabilities. This scenario is observed in the experiment of the head-on collision of two vortex rings (e.g., Lim & Nickels, 1993), in which the role of the dye is analogous to the vortex-surface scalar field used in the present study to identify the vortical structures in the Lagrangian sense.

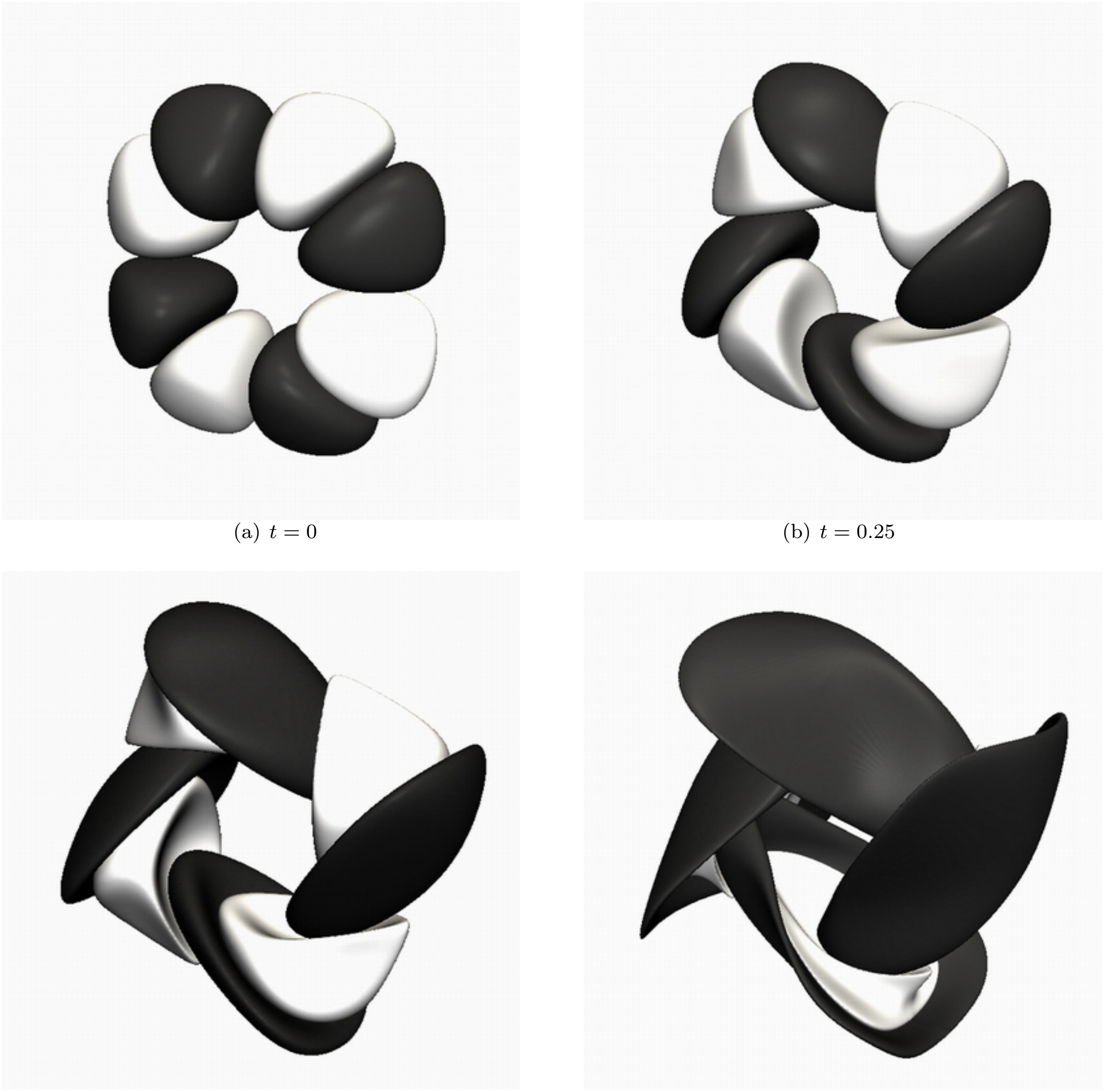
(a) $t = 0$
(b) $t = 0.25$
(c) $t = 0.5$
(d) $t = 1$

Figure 4.17: Vortex surfaces (iso-surfaces of $\hat{\phi} = \pm 0.015$) in the KP flow at $Re = 1000$. These surfaces lie in the x–y symmetry plane at $z = 0$, where $-\pi/2 \le x, y \le \pi/2$

4.6 Results and discussion

In this study, we have developed a systematic methodology for the construction of VSFs for both TG and KP initial velocity–vorticity fields. The spatial constraint on a three-dimensional scalar field ϕ is converted to a system of linear homogenous equations with Fourier expansions. In particular, although it appears that an exact and unique ϕ for the KP flow with a finite set of Fourier modes cannot be found, we can construct a least-squares solution through an optimization problem with proposed basis functions that satisfy all KP symmetries. The somewhat elaborate scheme required to obtain vortex surfaces corresponding to the relatively simple KP initial vorticity field is surprising

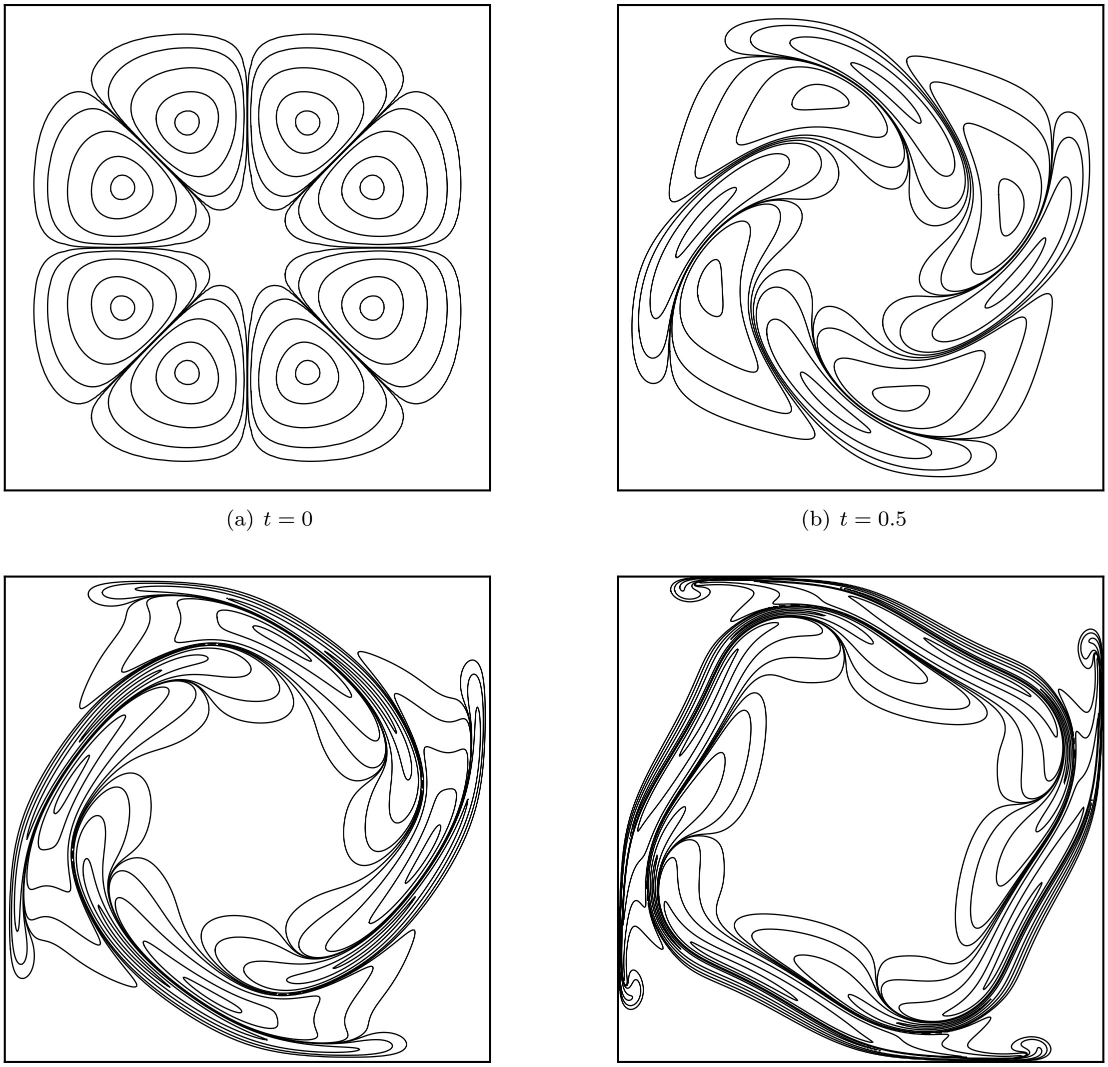
(a) $t = 0$ (b) $t = 0.5$ (c) $t = 1$ (d) $t = 1.5$

Figure 4.18: Iso-contour lines of $\hat{\phi} = \{\pm 0.001, \pm 0.01, \pm 0.1, \pm 0.5, \pm 0.9\}$ on the x–y plane-cut at $z = 0$ in the impermeable box for the KP flow at $Re = 1000$

and unexpected. We remark that the methodology presented in § 4.2 may not be applicable for every spatially periodic Eulerian vorticity field, for example, the nonintegrable ABC flow. The TG and KP flows are periodic and have relatively simple topology. All their vortex lines are closed and unknotted at the initial time. General three-dimensional periodic vorticity fields could exhibit such complex topologies that a ϕ, even itself non-spatially periodic, which satisfies the constraint (4.3), may not in general exist. This appears to be an open problem. In addition, the relations and differences between VSFs and the classical Clebsch representation are discussed.

The evolution equations of the VSF in both inviscid and viscous incompressible flows are derived in § 4.3. In the inviscid case, with a well-defined initial VSF, the VSF is equivalent to the Lagrangian

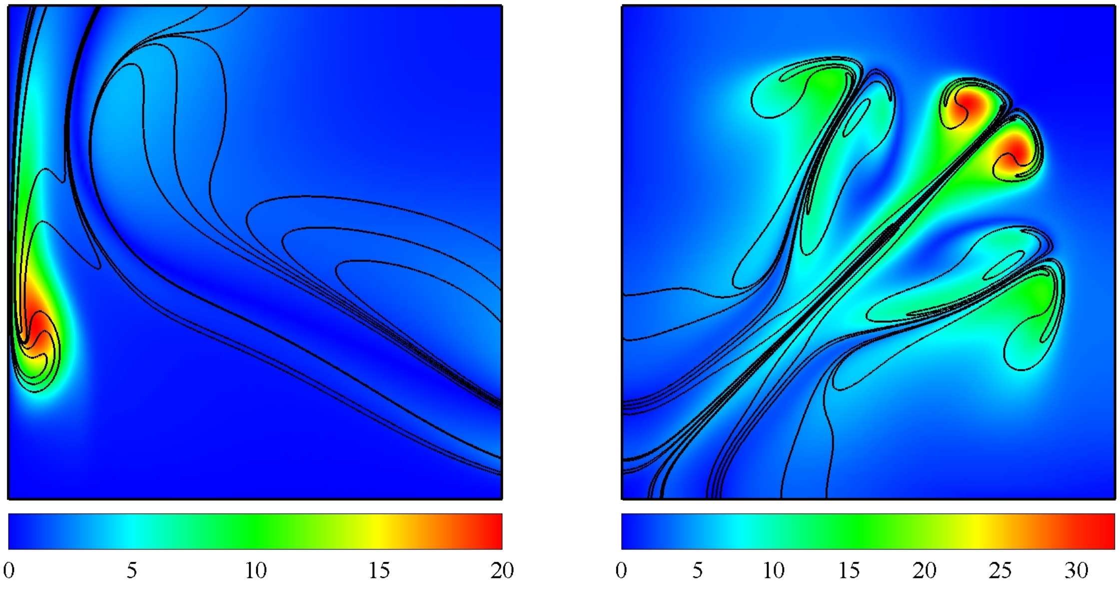

(a) x–y plane-cut at $z = 0$ (b) x–y plane-cut at $z = \pi/2$

Figure 4.19: Relations between vortex surfaces and vorticity fields at $t = 1.5$ in the KP flow at $Re = 1000$. Vortex surface cross-sections are expressed by contour lines of ϕ and the magnitude of $|\boldsymbol{\omega}|$ in shadings on the plane-cuts in the fundamental box

field and the nonuniqueness of the solution exists only up to relabeling. In the viscous case, solutions of equations describing a VSF, if they exist, are showed to be nonunique.

From our quantitative estimates, the relative error of vortex surfaces as Lagrangian surfaces is typically less than 5% in high-Reynolds-number TG and KP flows prior to times typical of a potential singularity time t^*. The error appears to be mainly associated with the topological constraint that prevents reconnection of Lagrangian structures, except possibly at singularities in a strictly Euler flow. This has the consequence that, for slightly viscous flows, vortex surfaces can be well approximated as Lagrangian structures prior to vortex reconnection. In temporal evolution, initial blob-like vortex surfaces are progressively stretched to sheet-like shapes so that neighboring vortex surfaces approach each other. This flattening process of vortex surfaces is quantified by the growth rate of the surface area and the averaged curvedness $\langle \hat{C} \rangle$. The local topology of vortex surfaces is well represented by the averaged absolute value of the shape index $\langle \hat{S} \rangle$, which indicates that more local hyperbolic shapes on the surfaces appear near a potential t^* than at the early stages of the evolution. We observed that local rolled-up shapes are predominantly located in the vicinity of high vorticity regions, which might be related to the subsequent transition to turbulence. Furthermore, visualization of the evolution of vortex surfaces shows a continuous dynamic process of vortex roll-up with certain symmetries, which was not observed in visualizations of iso-surfaces of vorticity magnitude.

An interesting problem suggested by the present study is the development of general numerical methods for the identification and tracking vortex surfaces in other flows, including viscous flows. In particular, the identification of vortex surfaces in vortex reconnection is important but challenging (Kida & Takaoka, 1994). This issue will be addressed in § 5. In addition, recent progress on the computation of invariant manifolds (e.g., see Krauskopf et al., 2005; Branicki & Wiggins, 2009) may shed light on the construction or identification of vortex surfaces. Another extension of the present study may address the relationship between the geometry of vortex surfaces and potential finite-time singularity in Euler flows (see Hou & Li, 2008). This, however, requires much higher resolution for both the Eulerian velocity field and the Lagrangian field than is employed presently. An adaptive mesh for ϕ in the Euler flow should be considered owing to the intermittently distributed nearly singular structures in vortex surfaces close to a potential t^*. Finally, the evolution of vortex surfaces may provide a reference for the development of vortex dynamics in a Lagrangian framework and new objective criteria for identifying vortical structures.

Chapter 5

Evolution of vortex-surface fields in viscous Taylor–Green and Kida–Pelz flows

5.1 Background and objectives

Conceptual vortex tubes and sheets have long been utilized as basic vortical structures or elements of the vortex-dynamic paradigm in fluid mechanics (e.g., Saffman, 1992; Batchelor, 1967). In particular, intermittency in high-Reynolds-number turbulence has been hypothesized to be related to the organized vortical structures with candidate tube-like or sheet-like geometries (see Pullin & Saffman, 1998). In a general sense, an open or closed vortex surface can be defined as a smooth surface or manifold embedded within a three-dimensional velocity field, which has the property that the local vorticity vector is tangent at every point on the surface. Although coherent bundles of vortex lines with strong vorticity and tube-like geometry have been observed (e.g., She et al., 1990; Jimenez et al., 1993) and analyzed (see Constantin, Procaccia & Segel, 1995) in turbulence, the existence of globally smooth vortex surfaces in general three-dimensional flows remains an open problem. Within the Clebsch representation (see Lamb, 1932; Truesdell, 1954), in § 4 we defined a vortex-surface field (VSF) as a smooth scalar field whose iso-surfaces are vortex surfaces and developed VSFs for both initial TG (see Taylor & Green, 1937; Brachet et al., 1983) and KP (see Kida, 1985; Boratav & Pelz, 1994) velocity fields which display simple topology and geometry.

For a strictly inviscid barotropic flow with conservative body forces, the Helmholtz vorticity theorem shows that Lagrangian material surfaces or Lagrangian fields which are vortex surfaces or VSFs, respectively, at time $t = 0$, remain so for $t > 0$. On the other hand, the breakdown of the frozen motion of vortex lines in viscous flow owing to violation of the Helmholtz theorem (e.g., Kida & Takaoka, 1994; Chen et al., 2006) underscores a fundamental problem associated with identifying vortex surfaces at different times in real flows and turbulence in particular. This can perhaps be interpreted as the root cause of numerical obstacles in the implementation of Lagrangian formulations of Navier–Stokes dynamics (e.g., Ohkitani & Constantin, 2003). As shown in § 4, although a Lagrangian field evolving from a VSF initial condition can provide an interesting approximation to a VSF for a short period in high-Reynolds-number flows, it cannot be used to identify signature topological changes in vortex lines or surfaces such as the vortex reconnection that is a crucial mechanism in turbulent transition and enstrophy generation (see Kida & Takaoka, 1994).

In this chapter, we consider the VSF evolution in viscous incompressible flows for which initial VSFs exist. Our examples are TG and KP flows. The level sets of a VSF at different times will be shown to reveal vortex dynamics in the sense of the geometry and topology of vortex surfaces. We begin in § 5.2 by obtaining equations governing VSFs for viscous incompressible flows. In § 5.3, we develop the numerical methods used presently for computing VSF evolution. The convergence properties of the proposed numerical scheme is then analyzed. The evolution of VSFs in both three-dimensional viscous TG and KP flows is presented in § 5.4 together with discussion of the corresponding vortex dynamics. Some conclusions are drawn in § 5.5.

5.2 Theoretical framework of the vortex-surface field

5.2.1 Governing equations

In a three-dimensional incompressible viscous flow, the velocity field is determined by the Navier–Stokes equations (4.48) with appropriate initial and boundary conditions. The definition of a VSF $\phi_v(\boldsymbol{x}, t)$ requires that the cosine of the angle between the vorticity $\boldsymbol{\omega}$ and $\nabla\phi_v$ satisfies

$$\lambda_\omega \equiv \frac{\boldsymbol{\omega} \cdot \nabla\phi_v}{|\boldsymbol{\omega}||\nabla\phi_v|} = 0, \tag{5.1}$$

pointwise within the domain of interest for all time. If (5.1) holds uniformly within the domain at $t = 0$ then the temporal evolution of the VSF is described for $t \geq 0$ by (4.32), where the material derivative is defined as

$$\frac{\mathrm{D}}{\mathrm{D}t} \equiv \frac{\partial}{\partial t} + \boldsymbol{u} \cdot \nabla.$$

From the equation of vorticity (2.30) and (4.32) and referring to the equation for the evolution of the Lagrangian field ϕ (2.15), in § 4.3 we obtained the equations governing the VSF ϕ_v as (4.41) and (4.42). In principal, given the evolution of $\boldsymbol{u}$ and $\boldsymbol{\omega}$, one can solve (4.41) for ϕ_v, where, at each t the function $\mathcal{L}$ is given by the solution of the hyperbolic partial differential equation (4.42). We show in appendix B, however, that a necessary condition for the existence and uniqueness of solutions to equations of the type (4.42) is not satisfied (see Mingyu et al., 1997). Hence, this approach explicitly fails for the computation of VSF evolution.

5.2.2 Restoration of uniqueness and approximate numerical solutions

To restore uniqueness we introduce a time-like variable τ, with the dimension [time/length], and let $\phi_v = \phi(\boldsymbol{x}, t; \tau)$ and $\mathcal{L} = \mathcal{L}(\boldsymbol{x}, t; \tau)$. We seek solutions

$$\phi_v = \lim_{\tau\to\infty} \phi_v(\boldsymbol{x}, t; \tau) \quad \text{and} \quad \mathcal{L} = \lim_{\tau\to\infty} \mathcal{L}(\boldsymbol{x}, t; \tau), \tag{5.2}$$

where $\mathcal{L}(\boldsymbol{x}, t; \tau)$ satisfies

$$\frac{\mathrm{D}}{\mathrm{D}t}(\boldsymbol{\omega} \cdot \nabla\phi_v) + \nu\frac{\partial\mathcal{L}}{\partial\tau} = 0, \tag{5.3}$$

for all $\boldsymbol{x}$ at fixed t. Equation (5.3) now replaces (4.32). From (2.30), (4.41), and (5.3) it can be then be shown that

$$\frac{\mathcal{D}\mathcal{L}}{\mathcal{D}\tau} = -\nabla\phi_v \cdot \nabla^2\boldsymbol{\omega}, \tag{5.4}$$

where the left-hand side is expressed in terms of the pseudo material-like 'vorticity' derivative defined as

$$\frac{\mathcal{D}}{\mathcal{D}\tau} \equiv \frac{\partial}{\partial\tau} + \boldsymbol{\omega} \cdot \nabla \tag{5.5}$$

based on the pseudo time τ and the frozen vorticity $\boldsymbol{\omega}(\boldsymbol{x}, t)$ at fixed t.

Now consider

$$\frac{\mathcal{D}\phi_v}{\mathcal{D}\tau} = Q, \tag{5.6}$$

where Q is a function to be chosen subsequently. Differentiating (4.41) with respect to τ and (5.6) with respect to t and equating expressions for $\partial^2\phi_v(\boldsymbol{x}, t; \tau)/(\partial t\partial\tau)$ with $\partial\boldsymbol{u}(\boldsymbol{x}, t)/\partial\tau = 0$ then yields

$$\frac{\partial}{\partial t}(\boldsymbol{\omega} \cdot \nabla\phi_v) + \nu\frac{\partial\mathcal{L}}{\partial\tau} = \frac{\partial Q}{\partial t} + \boldsymbol{u} \cdot \nabla\left(\frac{\partial\phi_v}{\partial\tau}\right). \tag{5.7}$$

From the above and using (5.3) and (5.6) we can obtain

$$\frac{\mathrm{D}}{\mathrm{D}t}(\boldsymbol{\omega} \cdot \nabla\phi_v) + \nu\frac{\partial\mathcal{L}}{\partial\tau} = \frac{\mathrm{D}Q}{\mathrm{D}t} = 0. \tag{5.8}$$

It seems that Q can be any Lagrangian field ϕ satisfying (2.15). In particular we can choose $Q = 0$, and then (5.6) becomes

$$\frac{\mathcal{D}\phi_v}{\mathcal{D}\tau} \equiv \frac{\partial\phi_v}{\partial\tau} + \boldsymbol{\omega} \cdot \nabla\phi_v = 0. \tag{5.9}$$

With $\boldsymbol{\omega}$ given at fixed t, (5.4) and (5.9) then define the evolution for $\tau > 0$ of $\phi_v(\boldsymbol{x}, t; \tau)$ and $\mathcal{L}(\boldsymbol{x}, t; \tau)$. While it is expected that integration forward in τ for these equations would lead to exponentially small structures as $\tau \to \infty$ without diffusion terms, they have unique viscosity solutions (Crandall & Lions, 1983) for given smooth initial conditions. Hence, we regularize both equations as

$$\frac{\mathcal{D}\mathcal{L}}{\mathcal{D}\tau} = -\nabla\phi_v \cdot \nabla^2\boldsymbol{\omega} + \epsilon\nabla^2\mathcal{L}, \tag{5.10}$$

$$\frac{\mathcal{D}\phi_v}{\mathcal{D}\tau} = \epsilon\nabla^2\phi_v, \tag{5.11}$$

where $\epsilon \ll 1$. At fixed t, the limit (5.2) can be obtained by solving (5.10) and (5.11) simultaneously. It remains to be demonstrated that this limit is 'steady' in τ.

5.3 Numerical overview

5.3.1 Numerical methods

The Navier–Stokes equations (4.48) in a periodic box of side 2π were computed by a standard pseudo-spectral method on a uniform grid N^3 for the Reynolds number $Re = 1/\nu$ in the period from $t = 0$ to $t = t_{max}$. The aliasing error was removed by use of a 16th-order exponential filter (Shu et al., 2005). The scalar equations (4.41) and (5.9) were advanced in t and τ, respectively, using the third-order TVD Runge–Kutta method and the convection terms were treated by the fifth-order weighted essentially non-oscillatory (WENO) scheme (Jiang & Shu, 1996). The time steps Δt and $\Delta\tau$ were chosen to ensure that the corresponding CFL numbers

$$\mathrm{CFL}_t = \frac{\Delta t}{\Delta x}\max(|u_x|,|u_y|,|u_z|) \qquad \text{and} \qquad \mathrm{CFL}_\tau = \frac{\Delta\tau}{\Delta x}\max(|\omega_x|,|\omega_y|,|\omega_z|),$$

for (4.41) and (5.9) were 0.5 or less for numerical stability and accuracy, where $\Delta x = 2\pi/N$. It is noted that $\Delta\tau$ could be much less than Δt when $|\boldsymbol{\omega}| \gg |\boldsymbol{u}|$ at some time.

For TG flows, the initial fields for (4.48) and (4.41) were chosen as

$$\boldsymbol{u}(\boldsymbol{x}, t = 0) = (\sin x\cos y\cos z, -\cos x\sin y\cos z, 0), \tag{5.12}$$

and

$$\phi_v(\boldsymbol{x}, t = 0) = (\cos 2x - \cos 2y)\cos z. \tag{5.13}$$

For KP flows, $\boldsymbol{u}(\boldsymbol{x}, t = 0)$ is given in (4.14) and $\phi_v(\boldsymbol{x}, t = 0)$ was obtained numerically in § 4.2.3 by an expansion based on optimal basis functions with the same octahedral symmetries as the KP initial field. In addition, the TG and KP symmetries (Brachet et al., 1983; Kida, 1985) were utilized to reduce the computational time and scale. Parameters of the runs in the present study are listed in table 5.1. As shown in figure 5.1, the dissipation rate ε in both flows increases at early time and approaches a peak after a finite time, which can indicate the transition from initial smooth flow to turbulent flow at high Reynolds numbers (Brachet et al., 1983; Boratav & Pelz, 1994).

Table 5.1: Parameters of the study for TG and KP flows

Run	TG1	TG2	TG3	TG4	TG5	KP1	KP2
Re	50	100	200	400	800	200	400
N^3	128^3	256^3	256^3	512^3	512^3	512^3	512^3
t_{max}	10	10	10	10	10	3	3

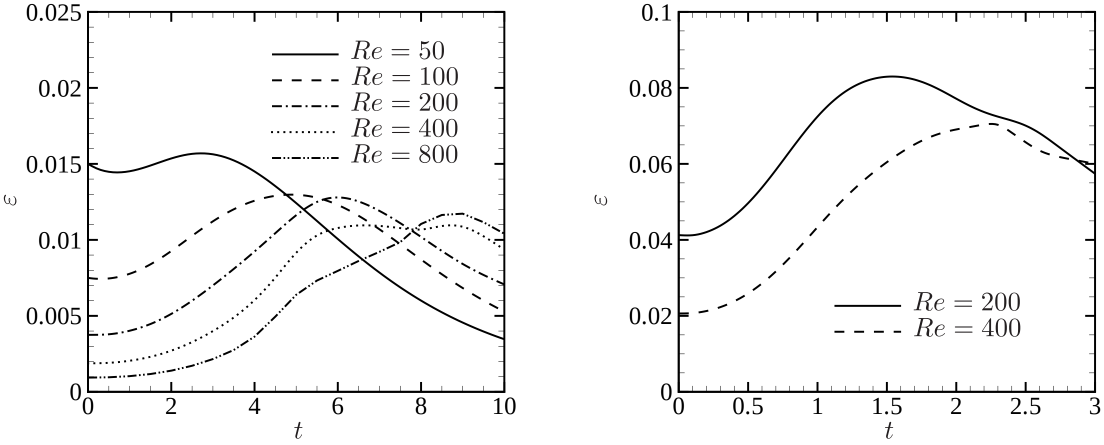

(a) TG flow

(b) KP flow

Figure 5.1: Dissipation rate

5.3.2 Numerical implementation for computing the vortex-surface field

The exact solution of the VSF satisfies (5.1) for all time. However, from (4.47) it appears that $|\nabla\phi_v|$ tends to become unbounded for long times in evolution even from a smooth initial field. In other words, we might not be able to find a globally smooth ϕ_v with a finite resolution for all time. Hence, we introduce a filtering or artificial dissipation mechanism for a smooth VSF in the evolution and at the same time keep the volume averaged $\langle|\lambda_\omega|\rangle$ as small as possible. It is noted that the implicit numerical viscosity in the finite-difference WENO scheme can keep $|\nabla\phi_v|$ finite as shown in (5.11), where $\epsilon = \epsilon_{\mathrm{WENO}}(\boldsymbol{x})$ depends on the smoothness of the discretized local ϕ_v that is determined by local $\nabla\phi_v$ and resolution N (Jiang & Shu, 1996). Other regularization methods, e.g., using an explicit numerical viscosity or a subgrid scale model for the diffusion term, would be also helpful to solve (5.11) with a finite resolution.

In the implementation, we solved (4.41) and (4.48) with $\mathcal{L} = 0$ simultaneously in time t. For each time step, only (5.11) was computed for a period $T_\tau = N_\tau\Delta\tau$ in the pseudo time τ to implicitly determine $\mathcal{L}$ in (4.42) by (5.8) rather than solving (5.10) and (5.11) simultaneously. This can avoid discretized errors for the term $\nabla\phi_v \cdot \nabla^2\boldsymbol{\omega}$ with high order derivatives in (5.10). Therefore, within a single time step the VSF was computed as

$$\frac{\partial \phi_v^*(\boldsymbol{x},t)}{\partial t} + \boldsymbol{u}(\boldsymbol{x},t)\cdot\nabla\phi_v^*(\boldsymbol{x},t) = \epsilon_{\mathrm{WENO}}(\boldsymbol{x},t)\nabla\phi_v^*(\boldsymbol{x},t), \quad t \geq 0, \tag{5.14}$$

and then at fixed time t

$$\frac{\partial \phi_v(\boldsymbol{x},t;\tau)}{\partial \tau} + \boldsymbol{\omega}(\boldsymbol{x},t)\cdot\nabla\phi_v(\boldsymbol{x},t;\tau) = \epsilon_{\mathrm{WENO}}(\boldsymbol{x},t;\tau)\nabla\phi_v(\boldsymbol{x},t;\tau), \quad 0 \leq \tau \leq T_\tau, \tag{5.15}$$

with

$$\phi_v(\boldsymbol{x},t;\tau=0) = \phi_v^*(\boldsymbol{x},t) \tag{5.16}$$

to obtain the approximate solution for (5.2). Finally, $\phi_v^*(\boldsymbol{x},t)$ in (5.14) is updated by $\phi_v(\boldsymbol{x},t;\tau=T_\tau)$ for every time step. As sketched in figure 5.2, (5.14) serves as the prediction step and (5.15) as the correction step.

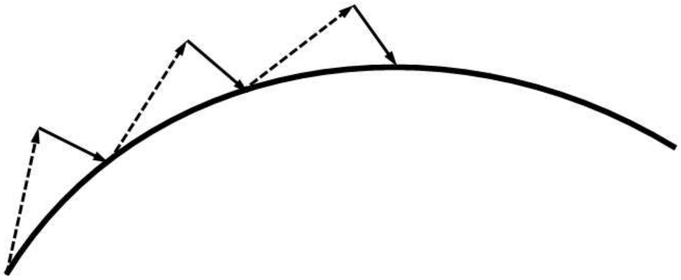

Figure 5.2: Sketch of the numerical implementation for computing the VSF. Solid curve: solution of the VSF; dashed arrow: prediction step (5.14); solid arrow: correction step (5.15)

5.3.3 Convergence of numerical solutions

For a fixed time t, finite $\langle|\lambda_\omega|\rangle$ could be generated in (5.14) because of the deviation between the temporary scalar field ϕ_v^* and the VSF ϕ_v, while $\langle|\lambda_\omega|\rangle$ can be reduced by using (5.15). Next we will analyze the convergence of the correction step (5.15) onto the approximate VSF.

Using (5.11) and $\partial\boldsymbol{\omega}(\boldsymbol{x},t)/\partial\tau = 0$ at fixed t, and following a line of analysis applied in §§ 2.4.3 and 4.5.1 to a Lagrangian field, we can show, after some algebra, that

$$\frac{\mathcal{D}|\nabla\phi_v|}{\mathcal{D}\tau} = \frac{1}{|\nabla\phi_v|}(-(\nabla\phi_v\cdot\boldsymbol{S}_\omega\cdot\nabla\phi_v) + \epsilon\nabla\phi_v\cdot\nabla^2\nabla\phi_v), \tag{5.17}$$

$$\frac{\mathcal{D}}{\mathcal{D}\tau}(\boldsymbol{\omega}\cdot\nabla\phi_v) = \epsilon\boldsymbol{\omega}\cdot\nabla^2\nabla\phi_v. \tag{5.18}$$

The equation of λ_ω, the cosine of the angle between $\boldsymbol{\omega}$ and $\nabla\phi_v$ as a function of the pseudo time τ

can then be obtained as

$$\frac{\mathcal{D}\lambda_\omega}{\mathcal{D}\tau} = \mathcal{A}\lambda_\omega + \mathcal{B}, \tag{5.19}$$

with

$$\mathcal{A}(\boldsymbol{x},\tau) = \boldsymbol{n}_v \cdot \boldsymbol{S}_\omega \cdot \boldsymbol{n}_v - \boldsymbol{n}_\omega \cdot \nabla|\boldsymbol{\omega}| - \epsilon R_\Phi \boldsymbol{n}_v \cdot \boldsymbol{n}_\Phi, \tag{5.20}$$

$$\mathcal{B}(\boldsymbol{x},\tau) = \epsilon R_\Phi \boldsymbol{n}_\omega \cdot \boldsymbol{n}_\Phi, \tag{5.21}$$

where the symmetric part of the vorticity-gradient tensor $\boldsymbol{S}_\omega$ has entries $S_{\omega,ij} = \frac{1}{2}(\partial\omega_i/\partial x_j + \partial\omega_j/\partial x_i)$, and unit vectors and a dimensionless ratio are, respectively,

$$\boldsymbol{n}_\omega = \frac{\boldsymbol{\omega}}{|\boldsymbol{\omega}|}, \quad \boldsymbol{n}_v = \frac{\nabla\phi_v}{|\nabla\phi_v|}, \quad \boldsymbol{n}_\Phi = \frac{\nabla^2\nabla\phi_v}{|\nabla^2\nabla\phi_v|}, \quad R_\Phi = \frac{|\nabla^2\nabla\phi_v|}{|\nabla\phi_v|}. \tag{5.22}$$

Since $\nabla\cdot\boldsymbol{\omega} = 0$, the eigenvalues of $\boldsymbol{S}_\omega$ satisfy $\Gamma_\alpha + \Gamma_\beta + \Gamma_\gamma = 0$. By analogy with the analysis in § 2.4.3, we then expect that $\nabla\phi_v$ will tend to align with eigenvectors of $\boldsymbol{S}_\omega$ with negative eigenvalues. Since there is no preferred alignment between $\boldsymbol{n}_\omega$ and $\nabla|\boldsymbol{\omega}|$, the leading term $\langle \boldsymbol{n}_v \cdot \boldsymbol{S}_\omega \cdot \boldsymbol{n}_v \rangle$ in $\langle\mathcal{A}\rangle$ should be statistically negative. This suggests that the solution of (5.11) will take the form

$$\langle|\lambda_\omega(t,\tau)|\rangle \sim \langle|\lambda_\omega(t,\tau=0)|\rangle \exp(\langle\mathcal{A}\rangle\tau) + O(\epsilon R_\Phi), \quad 0 \le \tau \le T_\tau. \tag{5.23}$$

Hence, for an initial ϕ_v with a finite $\langle|\lambda_\omega|\rangle$, the solution of (5.11) appears to show exponential decaying at the beginning, but this trend appears to be mitigated by the inhomogeneous term $\mathcal{B} \sim O(\epsilon R_\Phi)$ in (5.19) controlled by the numerical viscosity that depends on the resolution at late τ.

5.3.4 Numerical experiments on the convergence of numerical solutions

Using the initial condition given by an exact VSF (5.13), the temporal evolution of $\langle|\lambda_\omega|\rangle$ in the TG flow for $Re = 100$ and $N = 256$ is shown in figure 5.3(a). At fixed t we find that $\langle|\lambda_\omega|\rangle$ decreases to a small value with increasing computational period T_τ for (5.15) obtained by increasing N_τ. We define the L_∞ error norm $\|\langle|\lambda_\omega|\rangle\|_\infty$ as the maximum value of $\langle|\lambda_\omega|\rangle$ in the evolution of ϕ_v from $t = 0$ to $t = t_{max}$. Figure 5.3(b) shows the effect of the resolution on the convergence of the VSF solution. We can see that smaller $\|\langle|\lambda_\omega|\rangle\|_\infty$ for the same N_τ are obtained in the runs with larger N because the numerical viscosity ϵ is reduced by increasing grid resolution (Jiang & Shu, 1996). This implies a longer period with exponential decay dominated by the first term in the right-hand side of (5.23). The time history of $\langle|\lambda_\omega|\rangle$ in TG and KP flows at different Reynolds numbers is shown in figure 5.4, where $N_\tau = 50$ for all runs and values of N are used as listed in table 5.1. These are chosen to ensure that the maximum $\|\langle|\lambda_\omega|\rangle\|_\infty \approx 0.03$ which is equivalent to 3% of the possible maximum $|\lambda_\omega|$. For comparison, also displayed in figure 5.4 are temporal evolutions of $\langle|\lambda_\omega|\rangle$ for Lagrangian fields ϕ governed by (2.15) with the same initial conditions for the VSF simulations. The increase in $\langle|\lambda_\omega|\rangle$

with time in the evolution of Lagrangian fields occurs because the Helmholtz vorticity theorem is violated for viscous flow. In contrast, $\langle|\lambda_\omega|\rangle$ in the VSF simulations are substantially reduced by solving (5.14) and (5.15).

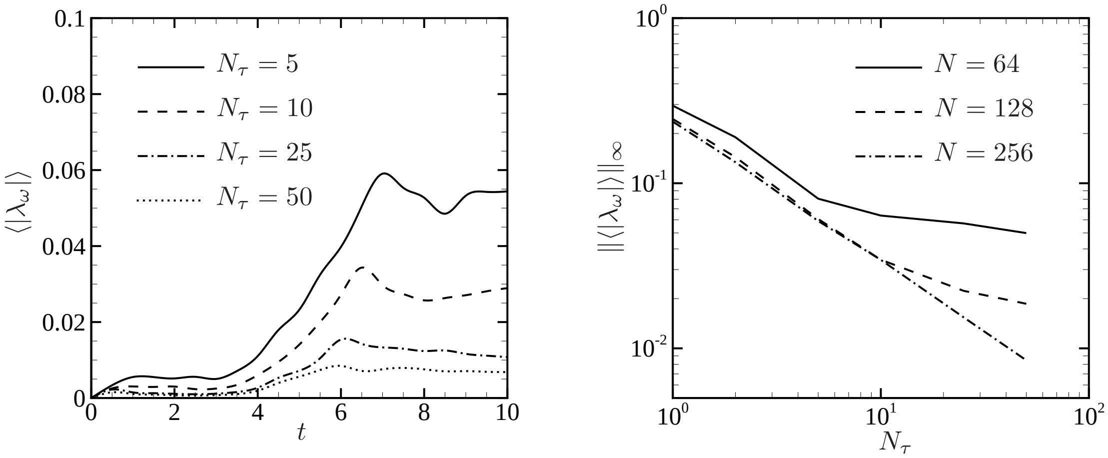

(a) temporal evolution of $\langle|\lambda_\omega|\rangle$, $N = 256$

(b) dependence of $\|\langle|\lambda_\omega|\rangle\|_\infty$ on N and N_τ

Figure 5.3: Convergence studies of the numerical solutions for the VSF in the TG flow at $Re = 100$

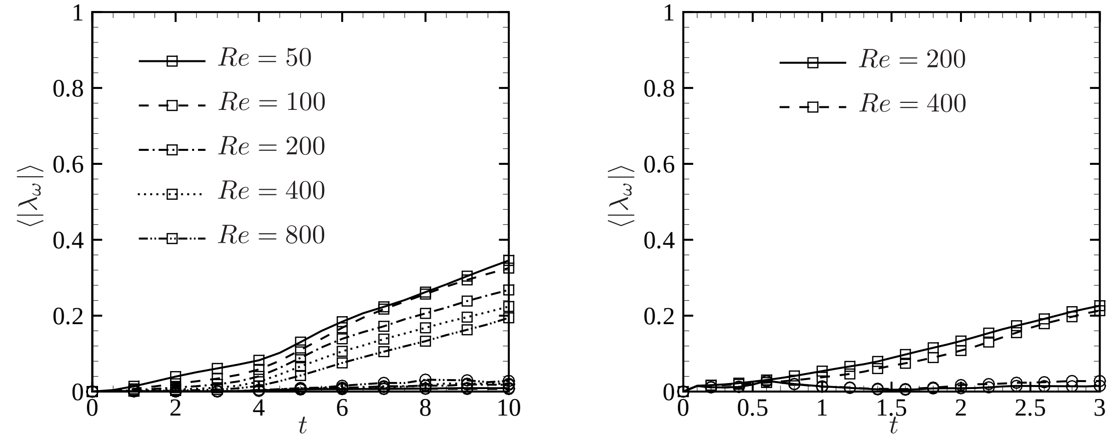

(a) TG flow

(b) KP flow

Figure 5.4: Temporal evolution of $\langle|\lambda_\omega|\rangle$ in TG and KP flows at different Reynolds numbers (□: Lagrangian field with the initial VSF; ○: VSF)

5.4 Numerical simulation and results

5.4.1 Evolution of vortex-surface fields in Taylor–Green flows

The evolution of vortex surfaces obtained from the VSF ϕ_v in the TG flow at $Re = 400$ within the periodic domain $0 \leq x, y, z \leq 2\pi$ is shown in figure 5.5. Vortex surfaces can be extracted as iso-surfaces of the VSFs at different times. Here, the scaled contour level is defined as (4.56). Color on the extracted vortex surfaces is rendered by $0 \leq |\boldsymbol{\omega}| \leq 12$ from blue to red. We remark that since ϕ_v is not conserved in the evolution, its range may change as a result of numerical dissipation in (5.14) and (5.15). Some vortex lines are integrated from points on the iso-surfaces of ϕ_v. We can see that all lie almost on the vortex surfaces owing to very small $\langle|\lambda_\omega|\rangle$ in the simulation.

As shown in figure 5.5(a), all the closed and unknotted vortex lines have the same direction on each surface. All the surfaces have the same dynamics but they move in different directions under the TG symmetries (Brachet et al., 1983). In figures 5.5(b) and 5.5(c), the vortex surfaces are stretched and gradually approach to each other but the topology of both the vortex surfaces and vortex lines on the surfaces is unchanged. In figure 5.5(d), incipient vortex reconnection, which is usually characterized by topological changes of vortex lines and surfaces (see Kida & Takaoka, 1994), appears to begin at impermeable planes (e.g., $x = \pi$) (Brachet et al., 1983) and junctions between anti-parallel vortex surfaces roughly from $t = 4$ to $t = 5$. Just prior to reconnection the directions of vortex lines on neighboring vortex surfaces (see figure 5.5(c)) are opposite, indicating that reconnection at the impermeable faces is the result of a simple vorticity cancelation as sketched in figure 3 (a) in Kida & Takaoka (1994).

In figure 5.5(e), vortex tubes (actually vortex rings in the whole periodic domain) are rolled up at the edges of vortex surfaces around $t = 5$. We can see that significant vorticity intensification occurs near the joint of anti-parallel vortex tubes (e.g., Siggia, 1985; Kerr, 1993). Based on the directionality of vorticity on these tubes in figure 5.6(a) combined with qualitative interpretation of the Biot–Savart law, we conclude that the vortex tubes, exhibiting a high-degree of symmetry, are stretched by the induced velocity from neighboring ones as sketched in figure 5.6(b).

In addition, the vortex tubes appear twisted either by self-induced dynamics or interaction with others. Figure 5.5(f) shows a tangle of interacting vortex surfaces and tubes at a late time $t = 7$. This may be interpreted as exemplifying a common archetypal picture of turbulence in terms of vortices or vortex tubes. To obtain the VSF at a full turbulent-like state with the Kolmogorov five-third scaling of the velocity spectrum, we would need to simulate the TG flow for $Re \geq 1600$ at $t = 8 \sim 9$ (Brachet et al., 1983). The resolution for the corresponding VSF simulation with an acceptably small $\langle|\lambda_\omega|\rangle$ would be $N^3 = 2048^3$ or higher.

Using results obtained from simulations listed in table 5.1 we find that vortex surfaces at different Reynolds numbers appear to have similar topology and evolutionary geometries in $0 \leq t \leq 4$.

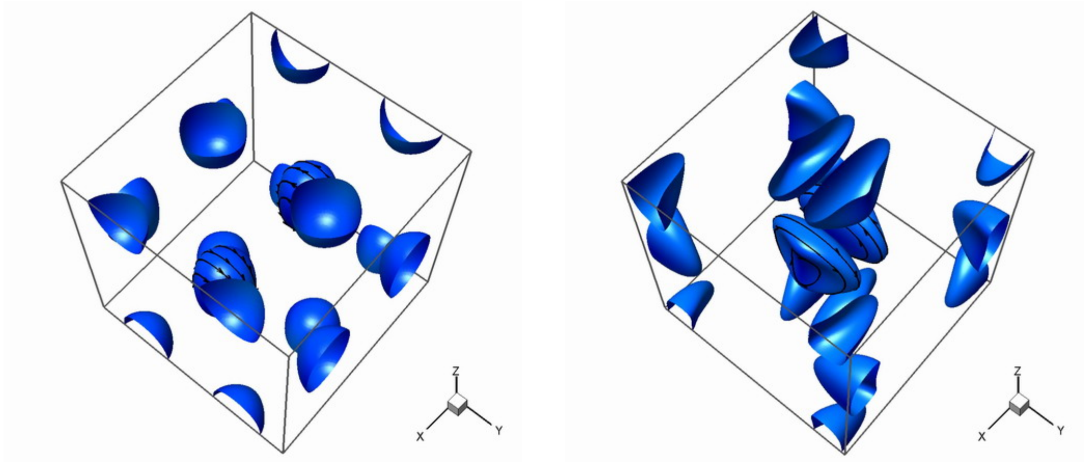

(a) $t = 1$ (b) $t = 1.5$

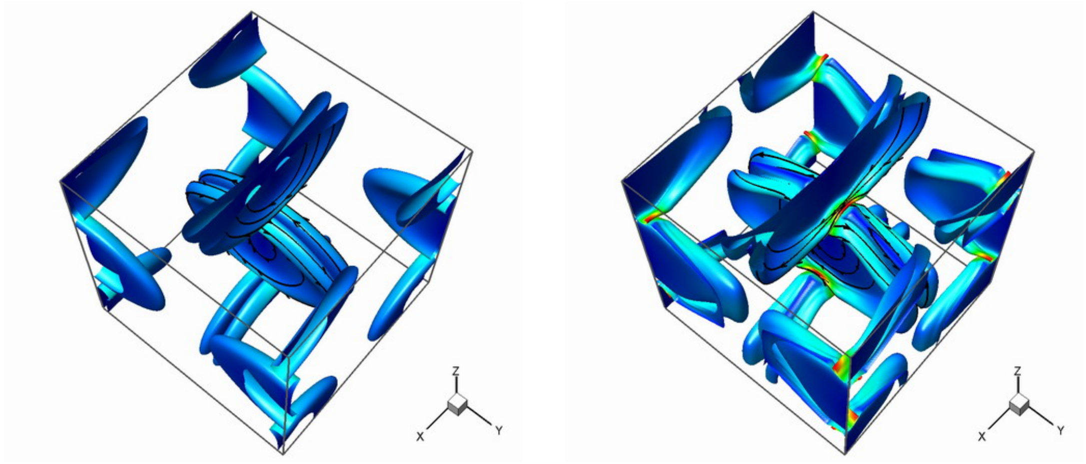

(c) $t = 3$ (d) $t = 4.5$

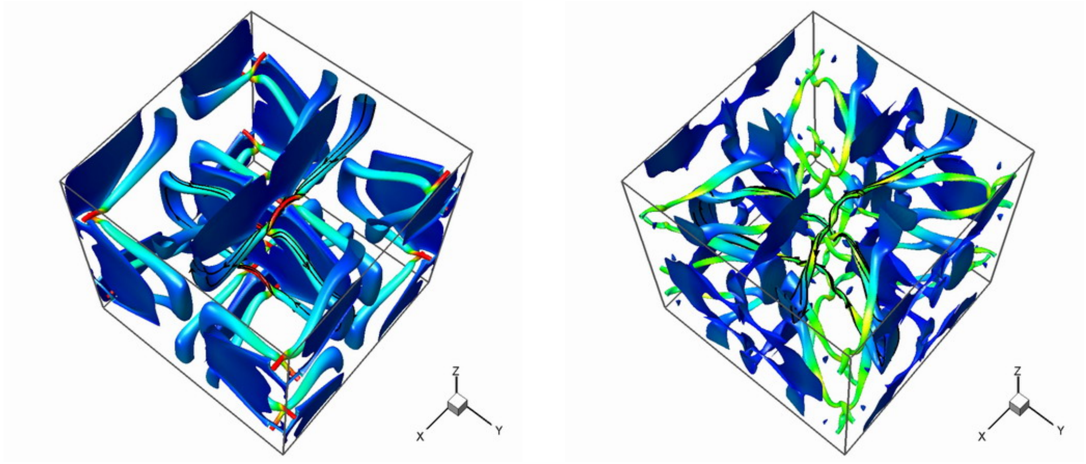

(e) $t = 5$ (f) $t = 7$

Figure 5.5: Evolution of the VSF in the TG flow at $Re = 400$. Some vortex lines are integrated and plotted on the iso-surfaces at $\hat{\phi} = 0.5$ (a–e) and $\hat{\phi} = 0.4$ (f). Color on the surfaces is rendered by $0 \leq |\boldsymbol{\omega}| \leq 12$ from blue to red

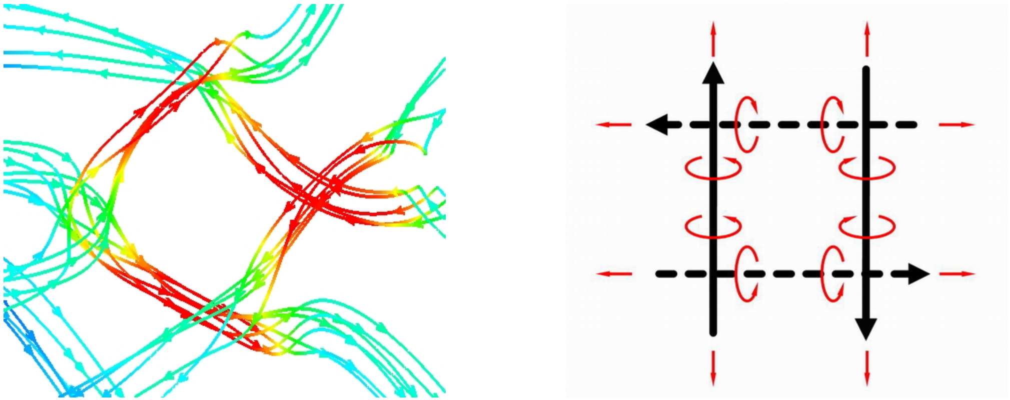

(a) typical vortex lines with strong vorticity

(b) configuration of the intensification of vortex lines (solid lines at the top and dashed lines at the bottom, induced velocity shown in red arrows)

Figure 5.6: Interacting vortex lines on the tube-like vortex-surfaces at $t = 5$ in the TG flow at $Re = 400$ in figure 5.5(e). Color on the lines is rendered by $0 \leq |\boldsymbol{\omega}| \leq 12$ from blue to red. The rapid local intensification of the vorticity could be explained by the interaction of anti-parallel vortex tubes and the Biot–Savart law

However, as shown in figure 5.7, the rolling-up of vortex tubes around $t = 5$ observed for all simulations with $Re \geq 100$ is not seen in the low-Reynolds-number TG flow at $Re = 50$. This suggests that the tube-rolling event is a dynamical requirement for the transition from a smooth velocity field to turbulence in the TG flow. From $t = 4$ to $t = 8$, the vortex surfaces at $Re = 200$ to $Re = 800$ appear to have the same topology while the geometry of vortex surfaces in high-Re flows is more complicated than that in low-Re flows. For instance, the vortex surfaces for TG flow at $Re = 400$ and $Re = 800$ are compared at $t = 7.5$ in figure 5.8.

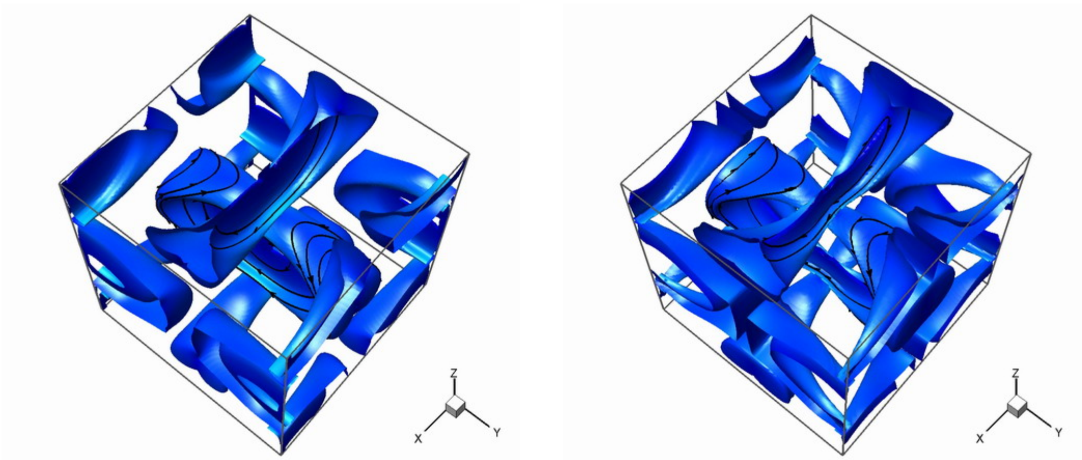

(a) $t = 5$

(b) $t = 6$

Figure 5.7: Evolution of the VSF in the TG flow at $Re = 50$. Some vortex lines are integrated and plotted on the iso-surfaces at $\hat{\phi} = 0.5$. Color on the surfaces is rendered by $0 \leq |\boldsymbol{\omega}| \leq 12$ from blue to red

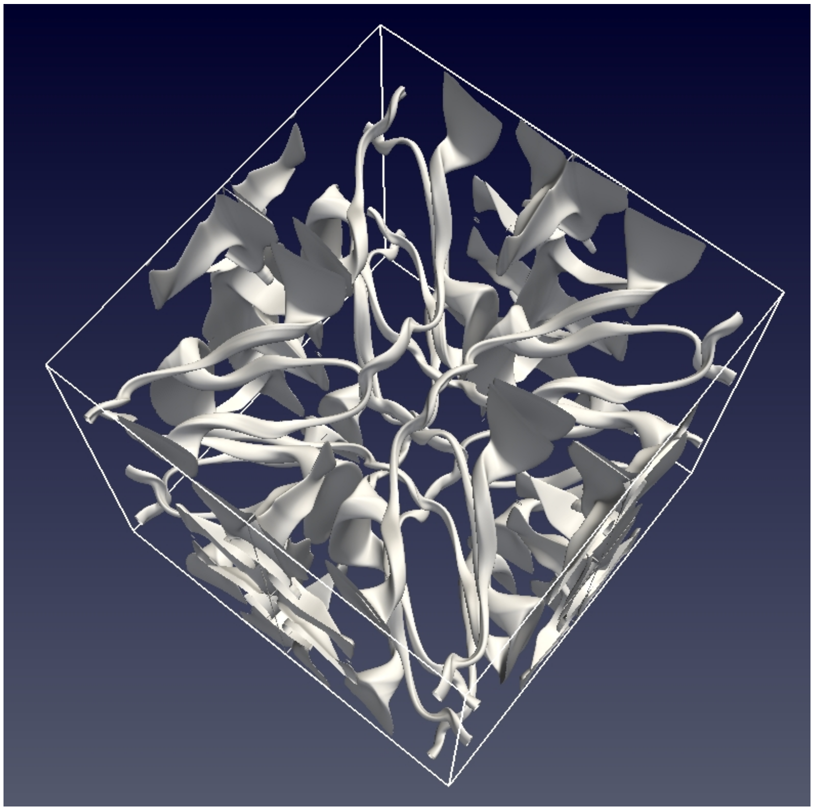

(a) $Re = 400$

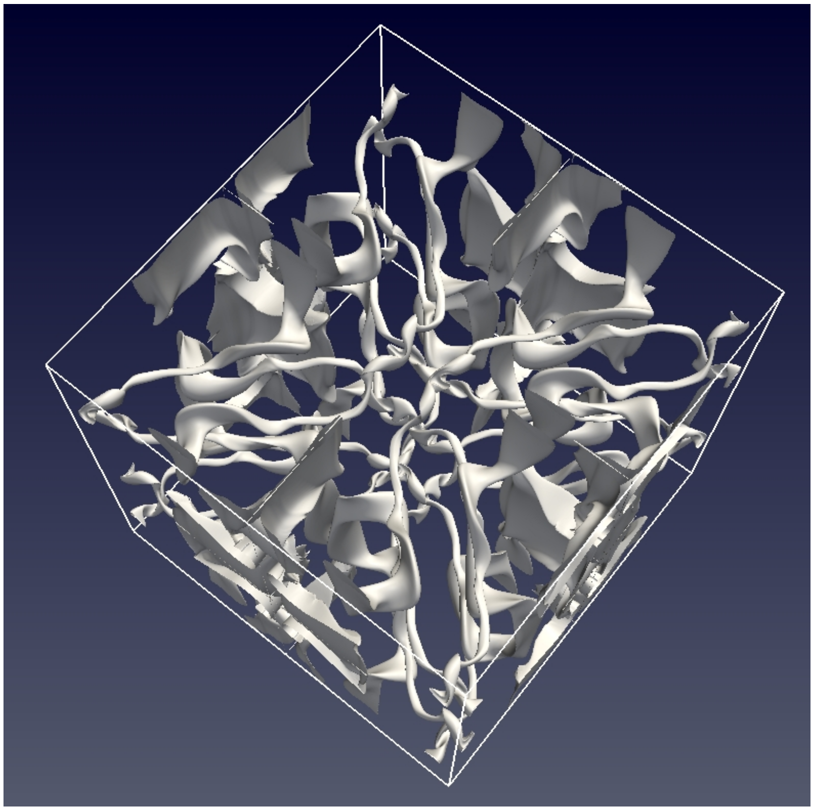

(b) $Re = 800$

Figure 5.8: Vortex surfaces in TG flows for different Reynolds numbers at $t = 7.5$

We can see that the vortex tubes at $Re = 800$ show more obvious helical geometry (e.g., Ricca, 1994; Fukumoto & Okulov, 2005), which can generate more intense small-scale velocity fields, than that at $Re = 400$.

In § 2.5 and § 3.4, we found that the geometry of Lagrangian structures at a late time appears to be insensible to their initial shapes in isotropic turbulence and turbulent channel flow. Likewise, as shown in figures 5.9(a)–5.9(c), the VSFs from independent initial VSFs ϕ_0, such as (5.13), $\phi_0 = \cos x \cos y \cos z$, and $\phi_0 = \cos x \cos^3 y \cos^2 z$ can produce very similar vortex-surface geometries in the same TG flow after a long time. Additionally, in figure 5.9(d), intersections of different vortex surfaces from independent ϕ_0, as the Clebsch potentials (e.g., Lamb, 1932), can represent vortex lines. This provides a possible method to study the evolution of vortex lines in simple viscous flows using a Lagrangian formulation.

5.4.2 Evolution of vortex-surface fields in Kida–Pelz flows

The evolution of iso-surfaces of the VSF in the KP flow at $Re = 200$ is shown in figure 5.10 within a sub domain $\pi/2 \leq x \leq 3\pi/2$ and $0 \leq y, z \leq \pi$. The vortex surfaces in other subdomains have the same dynamics but move in different directions under the KP symmetries (Kida, 1985). In contrast to the initial vortex surfaces for the TG flow in figures 5.5(a), in the KP flow the vortex lines on neighboring vortex surfaces have the same direction in figure 5.10(a). Again appealing to an interpretation of the sense of the velocities induced by the Biot–Savart law indicates that all the vortex surfaces are wound in the same direction and rotate with the z-axis at the center. This produces the predominant large-scale spiral signatures for the vortex surfaces in the KP flow. In the structural evolution, eight head-to-tail connected vortex surfaces initially form a ring and the blob-like vortex surfaces are progressively distorted into two types of shell-like shapes prior to vortex reconnection. As shown in figure 5.10(d), rolled-up structures appear at the edge of vortex surfaces in the evolution. The neighboring vortex surfaces are reconnected around $t = 2$ in figure 5.10(e) and stretched structures with complicated geometries are generated at the joint of vortex surfaces at the later stage in figure 5.10(f). The evolutionary geometry of vortex surfaces in both TG and KP flows clearly reveal a scale cascade from large scales with blob-like geometry to small scales with tube-like or sheet-like geometry in the breakdown process.

5.5 Results and discussion

In the present study, we have developed a numerical method for computing VSF evolution in some simple viscous incompressible flows. Our starting point is the expansion of the space of independent co-ordinates of a set of equations that formally describe the temporal evolution of a VSF, to an extended domain containing a pseudo-time co-ordinate. This appears to restore uniqueness to the

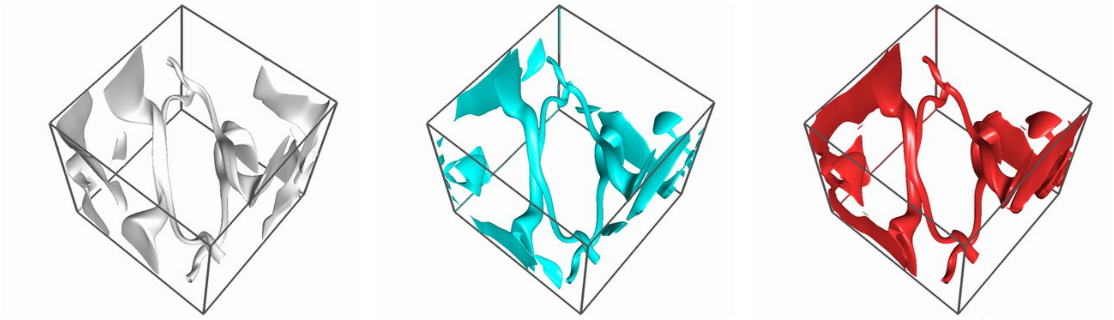

(a) $\phi_0 = (\cos 2x - \cos 2y) \cos z$ (b) $\phi_0 = \cos x \cos y \cos z$ (c) $\phi_0 = \cos x \cos^3 y \cos^2 z$

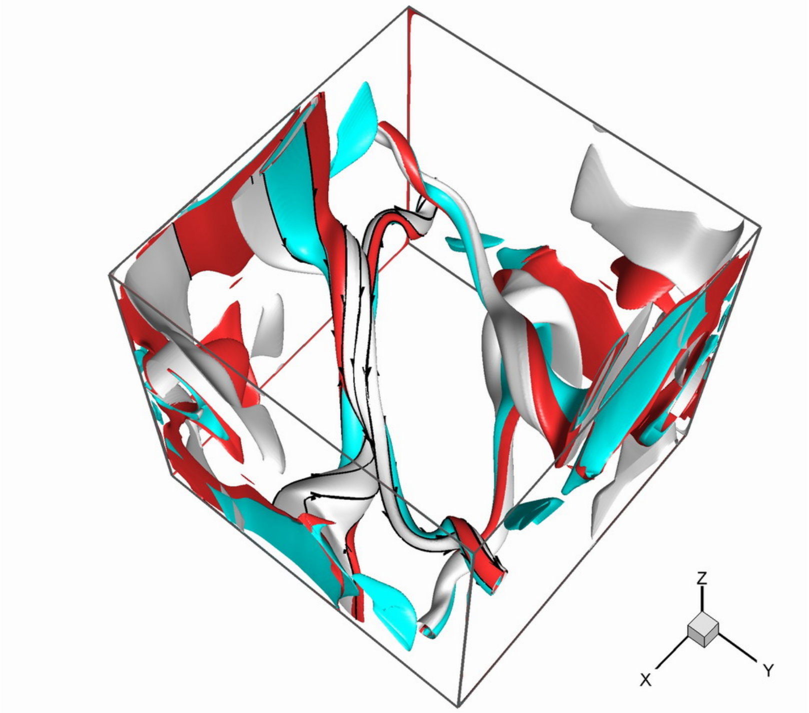

(d) Vortex surfaces from three independent ϕ_0 (shown above). Some vortex lines are integrated and plotted on the surfaces, in particular, on the intersections between different vortex surfaces from independent ϕ_0.

Figure 5.9: Vortex surfaces from three independent initial VSFs (white: $\phi_0 = (\cos 2x - \cos 2y) \cos z$; light blue: $\phi_0 = \cos x \cos y \cos z$; red: $\phi_0 = \cos x \cos^3 y \cos^2 z$) in the TG flow for $Re = 400$ at $t = 7.5$. The surfaces are shown in the sub domain $0 \le x, y, z \le \pi$

otherwise indeterminate initial boundary-value problem and can be interpreted as a correction step on the original VSF governing equations. There is then some similarity with generic level set methodologies (e.g., Osher & Fedkiw, 2003). In the absence of a physical diffusion term, by analogy to the scalar advection equation describing a Lagrangian field, solutions of the extended equation set for VSFs are expected to develop exponentially small scales in the long pseudo-time limit. In numerical implementation, this is handled presently through regularization provided by the implicit numerical dissipation inherent in the numerical WENO scheme used. Our numerical method shows exponential convergence in terms of the pseudo time up to an error threshold that is a function of

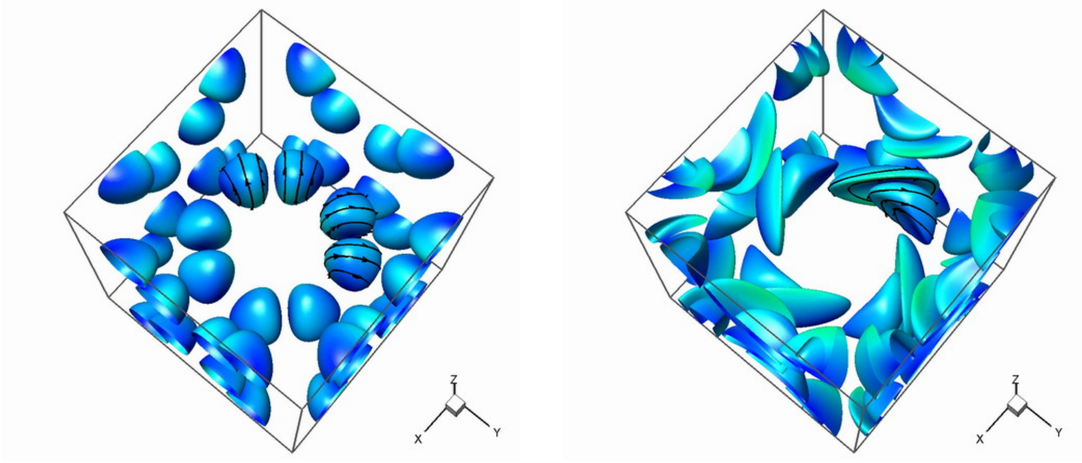

(a) $t = 0$, $\hat{\phi} = 0.15$ (b) $t = 0.5$, $\hat{\phi} = 0.15$

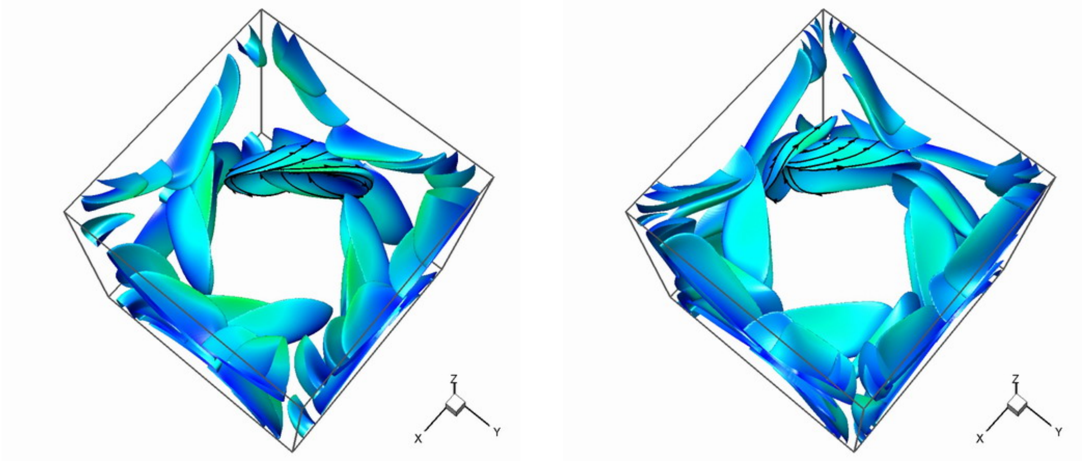

(c) $t = 1.0$, $\hat{\phi} = 0.15$ (d) $t = 1.5$, $\hat{\phi} = 0.1$

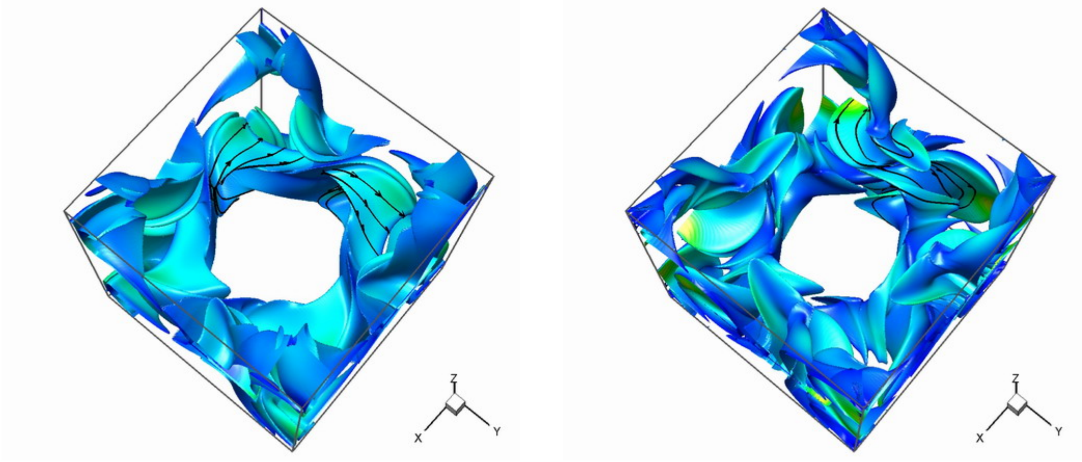

(e) $t = 2.0$, $\hat{\phi} = 0.05$ (f) $t = 2.5$, $\hat{\phi} = 0.025$

Figure 5.10: Evolution of the VSF in the KP flow at $Re = 200$. Some vortex lines are integrated and plotted on the iso-surfaces at $\hat{\phi}$. Color on the surfaces is rendered by $0 \leq |\boldsymbol{\omega}| \leq 15$ from blue to red

the grid resolution used for the vortex-surface equations.

The present scheme has been applied in TG and KP flows for real-time periods such that the L_∞ error norm remains at a level sufficiently small that smoothed vortex surfaces, obtained as iso-surfaces of the continuous VSFs, can be extracted. The simulation durations are long enough to reveal the continuous evolutionary geometry of vortex-surface evolution motion from smooth, laminar-like behavior flows through a 'transition' to a turbulent-like state. The signature of this transition is the onset of topological and geometrical changes in the vortex-surface structure. Pictorially this corresponds to some typical scenarios of vortex dynamics in turbulence, e.g., the collapse of vortex surfaces and vortex reconnection, rolling-up of vortex tubes, vorticity intensification between anti-parallel vortex tubes, and vortex stretching and twisting.

Presently we have numerically simulated VSF evolution only for simple viscous flows with strong symmetries. The computational cost of the correction step in pseudo time with the current algorithm occupies the major part in the simulation. In order to be applied generally to more complex vortical flows, a technique for accelerated convergence in pseudo-time would probably be required both for generating an initial VSF from a given initial vorticity field and also for tracking the subsequent VSF evolution. Without this it seems unlikely that the present method would provide a viable alternative to existing schemes for the purposes of generic, instantaneous flow visualization.

Our approach nevertheless enables, in a novel way, the observation of the timewise evolution of smoothed VSFs in viscous flows, which, to the best of our knowledge has hitherto been thought to have no dynamical meaning as an initial-boundary value problem. For this reason alone the application of the present algorithm to special cases of interesting canonical flows, at some computational cost, may be justified. In addition, relevant topological methods based on contact structures (Ghrist & Komendarczyk, 2002) or vector segments (Wang, 2010) might be useful to improve the current methodology for more general flows.

Finally, we remark that globally smoothed VSFs may not exist in general flows when the vorticity field is not integrable, in which case a surrogate field with acceptably small $\langle|\lambda_\omega|\rangle$ could be obtained by using (5.11).

Chapter 6

Conclusions

6.1 Lagrangian structures in homogenous isotropic turbulence

With the introduction of the Lagrangian description of fluid dynamics, we report the multi-scale geometric analysis of Lagrangian structures in forced isotropic turbulence and also with a frozen turbulent field. A particle-backward-tracking method, which is stable and topology preserving, was applied to obtain the Lagrangian field ϕ governed by the pure advection equation in the Eulerian form $\partial_t \phi + \boldsymbol{u} \cdot \nabla \phi = 0$. The temporal evolution of Lagrangian structures was first obtained by extracting iso-surfaces of ϕ with resolution 1024^3 at different times, from $t = 0$ to $t = T_e$. The surface area growth rate of the Lagrangian structure was quantified and the formation of stretched and rolled-up structures observed in straining regions and stretched vortex tubes, respectively.

The multi-scale geometric analysis of Bermejo-Moreno & Pullin (2008) has been applied to the evolution of ϕ to extract structures at different length scales and to characterize their non-local geometry in a space of reduced geometrical parameters. In this multi-scale sense, we observed, for the evolving turbulent velocity field, an evolutionary breakdown of initially large-scale Lagrangian structures that first distort and then either themselves are broken down or stretched laterally into sheets. Moreover, after a finite time, this progression appears to be insensible to the form of the initially smooth Lagrangian field. In comparison with the statistical geometry of instantaneous passive scalar and enstrophy fields in turbulence obtained by Bermejo-Moreno & Pullin (2008) and Bermejo-Moreno et al. (2009), Lagrangian structures tend to exhibit more prevalent sheet-like shapes at intermediate and small scales. For the frozen flow, the Lagrangian field appears to be attracted onto a stream-surface field and it develops less complex multi-scale geometry than found for the turbulent velocity field. In the latter case, there appears to be a tendency for the Lagrangian field to move towards a vortex-surface field (VSF) of the evolving turbulent flow but this is mitigated by cumulative viscous effects.

6.2 Lagrangian and Eulerian structures in turbulent channel flow

For wall turbulence, we report the detailed multi-scale and multi-directional geometric study of both evolving Lagrangian and also instantaneous Eulerian structures in turbulent channel flow at low and moderate Reynolds numbers. The Lagrangian structures were obtained by tracking the Lagrangian field, and Eulerian structures were extracted from the swirling strength field at a time instant. The multi-scale and multi-directional geometric analysis, based on the mirror-extended curvelet transform, was developed to quantify the geometry, including the averaged inclination and sweep angles, of both structures at up to eight scales ranging from the half-height δ of the channel to several viscous length scales δ_ν. Here, the inclination angle is on the plane of the streamwise and wall-normal directions, and the sweep angle is on the plane of streamwise and spanwise directions.

The results showed that coherent quasi-streamwise structures in the near-wall region are composed of inclined objects with averaged inclination angle 35°–45°, averaged sweep angle 30°–40°, and characteristic scale $20\delta_\nu$, and 'curved legs' with averaged inclination angle 20°–30°, averaged sweep angle 15°–30°, and length scale $5\delta_\nu$–$10\delta_\nu$. The temporal evolution of Lagrangian structures showed increasing inclination and sweep angles with time, which may correspond to the lifting process of near-wall quasi-streamwise vortices. The large-scale structures that appear to be composed of a number of individual small-scale objects were detected using cross-correlations between Eulerian structures with large and small scales. These packets are located at the near-wall region with the typical height 0.25δ and may extend over 10δ in the streamwise direction in moderate-Reynolds-number, long channel flows. In addition, the effects of the Reynolds number and comparisons between Lagrangian and Eulerian structures were discussed.

6.3 Lagrangian and vortex-surface fields in Taylor–Green and Kida–Pelz flows

For a strictly inviscid barotropic flow with conservative body forces, the Helmholtz vorticity theorem shows that material or Lagrangian surfaces which are vortex surfaces at time $t = 0$, remain so for $t > 0$. In this study, a systematic methodology was developed for constructing smooth scalar fields $\phi_v(x, y, z, t = 0)$ for TG and KP velocity fields, which at $t = 0$, satisfy $\boldsymbol{\omega} \cdot \nabla\phi_v = 0$. We referred to such fields as VSFs. Then, for some constant C, iso-surfaces $\phi_v = C$ define vortex surfaces. It was shown that, given the vorticity, our definition of a VSF admits nonuniqueness and this is presently resolved numerically using an optimization approach. In addition, the relations between VSFs and the classical Clebsch presentation were discussed for flows with the zero helicity. Equations describing the evolution of VSFs were then obtained for both inviscid and viscous incompressible flows. Both uniqueness and the distinction separating the evolution of VSFs and Lagrangian fields were discussed.

By tracking ϕ_v as a Lagrangian field in slightly viscous flows, we showed that the well-defined evolution of Lagrangian surfaces that are initially vortex surfaces can be a good approximation to vortex surfaces at later times prior to vortex reconnection. In the evolution of such Lagrangian fields, we observed that initially blob-like vortex surfaces are progressively stretched to sheet-like shapes so that neighboring portions approach each other, with subsequent rolling up of structures near the interface, which reveals more information on dynamics than the iso-surfaces of vorticity magnitude. The non-local geometry in the evolution was quantified by two differential geometry properties. Rolled-up local shapes were found in the Lagrangian structures that were initially vortex surfaces close to the time of vortex reconnection. It was hypothesized that this is related to the formation of the very high vorticity regions.

In order to investigate continuous vortex dynamics based on a Lagrangian-like formulation, we developed a theoretical framework and a numerical method for computation of the evolution of a VSF in viscous incompressible flows with simple topology and geometry. Vortex surfaces were then extracted as iso-surfaces of the VSFs at different times. This clarifies the vortex dynamics of VSF evolution in viscous TG and KP flows including the collapse of vortex surfaces and vortex reconnection, rolling-up of vortex tubes, vorticity intensification between anti-parallel vortex tubes, and vortex stretching and twisting. A possible scenario for explaining the transition from a smooth laminar flow to turbulent flow in terms of topology of vortex surfaces was discussed.

Appendix A

Orthogonal basis functions with Kida–Pelz symmetries

We propose an expansion of the VSF ϕ_{KP} based on the following fundamental functions, or linear combinations thereof, which satisfy the symmetries (Kida, 1985) in the KP flow

$$\begin{aligned} f_0(M,N,L) &= (\cos m_1 x \cos m_0 y - \cos m_0 x \cos m_1 y) \\ &\quad \times(\cos n_1 y \cos n_0 z - \cos n_0 y \cos n_1 z) \\ &\quad \times(\cos l_1 z \cos l_0 x - \cos l_0 z \cos l_1 x), \end{aligned} \tag{A.1}$$

where the wavenumber pairs

$$M = \{m_0, m_1\},\ N = \{n_0, n_1\},\ L = \{l_0, l_1\}$$

are chosen by the following procedure:

i. Each wavenumber pair M, N, or L contains two different odd wavenumbers with $1 \le m_0 < m_1$, $1 \le n_0 < n_1$, and $1 \le l_0 < l_1$. Let

$$K_\psi = \max(m_1) = \max(n_1) = \max(l_1),$$

and the maximum wavenumber $K_F = 2K_\psi$ in all the $f_0(M,N,L)$ considered for the approximation. The corresponding number of wavenumber pairs is

$$N_{pr} = (K_\psi^2 - 1)/8. \tag{A.2}$$

ii. A list of wavenumber pairs obtained in the last step is built and sorted by the sum $\Sigma_p = 2m_0 + m_1$ for each pair. Then each wavenumber pair is labeled by a pair index number I_p from 1 to N_{pr} by the sequence in the list. When a number of wavenumber pairs have the same

Table A.1: List of wavenumber pairs ($K_\psi = 17$)

Index number I_p	1	2	3	4	5	6	...	35	36
Wavenumber pair	$(1,3)$	$(1,5)$	$(1,7)$	$(1,9)$	$(3,5)$	$(1,11)$	...	$(13,17)$	$(15,17)$
Σ_p	5	7	9	11	11	13	...	43	47

Σ_p, the pair with a smaller m_0 has a smaller I_p. For example, a list of wavenumber pairs for $K_\psi = 17$ is shown in table A.1. Here, we remark that the sequence in the list of wavenumber pairs may slightly affect the final solution quality and the convergence rate.

iii. Each basis function ψ_i is based on two types of combinations of the fundamental solution (A.1). The first type is

$$\psi_i = f_0(M_i, N_i, L_i), \quad 1 \le i \le N_{pr} \tag{A.3}$$

where the wavenumber pair is determined by its subscript corresponding to the pair index number I_p. The second type is

$$\psi_i = f_0(M_a, N_b, L_b) + f_0(M_b, N_a, L_b) + f_0(M_b, N_b, L_a), \quad N_{pr} + 1 \le i \le N_\psi, \tag{A.4}$$

with

$$i = aN_{pr} - \frac{1}{2}a(a+1) + b, \quad 1 \le a \le N_{pr} - 1, \quad a + 1 \le b \le N_{pr}, \tag{A.5}$$

and the total number of the basis functions

$$N_\psi = \frac{1}{2}N_{pr}(N_{pr} + 1). \tag{A.6}$$

We find that both types of ψ_i satisfy the reflectional symmetry about all three zero planes, and the rotational symmetry is expressed by the permutation symmetry:

$$\psi_i(x, y, z) = \psi_i(z, x, y) = \psi_i(y, z, x).$$

In other words, the basis function ψ_i is invariant under the action of the full octahedral symmetry group to match the same symmetry property in the KP flow (Pelz, 2001).

Finally, orthogonal basis functions $\widetilde{\psi}_i$ are obtained from ψ_i by the Gram–Schmidt orthogonalization,

$$\widetilde{\psi}_1 = \psi_1 / \|\psi_1\|, \tag{A.7}$$

with

$$\|f\| = \left(\int_0^{2\pi} \int_0^{2\pi} \int_0^{2\pi} f \, \mathrm{d}x \, \mathrm{d}y \, \mathrm{d}z \right)^{1/2},$$

and then

$$\begin{aligned}\psi_i' &= \psi_i - \sum_{j=1}^{i-1} \langle \psi_i, \widetilde{\psi}_j \rangle \widetilde{\psi}_j, \quad i \geq 2, \\ \widetilde{\psi}_i &= \psi_i' / \|\psi_i\|,\end{aligned} \tag{A.8}$$

with

$$\langle f_1, f_2 \rangle = \left(\int_0^{2\pi} \int_0^{2\pi} \int_0^{2\pi} f_1 f_2 \, \mathrm{d}x \, \mathrm{d}y \, \mathrm{d}z \right)^{1/2}.$$

Appendix B

Computation of vortex-surface fields in incompressible viscous flow using the spectral method

From § 4.3, for ϕ_v to evolve as the VSF in a viscous flow satisfying (4.32), we must solve (4.41), (4.42), and (4.48) simultaneously. Here, (4.42) is a special case of the generalized first-order PDE:

$$\omega_j(\boldsymbol{x})\frac{\partial \mathcal{L}(\boldsymbol{x})}{\partial x_j} + B(\boldsymbol{x})\mathcal{L}(\boldsymbol{x}) = f(\boldsymbol{x}). \tag{B.1}$$

With the finite Fourier expansion

$$\mathcal{L}(\boldsymbol{x}) = \sum_{\boldsymbol{k}} \hat{\mathcal{L}}(\boldsymbol{k})\mathrm{e}^{\mathrm{i}\boldsymbol{k}\cdot\boldsymbol{x}}, \tag{B.2}$$

(B.1) could be computed by a spectral method (see Mingyu et al., 1997). By multiplying $\mathrm{e}^{-\mathrm{i}\boldsymbol{k}'\cdot\boldsymbol{x}}$ on both sides of (B.1), we can obtain the k'-th equation for a linear system

$$\sum_{\boldsymbol{k}} (\mathrm{i}k_j\hat{\omega}_j(\boldsymbol{k}'-\boldsymbol{k}) + \hat{B}(\boldsymbol{k}'-\boldsymbol{k}))\hat{\mathcal{L}}(\boldsymbol{k}) = \hat{f}(\boldsymbol{k}'), \tag{B.3}$$

where

$$\begin{aligned}
\hat{\omega}_j(\boldsymbol{k}'-\boldsymbol{k}) &= \frac{1}{(2\pi)^3}\int \omega_j(\boldsymbol{x})\mathrm{e}^{-\mathrm{i}(\boldsymbol{k}'-\boldsymbol{k})\cdot\boldsymbol{x}}\mathrm{d}\boldsymbol{x},\\
\hat{B}(\boldsymbol{k}'-\boldsymbol{k}) &= \frac{1}{(2\pi)^3}\int B(\boldsymbol{x})\mathrm{e}^{-\mathrm{i}(\boldsymbol{k}'-\boldsymbol{k})\cdot\boldsymbol{x}}\mathrm{d}\boldsymbol{x},\\
\hat{f}(\boldsymbol{k}') &= \frac{1}{(2\pi)^3}\int f(\boldsymbol{x})\mathrm{e}^{-\mathrm{i}\boldsymbol{k}'\cdot\boldsymbol{x}}\mathrm{d}\boldsymbol{x}.
\end{aligned}$$

The PDE system (B.1) is said to be dissipative if the following condition holds (Mingyu et al., 1997):

$$\left\langle \left(B - \frac{1}{2}(\nabla\cdot\boldsymbol{\omega})\right)\boldsymbol{\eta}, \boldsymbol{\eta}\right\rangle > 0, \forall\boldsymbol{\eta}\in\mathbb{R}^n. \tag{B.4}$$

Then (B.1) and the discrete system (B.3) have a unique solution. For (4.42), $f = -\nabla\phi\cdot\nabla^2\boldsymbol{\omega}$, $B = 0$, $\nabla\cdot\boldsymbol{\omega} = 0$, and the condition (B.4) for existence and uniqueness is not satisfied. We have nonetheless numerically demonstrated the existence of solutions to (B.1) with $B = f = 0$ defining a VSF for the KP vorticity (4.15) by using an optimization formulation in § 4.2.3.

Some explorative solutions have been performed for the VSF in the TG flow. The Navier–Stokes equations (4.48) were solved by the pseudo-spectral method, using the TG initial conditions (4.9) with $\theta = 0$ and at Reynolds numbers $Re = 25$ and $Re = 50$ on the grids 64^3. For each simulation, two separate scalar simulations were performed, both with initial scalar fields given by the TG VSF (4.12). In the Lagrangian simulation, (2.15) was calculated as a Lagrangian field ϕ using the backward-particle-tracking method as described in § 2.3.2. For this case, $\phi = \phi_v$ at $t = 0$ but does not remain a VSF. In the vortex-surface simulation, (4.41) and (4.42) were solved for ϕ_v and $\mathcal{L}$. Since (4.41) contains a source term, the backward-tracking-particle method cannot be utilized. Instead this equation was solved by a finite-difference method where the convection term was treated using a fifth-order WENO scheme (Jiang & Shu, 1996). The spectral method (see (B.3)) was utilized to solve (4.42). This produces a linear system

$$\boldsymbol{A}\boldsymbol{L} = \boldsymbol{b}, \tag{B.5}$$

where $\boldsymbol{L}$ is the $1 \times n$ vector of Fourier coefficients for $\mathcal{L}$ and n is determined by the number of effective Fourier modes after dealiasing. It is noted that considering the TG symmetries (Brachet et al., 1983), the Fourier representation for $\mathcal{L}$ in the TG flow could be

$$\mathcal{L}(\boldsymbol{x}) = \sum_{k_1}\sum_{k_2}\sum_{k_3}\hat{\mathcal{L}}(k_1, k_2, k_3)\cos k_1 x \cos k_2 y \cos k_3 z \tag{B.6}$$

and $\hat{\mathcal{L}}$ vanishes unless k_1, k_2, k_3 are either all even or all odd integers.

Owing to nonuniqueness of (4.42), the $n \times n$ matrix $\boldsymbol{A}$ becomes rank-deficient and ill-conditioned. Further conditions on solutions of (4.42) are therefore required. Integrating the difference between (4.41) and (2.15) over a $(2\pi)^3$ domain in physical space with periodic boundary conditions on all quantities gives

$$\int_0^{2\pi}\int_0^{2\pi}\int_0^{2\pi}\left(\frac{\mathrm{D}\phi_v}{\mathrm{D}t} - \frac{\mathrm{D}\phi}{\mathrm{D}t}\right)^2 \mathrm{d}x\,\mathrm{d}y\,\mathrm{d}z = \nu^2\int_0^{2\pi}\int_0^{2\pi}\int_0^{2\pi}\mathcal{L}^2\mathrm{d}x\,\mathrm{d}y\,\mathrm{d}z. \tag{B.7}$$

For $\nu = 0$, the volume integral of $\mathcal{L}^2$ is zero in the Lagrangian case. A reasonable choice for $\nu \neq 0$ could then be minimizing the integral of $|\mathcal{L}|$. With the Fourier method, the minimum norm solution was obtained which minimizes $\|\boldsymbol{L}\|_2$ in (B.5) using the singular value decomposition in LAPACK (Anderson et al., 1999). Here, $\boldsymbol{A} = \boldsymbol{U}\boldsymbol{\Sigma}\boldsymbol{V}^T$, where $\boldsymbol{U}$ and $\boldsymbol{V}$ are $n \times n$ satisfying $\boldsymbol{U}^T\boldsymbol{U} = \boldsymbol{I}$ and

$\boldsymbol{V}^T\boldsymbol{V} = \boldsymbol{I}$, respectively, and $\boldsymbol{\Sigma} = \mathrm{diag}(\sigma_1, \ldots, \sigma_n)$ where singular values $\sigma_1 \geq \cdots \geq \sigma_n \geq 0$. In the implementation, singular values $\sigma_i \leq r_\sigma \sigma_1$ are treated as zero, where r_σ is a small number.

The volume-averaged $|\lambda_\omega|$ for the Lagrangian simulation and $|\lambda_\omega^v|$ for the vortex-surface simulation are plotted in figure B.1, where λ_ω^v is the cosine of the angle between $\boldsymbol{\omega}$ and $\nabla\phi_v$. It may be seen that $\langle|\lambda_\omega^v|\rangle$ in the vortex-surface simulation is substantially less than $\langle|\lambda_\omega|\rangle$ in the Lagrangian simulation, but that this is not sufficiently small. Visual inspection of iso-surfaces of the scalar fields (not shown), however, indicate that the attachment of vortex lines to the iso-surface is substantially superior for the vortex-surface simulations than for the Lagrangian simulations. More investigations on the evolution of VSFs in a viscous flow are addressed in § 5.

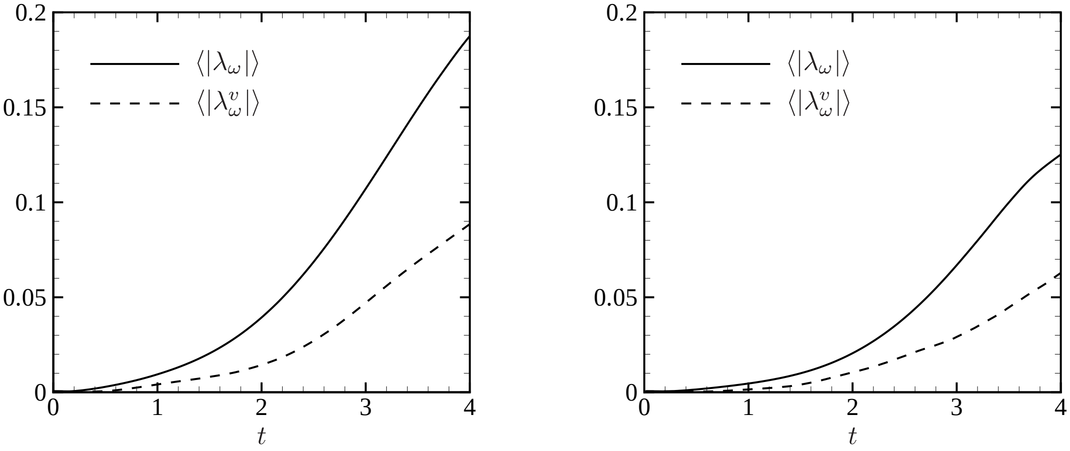

(a) $Re = 25$

(b) $Re = 50$

Figure B.1: Temporal evolution of the volume-averaged $|\lambda_\omega|$ for Lagrangian simulations and $|\lambda_\omega^v|$ for vortex-surface simulations in the viscous TG flow at low Reynolds numbers

Bibliography

Adrian, R. J. 2007 Hairpin vortex organization in wall turbulence. *Phys. Fluids* **19**, 041301.

Adrian, R. J. & Liu, Z. C. 2002 Observation of vortex packets in direct numerical simulation of fully turbulent channel flow. *J. Visual.* **5**, 9–19.

del Álamo, J. C., Jiménez, J., Zandonade, P. & Moser, R. D. 2004 Scaling of the energy spectra of turbulent channels. *J. Fluid Mech.* **500**, 135–144.

Anderson, E., Bai, Z., Bischof, C., Blackford, S., Demmel, J., Dongarra, J., Du Croz, J., Greenbaum, A., Hammarling, S., McKenney, A. & Sorensen, D. 1999 *LAPACK Users' Guide*, 3rd edn. Society for Industrial and Applied Mathematics.

Aref, H. 1984 Stirring by chaotic advection. *J. Fluid Mech.* **143**, 1–21.

Ashurst, W. T., Kerstein, A. R., Kerr, R. M. & Gibson, C. H. 1987 Alignment of vorticity and scalar gradient with strain rate in simulated Navier–Stokes turbulence. *Phys. Fluid* **30**, 2343–2353.

Bamberger, R. H. & Smith, M. J. T. 1992 A filter bank for the directional decomposition of images—Theory and design. *IEEE Trans. Signal Process.* **40**, 882–893.

Bandyopadhyay, P. 1980 Large structure with a characteristic upstream interface in turbulent boundary-layers. *Phys. Fluids* **23**, 2326–2327.

Batchelor, G. K. 1952a Diffusion in a field of homogeneous turbulence. II. The relative motion of particles. *Proc. Cambridge Philos. Soc.* **48**, 345–362.

Batchelor, G. K. 1952b The effect of homogeneous turbulence on material lines and surfaces. *Proc. Roy. Soc. Lond. A* **213**, 349–366.

Batchelor, G. K. 1967 *An Introduction to Fluid Dynamics*. Cambridge University Press.

Bermejo-Moreno, I. & Pullin, D. I. 2008 On the non-local geometry of turbulence. *J. Fluid Mech.* **603**, 101–135.

Bermejo-Moreno, I., Pullin, D. I. & Horiuti, K. 2009 Geometry of enstrophy and dissipation, grid resolution effects and proximity issues in turbulence. *J. Fluid Mech.* **620**, 121–166.

Boratav, O. N. & Pelz, R. B. 1994 Direct numerical simulation of transition to turbulence from a high-symmetry initial condition. *Phys. Fluids* **6**, 2757–2784.

Bourgoin, M., Ouellette, N. T., Xu, H. T., Berg, J. & Bodenschatz, E. 2006 The role of pair dispersion in turbulent flow. *Science* **311**, 835–838.

Brachet, M. E., Meiron, D. I., Orszag, S. A., Nickel, B. G., Morf, R. H. & Frisch, U. 1983 Small-scale structure of the Taylor–Green vortex. *J. Fluid Mech.* **130**, 411–452.

Brachet, M. E., Meneguzzi, M., Vincent, A., Politano, H. & Sulem, P. L. 1992 Numerical evidence of smooth self-similar dynamics and possibility of subsequent collapse for three-dimensional ideal flows. *Phys. Fluids A* **4**, 2845–2854.

Branicki, M. & Wiggins, S. 2009 An adaptive method for computing invariant manifolds in non-autonomous, three-dimensional dynamical systems. *Physica D* **238**, 1625–1657.

Brethouwer, G., Hunt, J. C. R. & Nieuwstadt, F. T. M. 2003 Micro-structure and Lagrangian statistics of the scalar field with a mean gradient in isotropic turbulence. *J. Fluid Mech.* **474**, 193–225.

Candès, E., Demanet, L., Donoho, D. & Ying, L. 2006 Fast discrete curvelet transforms. *Multiscale Model. Simul.* **5**, 861–899.

Cartes, C., Bustamante, M. D. & Brachet, M. E. 2007 Generalized Eulerian–Lagrangian description of Navier–Stokes dynamics. *Phys. Fluids* **19**, 077101.

Chakraborty, P., Balachandar, S. & Adrian, R. J. 2005 On the relationships between local vortex identification schemes. *J. Fluid Mech.* **535**, 189–214.

Chen, S., Eyink, G. L., Wan, M. & Xiao, Z. 2006 Is the Kelvin theorem valid for high Reynolds number turbulence? *Phys. Rev. Lett.* **97**, 144505.

Chertkov, M., Pumir, A. & Shraiman, B. I. 1999 Lagrangian tetrad dynamics and the phenomenology of turbulence. *Phys. Fluids* **11**, 2394–2410.

Chong, M. S., Perry, A. E. & Cantwell, B. J. 1990 A general classification of three-dimensional flow fields. *Phys. Fluids A* **2**, 765–777.

Christensen, K. T. & Adrian, R. J. 2001 Statistical evidence of hairpin vortex packets in wall turbulence. *J. Fluid Mech.* **431**, 433–443.

CHUNG, D. & PULLIN, D. I. 2009 Large-eddy simulation and wall modelling of turbulent channel flow. *J. Fluid Mech.* **631**, 281–309.

CLEBSCH, A. 1859 Ueber die Integration der hydrodynamischen Gleichungen. *J. Reine Angew. Math.* **56**, 1–10.

CONSTANTIN, P. 2001 An Eulerian–Lagrangian approach to the Navier–Stokes equations. *Commun. Math. Phys.* **216**, 663–686.

CONSTANTIN, P., MAJDA, A. J. & TABAK, E. 1994 Formation of strong fronts in the 2-D quasi-geostrophic thermal active scalar. *Nonlinearity* **7**, 1495–1533.

CONSTANTIN, P., PROCACCIA, I. & SEGEL, D. 1995 Creation and dynamics of vortex tubes in three-dimensional turbulence. *Phys. Rev. E* **51**, 3207–3222.

CRANDALL, M. G. & LIONS, P. L. 1983 Viscosity solutions of Hamilton–Jacobi equations. *Trans. Am. Math. Soc.* **277**, 1–42.

DAVIDSON, P. A. 2004 *Turbulence: An introduction for scientists and engineers*. Oxford University Press.

DEMANET, L. & YING, L. 2007 Curvelets and wave atoms for mirror-extended images. In *Proceedings of the Society of Photo–optical Instrumentation Engineers (SPIE)*, vol. 6701, p. 67010J. SPIE.

DIECI, L., LORENZ, J. & RUSSELL, R. D. 1991 Numerical calculation of invariant tori. *SIAM J. Sci. Stat. Comput.* **12**, 607–647.

DOMBRE, T., FRISCH, U., GREENE, J. M., HENON, M., MEHR, A. & SOWARD, A. M. 1986 Chaotic streamlines in the ABC flows. *J. Fluid Mech.* **167**, 353–391.

ERTEL, H. 1942 Ein neuer hydrodynamischer Wirbelsatz. *Meteorol Z.* **59**, 271–281.

FALCO, R. E. 1977 Coherent motions in outer region of turbulent boundary-layers. *Phys. Fluids* **20**, S124–S132.

FARGE, M. 1992 Wavelet transforms and their applications to turbulence. *Annu. Rev. Fluid Mech.* **24**, 395–457.

FUKUMOTO, Y. & OKULOV, V. L. 2005 The velocity field induced by a helical vortex tube. *Phys. Fluids* **17**, 107101.

GANAPATHISUBRAMANI, B., LONGMIRE, E. K. & MARUSIC, I. 2006 Experimental investigation of vortex properties in a turbulent boundary layer. *Phys. Fluids* **18**, 055105.

Ghrist, R. & Komendarczyk, R. 2002 Topological features of inviscid flows. In *Introduction to the Geometry and Topology of Fluid Flows, NATO-ASI Series II*, vol. 47, pp. 183–202. Kluwer Press.

Girimaji, S. S. & Pope, S. B. 1990 Material-element deformation in isotropic turbulence. *J. Fluid Mech.* **220**, 427–458.

Golub, G. H. & Van Loan, C. F. 1996 *Matrix computations*, 3rd edn. The Johns Hopkins University Press.

Goto, S. & Kida, S. 2007 Reynolds-number dependence of line and surface stretching in turbulence: folding effects. *J. Fluid Mech.* **586**, 59–81.

Green, M. A., Rowley, C. W. & Haller, G. 2007 Detection of Lagrangian coherent structures in three-dimensional turbulence. *J. Fluid Mech.* **572**, 111–120.

Guala, M., Hommema, S. E. & Adrian, R. J. 2006 Large-scale and very-large-scale motions in turbulent pipe flow. *J. Fluid Mech.* **554**, 521–542.

Haller, G. 2001 Distinguished material surfaces and coherent structures in three-dimensional fluid flows. *Physica D* **149**, 248–277.

Haller, G. 2005 An objective definition of a vortex. *J. Fluid Mech.* **525**, 1–26.

Head, M. R. & Bandyopadhyay, P. 1981 New aspects of turbulent boundary-layer structure. *J. Fluid Mech.* **107**, 297–338.

Helmholtz, H. 1858 Über Integrale der hydrodynamischen Gleichungen welche den Wribelbewegungen ensprechen **55**, 25–55.

Hinze, J. O. 1975 *Turbulence*, 2nd edn. McGrow-Hill.

Honkan, A. & Andreopoulos, Y. 1997 Vorticity, strain-rate and dissipation characteristics in the near-wall region of turbulent boundary layers. *J. Fluid Mech.* **350**, 29–96.

Hou, T. Y. & Li, R. 2008 Blowup or no blowup? the interplay between theory and numerics. *Physica D* **237**, 1937–1944.

Hunt, J. C. R., Wray, A. A. & Moin, P. 1988 Eddies, stream, and convergence zones in turbulent flows. *Center for Turbulence Research Report CTR-S88* pp. 193–208.

Hutchins, N. & Marusic, I. 2007 Evidence of very long meandering features in the logarithmic region of turbulent boundary layers. *J. Fluid Mech.* **579**, 1–28.

Jeong, J. & Hussain, F. 1995 On the identification of a vortex. *J. Fluid Mech.* **285**, 69–94.

Jiang, G. S. & Shu, C. W. 1996 Efficient implementation of weighted ENO schemes. *J. Comput. Phys.* **126**, 202–228.

Jiménez, J., del Álamo, J. C. & Flores, O. 2004 The large-scale dynamics of near-wall turbulence. *J. Fluid Mech.* **505**, 179–199.

Jimenez, J., Wray, A. A., Saffman, P. G. & Rogallo, R. S. 1993 The structure of intense vorticity in isotropic turbulence. *J. Fluid Mech.* **255**, 65–90.

Kerr, R. M. 1993 Evidence for a singularity of the three-dimensional, incompressible Euler equations. *Phys. Fluids A* **5**, 1725–1746.

Kida, S. 1985 Three-dimensional periodic flows with high-symmetry. *J. Phys. Soc. Jpn.* **54**, 2132–2136.

Kida, S. & Takaoka, M. 1994 Vortex reconnection. *Annu. Rev. Fluid Mech.* **26**, 169–189.

Kim, J., Moin, P. & Moser, R. 1987 Turbulence statistics in fully-developed channel flow at low Reynolds-number. *J. Fluid Mech.* **177**, 133–166.

Kim, K. C. & Adrian, R. J. 1999 Very large-scale motion in the outer layer. *Phys. Fluids* **11**, 417–422.

Kline, S. J., Reynolds, W. C., Schraub, F. A. & Runstadl, P. W. 1967 Structure of turbulent boundary layers. *J. Fluid Mech.* **30**, 741–773.

Koenderink, J. J. & Van Doorn, A. J. 1992 Surface shape and curvature scales. *Image Vision Comput.* **10**, 557–564.

Kraichnan, R. H. 1965 Lagrangian-history closure approximation for turbulence. *Phys. Fluids* **8**, 575–598.

Krauskopf, B., Osinga, H. M., Doedel, E. J., Henderson, M. E., Guckenheimer, J., Vladimirsky, A., Dellnitz, M. & Junge, O. 2005 A survey of methods for computing (un)stable manifold of vector fields. *Int. J. Bifurcat. Chaos* **15**, 763–791.

Lamb, H. 1932 *Hydrodynamics*, 6th edn. Cambridge University Press.

Leonard, A. 2009 The universal structure of high-curvature regions of material lines in chaotic flows. *J. Fluid Mech.* **622**, 167–175.

LeVeque, R. J. 1992 *Numerical methods for conservation laws*, 2nd edn. Birkhäuser Verlag.

Li, Y. & Meneveau, C. 2007 Material deformation in a restricted euler model for turbulent flows: Analytic solution and numerical tests. *Phys. Fluids* **19**, 015104.

LIM, T. T. & NICKELS, T. B. 1993 Instability and reconnection in the head-on collision of two vortex rings. *Nature* **357**, 225–227.

LINDSAY, K. & KRASNY, R. 2001 A particle method and adaptive treecode for vortex sheet motion in three-dimensional flow. *J. Comput. Phys.* **172**, 879–907.

LIU, Z. C., LANDRETH, C. C., ADRIAN, R. J. & HANRATTY, T. J. 1991 High-resolution measurement of turbulent structure in a channel with particle image velocimetry. *Exp. Fluids* **10**, 301–312.

LU, L. & DOERING, C. R. 2008 Limits on enstrophy growth for solutions of the three-dimensional Navier-Stokes equations. *Indiana U. Math. J.* **57**, 2693–2727.

LUNDGREN, T. S. 1982 Strained spiral vortex model for turbulent fine structure. *Phys. Fluid* **25**, 2193–2203.

MA, J., HUSSAINI, M. Y., VASILYEV, O. V. & LE DIMET, F.-X. 2009 Multiscale geometric analysis of turbulence by curvelets. *Phys. Fluids* **21**, 075104.

MAJDA, A. J. & BERTOZZI, A. L. 2001 *Vorticity and incompressible flow*. Cambridge University Press.

MARSDEN, J. E. & HUGHES, T. J. R. 1994 *Mathematical foundations of elasticity*. Dover.

MARUSIC, I. 2001 On the role of large-scale structures in wall turbulence. *Phys. Fluids* **13**, 735–743.

MARUSIC, I., MCKEON, B. J., MONKEWITZ, P. A., NAGIB, H. M., SMITS, A. J. & SREENIVASAN, K. R. 2010 Wall-bounded turbulent flows at high Reynolds numbers: Recent advances and key issues. *Phys. Fluids* **22**, 065103.

MENEVEAU, C. 1991 Analysis of turbulence in the orthonormal wavelet representation. *J. Fluid Mech.* **232**, 469–520.

MINGYU, H., KÜPPER, T. & MASBAUM, N. 1997 Computation of invariant tori by the Fourier methods. *SIAM J. Sci. Comput.* **18**, 918–942.

MISRA, A. & PULLIN, D. I. 1997 A vortex-based subgrid stress model for large-eddy simulation. *Phys. Fluids* **9**, 2443–2454.

MOIN, P. & KIM, J. 1982 Numerical investigation of turbulent channel flow. *J. Fluid Mech.* **118**, 341–377.

MOIN, P. & KIM, J. 1985 The structure of the vorticity field in turbulent channel flow. Part 1. Analysis of instantaneous fields and statistical correlations. *J. Fluid Mech.* **155**, 441–464.

Moisy, F. & Jiménez, J. 2004 Geometry and clustering of intense structures in isotropic turbulence. *J. Fluid Mech.* **513**, 111–133.

Monin, A. S. & Yaglom, A. M. 1975 *Statistical fluid mechanics of turbulence*. The MIT Press.

Moser, R. D., Kim, J. & Mansour, N. N. 1999 Direct numerical simulation of turbulent channel flow up to $Re_\tau = 590$. *Phys. Fluids* **11**, 943–945.

Nahum, A. & Seifert, A. 2006 Technique for backward particle tracking in a flow field. *Phys. Rev. E* **74**, 016701.

Nore, C., Abid, M. & Brachet, M. E. 1997 Decaying Kolmogorov turbulence in a model of superflow. *Phys. Fluids* **9**, 2644–2669.

Ohkitani, K. 2008 A geometrical study of 3D incompressible Euler flows with Clebsch potentials—a long-lived Euler flow and its power-law energy spectrum. *Physica D* **237**, 2020–2027.

Ohkitani, K. & Constantin, P. 2003 Numerical study of the Eulerian–Lagrangian formulation of the Navier-Stokes equations. *Phys. Fluids* **15**, 3251–3254.

Okamoto, N., Yoshimatsu, K., Schneider, K., Farge, M. & Kaneda, Y. 2007 Coherent vortices in high resolution direct numerical simulation of homogeneous isotropic turbulence: A wavelet viewpoint. *Phys. Fluids* **19**, 115109.

Ong, L. & Wallace, J. M. 1998 Joint probability density analysis of the structure and dynamics of the vorticity field of a turbulent boundary layer. *J. Fluid Mech.* **367**, 291–328.

Osher, S. & Fedkiw, R. 2003 *Level set methods and dynamic implicit surfaces*. Springer.

Panton, R. L. 2001 Overview of the self-sustaining mechanisms of wall turbulence. *Prog. Aerosp. Sci.* **37**, 341–383.

Pelz, R. B. 2001 Symmetry and the hydrodynamic blow-up problem. *J. Fluid Mech.* **444**, 299–320.

Peng, J. & Dabiri, J. O. 2008 An overview of a Lagrangian method for analysis of animal wake dynamics. *J. Exp. Biol.* **211**, 280–287.

Perry, A. E. & Chong, M. S. 1982 On the mechanism of wall turbulence. *J. Fluid Mech.* **119**, 173–217.

Perry, A. E., Henbest, S. & Chong, M.S. 1986 A theoretical and experimental-study of wall turbulence. *J. Fluid Mech.* **165**, 163–199.

Perry, A. E. & Marusic, I. 1995 A wall-wake model for the turbulence structure of boundary-layers. Part 1. Extension of the attached eddy hypothesis. *J. Fluid Mech.* **298**, 361–388.

Pope, S. B. 1987 Turbulent premixed flames. *Annu. Rev. Fluid Mech.* **19**, 237–270.

Pope, S. B. 2000 *Turbulent flows*. Cambridge University Press.

Pope, S. B., Yueng, P. K. & Girimaji, S. S. 1989 The curvature of material surfaces in isotropic turbulence. *Phys. Fluids A* **1**, 2010–2018.

Pullin, D. I. 1981 The non-linear behavior of a constant vorticity layer at a wall. *J. Fluid Mech.* **108**, 401–421.

Pullin, D. I. & Saffman, P. G. 1993 On the Lundgren–Townsend model of turbulent fine scales. *Phys. Fluid A* **5**, 126–145.

Pullin, D. I. & Saffman, P. G. 1998 Vortex dynamics in turbulence. *Annu. Rev. Fluid Mech.* **30**, 31–51.

Pumir, A., Shraiman, B. I. & Chertkov, M. 2000 Geometry of Lagrangian dispersion in turbulence. *Phys. Rev. Lett.* **85**, 5324–5327.

Pumir, A, Shraiman, B. I. & Siggia, E. D. 1992 Vortex morphology and Kelvin theorem. *Phys. Rev. A* **45**, R5351–R5354.

Pumir, A. & Siggia, E. 1990 Collapsing solutions to the 3-D Euler equations. *Phys. Fluids A* **2**, 220–241.

Rhines, P. B. & Young, W. R. 1983 How rapidly is a passive scalar mixed within closed streamlines? *J. Fluid Mech.* **133**, 133–145.

Ricca, R. L. 1994 The effect of torsion on the motion of a helical vortex filament. *J. Fluid Mech.* **273**, 241–259.

Robinson, S. K. 1991 Coherent motions in the turbulent boundary layer. *Annu. Rev. Fluid Mech.* **23**, 601–639.

Ruetsch, G. R. & Maxey, M. R. 1992 The evolution of small-scale structures in homogeneous isotropic turbulence. *Phys. Fluid A* **4**, 2747–2760.

Russo, G. & Smereka, P. 1999 Impulse formulation of the Euler equations: General properties and numerical methods. *J. Fluid Mech.* **391**, 189–209.

Saffman, P. G. 1992 *Vortex dynamics*. Cambridge University Press.

Salazar, J. P. L. C. & Collins, L. R. 2009 Two-particle dispersion in isotropic turbulent flows. *Annu. Rev. Fluid Mech.* **41**, 405–432.

SALMON, R. 1988 Hamiltonian fluid mechanics. *Annu. Rev. Fluid Mech.* **20**, 225–256.

SAWFORD, B. 2001 Turbulent relative dispersion. *Annu. Rev. Fluid Mech.* **33**, 289–317.

SCHUMACHER, J., SREENIVASAN, K. R. & YEUNG, P. K. 2005 Very fine structures in scalar mixing. *J. Fluid Mech.* **531**, 113–122.

SHE, Z. S., JACKSON, E. & ORSZAG, S. A. 1990 Intermittent vortex structures in homogeneous isotropic turbulence. *Nature* **344**, 226–228.

SHU, C. W., DON, W. S., GOTTLIEB, D., SCHILLING, O. & JAMESON, L. 2005 Numerical convergence study of nearly incompressible, inviscid Taylor-Green vortex flow. *J. Sci. Comput.* **24**, 569–595.

SIGGIA, E. D. 1985 Collapse and amplification of a vortex filament. *Phys. Fluids* **28**, 794–805.

SPALART, R. R., MOSER, R. D. & ROGERS, M. M. 1991 Spectral methods for the Navier-Stokes equations with one infinite and two periodic directions. *J. Comput. Phys.* **96**, 297–324.

STAM, J. 1999 Stable fluids. In *SIGGRAPH'99: Proceedings of the 26th annual conference on Computer graphics and interactive techniques*, pp. 121–128. New York, USA: ACM Press/Addison-Wesley Publishing Co.

TAYLOR, G. I. 1922 Diffusion by continuous movements. *Proc. Lond. Math. Soc.* **20**, 196–212.

TAYLOR, G. I. & GREEN, A. E. 1937 Mechanism of the production of small eddies from large ones. *Proc. Roy. Soc. Lond. A* **158**, 499–521.

THEODORSEN, T. 1952 Mechanism of turbulence. In *Proceedings of the Second Midwestern Conference on Fluid Mechanics, March 17–19*, pp. 1–18. Ohio State University, Columbus, OH.

TOSCHI, F. & BODENSCHATZ, E. 2009 Lagrangian properties of particles in turbulence. *Annu. Rev. Fluid Mech.* **41**, 375–404.

TOWNSEND, A. A. 1976 *The structure of turbulent shear flow*, 2nd edn. Cambridge University Press.

TRUESDELL, C. 1954 *The kinematics of vorticity*. Indiana University Press.

WALLACE, J. M., BRODKEY, R. S. & ECKELMAN, H. 1972 Wall region in turbulent shear flow. *J. Fluid Mech.* **54**, 39–48.

WANG, L. 2010 On properties of fluid turbulence along streamlines. *J. Fluid Mech.* **648**, 183–203.

WANG, L. P. & PETERS, N. 2006 The length-scale distribution function of the distance between extremal points in passive scalar turbulence. *J. Fluid Mech.* **554**, 457–475.

Warhaft, Z. 2000 Passive scalars in turbulent flows. *Annu. Rev. Fluid Mech.* **32**, 203–240.

Wolfram Research, Inc. 2008 *Mathematica.* v7.0.

Wu, X. & Moin, P. 2009 Direct numerical simulation of turbulence in a nominally zero-pressure-gradient flat-plate boundary layer. *J. Fluid Mech.* **630**, 5–41.

Xu, H., Ouellette, N. T. & Bodenschatz, E. 2008 Evolution of geometric structures in intense turbulence. *New J. Phys.* **10**, 013012.

Yang, Y., He, G.-W. & Wang, L.-P. 2008 Effects of subgrid-scale modeling on Lagrangian statistics in large-eddy simulation. *J. Turbul.* **9** (8), 1–24.

Yeung, P. K. 2002 Lagrangian investigations of turbulence. *Annu. Rev. Fluid Mech.* **34**, 115–142.

Yeung, P. K. & Pope, S. B. 1988 An algorithm for tracking fluid particles in numerical simulations of homogeneous turbulence. *J. Comput. Phys.* **79**, 373–416.

Ying, L., Demanet, L. & Candès, E. 2005 3D discrete curvelet transform. In *Proceedings of the Society of Photo–optical Instrumentation Engineers (SPIE)*, vol. 5914, pp. 351–361. SPIE.

Zhou, J., Adrian, R. J., Balachandar, S. & Kendall, T. M. 1999 Mechanisms for generating coherent packets of hairpin vortices in channel flow. *J. Fluid Mech.* **387**, 353–396.